



**HAL**  
open science

# Development of numerical simulation method for nonlinear elastodynamic : application to acoustic imaging of defect with the help of cavity chaotic transducer

Yifeng Li

► **To cite this version:**

Yifeng Li. Development of numerical simulation method for nonlinear elastodynamic : application to acoustic imaging of defect with the help of cavity chaotic transducer. Other. Ecole Centrale de Lille, 2009. English. NNT : 2009ECLI0014 . tel-00578755

**HAL Id: tel-00578755**

**<https://theses.hal.science/tel-00578755>**

Submitted on 22 Mar 2011

**HAL** is a multi-disciplinary open access archive for the deposit and dissemination of scientific research documents, whether they are published or not. The documents may come from teaching and research institutions in France or abroad, or from public or private research centers.

L'archive ouverte pluridisciplinaire **HAL**, est destinée au dépôt et à la diffusion de documents scientifiques de niveau recherche, publiés ou non, émanant des établissements d'enseignement et de recherche français ou étrangers, des laboratoires publics ou privés.

N° d'ordre: 106

ECOLE CENTRALE DE LILLE

## THESE

présentée en vue  
d'obtenir le grade de

## DOCTEUR

en

Spécialité: Micro et Nano Technologies, Acoustique et Télécommunications

par

**YiFeng LI**

DOCTORAT DELIVRE PAR L'ECOLE CENTRALE DE LILLE

Titre de la Thèse:

**Développement d'outils de simulation numérique pour l'élastodynamique non linéaire: Application à l'imagerie acoustique de défauts à l'aide de transducteur à cavité chaotique.**

Soutenue le 9 juillet devant le jury d'examen:

<b>Président</b>	<i>François Coulouvrat, DR, Institut Jean le Rond d'Alembert – UMR 7190</i>
<b>Rapporteur</b>	<i>Jean Pierre Remenieras, IR HDR, Inserm U930 - CNRS FRE 2448</i>
<b>Rapporteur</b>	<i>Koen Van Den Abeele, PR, K.U. leuven Campus Kortrijk</i>
<b>Membre</b>	<i>Philippe Pernod, PR, Ecole Centrale de Lille</i>
<b>Membre</b>	<i>Vladimir Preobrazensky, PR, Ecole Centrale de Lille</i>
<b>Directeur de thèse</b>	<i>Olivier Bou Matar – Lacaze, PR, Ecole Centrale de Lille</i>

Thèse préparée dans le Laboratoire IEMN

Ecole Doctorale SPI 072 (Lille I, Lille III, Artois, ULCO, UVHC, EC Lille)



# CONTENTS

<b>CONTENTS</b> .....	<b>I</b>
<b>RESUME</b> .....	<b>1</b>
<b>INTRODUCTION</b> .....	<b>16</b>
<b>CHAPTER 1: INTRODUCTION TO NONLINEAR NONDESTRUCTIVE TESTING AND IMAGING...</b>	<b>21</b>
<b>1.1 Introduction</b> .....	<b>21</b>
<b>1.2 Nonlinear Nondestructive Testing and Imaging Methods</b> .....	<b>21</b>
1.2.1 NEWS Methods .....	21
1.2.2 Linear and Nonlinear Ultrasonic Imaging Methods for NDT .....	22
1.2.3 TR and NEWS Combined Methods .....	23
<b>1.3 Nonlinear Elasticity and Elastodynamic Equations</b> .....	<b>28</b>
1.3.1 Nonlinear 1D Propagation Model in Heterogeneous Elastic Media .....	28
1.3.2 “Classical” and “Non-classical” Nonlinear Elasticity.....	29
1.3.3 Nonlinear Elastodynamic System of Equations .....	40
<b>1.4 Numerical Simulation Methods</b> .....	<b>44</b>
1.4.1 Finite Difference Method .....	45
1.4.2 Finite Volume Method.....	46
1.4.3 Finite Element Method.....	48
1.4.4 Pseudo-Spectral Method .....	50
1.4.5 Discontinuous Galerkin Finite Element Method .....	51
<b>1.5 Pseudo-Spectral Simulation of 1D Nonlinear Propagation in Elastic Media</b> .....	<b>54</b>
1.5.1 The Elastic Wave Solver .....	54
1.5.2 Shock Wave Simulation .....	57
1.5.3 Rod Resonance Simulation .....	60
<b>1.6 Conclusion</b> .....	<b>62</b>
<b>CHAPTER 2: THE NODAL DISCONTINUOUS GALERKIN METHOD</b> .....	<b>64</b>
<b>2.1 Introduction</b> .....	<b>64</b>
<b>2.2 Discontinuous Galerkin Finite Element Method Scheme in 2D</b> .....	<b>66</b>
2.2.1 General Formulation of Discontinuous Galerkin Schemes.....	66
2.2.2 Defining Discontinuous Galerkin Operators on Triangular Elements .....	68
2.2.3 Numerical Fluxes in the Discontinuous Galerkin Method .....	72
2.2.4 Discontinuous Galerkin Operators on Quadrilateral Element.....	74
2.2.5 Time-Stepping and Discrete Stability .....	76
<b>2.3 Boundary Conditions</b> .....	<b>78</b>
2.3.1 Open Boundaries .....	78
2.3.2 Stress Free and Fixed Surface Boundaries.....	78
<b>2.4 Sources</b> .....	<b>80</b>

<b>2.5 Numerical Validation: Comparison with Analytical Solutions.....</b>	<b>81</b>
2.5.1 Linear Isotropic Simulation of Lamb’s Problem.....	82
2.5.2 Linear Simulation of Elastic Waves Propagation in Anisotropic Apatite Material.....	85
2.5.3 Attenuation.....	87
2.5.4 Simulation of Wave Propagation in “Classical” Nonlinear Elastodynamic Material .....	90
<b>2.6 Conclusion.....</b>	<b>96</b>
<b>CHAPTER 3: PML ABSORBING BOUNDARY CONDITION .....</b>	<b>97</b>
<b>3.1 Introduction.....</b>	<b>97</b>
<b>3.2 C-PML for Second-Order Elastodynamic Wave Equations .....</b>	<b>98</b>
3.2.1 Wave Equations for Anisotropic Solid in 2D .....	98
3.2.2 C-PML Elastic Wave Equations in Frequency Domain.....	99
3.2.3 Interpretation of C-PML as an Anisotropic Solid Medium .....	100
3.2.4 C-PML Elastic Wave Equations in Time Domain .....	101
3.2.5 Numerical Simulations .....	103
<b>3.3 C-PML Formulation for Piezoelectric Solid.....</b>	<b>111</b>
3.3.1 Wave Equations for Piezoelectric Solid in 2D .....	112
3.3.2 Formulation of C-PML in Frequency Domain .....	112
3.3.3 Formulation of C-PML in Time Domain.....	114
3.3.4 Numerical Simulations .....	117
<b>3.4 Nearly Perfectly Matched Layer (NPML) for Elastic Solid.....</b>	<b>121</b>
3.4.1 Formulation of NPML for Elastic Wave Propagation .....	121
3.4.2 Comparison of NPML with C-PML.....	123
<b>3.5 Stabilized Absorbing Boundary Layer.....</b>	<b>129</b>
3.5.1 Formulation of Stabilized Absorbing Boundary Layer.....	129
3.5.2 Stability Analysis .....	131
3.5.3 Numerical Simulations of MPML for Anisotropic Solid Medium .....	135
3.5.4 Application to Propagation in Isotropic and Piezoelectric Plate .....	138
<b>3.6 Conclusion.....</b>	<b>142</b>
<b>CHAPTER 4: APPLICATION OF CHAOTIC CAVITY TRANSDUCER TO LINEAR AND NONLINEAR ELASTIC IMAGING .....</b>	<b>144</b>
<b>4.1 Introduction.....</b>	<b>144</b>
<b>4.2 Principle of Chaotic Cavity Transducer .....</b>	<b>145</b>
4.2.1 Principle of One Channel Time Reversal Acoustic.....	145
4.2.2 An Instructive Experiment .....	149
4.2.3 Chaotic Cavity Transducer.....	152
4.2.4 Signal Processing Methodology .....	152
4.2.5 Numerical Simulations of Chaotic Cavity Transducer .....	157
<b>4.3 Experiments in a Reverberant Medium.....</b>	<b>163</b>
4.3.1 Set-up of the Experiment .....	163
4.3.2 Experimental Results .....	163

CONTENTS

4.3.3 Contrast of the Retro-Focalized Signal.....	168
4.4 Experiments on a Non-Reverberant Medium .....	171
4.5 Nonlinear Acoustic Imaging with Chaotic Cavity Transducer.....	174
4.5.1 TR-NEWS Experiment with Chaotic Cavity Transducer.....	174
4.5.2 NEWS-TR Experiment with Chaotic Cavity Transducer.....	176
4.6 Conclusion.....	178
CONCLUSION .....	180
APPENDIX A: ANALYTICAL SOLUTION FOR THE PROPAGATION OF ELASTIC WAVES IN UNBOUNDED ANISOTROPIC SOLID.....	183
APPENDIX B: C-PML MEMORY VARIABLES EVOLUTION EQUATIONS .....	185
BIBLIOGRAPHY .....	187
PUBLICATION LIST .....	200



## RESUME

Les avancées récentes dans le domaine des matériaux innovants nécessitent le développement de techniques de Contrôle Non Destructif (CND) et d'imagerie qui permettent la quantification et la localisation de défauts micro-structuraux dans une large variété de matériaux, et cela durant leur fabrication et toute leur durée de vie. Le contrôle de ces matériaux, incluant entre autre les alliages, les bétons et les composites assure à la fois leur qualité et leur fiabilité. La principale difficulté, pour la caractérisation d'un processus de détérioration d'une structure, provient du fait que le matériau ne présente généralement que peu de signes d'endommagement avant l'apparition de délaminations ou de macro-fissures. Parmi les techniques actuelles de CND, les méthodes ultrasonores sont considérées comme des outils performants, et ont connu un essor considérable ces dernières décennies. Généralement, elles reposent sur des principes d'acoustique linéaire, et sont limitées à la détection de défauts de grande taille.

Du fait d'une intense activité de recherche dans le domaine de l'acoustique non linéaire, un type de méthodes innovantes de CND, appelées "Nonlinear Elastic Wave Spectroscopy" (NEWS), ont récemment été développées afin de détecter de manière précoce l'apparition d'endommagement. Le concept de base des méthodes NEWS repose sur le fait que la formation de défauts à l'intérieure d'une structure puisse être détectée immédiatement par l'augmentation des paramètres non linéaires. De nombreuses études ont démontré de manière irréfutable que la forte non linéarité macroscopique du matériau était fortement liée à la quantité de micro- imperfections, comme des fissures ou des liaisons faibles, qu'il contient. En effet, ces imperfections ont un comportement tellement non linéaire, que même une excitation acoustique de faible amplitude produit une réponse macroscopique mesurable. Les méthodes NEWS utilisées, dans un premier temps, pour la détermination globale de l'état de fatigue de structure, ont été récemment étendues afin d'imager des défauts en utilisant des techniques de vibrométrie laser, des ultrasons aériens ou de la cartographie d'onde de cisaillement. Depuis environ cinq ans, l'idée de combiner les attraits des méthodes NEWS et du Retournement Temporel Acoustique (RTA), qui fournit la possibilité de focaliser des ondes ultrasonores, aussi bien dans le temps que l'espace, et cela quelque soit la position de la source et de l'hétérogénéité du milieu de propagation, a été proposée pour l'imagerie non linéaire de défauts. Les principes d'imagerie non linéaire basés sur cette combinaison, retournement temporel / effet non linéaires, peuvent être classés en deux catégories que l'on appelle généralement NEWS-TR et TR-NEWS comme l'indique la Figure 1.

## RESUME

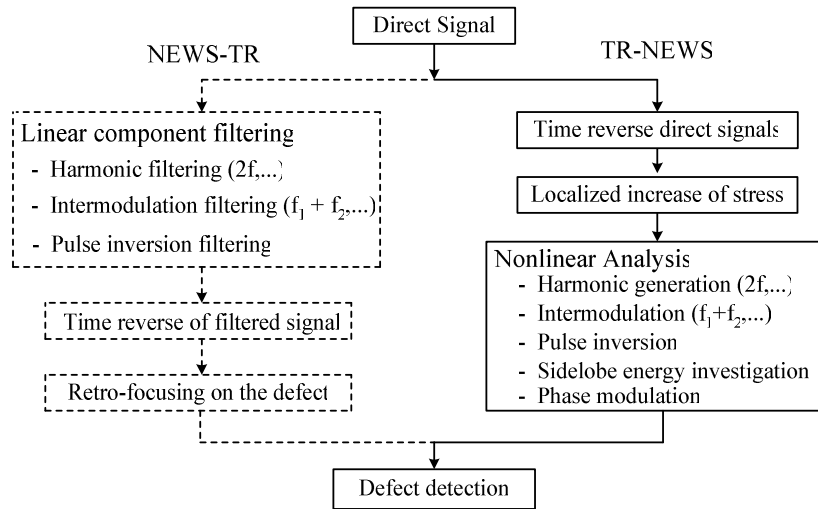


**Fig. 1** Méthodes de détection de défauts basées sur une combinaison du RTA et des méthodes NEWS.

Les méthodes NEWS-TR, pour lesquelles on filtre d'abord les composantes non linéaires de la réponse de l'échantillon à une excitation globale, puis on utilise le processus de retournement temporel, permettent de focaliser l'énergie sur le défaut. Les méthodes TR-NEWS, pour lesquelles les deux processus sont inversés, permettent d'augmenter localement les contraintes. On peut ainsi regarder la réponse non linéaire de l'échantillon à une excitation de forte amplitude cette fois-ci localisée. Dans la majorité des applications en CND de ce concept, un système de RTA à un canal a été utilisé en collant directement sur l'échantillon une céramique piézoélectrique comme le montre la Figure 2. Dans un premier temps on envoie un signal source à l'aide d'un transducteur piézoélectrique. La vitesse particulière est mesurée par un vibromètre laser en un point donné. Le signal obtenu est un signal multi réverbérant, si on veut que le procédé fonctionne. Puis on envoie le signal retourné temporellement à l'aide du même transducteur. Enfin, si on mesure la vitesse particulière juste autour du même point, on constate que l'onde se focalise sur cette même position et qu'elle se re-comprime temporellement. L'échantillon doit alors être suffisamment petit pour pouvoir être considéré comme réverbérant dans la bande de fréquences utilisées, afin que la focalisation par RTA à un canal fonctionne. Dans l'industrie aéronautique, les structures sont fréquemment des plaques de grandes dimensions fabriquées dans des matériaux composites fortement atténuants. L'imagerie ultrasonore de ces structures pour des fins de contrôle santé intégré a souvent été réalisée à l'aide d'onde de Lamb. Mais dans de tels échantillons non réverbérants la méthode de focalisation par RTA est difficilement applicable.

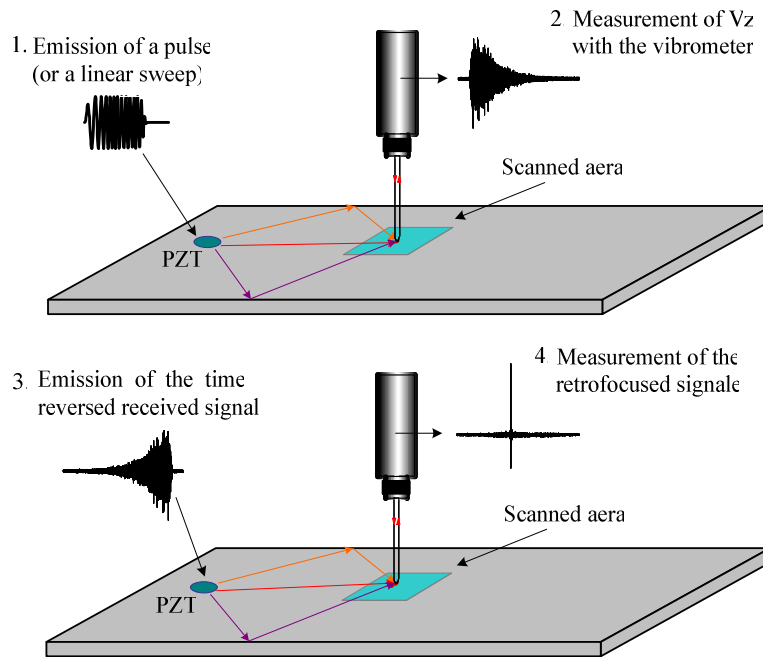


**Fig. 2** Principe du Retournement Temporel (RT) à un canal pour la focalisation d'une onde élastique dans un échantillon solide réverbérant.

Dans cette thèse nous proposons de développer un système d'imagerie ultrasonore innovante de micro-défauts basé sur l'utilisation conjointe de technique NEWS et du concept de "transducteur à cavité chaotique". Ce transducteur correspond à la combinaison d'une céramique piézoélectrique collée sur une cavité de forme chaotique et du principe de retournement temporel comme le montre la Figure 3. L'onde générée par la céramique se propage dans la cavité. A chaque fois que l'onde arrive sur l'interface entre la cavité et l'échantillon une partie de l'énergie reste dans la cavité et subie des réflexions multiples. L'autre partie de l'énergie est transmise dans l'échantillon. Ici même si l'échantillon n'est pas réverbérant, le processus utilise les modes propres de la cavité. Les avantages des Transducteurs à cavité chaotique sont les suivants : il n'y a plus d'influence de la géométrie de l'échantillon et on peut l'utiliser pour des échantillons non réverbérants. Par contre, l'énergie transmise à l'échantillon sera moins importante.

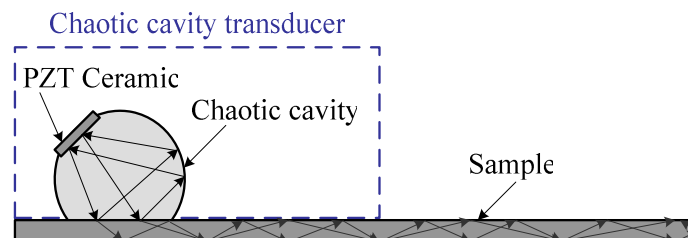


**Fig. 3** Principe des "transducteurs à cavité chaotique".

La faisabilité et les performances de ce nouveau système sont explorées par des simulations numériques. Des paramètres optimaux d'utilisation pour une implémentation expérimentale sont proposés. Ainsi, une grande partie des travaux menés dans le cadre de cette thèse se rattache au domaine de la détection et de l'imagerie de défauts par acoustique non linéaire, et tout particulièrement sur le développement d'outils numériques permettant l'amélioration de telles techniques d'imagerie.

Un schéma d'éléments finis de type Galerkin Discontinu (GD), une combinaison judicieuse des méthodes d'éléments finis et de volumes finis, est présentée. Différents flux numériques, comme le flux de Lax-Freidrich ou de Godunov, et l'introduction de conditions aux limites libres ou sans contraintes sont présentés. Les principales contributions de cette thèse au développement du code numérique sont l'introduction de l'elastodynamique non linéaire, et la possibilité d'utiliser des éléments quadrilatéraux. De plus, un type de zone absorbante parfaitement adaptée (PML), appelée "Nearly Perfectly Matched Layer" (NPML), pouvant être facilement intégrée au code numérique DG a aussi été développé. Enfin, une implémentation par sous domaine a été introduite afin d'améliorer l'efficacité du schéma numérique lorsque les PML sont utilisées. Celle-ci permettra d'autre part d'implémenter facilement des problèmes multi- physiques. Afin de valider l'implémentation du schéma de Galerkin Discontinu des configurations de test ont été réalisées. La première simulation correspond au problème de Lamb dans un matériau isotrope linéaire. Une source impose une contrainte ponctuelle sur une interface libre. Deux récepteurs sont positionnés à 850 et 1200 m de la source sur la même interface. La Figure 4 montre les fronts d'onde au temps 0.7 secondes. Maintenant si on compare les vitesses particulières horizontales et verticales calculées pour les deux récepteurs avec des solutions analytiques, on trouve que la correspondance est excellente dans tous les cas comme le montre la Figure 5. D'autres simulations de propagation dans un milieu anisotrope valident encore l'implémentation du schéma DG à l'aide de comparaisons avec des solutions analytiques connues.

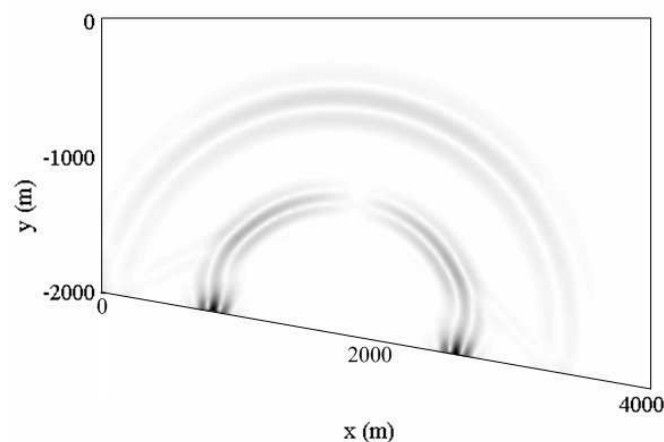


**Fig. 4** Amplitude de la vitesse  $v$  à  $t = 0.7$  s calculée avec un schéma RK-DG-FEM O5 utilisant des éléments triangulaire.

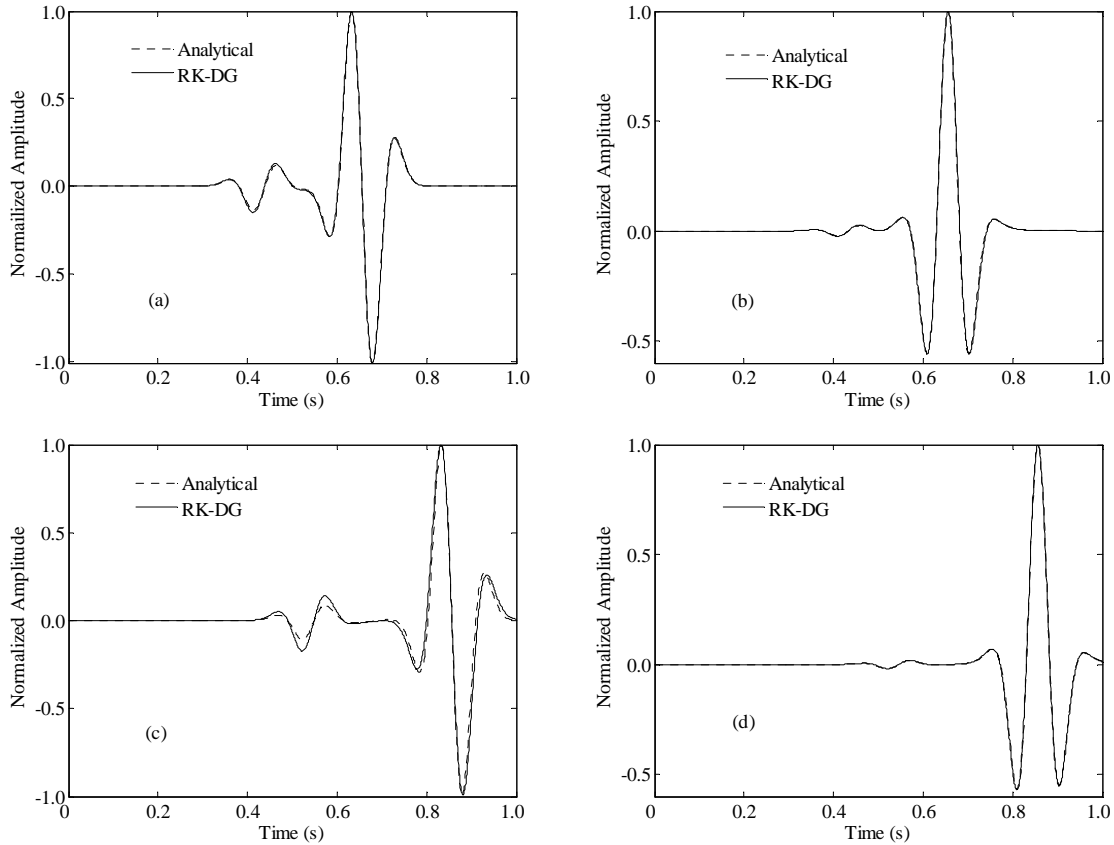


**Fig. 5** Comparaison d'une solution analytique de référence avec des résultats de simulation obtenus pour deux récepteurs en utilisant un schéma d'ordre 5 RK-DG-FEM O5. La première colonne (a) et (b) sont pour le récepteur 1 et la seconde colonne (c) et (d) pour le récepteur 2. Dans ligne la figure de droite présente la vitesse particulière horizontale et la figure de gauche la vitesse particulière verticale.

Dans le cas non linéaire, comme très peu de résultats analytiques sont disponibles, la propagation d'une onde plane a été considérée. Pour faire cette simulation, on a utilisé une ligne source. On voit sur la Figure 6 les fronts d'onde au temps 0.48 seconde. Sur la Figure 7, les spectres des signaux calculés à des distances de 3, 6 et 10 longueurs d'onde de la source montrent qu'une composante de l'onde transverse apparaît sur  $V_x$ . Cela correspond à un couplage entre l'onde transverse et longitudinale. D'une part les composantes aux deuxièmes harmoniques de  $V_x$  se déforment fortement au cours de la propagation et leurs amplitudes n'augmentent pas en fonction de la distance, contrairement à ce qui est obtenu dans un fluide. Les résultats obtenus sont en parfait accord avec ceux de résultats de simulations numériques publiés dans la littérature, et de solutions analytiques approchées.

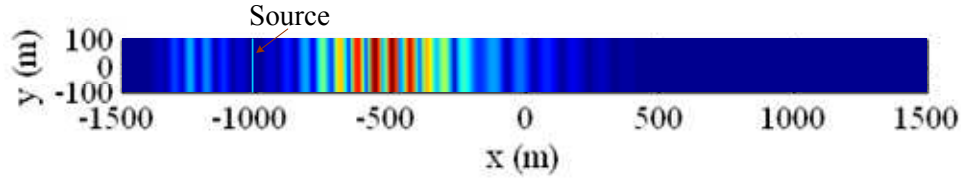


**Fig. 6** Amplitude de la vitesse pour une onde plane dans un milieu non linéaire à  $t = 0.48$  s obtenue avec un schéma RK-DG-FEM O5 utilisant des éléments quadrilatéraux.

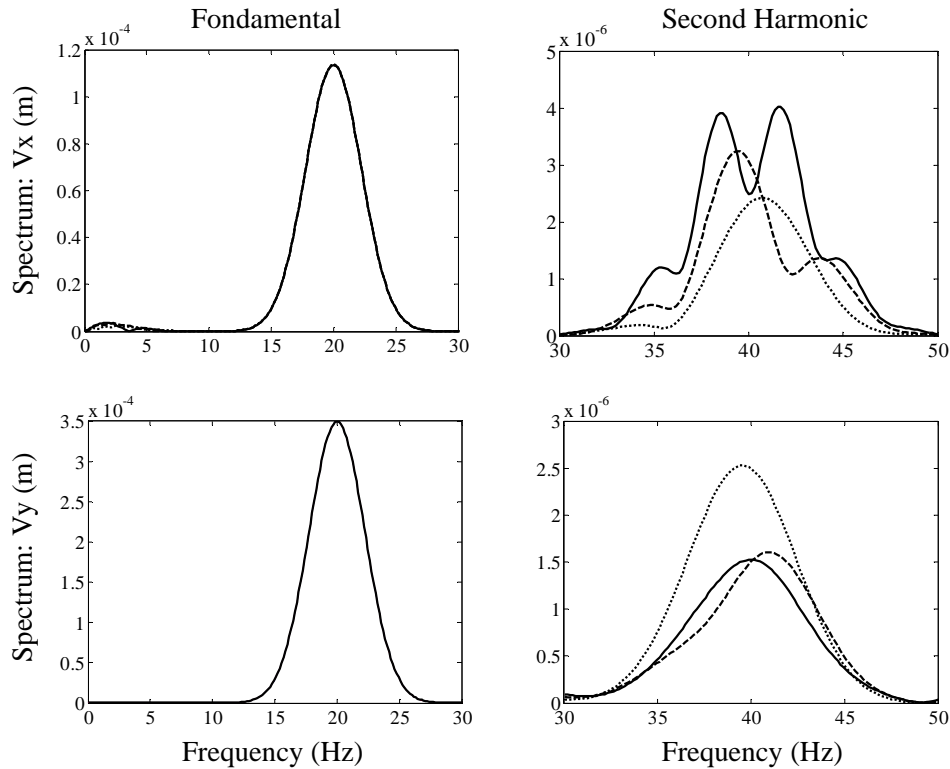


**Fig. 7** Spectres des vitesse  $V_x$  (première ligne) et verticale  $V_y$  (deuxième ligne) des signaux obtenus numériquement pour la propagation d'une onde plane dans un milieu non linéaire à des distances de 3 (ligne de points), 6 (ligne pointillée) et 10 (ligne solide) longueurs d'onde longitudinale.

Pour simuler la propagation dans un milieu infini ou semi infini, nous avons choisi d'introduire des PML. Les PML (Perfectly Matched Layer) sont des zones à la fois atténuantes et possédant la propriété d'être parfaitement adaptée en impédance avec le domaine de calcul quelque soit l'angle d'incidence et la fréquence. Une nouvelle formulation des C-PML, basée sur le système du deuxième ordre décrivant, à l'aide d'une formulation déplacement / contrainte, la propagation d'ondes élastiques dans des solides anisotropes et piézoélectriques, est introduite. Cette formulation est implémentée dans un code commercial d'éléments finis (COMSOL Multiphysics) et dans un code pseudo spectral. Les résultats de simulation, pour des solides anisotropes et piézoélectriques, confirment l'excellente capacité d'absorption des C-PML pour des simulations d'ondes de surfaces et de domaines de calcul allongés, comme le montre la Figure 8.

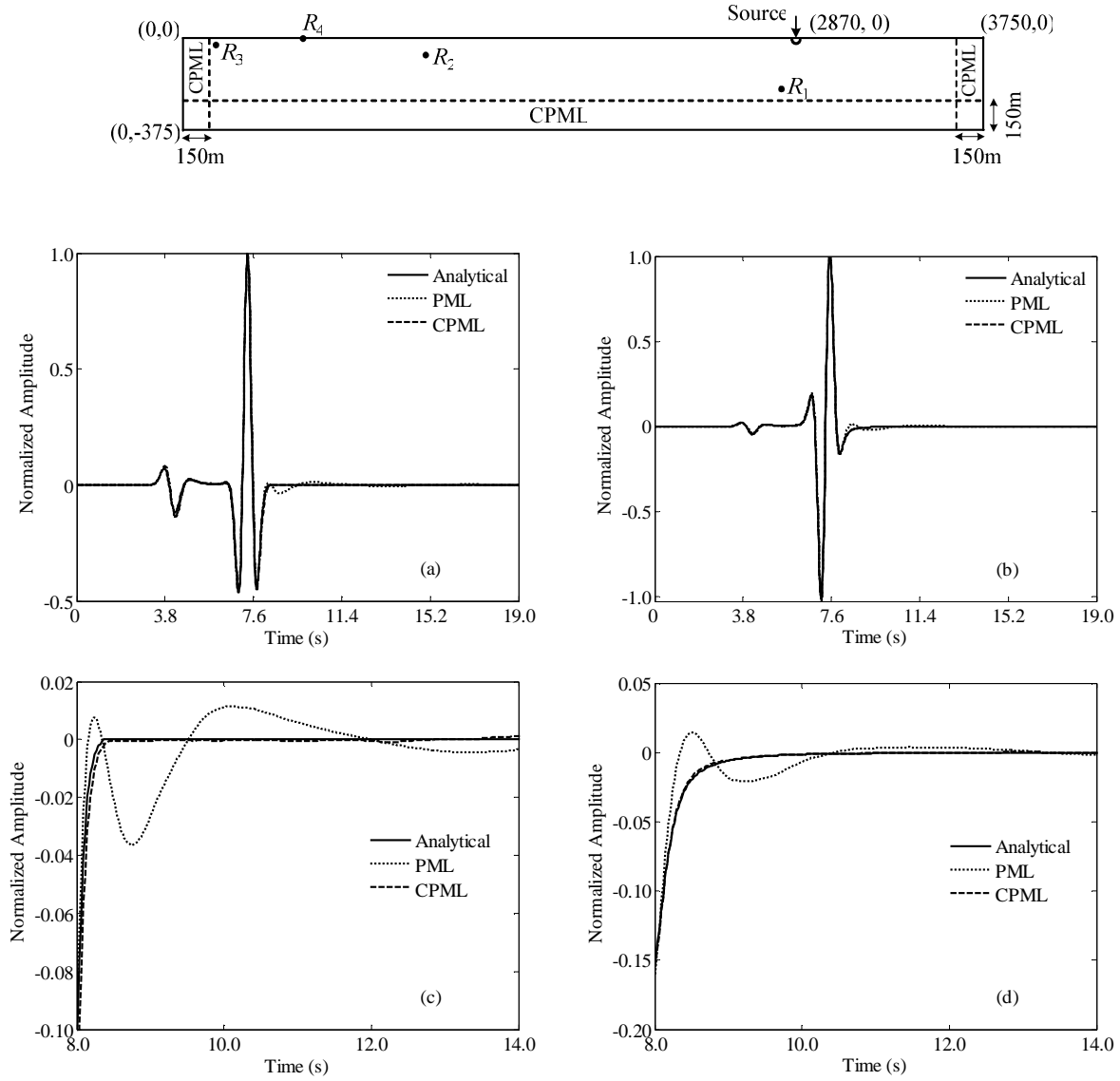


**Fig. 8** Model utilise pour la simulation de la propagation d'ondes de surface dans un solide isotrope allongé. Les C-PML sont positionnées sur la droite, la gauche et le bas du domaine de calcul. L'interface supérieure est une surface libre. Les positions de la source  $S$  et quatre récepteurs ( $R_1$ ,  $R_2$ ,  $R_3$ ,  $R_4$ ) sont aussi présentées. Les évolutions temporelles des composantes horizontale  $u_1$  (a) et verticale  $u_2$  (b) du déplacement particulaire au récepteur  $R_4$  obtenues par une solution analytique (ligne solide) et numériquement avec des C-PML (ligne pointillée) et des PML (ligne de points) sont comparées. (c) and (d) sont des zooms de (a) et (b) respectivement, montrant le bénéfice d'utiliser des C-PML au lieu de PML.

Dans toutes les implémentations présentées des C-PML, des équations différentielles aux dérivés partielles sont introduites pour faire évoluer dans le temps les variables supplémentaires introduites par les C-PML. Ces équations différentielles aux dérivés partielles, du fait qu'elles contiennent des dérivées spatiales, sont difficiles à introduire dans le code DG développé, et tout particulièrement lorsqu'un flux numérique de type Godunov est utilisé. Pour palier à cette difficulté, les NPML sont appliquées à la propagation d'ondes élastiques dans les milieux anisotropes. Le principal intérêt de cette formulation de zone

absorbante parfaitement adaptée est lié au fait que le système d'équations reste sous une forme identique au système de départ, c'est-à-dire fortement hyperbolique, et que les flux modifiés par les PML sont reliés aux flux physiques par de simples équations différentielles ordinaires. Ce dernier point réduit considérablement la difficulté et le temps de calcul. De plus, ces NPML ont exactement les mêmes propriétés d'absorption que les C-PML, comme le montre les Figures 9 et 10 qui présentent un calcul de propagation d'onde élastique dans le solide anisotrope dont les constantes sont données dans le tableau 1. On constate sur la Figure 9 que même avec une dynamique de 100 dB les NPML absorbent parfaitement les ondes. De plus si on calcul l'énergie contenue dans la zone de calcul hors PML au cours du temps pour les NPML et les C-PML on constate que les résultats obtenus sont parfaitement identiques (Figure 10). On voit donc que l'approximation faite pour la dérivation des NPML n'a pas d'impact sur leur qualité d'absorption.

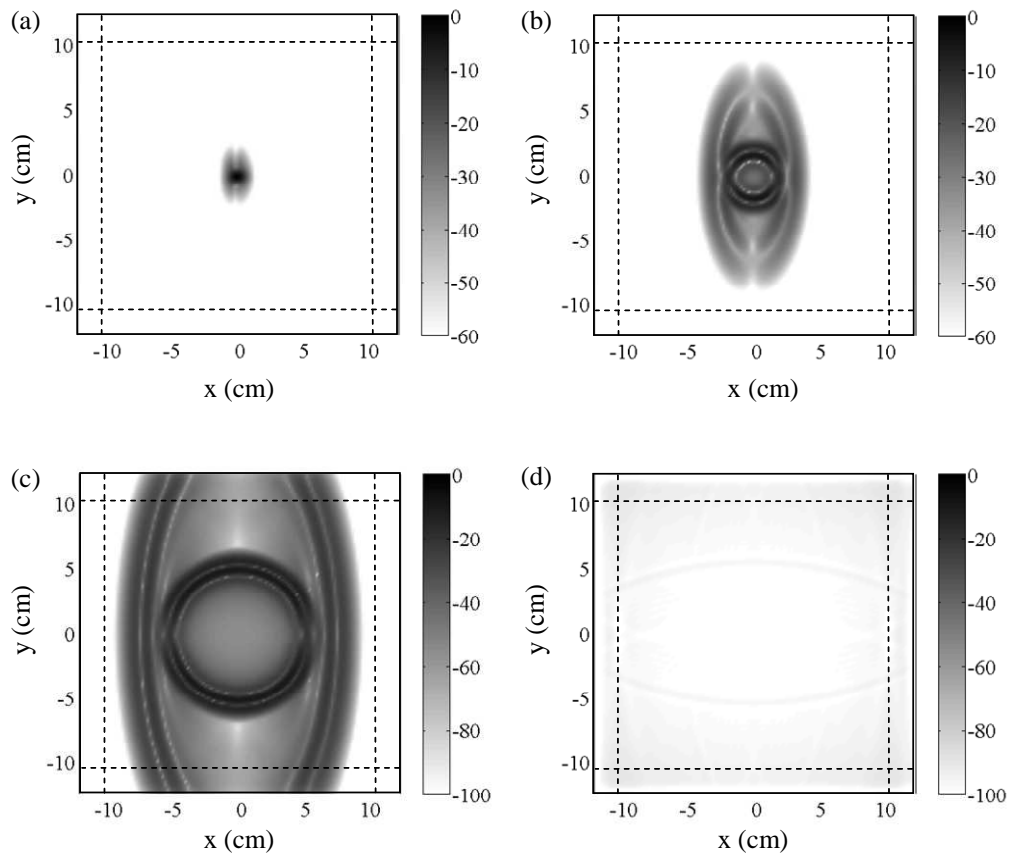


**Fig. 9** Amplitude des déplacements obtenue lors la propagation d'une onde élastique dans un milieu orthotrope (milieu I) aux instants (a)  $t = 5 \mu\text{s}$ , (b)  $t = 15 \mu\text{s}$ , (c)  $t = 30 \mu\text{s}$ , and (d)  $t = 125 \mu\text{s}$ . Les figures sont en échelle logarithmique (dB) avec une amplitude de 10 nm comme référence.

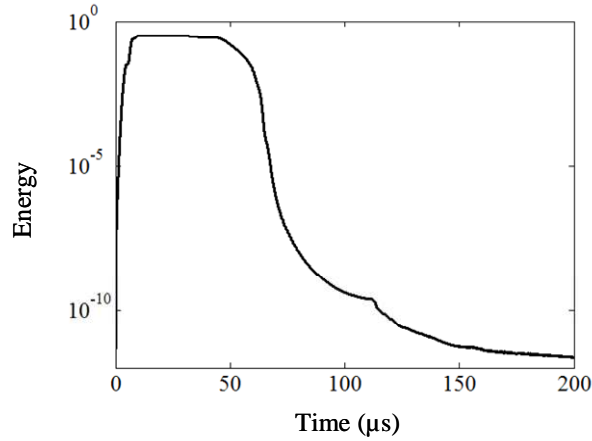


**Fig. 10** Evolution temporelle de l'énergie dans le domaine de calcul, hors PML, pour les C-PML (ligne pointillée) et les NPML (ligne solide) pour un solide orthotrope (milieu I), pour les mêmes conditions que celles utilisées pour obtenir la Figure 9.

**Tab. 1** Propriétés des matériaux orthotropes utilisés lors des simulations.

Material	$\rho$ (kg/m <sup>3</sup> )	$C_{11}$ (GPa)	$C_{22}$ (GPa)	$C_{12}$ (GPa)	$C_{66}$ (GPa)
<b>I</b>	4000	40	200	38	20
<b>III</b>	4000	40	200	75	20

Il est connu que pour certains matériaux anisotropes les PML sont instables. Si on refait les calculs précédents dans un matériau noté III ici dont les constantes sont identiques au cas précédent sauf pour  $C_{12}$ . La figure 11 montre que les ondes entrant dans la PML sont amplifiées au lieu d'être atténuées.

## RESUME

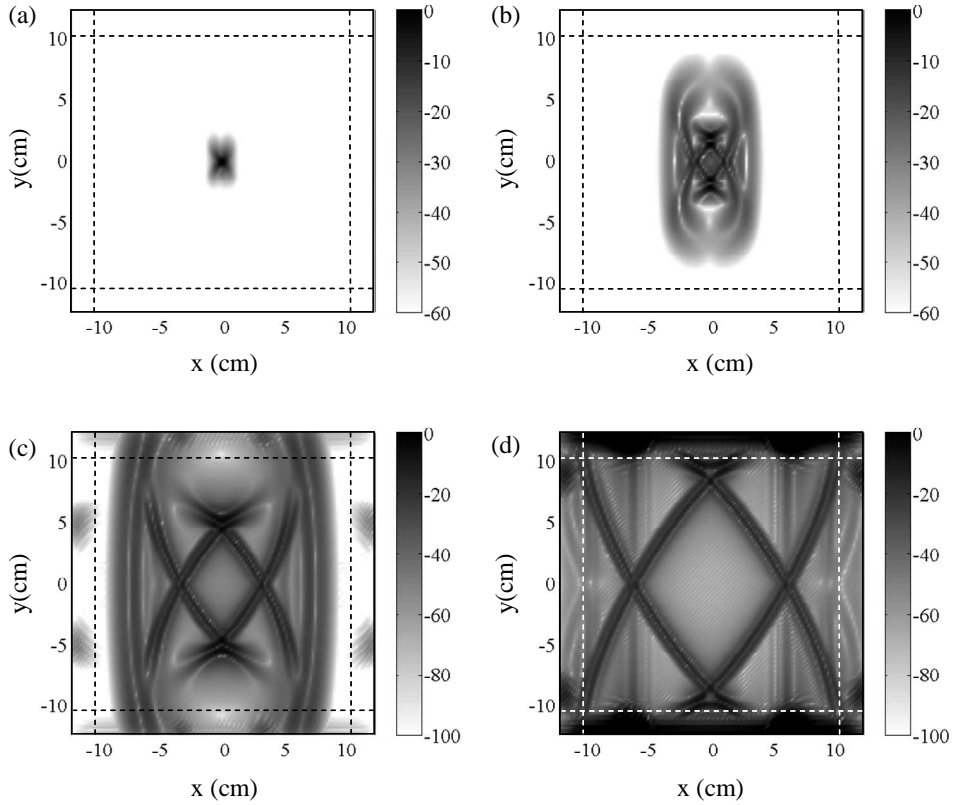


**Fig. 11** Amplitude des déplacements obtenue lors la propagation d'une onde élastique dans un milieu orthotrope (milieu III) aux instants (a)  $t = 5 \mu\text{s}$ , (b)  $t = 15 \mu\text{s}$ , (c)  $t = 30 \mu\text{s}$ , and (d)  $t = 50 \mu\text{s}$ . Les figures sont en échelle logarithmique (dB) avec une amplitude de 10 nm comme référence. Des instabilités apparaissent dans les NPML.

En fait, il a été montré par Bécache que si on regardait les courbes de lenteurs du matériau (Figure 12) alors celles qui présentaient des parties pour lesquelles les vitesses de phase et de groupe étaient de signe inverse, correspondaient à des zones d'instabilités des PML suivant  $x$  en bleu ou  $y$  en violet.

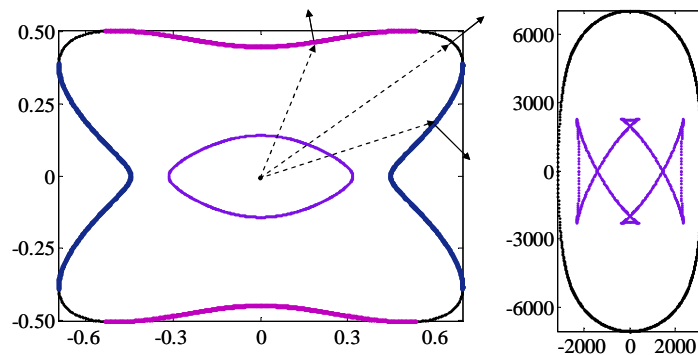


**Fig. 12** Courbe de lenteur (à gauche) et fronts d'ondes (droite) pour le milieu III. Les lignes violettes correspondent à des directions d'incidence pour lesquelles les NPLM suivant  $x$  sont instables. Les lignes bleues correspondent à des directions d'incidence pour lesquelles les NPLM suivant  $y$  sont instables.

En suivant le concept de "MPML" introduit récemment dans la littérature, nous considérons un mélange de C-PML et de zone atténuante, en contrôlant la proportion de chacun de ces deux types de zone absorbante afin de stabiliser les C-PML ou les NPML. Il est démontré que ces C-PML stabilisées ne sont alors plus parfaitement adaptées en impédance au reste du domaine de calcul. Une étude complète de stabilité est menée. Elle permet de donner une interprétation physique du critère de stabilité obtenu précédemment dans la littérature pour les "MPML" : Les vitesses de groupe et de phase de l'onde incidente dans la PML doivent posséder le même signe. Sur la Figure 13 on voit que le calcul de propagation d'onde élastique dans le milieu III n'explose plus lorsque l'on utilise des MPML. Par contre le niveau d'ondes réfléchies est bien supérieur à celui obtenu avec seulement des C-PML dans le milieu I.

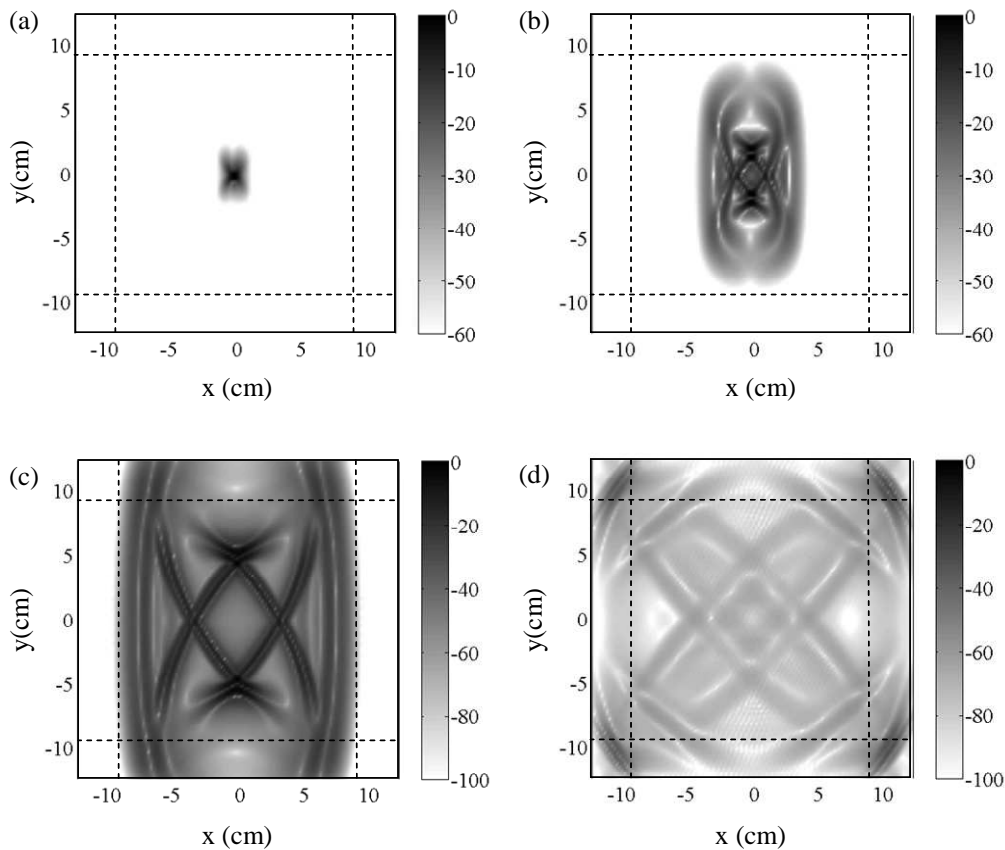


**Fig. 13** Amplitude des déplacements obtenue lors la propagation d'une onde élastique dans un milieu orthotrope (milieu III) aux instants (a)  $t = 5 \mu\text{s}$ , (b)  $t = 15 \mu\text{s}$ , (c)  $t = 30 \mu\text{s}$ , and (d)  $t = 125 \mu\text{s}$ . Les figures sont en échelle logarithmique (dB) avec une amplitude de 10 nm comme référence. Aucune instabilités n'apparaissent pour les MPML utilisées.

Pour la simulation des ondes de Lamb, ces C-PML stabilisées permettent d'absorber les modes inverses. Cette absorption se fait au détriment de la longueur de la zone absorbante qui doit alors être d'au moins deux fois la longueur d'onde la plus grande existante dans la plaque

pour la plage de fréquence considérée. Dans ce cas le niveau de réflexion obtenu est -80dB par rapport à l'énergie incidente.

Finalement, une étude numérique et expérimentale sur l'utilisation du concept de "transducteur à cavité chaotique" pour la focalisation dans un milieu solide, réverbérant ou non, en utilisant une seule source est réalisée. Les méthodes de retournement temporel, de filtre inverse et de retournement temporel 1-bit sont présentées et comparées. Dans le but de transmettre plus d'énergie dans le milieu et augmenter le rapport signal sur bruit, un signal source modulé en fréquence est utilisé. L'utilisation de la méthode de filtrage inverse à la place du retournement temporel permet lors du processus de focalisation de tirer avantage de tous les modes propres de la cavité, y compris ceux de faible énergie qui sont peu exploités par le retournement temporel. Cela améliore la re-compression temporelle ainsi que le rapport signal sur bruit (Figure 14).

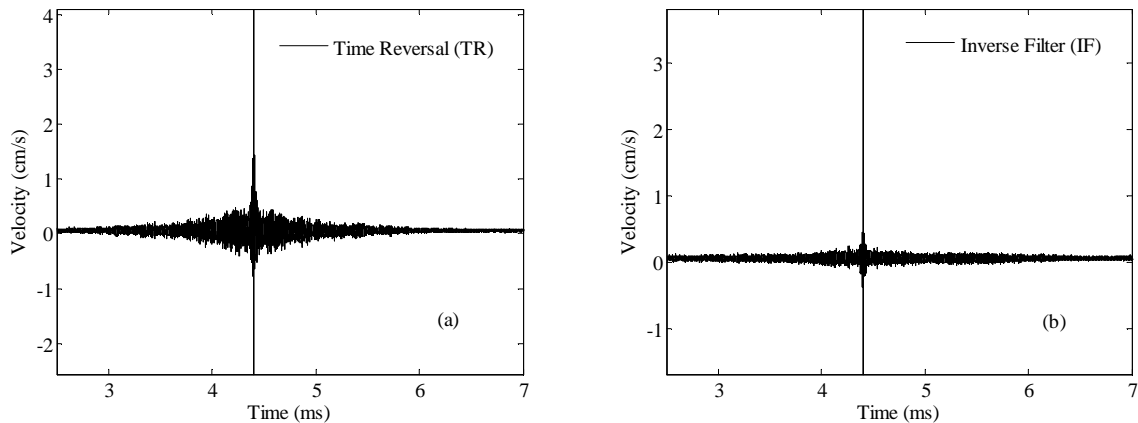


**Fig. 14** Comparaison des signaux de recompression temporelle obtenus pour la focalisation par (a) Retournement Temporel (TR), (b) et Filtre Inverse (IF).

Un des principaux avantages de l'utilisation d'une cavité chaotique, démontré aussi bien numériquement (Figure 15) qu'expérimentalement, est la suppression des images fantômes et des effets de bords généralement présents lors du processus de rétro-focalisation. Les résultats expérimentaux obtenus dans un échantillon réverbérant d'acier démontrent la capacité du "transducteur à cavité chaotique" à focaliser y compris sur les bords de l'échantillon (Figure 16).

## RESUME

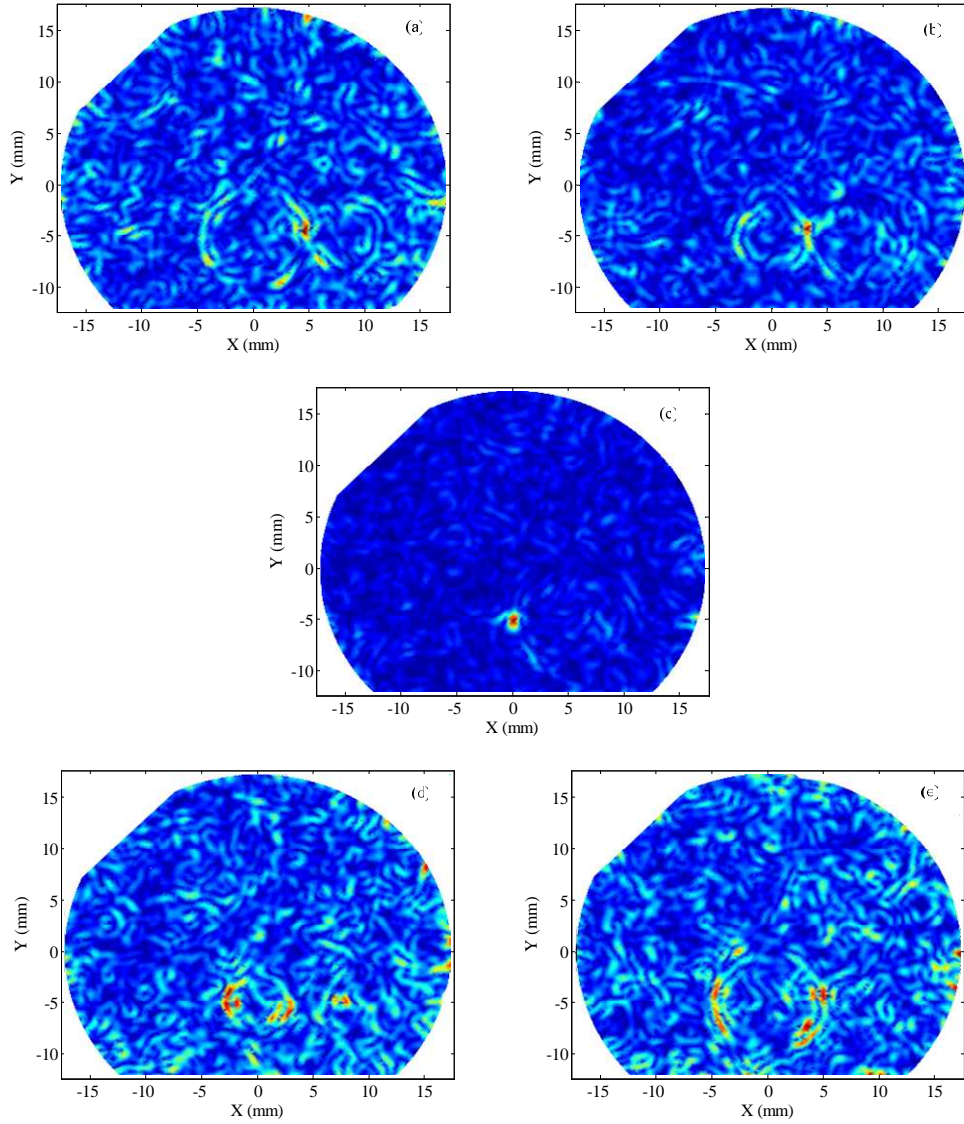


**Fig. 15** Vitesse particulaire calculée à l'aide d'un schéma RK-DG-FEM O4 à cinq instants autour du temps de recompression temporelle, pour une cavité chaotique en cuivre. (a)  $t = 149 \mu\text{s}$ , (b)  $t = 149.3 \mu\text{s}$ , (c)  $t = 149.6 \mu\text{s}$ , (d)  $t = 149.9 \mu\text{s}$ , and (e)  $t = 150.5 \mu\text{s}$ .

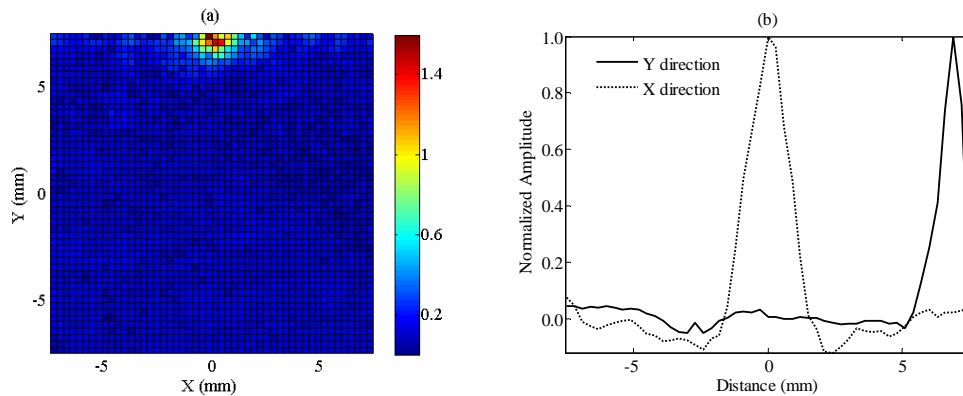


**Fig. 16** Expérience de focalisation par Retournement Temporel (TR) sur un point placé directement sur le bord de l'échantillon. (a) Image 2D, (b) distribution spatiale du signal focalise suivant  $x$  et  $y$  à l'instant  $T_r = 0 \mu\text{s}$ .

Les expériences menées sur une plaque de composite non réverbérante, de 2 mm d'épaisseur, démontrent un deuxième intérêt des cavités chaotiques : la possibilité de focaliser dans un échantillon non réverbérant comme le montre la Figure 17.

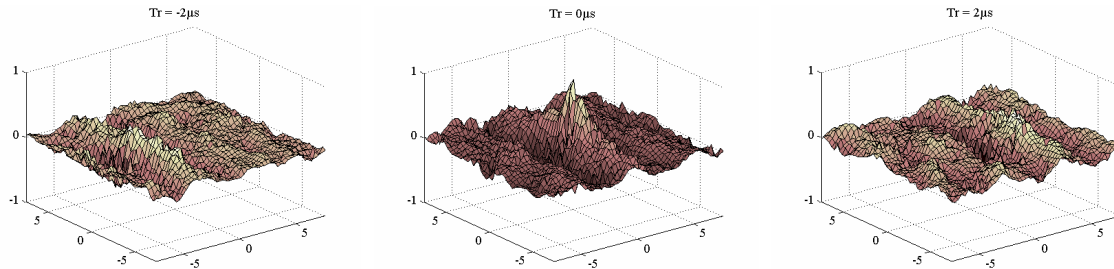


**Fig. 17** Vitesse particulière à différents instants montrant le processus de retro-focalisation dans la plaque composite non réverbérante à l'aide d'une cavité de  $1 \times 2 \times 12$  cm.

Dans ce cas, l'échantillon ne contribue pas au processus de focalisation qui est obtenu par des ondes provenant directement du transducteur, et non plus de toutes les directions entourant le point focal comme c'est le cas pour un échantillon réverbérant (Figure 18).

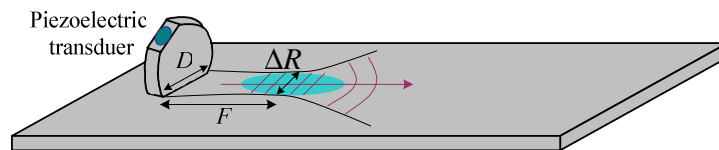


**Fig. 18** Explication schématique du fonctionnement d'un "transducteur à cavité chaotique" place sur un échantillon non réverbérant.

Nous avons aussi démontré qu'un "transducteur à cavité chaotique" peut être utilisé, conjointement avec les méthodes d'inversion d'impulsion et de retournement temporel 1-bit, afin de réaliser une image de non linéarités localisées (Figure 19).

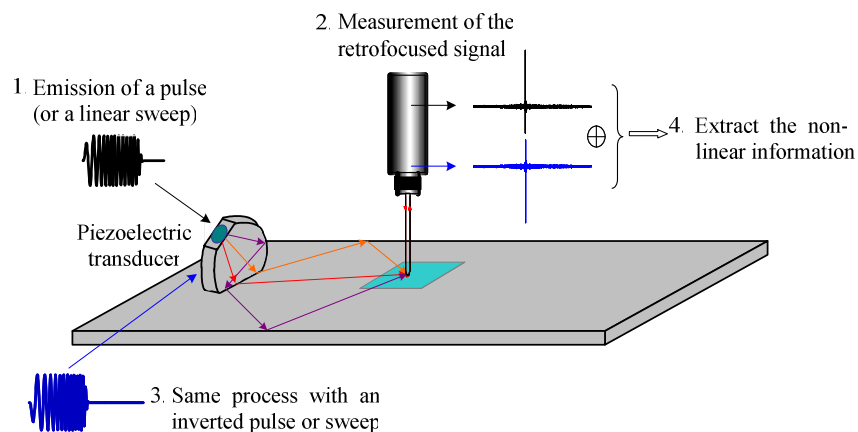


**Fig. 19** Principe de la méthode TR-NEWS utilisant un "transducteur à cavité chaotique".

L'image préliminaire, présentée sur la Figure 20, d'une fissure à la surface d'un échantillon d'acier montre les potentialités des "transducteurs à cavité chaotique" pour l'imagerie ultrasonore non linéaire de défauts. De plus, la contribution principale de la fissure provient de son extrémité, confirmant des résultats publiés récemment.

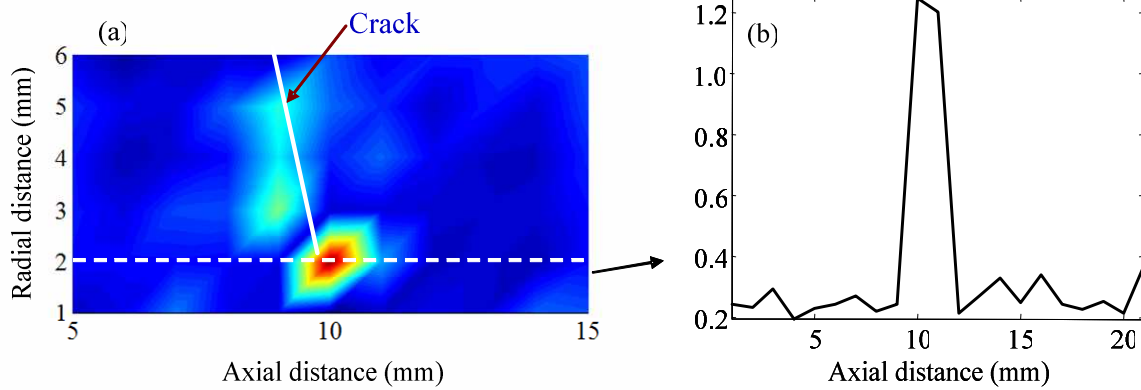


**Fig. 20** Image of a crack at the surface of a steel sample obtained with a combination of TR-NEWS method and "chaotic cavity transducer".

Ainsi, en conclusion, nous pouvons dire que cette thèse pose la première brique pour le développement du concept de contrôle santé intégré par une technique d'imagerie ultrasonore non linéaire utilisant des "transducteur à cavité chaotique" pour la détection précoce de l'endommagement de structures solides.



## INTRODUCTION

Recent advances in modern material technology require the development of non-destructive testing (NDT) and imaging techniques that allow the quantification and localization of micro-structural damage in a wide variety of materials during their manufacture and life cycle. The monitoring of these materials, including alloys, cements, concretes and composites, ensures both their quality and durability. The aim of NDT is to identify and locate physical defects which are unacceptable without causing any damage to the material structure under test. Among the most used NDT methods we can cite magnetic field, eddy-current, radiography, thermal field, vibration, and ultrasonic methods. The first two methods are generally used to detect surface breaking or near surface defects in metallic samples. The later four, more general, are used to detect buried features as well as surface breaking defects. They may also be employed where a quantitative analysis is required. Unfortunately, these traditional NDT techniques are often not sufficiently sensitive to the presence of incipient and progressive damage. Indeed, the main difficulty in the characterization of a degradation process in structural materials relates to the fact that the material exhibits very few measurable signs of damage prior to the onset of delaminations or macro-cracks. In fact, traditional NDT techniques do not show any significant sign of degradation before the first 80-90% of the fatigue life which is in general too late to make any modification or repair of the structure.

Over the cited NDT methods, ultrasonic techniques have been considered as excellent tools and their applications have been increasing rapidly over the last few decades. They are generally based on the principles of linear acoustic. This includes effects of reflection, scattering, transmission, and absorption of probe acoustic energy. The presence of any structural or material inhomogeneities leads to phase and/or amplitude variations of received signals while its frequency content is still the same as the one of the emitted signals. So, such systems are currently limited to the detection of large defects that produce significant linear scatter. From the mechanical or acoustical point of view, the effects of damage on a structure can be classified as linear or nonlinear. A linear damage situation is defined as the case when the initially linear-elastic structure remains linear-elastic after damage. Nonlinear damage is defined as the case when the initially linear-elastic structure behaves in a nonlinear manner after the damage has been introduced. One example of nonlinear damage is the formation of a fatigue crack that subsequently opens and closes under the normal operating vibration environment.

As a result of an intense worldwide research on nonlinear acoustics, dealing with the investigation of the amplitude dependence of material parameters such as wavespeed, or attenuation under the action of small dynamic strain (lower than  $10^{-4}$ ), a set of innovative

NDT methods, called Nonlinear Elastic Wave Spectroscopy (NEWS) techniques, have been recently developed to probe for the existence of damage with a superior sensitivity than traditional technologies. The concept of NEWS-based methods is that the internal damage can be measured directly with the instantaneous detection of an increase in the nonlinearity parameters. Moreover, a huge number of studies have demonstrated that the degree of macroscopic nonlinear behaviour of a material is strongly determined by the amount of micro-inhomogeneous imperfections as defects or weak bonds that exist within the material. Indeed, these imperfections have a so strong nonlinear behaviour, even under acoustic excitation, that become measurable on the macroscopic level. NEWS techniques developed include modulation experiments by frequency mixing of two distinct frequency sound waves, studies of the amplitude dependence of the resonance spectrum, nonlinear reverberation spectroscopy, phase modulation and investigations of slow dynamic behaviour. They have been applied for the evaluation of adhesives, the investigation of dislocations in pure metals, the study of fatigue cracking, etc.

The most well known example of NEWS is that of a tone-burst wave propagation which is used to probe the generation of second harmonic frequency components as a function of distance or amplitude. This method, known as harmonic imaging, has known a rapid growth, since the mid 90's, in ultrasonic medical imaging. It has demonstrated a tremendous increase of the contrast of the obtained images and speckle reduction capability. It is now available in commercial echographic systems providing high resolution images of tissues and organs. Although these results have resulted in a growing interest in the nonlinear acoustic effects in solids and have led to promising advances in the field of non-destructive micro-damage diagnostics, the development of such nonlinearity based imaging systems for solid materials is still at the beginning. Further development of these nonlinear imaging methods will be part of the topic of this thesis. Numerical simulations using nonlinear wave propagation models for complex and heterogeneously damaged materials are needed to support advanced practicability of these nonlinear ultrasonic imaging techniques.

NEWS methods have at first been applied for the global determination of the fatigue state of a structure, and recently extended to visualization techniques for imaging defect's nonlinearity distributions using laser vibrometry, airborne ultrasound, or shearography. In the last five years, the concept of merging the benefits of both NEWS and Time Reversal Acoustic (TRA), which provides the ability to focus ultrasonic waves in time and space, regardless of the position of the initial source and of the heterogeneity of the medium in which the wave propagates, has been proposed in order to realize images of defects in solid samples. In most NDT applications of this combination, a one channel TRA experiment has been used in which a piezoelectric (PZT) ceramic is glued directly to a sample. The sample is generally small enough to be considered as multi-reverberant in the frequency range of interest.

In aeronautical industry, the structures often are plate like components of large size made in composite a highly attenuating medium. When imaging these large structures for structural health monitoring, particular focus has been made on the use of guided Lamb waves. But such non-reverberant samples are difficult to work with the one channel TRA method. So, in this thesis we propose the development of an innovative micro-damage imaging system based on a combination of NEWS techniques and “chaotic cavity transducer” concept. It consists of a combination of a PZT ceramic glued to a cavity of chaotic shape on the hardware side with the time reversal principle on the software side, as it has been done recently for 3D imaging in fluid. The feasibility and capabilities of these new ideas will be explored by numerical simulations, and optimal operational parameters for experimental implementation will be suggested based on the modelling support. So, a large part of the research work conducted in this thesis is concentrated on the domain of nonlinear ultrasonic damage detection and imaging, and more precisely in the development of numerical simulation tools to help the improvement of such nonlinear imaging methods.

The outline of the thesis is as follows:

In the first chapter of this thesis ultrasonic NDT techniques based on NEWS methods and specially the ones which are combined with time reversal process, are reviewed. The nonlinear elastodynamic equations needed in the remainder of the thesis is then introduced, and different kinds of nonlinearity models, including “classical” and “non-classical” nonlinearity are discussed, because for a large class of elastic heterogeneous solid media, the conventional five-constant elasticity theory is often insufficient to explain anomalous nonlinear behaviours of these media. The comparison of nonlinear signatures of these different kinds of nonlinearity for shock wave generation and rod resonance is studied to help the determination of the predominant nonlinear mechanism in specific experiment. An introduction of the classical numerical methods including Finite Difference Method, Finite Volume Method (FVM), Finite Element Method (FEM), Pseudo-Spectral method and Discontinuous Galerkin Finite Element Method (DG-FEM), focusing mainly on their advantages and weaknesses is made.

As we want to simulate nonlinear elastic wave propagation in structures of complex geometry, we need, in order to reduce the number of cell to be used while maintaining a high degree of accuracy, a high-order numerical method with geometric flexibility. The second chapter gives a presentation of the chosen Discontinuous Galerkin Finite Element Method (DG-FEM), an intelligent combination of the FEM and FVM methods, utilizing a space of basis and test functions that mimics the FEM method but satisfying the equation in a sense closer to the FVM method. Indeed, in contrast to classical FEM, within the DG-FEM framework the solution can be discontinuous across the element interfaces, which allows

incorporating the well-established numerical flux functions from the FVM framework. How to implement the DG-FEM operators for nonlinear elastodynamic in a general, flexible, and robust manner is presented in detail. We discuss how to, in practice, assemble the computational grid and compute all the entities required to enable the implementation of the scheme, both for triangular and quadrilateral grids. Moreover, different choices of numerical fluxes are also discussed. The results of numerical simulations, based on the elastodynamic system equation and compared with analytical solutions, for isotropic and anisotropic linear or nonlinear medium, demonstrate the excellent precision and extensive range of application of the DG-FEM scheme. For each situation the result of the simulation is compared with an analytical solution to valid all the implementation of DG-FEM.

Numerical solutions of Partial Differential Equations for wave propagation require the truncation of an unbounded media to fit into computers with a limited memory and computation time. For such problems, an Absorbing Boundary Conditions is needed at the truncated boundary to eliminate the reflections from this boundary to the computational domain. The third chapter of this thesis provides an introduction of the Convolution Perfectly Matched Layer (C-PML) absorbing boundary condition, first introduced in 1994 for simulating electromagnetic waves in an unbounded media. Classically, C-PML has been introduced in first-order formulation of both electromagnetism and elastodynamic. In this chapter, we propose first to extend the C-PML absorbing layer to the second-order system describing elastic waves in displacement formulation in anisotropic solids. This second-order formulation is described in frequency and time domains both for elastic solid and piezoelectric medium. The efficiency of this second-order perfectly matched layer is then demonstrated based upon 2D benchmarks both for isotropic and anisotropic solids, and for bulk and surface wave propagation. An another kind of PML, more adapted to the developed DG-FEM scheme and simpler to implement, named Nearly Perfectly Matched Layer (NPML), also first proposed for electromagnetism, is extended for nonlinear elastodynamic. In some anisotropic media, numerical instabilities appear in the PML limiting the use of this absorbing layer. In order to stabilize the absorbing layer, the “Multiaxial Perfectly Matched Layer” (“MPML”) has been proposed. A complete study of the matching and stability properties of this “MPML” is presented. All this theoretical work is finally validated by numerical examples. A similar idea is used in the case of guided waves for frequencies where “inverse modes” with group and phase velocities of opposite signs are excited, where split field PML or C-PML do not work satisfactorily. Examples of stabilized absorbing layer are also presented for such guided waves case.

Finally, the fourth and last chapter of this thesis concerns the application of “chaotic cavity transducer” for the linear and nonlinear elastic wave imaging. The principles of the one channel TR focalization are first presented. Its astonishing behavior is linked to the ergodic property of the chaotic cavity, bearing the possibility to collect all information in only one

point. To improve the use of one channel TR in NDT application, we propose to use a “chaotic cavity transducer”, consisting of a combination of a PZT ceramic glued to a cavity of chaotic shape on the hardware side with the time reversal principle on the software side. Three signal processing techniques are studied in order to improve both the signal to noise ratio (contrast) and the quality of the focalization: Chirped excitation, Inverse Filter and 1 bit processing. We demonstrate numerically and experimentally that a transducer glued on a chaotic cavity can be used as an array of transducers, as it has been done recently for 3D imaging in fluid but for imaging applications in solid medium, and more precisely to nonlinear imaging of defects such as cracks. In this last case, the chaotic cavity transducer focusing process is used in combination with the pulse inversion method, by successively focusing a pulse and its inverse, and subsequently summing the two results to extract the nonlinear response of the sample at the focal position, and so obtain an image of localized nonlinearity.



# CHAPTER 1: INTRODUCTION TO NONLINEAR NONDESTRUCTIVE TESTING AND IMAGING

## 1.1 Introduction

In this chapter a brief introduction to nonlinear nondestructive testing and imaging and specially the ones which use time reversal process, will be reviewed. Because for a large class of elastic heterogeneous solid media, the conventional five-constant elasticity theory is often insufficient to explain anomalous nonlinear behaviour, different kind of nonlinearity models, including “classical” and “non-classical” nonlinearity will be discussed. The 2D and 3D nonlinear elastodynamic equations, expressed in a conservative form as needed by the Discontinuous Galerkin numerical method presented in the next chapter, will be then introduced.

Given a reliable model of wave propagation, numerical simulation in structures with complex geometry is often a prerequisite for real data interpretation, which will turn to be guidance for improving imaging systems. In order to explain the reasons of the choice of the used numerical scheme, classical numerical simulation methods, including Finite Difference Method, Finite Volume Method (FVM), Finite Element Method (FEM), Pseudo-Spectral method and Discontinuous Galerkin Finite Element Method (DG-FEM), will be presented and compared, focusing on their advantages and weaknesses.

The comparison of nonlinear signatures of the previously presented kinds of nonlinearity for shock wave generation and rod resonance will be studied to help the determination of the predominant nonlinear mechanism in specific experiments.

## 1.2 Nonlinear Nondestructive Testing and Imaging Methods

### 1.2.1 NEWS Methods

In the last few years, a strong interest for nondestructive testing methods based on nonlinear elastic effects in solid has grown, driven by the request from industry for sensitive quantification and localization of micro-structural damage. Researchers have developed innovative techniques that explicitly interrogate the material’s micromechanical behavior and its effect on wave propagation by investigating the amplitude dependence of macroscopically observable properties [101], [134], [189], [190], [191], [197]. Such techniques are termed

Nonlinear Elastic Wave Spectroscopy (NEWS) techniques. The basis of all NEWS techniques is to measure and analyze macroscopic signatures resulting from a local violation of the linear stress-strain relation at the micro-scale.

Several NEWS techniques have been developed to probe the existence of damage induced nonlinearity. One of the most frequently studied methods is harmonic analysis in the frequency domain [50], [135], consisting of measuring the second and higher harmonic amplitude versus the strain amplitude of the fundamental, which provides quantitative information about the nature of the nonlinearity. Another technique consists of parametric interactions between waves emitted in materials. The sample acts as a nonlinear frequency mixer, so that sum and difference frequency waves are created [1], [131]. In addition, modulations of amplitude [189] and phase [197] have been investigated in order to evaluate the classical nonlinear perturbation coefficient  $\beta$  coming from the Taylor expansion of stress-strain relation [87]. The study of resonance frequency provides key information about nonlinear behavior. By plotting the frequency shift as a function of the fundamental mode strain amplitude, it is observed that resonance amplitude distortion increases significantly with defect [191], [192]. Tests performed on a wide variety of materials subjected to different micro-damage mechanisms of mechanical, chemical and thermal origin, have shown that the sensitivity of such nonlinear methods to the detection of micro-scale features is far greater than that obtained with linear acoustical methods [134].

### **1.2.2 Linear and Nonlinear Ultrasonic Imaging Methods for NDT**

The most frequently used imaging techniques based on the analysis of ultrasonic signal generation and propagation are surface-scan imaging involving laser vibrometry, air-coupled ultrasonics and ultrasound thermography, ultrasound tomography; and time reversal (or wave phase conjugation) techniques. Laser vibrometry is a precise technology for non-contact vibration measurements, modal analysis and non-destructive testing for many areas of engineering. Linear laser vibrometry provides an extreme sensitivity (pico-meter range) in measuring and imaging vibration fields by evaluating the laser light scattered back from the vibrating object. Air-Coupled Ultrasound is another established method for remote defect imaging that has become a routine inspection technique in nondestructive testing for a wide range of materials and components [157]. A new generation of air-coupled ultrasonic transducers covering a wide frequency range up to few MHz enables to image faint acoustic fields scattered by tiny defects.

In addition to pure acoustic or ultrasonic scanning measurements, techniques based on thermal-acoustic interaction have been successfully used in several NDT configurations: SPATE [132] is a well known method for mechanical stress measurement under static loads. With higher frequency and efficient excitation, it is also possible to visualize the dissipated

energy that is released due to nonlinear effects. This technique is known as Ultrasound-Excited Thermography (ULT). Basic investigations [221] showed that the main advantage of ULT is the defect selective indication of material flaws by using elastic nonlinearity in defective material areas caused by friction or locally increased dissipation.

Multi-elements transducers are commonly used in ultrasonic medical imaging. They offer a great flexibility in the realisation of images, and advanced imaging techniques have been developed such as coded imaging, and dynamical focusing in reception. Most of these methods are now starting to be transferred to linear ultrasonic NDT applications, with the development of dedicated electronic systems (MultiX of the French society M2M).

In aeronautical industry, the main structures are plate like components of large size often made in composite a highly attenuating medium. When imaging these large structures for structural health monitoring, particular focus has been made on the use of guided Lamb waves [13], [14], [204]. Generally one tries to generate a single Lamb mode to simplify the measurement and understand how such wave is scattered by various linear defects. In this case the arrays are necessarily sparse with much interest in reducing the spatial density of the sensors in order to produce a cost effective system.

Unfortunately, these traditional NDT techniques are often not sufficiently sensitive to the presence of incipient and progressive damage. Indeed, the main difficulty in the characterization of a degradation process in structural materials relates to the fact that the material exhibits very few measurable signs of damage prior to the onset of delaminations or macro-cracks. To overcome this limited sensitivity of linear imaging methods, NEWS methods have recently been extended to visualization techniques for imaging defect's nonlinearity distributions using laser vibrometry [174], airborne ultrasound [175], shearography [161] or all optical photothermal and photoacoustic methods [82]. In the airborne ultrasound method, the defects, acting as localized sources of nonlinear vibrations, efficiently radiate higher harmonics into the surrounding air.

### 1.2.3 TR and NEWS Combined Methods

Time Reversal (TR) [68]-[70] is now a well known technique which have been developed in different fields including medical therapy, diagnostic, and underwater acoustics, due to its ability to provide spatial and temporal focusing of an ultrasonic wave. Time-reversal invariance in acoustics means that for every burst of sound  $s(r,t)$  emitted from a source, and which is reflected, refracted, or scattered by heterogeneities of the propagation medium, there exists a set of waves  $s(r,-t)$  that precisely retrace all these complex paths and converge at the original source, as if time were going backwards. This invariance is satisfied by the equation in non attenuating media. The TR process leads to a spatial focusing and a temporal compression. Spatial focusing means that the time-reversed field focuses back exactly at the

source. Temporal compression means that the time reversed signal at the source is similar to the signal previously emitted by the source. In other words, the result of a TR process is that waves recorded on the boundary are focused back in space and time on the acoustic source, or on the scattering targets inside the region that were acting as sources. For classical linear TR process, the returned signal focuses on the direct wave source position not on the defect [24], [71]. The size of the focal spot depends on source size and form, and on the frequency of the signal emitted. Concerning NDT applications, TR processes have been applied in several classical ultrasonic inspection methods: C-scan with immersed samples [40], Rayleigh and Lamb waves propagation in plates and hollow cylinders [98], [99], [145], and structural health monitoring [199], [172]. In these studies, it was shown that the TR principle improves the detection of flaws in heterogeneous materials for which the microstructure displays a strong speckle noise that is obstructing the observation of a defect echo in classical ultrasonic inspection. On the other hand, researchers have encountered a serious limitation of the traditional TR technique in the fact that only the strongest scatterer can be imaged. The application of the so-called *Décomposition de l'Opérateur de Retournement Temporel* (DORT) method [145], [146] and successive TR iterations [205], [130] may overcome this feature to some extent and may enhance the detection by focusing selectively on weaker scatterers. Using these advanced analysis and signal processing techniques, flaws with sizes even smaller than the wavelength can be detected in highly heterogeneous materials such as titanium alloys [147], [21].

Experiment with NEWS techniques have demonstrated that micro-damage is first of all a process of nonlinear scattering giving rise to the creation of higher harmonics, rather than to linear scattering effects. So, from this point of view, the classical TR procedure should be modified in such a way that the main signal treatment is concentrated on the nonlinear components of the signals.

Following the laboratory studies of the NEWS techniques, we can underline two important principles [112]: (1) the macroscopically observed nonlinear signatures originate from zones with micro-damage and micromechanical nonlinear stress-strain relations; (2) the nonlinear signatures are most efficiently generated at those locations where the strain within the sample is prevailing. These two principles can be used as the basis for new micro-damage visualization techniques based on nonlinear material properties. The NEWS methods allow characterization of the nonlinear behavior, but they do not provide information about defect localization. To overcome this problem, a method combining a Time Reversal (TR) process and a nonlinear treatment has been proposed [23], [176].

For combining the nonlinearity based TR process with the NEWS methods, two technologies have been proposed, depending on whether nonlinear treatment is performed before or after the TR process. As presented in Fig 1.1, these two methodologies are defined as

TR-NEWS, with nonlinear analysis as a post-treatment of time reversal, and as NEWS-TR, with nonlinear analysis as a pre-treatment of time reversal [112].

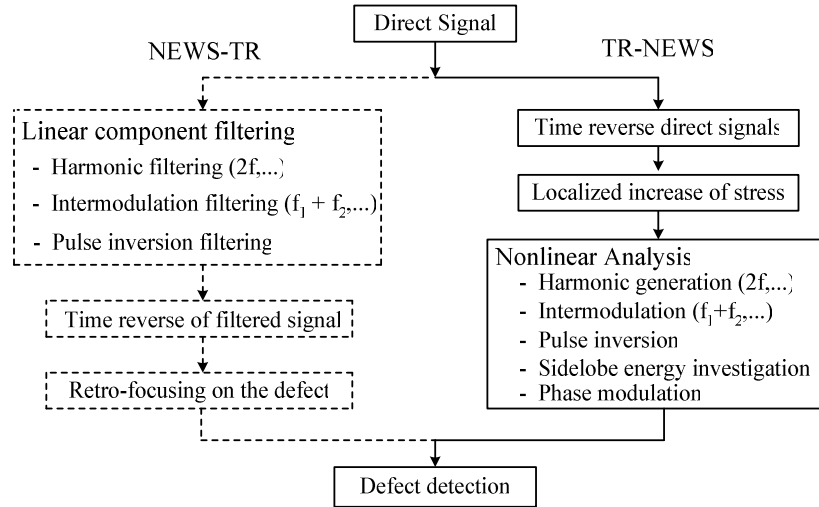


**Fig. 1.1** Defect detection methods based on a combination of TR and NEWS methods.

The TR-NEWS method, which consists in increasing locally the stress field using properties of linear TR and subsequently applying nonlinear analysis, has been experimentally demonstrated by Sutin *et al.* [176]. It seems to have a wide potential for application in solid ultrasound imaging for nondestructive testing [112], [184]. For TR-NEWS technology, different experimental set-ups have been recently proposed [26], [81], [112], [176], [184]. In these experiments, generally, two high frequency signals are used to excite the medium. Then, an analysis of the intermodulation of the retro-focalized signals point by point on the imaged area is made. In the experiment of Le Bas *et al.* [112], a 1MHz signal ( $f_1$ ) is first sent to a first source, and the out of plane particle velocity is recorded at a chosen location using a laser vibrometer. A second signal with a 200 kHz frequency ( $f_2$ ) is sent at a second source and again a laser vibrometer records the signal at the same position. Both recorded signals are then time reversed and reemitted from their corresponding original transducer at exactly the same time. Doing so, the time reversal principle makes sure that both signals arrive at the same time at the fixed point where the laser picks up the out of plane vibration. The intermodulation at the focused signal in time is then analyzed in terms of the sum ( $f_1+f_2$ ) and difference ( $f_1-f_2$ ) spectrum components. This procedure is repeated for all points on a line crossing the flaw position. For an intact location the level of intermodulation is quite low. However, for a micro-damaged zone the intermodulation becomes very high. The nonlinearity signatures contained in the sum and difference frequencies have been obtained as function of the distance to the crack. At the position of the crack, the intermodulation signature is evidently much larger than elsewhere. A contrast about a factor of 10 was obtained.

Our TR-NEWS experiment has been realized on a fatigue steel sample combining a “chaotic cavity transducer” and a PI filtering method.

The other alternative to classical TR, called NEWS-TR, consist in selecting only the nonlinear or harmonic energy contained in the response signals and returning merely this part back into the medium by the time reversal process. Doing so, the time reversed signal will focus on the micro-damaged area, which is where the harmonics were created, while linear scatters will not show up at all [24], [77]. This method has been described for the first time by Bou Matar *et al.* [23] and has only been validated experimentally recently [185]. The nonlinear TR process has recently been demonstrated to be highly valuable for ultrasound imaging of damaging in solid [79], [77], [176], [219]. Moreover, similar ideas have already been used in fluids where Wave Phase Conjugation (WPC) in nonlinear regime has been demonstrated for nonlinear ultrasonic imaging [30], [31]. WPC is known as the spectral representation of TR transformation. The WPC technique, which originated in the field of nonlinear optics, has been adapted and applied for ultrasonic research applications in the 1980's by the scientific group of the Wave Research Center of the General Physics Institute of the Russian Academy of Sciences [33]. The original parametric method for acoustic WPC producing a giant (>80 dB) amplification was elaborated for the first time by this group [29]. The advantage of the parametric WPC technique is its capability, by principle, to use a single element time reversal mirror [29], [30].

In the NEWS-TR technology, two filtering methods have been investigated to return only the nonlinear parts (harmonics) of the received signal, i.e., harmonic filtering and pulse inversion (PI) [71], [79]. For the harmonic filtering, one option consists of selecting only the nonlinear or harmonic energy contained in the response signals and returning only this part back into the medium by the time reversal process. Pulse inversion is an alternative filtering procedure based on the fact that the phase inversion of a pulsed excitation signal ( $180^\circ$  phase shift) will lead to the exact inverted phase signal within a linear medium [169]. But, this is not the case in a nonlinear (or micro-damaged) material due to the generation of harmonics. Advantage of this information is taken by adding the response from two phase-inverted pulses (positive and negative) and sending back the sum to the receivers.

A numerical study of the comparison of the two proposed filtering methods for NEWS-TR technique, used for detecting defects with a nonlinear hysteretic behavior, has been conducted in 2D [79] and 3D [80]. Hysteretic nonlinearity exhibiting high level of odd harmonics, the third harmonic signal is extracted in these numerical simulations. The results show that the higher the frequency, the greater the increase in retro-focusing quality and decreasing the source size reduces the retro-focusing quality. The simulation results demonstrate that the main difference between these two methods of filtering (harmonic filtering and pulse inversion) are: (1) Pulse inversion filtering is better for the defect detection

near the edge of the sample, all information related to the linear propagation in the medium is eliminated with pulse inversion filtering contrary to that with harmonic filtering; (2) Harmonics filtering is more precise than pulse inversion filtering when the defect is located between the emitter and receiver, the higher the harmonics frequency, the smaller the retro-focusing spot size will be. An experiment of NEWS-TR with a pulse inversion filtering has been presented by Le Bas *et al.* [112]. A not perfect, but encouraging result has been obtained with a one channel time reversal process in a PMMA glass material.

Recently a scale subtraction filtering method to reveal the nonlinearity has been proposed [164]. It seems to be a valuable alternative to pulse inversion as it is sensitive not only to even harmonics but to both even and odd harmonics [165]. It has been recently experimentally validated [28].

At this stage we can envisage the development of a hybrid experimental-numerical approach for NEWS-TR. One can use real signal recordings from a microdamaged object as input to a numerical reconstruction procedure which involves the filtering of nonlinear components and back-propagation in a linear wave propagation model. Indeed, it is important to realize that – once the receiver signals have been acquired – the time-reversal process can be performed numerically by computers using adequate (linear) material models. This allows to “see inside” the sample, and to localize the best focusing region even if this region is not located on one of the surfaces accessible to the transducers. The result of a preliminary test realized on a 27×74×95 cm PMMA sample with a laser made defect in its middle is displayed on Fig. 1.2. An elastic wave is generated inside the sample by applying an electric excitation to a PZT ceramic directly glued on the sample. The out of plane particle velocity is measured along one line (shown on Fig 1.2) with a laser vibrometer with a 1mm step. This experimental part of the test has been realized by P.Y. LeBas and K. Van Den Abeele. The experimental data have then been filtered in order to conserve only the third harmonic of the central frequency of the emitted pulse and time reversed. The obtained signals are numerically backward propagated, using a 3D Pseudo Spectral scheme [80], to the source of nonlinearity. The obtained result, on the surface of the sample on which the PZT ceramic is glued and the laser measurements have been made, is displayed on Fig1.2(a). It appears that, due to a not perfect gluing between the sample and the PZT ceramic, this latter is a source of nonlinearity. The obtained result, on the plane of the defect, Fig1.2(a), shown only a small signal propagating backward to the defect.

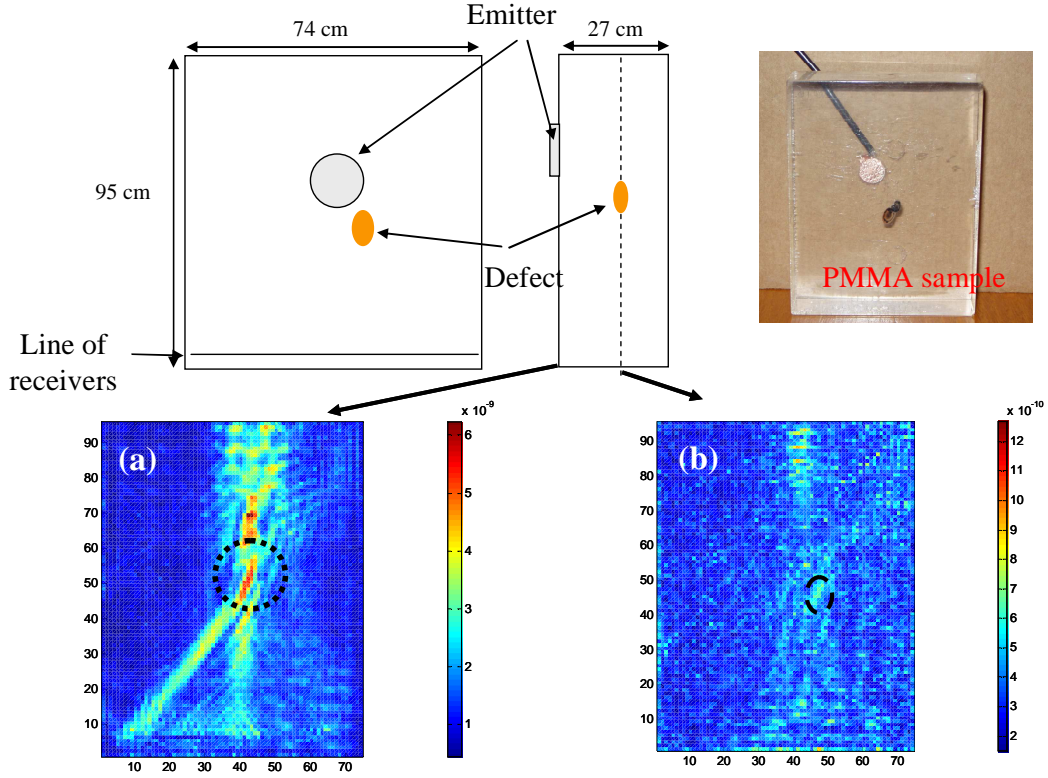


**Fig. 1.2** Experimental set-up and PMMA sample geometry used in the hybrid experimental-numerical NEWS-TR approach.

### 1.3 Nonlinear Elasticity and Elastodynamic Equations

In this part, different kinds of “classical” and “non-classical” nonlinearity will be presented for elastic solid medium. A one-dimensional hyperbolic equation model for a compressional wave propagating in a heterogeneous medium will be introduced. The fundamental nonlinear elastodynamic equations expressed in a conservative form, as needed by the Discontinuous Galerkin numerical method introduced in the next chapter, will be presented for 2D and 3D simulations.

#### 1.3.1 Nonlinear 1D Propagation Model in Heterogeneous Elastic Media

Consider a heterogeneous medium in which a compressional wave propagates. This propagation is modeled by the following one-dimensional hyperbolic system of equations:

$$\frac{\partial v}{\partial t} = \frac{1}{\rho_0} \frac{\partial \tau}{\partial z}, \quad (1.1)$$

$$\frac{\partial \tau}{\partial t} = K(t) \frac{\partial v}{\partial z}, \quad (1.2)$$

where  $\rho_0$  and  $K$  are respectively the density and the elastic modulus of the material,  $v$  is the particle velocity, and  $\tau$  is the longitudinal stress. Here, the modulus

$$K = \frac{\partial \tau}{\partial \varepsilon}, \quad (1.3)$$

where  $\varepsilon$  is the strain, is considered as time dependent in order to introduce the nonlinearity, which can be considered of different kind, e.g. quadratic and cubic, Bi-modular, Nazarov, or PM space hysteretic, as described in the next section.

### 1.3.2 “Classical” and “Non-classical” Nonlinear Elasticity

For homogeneous isotropic solid media, traditionally, the propagation and interaction of acoustic waves is described in terms of the five-constant or nine constant elasticity theory [110], [215], which is based on developing the elastic energy as an analytic function of the strain field, and in which quadratic or cubic corrections are applied to the linear Hooke’s law. This is done by constructing the scalar invariants of the strain tensor. For a 1D elastic solid medium, longitudinal strain  $\varepsilon$  is related to the corresponding stress tensor component  $\tau$  by [142]

$$\tau(\varepsilon) = E(\varepsilon - \Gamma \varepsilon^2), \quad (1.4)$$

where  $E$  is the elastic modulus and  $\Gamma$  is a parameter used as a measure of medium nonlinearity. For isotropic solids, within the framework of the “five-constant” elasticity theory one has [142]

$$\Gamma = \frac{3}{2} + \frac{(A + B + C)}{\rho_0 c_0^2}. \quad (1.5)$$

Here  $A$ ,  $B$  and  $C$  are third-order Landau elastic moduli. In homogeneous solids, such nonlinearity is caused by the dependence of intermolecular forces on the molecular displacement, leading to typical  $\Gamma$  value of the order of unity (for example  $\Gamma = 4.4$  in steel).

However, for elastic heterogeneous solid media, e.g., granular, rubber-like porous, rock, cement, concrete, composites and crack-containing elastic media, the elastic nonlinear behavior is significantly different from the “classical” nonlinear behavior described by the traditional nonlinear “five-constant” theory of Landau [110]. Amongst other things the parameter of acoustic nonlinearity  $\Gamma$  proves to be larger than in “ordinary” homogeneous solids. The model of Eqs. (1.4) and (1.5) can not express the physical stress-strain relation of these materials. The inner structure of such media is characterized by presence of various heterogeneities and defects whose size is large compared with the inter-atom distance, but is small with respect to the characteristic scale of the acoustic perturbation. Moreover, acoustic waves can interact in such micro-inhomogeneous media much more intensively than in

homogeneous media. Many theoretical and experimental researches work have been done for different heterogeneous medium and interpreted with a large amount of different models. In the following we call this kind of nonlinearity “non-classical” nonlinearity for differentiating them from the “classical” nonlinearity.

In this section, four kinds of nonlinearity will be present, including “classical” quadratic and cubic nonlinearity model and three “non-classical” nonlinearity models. Moreover, linear and nonlinear attenuation are introduced in the wave equation.

### 1.3.2.1 Quadratic and Cubic Nonlinearity

The “classical” quadratic nonlinearity was given by Eq. (1.4). This model can be extended to cubic nonlinearity by introducing the following constitutive equation [75]:

$$\tau(\varepsilon) = E(\varepsilon - \Gamma\varepsilon^2 - \delta\varepsilon^3), \quad (1.6)$$

where  $\Gamma$  and  $\delta$  are respectively quadratic and cubic nonlinear parameters. Then, according to Eq. (1.3), the elastic modulus is:

$$K = E(1 - 2\Gamma\varepsilon - 3\delta\varepsilon^2). \quad (1.7)$$

Even if “Classical nonlinearity” corresponds to this case, this model can be used to describe some medium with strong nonlinearity, as for example elastic medium with cylindrical pores [142], [141].

### 1.3.2.2 Bi-modular Elasticity Nonlinearity

Nazarov *et al.* [135] and Ostrovsky [142] have presented a “non-classical” Bi-modular model, which has different elastic moduli on compression and on stretch. The equation of state of this kind of media can be represented by a piecewise linear function

$$\tau(\varepsilon) = \begin{cases} E_+ \varepsilon, & \varepsilon > 0 \\ E_- \varepsilon, & \varepsilon < 0 \end{cases}, \quad (1.8)$$

where  $E_+$  and  $E_-$  are the elastic moduli of the medium in compression and in tension, respectively, and  $E_+ < E_-$ . The corresponding stress-strain curve is plotted in Fig. 1.3.

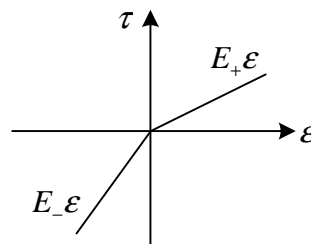


**Fig. 1.3** Stress-strain curve of the Bi-modular model.

In this case, the modulus is simply given by:

$$K = \begin{cases} E_+ & \varepsilon > 0 \\ E_- & \varepsilon < 0 \end{cases}. \quad (1.9)$$

This bi-modular model, with  $E_+ \approx 0 \ll E_-$ , has been widely used to simulate “clapping” cracks, behaviour which has been experimentally observed when high amplitude waves (generally low frequency) interact with small sized cracks [153], [32], [173].

### 1.3.2.3 Nazarov Model of Hysteretic Nonlinearity

In recent years, nonlinear wave process occurring in various micro-inhomogeneous media have been more and more often described by equations of state containing an hysteretic nonlinearity [134], [135], [137], [138], [85], [124], [140]. Hysteretic properties are typical of many micro-inhomogeneous media.

Nazarov *et al.* [134], [135], [137], [138] have proposed two kinds of models: an inelastic hysteretic model and an elastic hysteretic model, for hysteretic nonlinearity, described by the following stress-strain relation:

$$\tau(\varepsilon, \dot{\varepsilon}) = E(\varepsilon - f(\varepsilon, \dot{\varepsilon})), \quad (1.10)$$

where  $f(\varepsilon, \dot{\varepsilon})$  is a nonlinear function of strain and strain rate.

In the inelastic hysteretic model, the nonlinear function has the form:

$$f(\varepsilon, \dot{\varepsilon}) = \alpha \varepsilon_m \varepsilon + \begin{cases} +\frac{\beta_1}{2} \varepsilon^2 - \frac{\beta_1 + \beta_2}{4} \varepsilon_m^2, & \dot{\varepsilon} > 0 \\ -\frac{\beta_2}{2} \varepsilon^2 + \frac{\beta_1 + \beta_2}{4} \varepsilon_m^2, & \dot{\varepsilon} < 0 \end{cases}, \quad (1.11)$$

where  $|\alpha| \varepsilon_m \ll 1$ ,  $|\beta_{1,2}| \varepsilon_m \ll 1$  and  $|\beta_{1,2}| \gg 1$ . This equation involves three independent nonlinear parameters  $\alpha$  and  $\beta_{1,2}$ , which are responsible for the variations of the elastic modulus and for the nonlinear loss. We can see that, when  $\alpha = 0$  and  $\beta_1 + \beta_2 = 0$ , the modification of the elastic modulus and the nonlinear loss are equal to zero and Eq. (1.11) describes a quadratic nonlinearity, as the “five-constant” elasticity theory.

In the elastic hysteretic model, the nonlinear function has the form:

$$f(\varepsilon, \dot{\varepsilon}) = \frac{1}{n} \begin{cases} \gamma_1 \varepsilon^n, & \varepsilon > 0 \quad \dot{\varepsilon} > 0 \\ -\gamma_2 \varepsilon^n + (\gamma_1 + \gamma_2) \varepsilon_m^{n-1} \varepsilon, & \varepsilon > 0 \quad \dot{\varepsilon} < 0 \\ -\gamma_3 \varepsilon^n, & \varepsilon < 0 \quad \dot{\varepsilon} < 0 \\ \gamma_4 \varepsilon^n - (\gamma_3 + \gamma_4) \varepsilon_m^{n-1} \varepsilon, & \varepsilon < 0 \quad \dot{\varepsilon} > 0 \end{cases}, \quad (1.12)$$

where  $|\gamma_{1,2}\epsilon_{m+}| \ll 1$ ,  $|\gamma_{3,4}\epsilon_{m-}| \ll 1$ ,  $|\gamma_{1-4}| \gg 1$ .  $\epsilon_{m+} > 0$  and  $\epsilon_{m-} < 0$  are the last maximum and minimum of strain at the considered position, respectively. There are five free parameters in this model: the exponent  $n$  and four nonlinear hysteretic constants of the medium  $\gamma_{1-4}$ . Eqs. (1.10) and (1.12) describe a broad class of media, depending on the relation between these parameters. When  $n = 2$  and  $\gamma_1 = -\gamma_2 = -\gamma_3 = \gamma_4 = 2\Gamma$ , Eq. (1.12) will reduce to Eq. (1.4) for “classical” quadratic nonlinearity. Experimental investigations of nonlinear phenomena in polycrystalline zinc show that typical value of  $n$  for non-annealed and annealed zinc [136] is 2 and 3, respectively. A plot of the stress-strain curve  $\tau = \tau(\epsilon, \dot{\epsilon})$ , is given in Fig. 1.4.

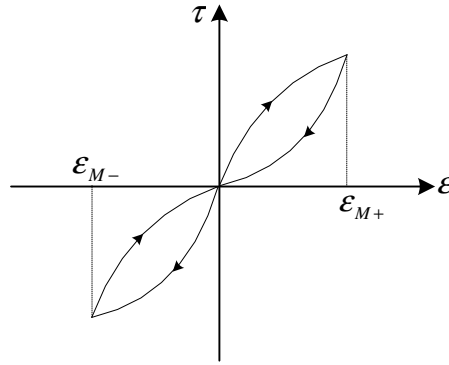


Fig. 1.4 Stress-strain curve of the Nazarov elastic hysteretic nonlinearity model.

In this elastic model, the modulus becomes:

$$K = E(1 - f'(\epsilon, \dot{\epsilon})), \quad (1.13)$$

where

$$f'(\epsilon, \dot{\epsilon}) = \begin{cases} \gamma_1 \epsilon^{n-1} & \epsilon > 0 \quad \dot{\epsilon} > 0 \\ -\gamma_2 \epsilon^{n-1} + (\gamma_1 + \gamma_2) \epsilon_{m+}^{n-1} / n & \epsilon > 0 \quad \dot{\epsilon} < 0 \\ -\gamma_3 \epsilon^{n-1} & \epsilon < 0 \quad \dot{\epsilon} < 0 \\ \gamma_4 \epsilon^{n-1} - (\gamma_3 + \gamma_4) \epsilon_{m-}^{n-1} / n & \epsilon < 0 \quad \dot{\epsilon} > 0 \end{cases}. \quad (1.14)$$

#### 1.3.2.4 PM-Space Model of Hysteretic Nonlinearity

For “non-classical” hysteretic nonlinearity, Ortin [140] Guyer and McCall [85], [124] have introduced another model to express the stress-strain equation, including both hysteresis and discrete points memory. This model proposes a theoretical framework taking the elastic properties of a macroscopic sample of material to result from the workings of a large number of mesoscopic elastic elements. These Hysteretic Element Units (HEU) can individually have complex hysteretic behavior and are responsible for the macroscopic linear and nonlinear elastic behavior. The most important portion of this theory is the Preisach-Mayergoyz space (PM-space), which provides an infinite number of state relations by tracking the behavior of

the individual elastic elements depending on the excitation and the pressure history. This theory uses static stress-strain data to determine the density of elastic elements in PM-space. This density takes the place of the five constants of the traditional theory. From the density, the dynamic elastic response of the system is determined. The connection between static and dynamic behavior, provided by the PM space picture, yields a qualitative and quantitative description of the relationship between the static and dynamic moduli.

In this model, no analytical expression of the bulk modulus is given. It is calculated by summation of the strain contribution of a numerous number of HEU. Each HEU is described by two characteristic stresses  $P_o$  and  $P_c$ , corresponding to the transition between two states when the stress is increased or decreased, respectively. One state corresponds to an “open” state and the other one to a “closed” state. Our implementation of the PM space model is based on the multiscale approach developed by Van Den Abeele *et al.* [193]. For each cell of the calculation grid (representing a mesoscopic level of the medium description),  $N_0$  hysteretic units are considered with different values of the two stresses characteristic. This representation is commonly termed “PM-space” and can be described mathematically by its density distribution  $f(P_o, P_c)$ , as shown on Fig. 1.5. Two kind of elementary hysteretic elements have been considered here, as shown on Fig. 1.6.

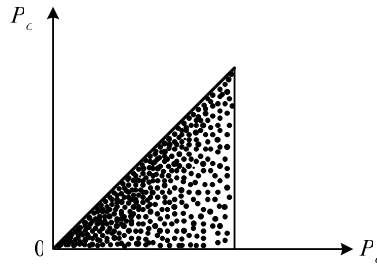


**Fig. 1.5** PM space representation of the density of HEU. Each dot represents one HEU.

The first model (Fig. 1.6(a)) is the one introduced by Guyer *et al.* [85]. This is the simplest one, and it can be shown that in this case the bulk modulus is given by:

$$\frac{1}{K} = \frac{1}{E(1 + \beta\tau + \delta\tau^2 + \dots)} + \frac{\partial \varepsilon_H}{\partial \tau}, \quad (1.15)$$

where  $\varepsilon_H$  is the strain contribution of the hysteretic elements, and  $\beta$  and  $\delta$  are “classical” quadratic and cubic nonlinear parameters. The strain variation as a function of stress induced by the HEUs can be calculated by:

$$\frac{\partial \varepsilon_H}{\partial \tau} = N_0 \int_{-\infty}^{P_c} dP_o \int_{P_o}^{+\infty} dP_c f(P_o, P_c) \frac{\partial \varepsilon_M}{\partial \tau}, \quad (1.16)$$

where  $\varepsilon_M$  is the strain contribution of each individual HEU.

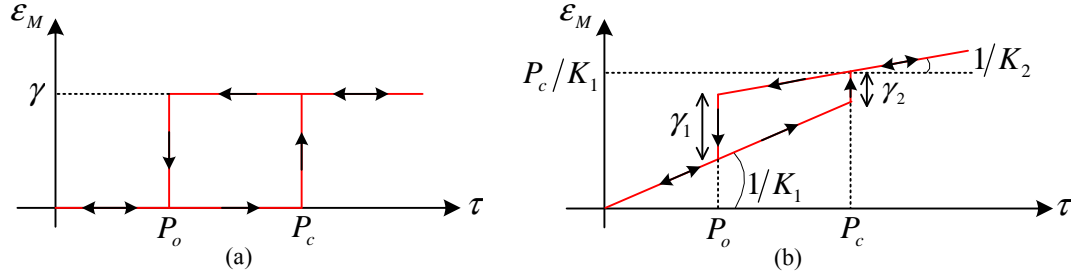


**Fig. 1.6** Elementary hysteretic elements used in the computation of the PM space model. (a) “inelastic” two states element, and (b) “elastic” two states elements. In each case, one state corresponds to an open state and the other one to a closed state, with a transition stress associated,  $P_o$  and  $P_c$  respectively.

For the first model, as shown in Fig. 1.6(a), when the stress increases,  $\partial\tau/\partial t > 0$ , then the strain variation for each elementary HEU is given by:

$$\begin{cases} \frac{\partial \varepsilon_M}{\partial t} = \gamma \delta(\tau - P_c) & \text{If HEU M is open} \\ \frac{\partial \varepsilon_M}{\partial t} = 0 & \text{If HEU M is closed} \end{cases}, \quad (1.17)$$

where  $\delta(x)$  is the delta Dirac function. Inserting Eq. (1.17) in Eq. (1.16) we obtain the strain variation induced by all the HEUs (inverse bulk modulus contribution of all the HEUs) as:

$$\frac{\partial \varepsilon_H}{\partial \tau} = \gamma \int_{-\infty}^{\tau} dP_o f(P_o, \tau) \Omega = \gamma \int_{O_2}^{\tau} dP_o f(P_o, \tau), \quad (1.18)$$

with  $\Omega = 1$  if the HEU is open, and  $\Omega = 0$  if it is closed.  $O_2$  is the “open” coordinate of the point  $A_2$  in the PM space (see Fig. 1.7). Now, if the stress decreases,  $\partial\tau/\partial t < 0$ , the induced strain variation, by each HEU, is:

$$\begin{cases} \frac{\partial \varepsilon_M}{\partial t} = \gamma \delta(\tau - P_o) & \text{If HEU M is closed} \\ \frac{\partial \varepsilon_M}{\partial t} = 0 & \text{If HEU M is open} \end{cases}, \quad (1.19)$$

and the overall strain variation:

$$\frac{\partial \varepsilon_H}{\partial \tau} = \gamma \int_{\tau}^{+\infty} dP_c f(\tau, P_c) \Omega = \gamma \int_{\tau}^{C_2} dP_c f(\tau, P_c), \quad (1.20)$$

with now  $\Omega = 1$  if the HEU is closed, and  $\Omega = 0$  if it is open.  $C_2$  is the “closed” coordinate of the point  $A_2$  in the PM-space. So, we have seen that the calculation of bulk modulus is reduced to follow the limit between the open and closed elements domains. The function  $\partial \varepsilon_H / \partial \tau = df_c(\tau) / d\tau$ , where  $f_c$  is the fraction of the PM-space area occupied by closed units, corresponds to the fact that only hysteretic units changing of state (open to closed or closed to open) at the actual stress  $\tau$  contribute to the inverse of the bulk modulus at this time.

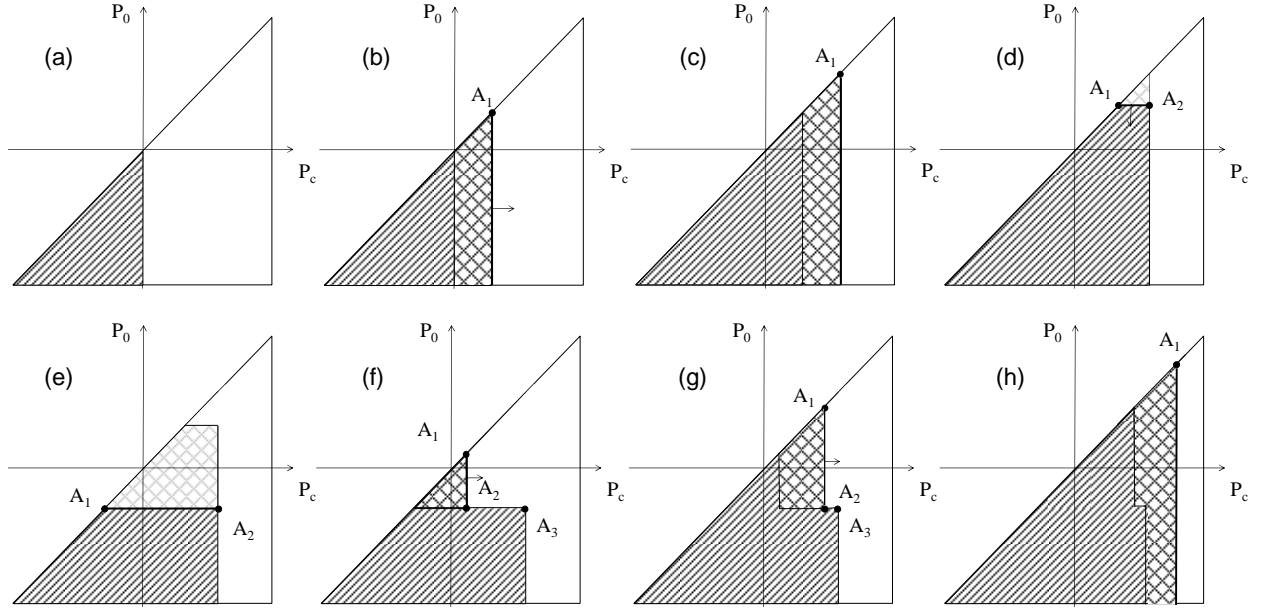


**Fig. 1.7** Evolution of the PM space domain during cycles of compression and rarefaction.

The second model (Fig. 1.6(b)) is an extension of the model of Scalenderi *et al.* [162] implemented in the LISA code, and shown in Fig. 1.8. The bulk modulus is already given by Eq. (1.15) where only  $\partial \varepsilon_H / \partial \tau$  need to be modified. Considering Fig. 1.6(b), the strain variation for each elementary HEU, if the stress is increasing, is now given by:

$$\begin{cases} \frac{\partial \varepsilon_M}{\partial t} = \gamma_2 \delta(\tau - P_c) + \frac{1}{K_2} + \left( \frac{1}{K_1} - \frac{1}{K_2} \right) u(P_c - \tau) & \text{If HEU M is open} \\ \frac{\partial \varepsilon_M}{\partial t} = \frac{1}{K_2} & \text{If HEU M is closed} \end{cases}, \quad (1.21)$$

where  $u(x)$  is the step function, and  $K_1$  and  $K_2$  correspond respectively to the bulk modulus of the HEUs in the open and closed states. Introducing these expressions in Eq. (1.16), the strain variation induced by all the HEUs becomes:

$$\begin{aligned} \frac{\partial \varepsilon_H}{\partial \tau} &= \int_{-\infty}^{\tau} dP_o \gamma_2 f(P_o, \tau) \Omega + \frac{1}{K_2} \int_{-\infty}^{P_c} dP_o \int_{P_o}^{+\infty} dP_c f(P_o, P_c) \\ &+ \left( \frac{1}{K_1} - \frac{1}{K_2} \right) \int_{-\infty}^{P_c} dP_o \int_{P_o}^{+\infty} dP_c u(P_c - \tau) f(P_o, P_c) \Omega \end{aligned}, \quad (1.22)$$

with  $\Omega = 1$  if the HEU is open, and  $\Omega = 0$  if it is closed. Finally, we obtain:

$$\begin{aligned} \frac{\partial \varepsilon_H}{\partial \tau} &= \int_{O_2}^{\tau} dP_o \gamma_2 f(P_o, \tau) + \frac{1}{K_2} \int_{-\infty}^{P_c} dP_o \int_{P_o}^{+\infty} dP_c f(P_o, P_c) \\ &+ \left( \frac{1}{K_1} - \frac{1}{K_2} \right) \int_{O_2}^{P_c} dP_o \int_{\tau}^{+\infty} dP_c f(P_o, P_c) \end{aligned}. \quad (1.23)$$

The first double integral term is the inverse of the bulk modulus contribution when all the HEUs are in the closed state. The second integral term is the modification of the inverse of the bulk modulus due to open HEUs, and the single integral term is the additional contribution to the inverse of the bulk modulus of the HEUs closing at the actual stress  $\tau$ . When the stress is decreased, similar, the strain variation for each elementary HEU is now given by:

$$\begin{cases} \frac{\partial \varepsilon_M}{\partial t} = \gamma_1 \delta(\tau - P_o) + \frac{1}{K_1} + \left( \frac{1}{K_2} - \frac{1}{K_1} \right) u(P_o - \tau) & \text{If HEU M is closed} \\ \frac{\partial \varepsilon_M}{\partial t} = \frac{1}{K_1} & \text{If HEU M is open} \end{cases}, \quad (1.24)$$

and the overall strain variation can be similarly obtained:

$$\begin{aligned} \frac{\partial \varepsilon_H}{\partial \tau} = & \int_{\tau}^{C_2} dP_c \gamma_1 f(\tau, P_c) + \frac{1}{K_1} \int_{-\infty}^{P_c} dP_o \int_{P_o}^{+\infty} dP_c f(P_o, P_c) \\ & + \left( \frac{1}{K_2} - \frac{1}{K_1} \right) \int_{-\infty}^{P_c} dP_o \int_{P_o}^{C_2} dP_c f(P_o, P_c) \end{aligned} \quad (1.25)$$

where now, the first double integral term is the inverse of the bulk modulus contribution when all the HEUs are in the open state. The second integral term is the modification of the inverse of the bulk modulus due to closed HEUs, and the single integral term is the additional contribution to the inverse of the bulk modulus of the HEUs opening at the actual stress  $\tau$ . In both cases of increasing and decreasing stress, the variation of  $\partial \varepsilon_H / \partial \tau$  can be calculated by looking at the closing or opening HEUs, respectively, between the actual and past value of the stress.

In the case shown in Fig. 1.8 the following relations have to be used to simplify Eq. (1.23) and Eq. (1.25)

$$\gamma_1 = \gamma = \frac{P_c - P_o}{K_1}, \quad \gamma_2 = 0, \quad \text{and} \quad \frac{1}{K_2} = 0. \quad (1.26)$$

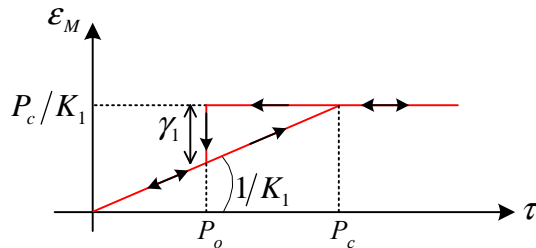


**Fig. 1.8** Elementary hysteretic elements as proposed by Scalenderi This case is a particular case of the “elastic” to state element described in Figure 1.6(b) when  $1/K_2 = 0$ . In this case the closed state corresponds to a true rigid state.

### 1.3.2.5 Nonlinear Attenuation

In some case, for example to explain Luxemburg-Gorky effect [212], [213], not only the bulk modulus depends nonlinearly on the strain but also the attenuation. To describe this phenomenon, Nazarov *et al.* [136] have introduced the following stress / strain relation:

$$\tau(\varepsilon) = E(\varepsilon - f(\varepsilon, \dot{\varepsilon})) + \alpha\rho_0(1 + g|\varepsilon|^s)\dot{\varepsilon} = \tau' + \tau'', \quad (1.27)$$

Introducing this constitutive equation in the equation of motion we obtain the following system:

$$\frac{\partial v}{\partial t} = \frac{1}{\rho_0} \frac{\partial(\tau' + \tau'')}{\partial z}, \quad (1.28)$$

$$\frac{\partial \tau'}{\partial t} = K(t) \frac{\partial v}{\partial z}, \quad (1.29)$$

with

$$\tau'' = \alpha\rho_0 \left( 1 + g \left| \frac{\partial u}{\partial z} \right|^s \right) \frac{\partial v}{\partial z} = \alpha\rho_0 (1 + g|\varepsilon|^s) \dot{\varepsilon}, \quad (1.30)$$

and  $K(t)$  is the elastic modulus given by one of the preceding nonlinear models.

### 1.3.2.6 Linear Attenuation

When the attenuation introduced by nonlinear effects is small, a linear attenuation needs to be introduced in simulations, especially when we consider resonant rods. This attenuation, and the dispersive effects associated are often quantified by the quality factor  $Q$ , which is, in many real materials, independent of the frequency. To introduce a constant  $Q$  in our simulations we used the methodology introduced by Blanch *et al.* [20]. For 1D, the viscoelastic hypothesis can be described as [154]:

$$\tau = K(t) \otimes \frac{\partial v}{\partial z}, \quad (1.31)$$

where the bulk modulus is given by:

$$K(t) = K_r \left( 1 - \sum_{l=1}^L \left( 1 - \frac{\tau_{el}}{\tau_{ol}} \right) e^{-t/\tau_{ol}} \right) u(t), \quad (1.32)$$

with  $K_r$  the relaxed bulk modulus corresponding to  $K(t)$ ,  $\tau_{ol}$  and  $\tau_{el}$  are the stress and strain relaxation times for the  $l$ -th of the  $L$  standard linear solids connected in parallel to model the viscoelastic properties of the considered solid in the frequency range of interest.

Taking the time derivative of Eq. (1.31) we obtain:

$$\frac{\partial \tau}{\partial t} = \frac{\partial K(t)}{\partial t} \otimes \frac{\partial v}{\partial z}, \quad (1.33)$$

with

$$\frac{\partial K(t)}{\partial t} = K_r \left( 1 - \sum_{l=1}^L \left( 1 - \frac{\tau_{el}}{\tau_{ol}} \right) e^{-t/\tau_{ol}} \right) \delta(t) + K_r \left( \sum_{l=1}^L \frac{1}{\tau_{ol}} \left( 1 - \frac{\tau_{el}}{\tau_{ol}} \right) e^{-t/\tau_{ol}} \right) u(t). \quad (1.34)$$

Introducing memory variables  $r_l$ , Eq. (1.33) can be re-written as:

$$\frac{\partial \tau}{\partial t} = K_r' \frac{\partial v}{\partial z} + \sum_{l=1}^L r_l, \quad (1.35)$$

where the following notations have been introduced:

$$K_r' = K_r \left( 1 - \sum_{l=1}^L \left( 1 - \frac{\tau_{el}}{\tau_{ol}} \right) \right), \quad (1.36)$$

and

$$r_l = K_r \left( \frac{1}{\tau_{ol}} \left( 1 - \frac{\tau_{el}}{\tau_{ol}} \right) e^{-t/\tau_{ol}} \right) u(t) \otimes \frac{\partial v}{\partial z}. \quad (1.37)$$

$r_l$  can be calculated with a first order differential equation:

$$\frac{\partial r_l}{\partial t} = -\frac{r_l}{\tau_{ol}} + K_r \left( \frac{1}{\tau_{ol}} \left( 1 - \frac{\tau_{el}}{\tau_{ol}} \right) \right) \frac{\partial v}{\partial z}, \quad (1.38)$$

obtained by time derivation of Eq. (1.37). The frequency evolution of the  $Q$ -factor corresponding to this model is [154]:

$$Q(\omega) = \frac{1 - L + \sum_{l=1}^L \frac{1 + \omega^2 \tau_{el} \tau_{ol}}{1 + \omega \tau_{ol}^2}}{\sum_{l=1}^L \frac{\omega(\tau_{el} - \tau_{ol})}{1 + \omega \tau_{ol}^2}}. \quad (1.39)$$

Now, to calculate the  $\tau_{ol}$  and the  $\tau_{el}$  we used the  $\tau$ -method introduced by Blanch *et al.* [20], [154], where we define the  $\tau$  variable as:

$$\tau = \frac{\tau_{el}}{\tau_{ol}} - 1, \quad (1.40)$$

with this new parameter, the  $Q$ -factor is given by:

$$Q(\omega) = \frac{1 + \sum_{l=1}^L \frac{\omega^2 \tau_{ol}^2}{1 + \omega \tau_{ol}^2} \tau}{\sum_{l=1}^L \frac{\omega \tau_{ol}}{1 + \omega \tau_{ol}^2} \tau}. \quad (1.41)$$

The  $\tau_{ol} = 1/\omega_l$  are distributed logarithmically over the frequency range of interest following the rule of thumb of about one per one-two octaves (for example, 6 relaxations are needed to realize simulations between 1 kHz and 1 MHz). When a constant  $Q$ -factor ( $Q_0$ ) is simulated,

the formula given by Blanch *et al.* [20], [154] (Eqs. (21)-(23) in their paper) is used. In the case of another frequency evolution of  $Q$ , an optimization algorithm is used to minimize over  $\tau$  the expression:

$$J = \int_{\omega_1}^{\omega_2} (\hat{Q}^{-1}(\omega, \tau, \tau_{\sigma l}) - Q^{-1}(\omega))^2 d\omega, \quad (1.42)$$

where  $\hat{Q}$  is the approximated  $Q$ -factor given by Eq. (1.41).

Knowing  $\tau_{\sigma l}$  and  $\tau$ , the corresponding bulk modulus at a given frequency  $\omega_0$  is:

$$K(\omega_0) = c_l^2(\omega_0) \rho_0 \operatorname{Re}^2 \left[ \sqrt{\frac{1}{1 + \sum_{l=1}^L \frac{j\omega_0 \tau_{\sigma l}}{1 + j\omega_0 \tau_{\sigma l}} \tau}} \right], \quad (1.43)$$

where  $c_l$  is the longitudinal wave velocity in the medium. So, when a resonant rod simulation is made, the bulk modulus at the resonant frequency need to be calculated by Eq. (1.43) for a given longitudinal wave velocity. Parameters obtained to simulate a constant  $Q$  factor of 80 between 1 kHz and 1 MHz are given in Table 1.1.

**Tab. 1.1** Parameters of the 7 relaxations needed to simulate a constant  $Q$  factor of 80.

N°	1	2	3	4	5	6	7
$\tau_{\sigma l}$	$3.98 \cdot 10^{-4}$	$7.96 \cdot 10^{-5}$	$1.59 \cdot 10^{-5}$	$3.18 \cdot 10^{-6}$	$6.37 \cdot 10^{-7}$	$1.27 \cdot 10^{-7}$	$2.55 \cdot 10^{-8}$
$\tau$				$1.31 \cdot 10^{-2}$			
$K(100\text{kHz})$				$3.657 \cdot 10^6$			

The evolution of  $Q$  as a function of frequency calculated with these parameters is shown in Fig. 1.9. This constant  $Q$  factor model corresponds to a linear frequency dependence of the attenuation (Fig. 1.10(a)) and to the dispersion presented in Fig. 1.10(b).

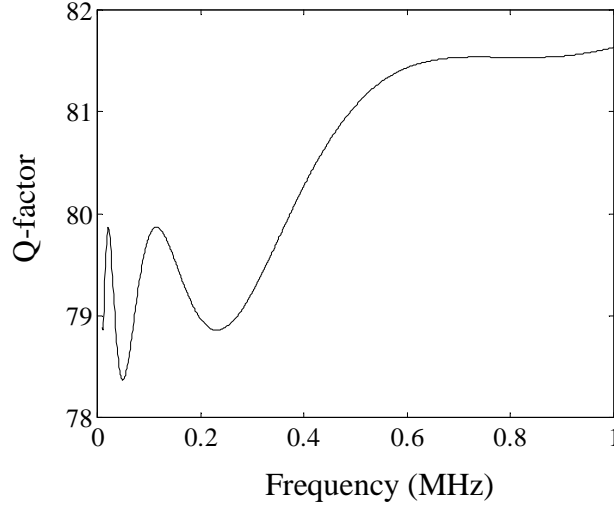


**Fig. 1.9** Obtained  $Q$ -factor as a function of frequency, by the  $\tau$ -method with 7 relaxations, in the case of a constant  $Q$ -factor of 80.

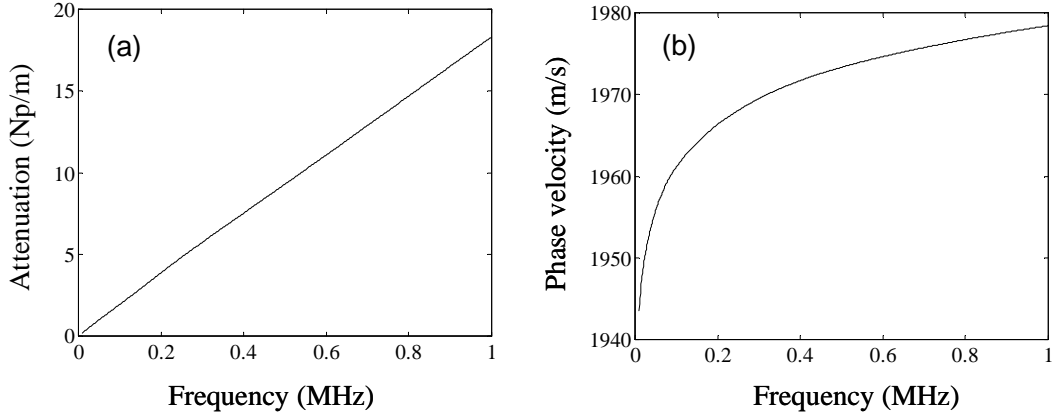


**Fig. 1.10** (a) Attenuation and (b) phase velocity as a function of frequency for the constant  $Q$  factor of 80 medium.

### 1.3.3 Nonlinear Elastodynamic System of Equations

For nonlinear elastodynamic solid medium, with “classical” and “non-classical” nonlinearities, it is more judicious to discretize the fundamental elastodynamic equations expressed in conservation form. The considered equation of motion can be written, with Einstein’s convention of summation:

$$\rho_0 \frac{\partial v_i}{\partial t} = \frac{\partial P_{ij}}{\partial a_j}, \quad (1.44)$$

where  $v_i$  are the components of the particle velocity vector,  $a_j$  are the components of the Lagrangian position vector,  $\rho_0$  is the density,  $P_{ij}$  are the components of the Piola-Kirchhoff tensor, and  $t$  is the time. These equations are completed by the constitutive relation:

$$P_{ij} = \rho_0 \frac{\partial W}{\partial F_{ij}}, \quad (1.45)$$

where  $W$  is the elastic energy density which depends on the considered nonlinear (or linear) model of elasticity, and  $F$  is the deformation gradient:

$$F_{ij} = \delta_{ij} + \frac{\partial u_i}{\partial a_j}, \quad (1.46)$$

where  $\delta_{ij}$  is the Dirac delta function, and  $u_i$  are the component of the displacement vector. For example, in the case of an anisotropic linear elastic solid the constitutive equations are given by the Hooke's law:

$$P_{ij} = \tau_{ij} = C_{ijkl} \epsilon_{kl}, \quad (1.47)$$

where  $C_{ijkl}$  are the elastic constants. Finally, the system is closed by the link between particle velocity and deformations gradient:

$$\frac{\partial F_{ij}}{\partial t} = \frac{\partial v_i}{\partial a_j}. \quad (1.48)$$

To resume, the system to be solved, in order to simulate propagation of elastic waves in nonlinear elastic solids, is written in the following conservation form:

$$\frac{\partial \mathbf{Q}(t, \mathbf{x})}{\partial t} = \frac{\partial \mathbf{F}_x}{\partial x} + \frac{\partial \mathbf{F}_y}{\partial y} + \frac{\partial \mathbf{F}_z}{\partial z}, \quad \mathbf{x} = [x, y, z] \in \Omega \in \mathbf{R}^3, \quad (1.49)$$

$\Omega$  is the global physical domain with boundary  $\partial\Omega$  and

$$\mathbf{Q} = \begin{pmatrix} \rho_0 v_1 \\ \rho_0 v_2 \\ \rho_0 v_3 \\ F_{11} \\ F_{22} \\ F_{33} \\ F_{23} \\ F_{32} \\ F_{13} \\ F_{31} \\ F_{12} \\ F_{21} \end{pmatrix}, \quad \mathbf{F}_x = \begin{pmatrix} P_{11} \\ P_{21} \\ P_{31} \\ v_1 \\ 0 \\ 0 \\ 0 \\ 0 \\ 0 \\ 0 \\ v_3 \\ v_2 \end{pmatrix}, \quad \mathbf{F}_y = \begin{pmatrix} P_{12} \\ P_{22} \\ P_{32} \\ 0 \\ v_2 \\ 0 \\ 0 \\ v_3 \\ 0 \\ 0 \\ v_1 \\ 0 \end{pmatrix}, \quad \mathbf{F}_z = \begin{pmatrix} P_{13} \\ P_{23} \\ P_{33} \\ 0 \\ 0 \\ v_3 \\ v_2 \\ 0 \\ v_1 \\ 0 \\ 0 \\ 0 \end{pmatrix}, \quad (1.50)$$

represent the state vector and the three components of the flux, respectively.

This system of equations is at the basis of all the numerical simulations of linear and nonlinear elastic wave propagation that have been realized with the Discontinuous Galerkin Finite Element Method (DG-FEM) [63], [64], [94], [103], [104], [148] presented in Chapter 2.

In the linear elastic case the the system of equations (1.49) can be rewritten in 2D as:

$$\frac{\partial \mathbf{Q}(t, \mathbf{x})}{\partial t} = \mathbf{A} \frac{\partial \mathbf{Q}}{\partial x} + \mathbf{B} \frac{\partial \mathbf{Q}}{\partial y}, \quad \mathbf{x} = [x, y] \in \Omega \in \mathbf{R}^2, \quad (1.51)$$

where

$$\mathbf{A} = \begin{bmatrix} 0 & 0 & C_{11} & C_{12} & 0 & 0 \\ 0 & 0 & 0 & 0 & C_{66} & C_{66} \\ 1/\rho_0 & 0 & 0 & 0 & 0 & 0 \\ 0 & 0 & 0 & 0 & 0 & 0 \\ 0 & 0 & 0 & 0 & 0 & 0 \\ 0 & 1/\rho_0 & 0 & 0 & 0 & 0 \end{bmatrix}, \quad (1.52)$$

and

$$\mathbf{B} = \begin{bmatrix} 0 & 0 & 0 & 0 & C_{66} & C_{66} \\ 0 & 0 & C_{12} & C_{22} & 0 & 0 \\ 0 & 0 & 0 & 0 & 0 & 0 \\ 0 & 1/\rho_0 & 0 & 0 & 0 & 0 \\ 1/\rho_0 & 0 & 0 & 0 & 0 & 0 \\ 0 & 0 & 0 & 0 & 0 & 0 \end{bmatrix}. \quad (1.53)$$

The classical nonlinear case will be described later in chapter 2. Now, to introduce “non-classical” nonlinearity, the methodology used in Ref. [79], and based on Kelvin notation, is used. The elastic constant tensor is written in Kelvin notation [52], [89] by pre and post multiplying the Voigt matrix by

$$\begin{pmatrix} 1 & 0 & 0 \\ 0 & 1 & 0 \\ 0 & 0 & \sqrt{2} \end{pmatrix}. \quad (1.54)$$

In the Kelvin notation the elastic coefficient tensor thus becomes:

$$\tilde{\mathbf{C}}_{IJ} = \begin{pmatrix} C_{11} & C_{12} & 0 \\ C_{12} & C_{22} & 0 \\ 0 & 0 & 2C_{66} \end{pmatrix}. \quad (1.55)$$

Using these notations, it can be shown that the 3 eigenvectors of the elastic constant tensor correspond to 3 eigenstress / eigenstrain vectors  $\tilde{\boldsymbol{\varepsilon}}^{(k)}$ :

$$\tilde{\boldsymbol{\varepsilon}}^{(1)} = \frac{1}{\sqrt{1+X_1^2}} \begin{pmatrix} X_1 \\ 1 \\ 0 \end{pmatrix}, \quad \tilde{\boldsymbol{\varepsilon}}^{(2)} = \frac{1}{\sqrt{1+X_2^2}} \begin{pmatrix} X_2 \\ 1 \\ 0 \end{pmatrix}, \quad \tilde{\boldsymbol{\varepsilon}}^{(3)} = \begin{pmatrix} 0 \\ 0 \\ 1 \end{pmatrix}, \quad (1.56)$$

with the associated eigenvalues  $\alpha_1$ ,  $\alpha_2$  and  $2C_{66}$ , respectively. The following notations have been introduced:

$$X_1 = -\frac{1}{C_{12}} \left( \frac{C_{22}}{2} - \frac{C_{11}}{2} - \frac{1}{2} \sqrt{C_{22}^2 - 2C_{11}C_{22} + C_{11}^2 + 4C_{12}^2} \right), \quad (1.57)$$

$$X_2 = -\frac{1}{C_{12}} \left( \frac{C_{22}}{2} - \frac{C_{11}}{2} + \frac{1}{2} \sqrt{C_{22}^2 - 2C_{11}C_{22} + C_{11}^2 + 4C_{12}^2} \right), \quad (1.58)$$

$$\alpha_1 = \frac{C_{22}}{2} + \frac{C_{11}}{2} + \frac{1}{2} \sqrt{C_{22}^2 - 2C_{11}C_{22} + C_{11}^2 + 4C_{12}^2}, \quad (1.59)$$

$$\alpha_2 = \frac{C_{22}}{2} + \frac{C_{11}}{2} - \frac{1}{2} \sqrt{C_{22}^2 - 2C_{11}C_{22} + C_{11}^2 + 4C_{12}^2}. \quad (1.60)$$

These vectors represent directions where applied stress and created strain are in the same direction. In this case, it is possible to use any of the scalar models described for 1D simulation, for each of these 3 directions. Only the associated eigenstiffness  $\Lambda^{(k)}$  is modified and the actualized elastic coefficient tensors in Voigt notation used in equations similar to Eqs. (1.51) or (1.52) are obtained by:

$$C_{IJ} = \sum_k \Lambda^{(k)} \tilde{\boldsymbol{\varepsilon}}^{(k)} \tilde{\boldsymbol{\varepsilon}}^{(k)T}, \quad (1.61)$$

Based on these Kelvin notations, the calculation steps are as follows:

1. Calculation of the 2D Kelvin stress vector:

$$\tilde{\boldsymbol{P}} = \begin{pmatrix} P_{xx} \\ P_{yy} \\ P_{xy} \sqrt{2} \\ P_{yx} \sqrt{2} \end{pmatrix}, \quad (1.62)$$

2. Calculation of the stress projections along the 3 eigenstress directions:

$$\tilde{P}^{(1)} = \frac{X_1}{\sqrt{1+X_1^2}} P_{xx} + \frac{1}{\sqrt{1+X_1^2}} P_{yy}, \quad \tilde{P}^{(2)} = \frac{X_2}{\sqrt{1+X_2^2}} P_{xx} + \frac{1}{\sqrt{1+X_2^2}} P_{yy}, \quad \tilde{P}^{(3)} = \tilde{P}^{(4)} = P_{xy} \sqrt{2}, \quad (1.63)$$

3. Modification of each associated eigenvalue  $E^{(i)}$  using the considered nonlinear model.

4. Calculation of the modified elastic tensor using the equations:

$$C_{11} = E^{(1)} \frac{X_1^2}{1+X_1^2} + E^{(2)} \frac{X_2^2}{1+X_2^2}, \quad (1.64)$$

$$C_{12} = E^{(1)} \frac{X_1}{1+X_1^2} + E^{(2)} \frac{X_2}{1+X_2^2}, \quad (1.65)$$

$$C_{22} = E^{(1)} \frac{1}{1 + X_1^2} + E^{(2)} \frac{1}{1 + X_2^2}, \quad (1.66)$$

$$C_{66} = \frac{E^{(3)}}{2}. \quad (1.67)$$

Finally, we can note that a molecular dynamic model has been proposed in Ref. [201] to calculate the stress-strain relation.

## 1.4 Numerical Simulation Methods

In many research domains, solving a Partial Differential Equation (PDE) computationally is needed in order to simulate the underlining physical process, and a large number of different methods have been developed for this. Among these are the widely used Finite Difference Method (FDM), Finite Volume Method (FVM), and Finite Element Method (FEM), which are all techniques used for long time to derive discrete representations of the spatial derivative operators. Pseudo-Spectral (PS) Method and Discontinuous Galerkin Finite Element Method (DG-FEM) have been developed for improving the efficiency of calculation and adding geometric flexibility. These methods will be reviewed and the advantages and weaknesses of these techniques will be discussed in the following subsections. To appreciate these different methods, we consider the one-dimensional scalar conservation law for the variable  $u(x, t)$

$$\frac{\partial u}{\partial t} + \frac{\partial f}{\partial x} = g, \quad x \in \Omega \quad (1.68)$$

where  $f(u)$  is the flux,  $g(x, t)$  is some prescribed forcing source. This equation is completed by an appropriate set of initial conditions and boundary conditions on the boundary  $\partial\Omega$ .

The construction of any numerical method for solving a partial differential equation requires one to consider the two following choices:

- How can the solution  $u(x, t)$  be represented by an approximate solution  $u_h(x, t)$ ?
- In which sense will the approximate solution  $u_h(x, t)$  satisfy the partial differential equation?

These two choices separate the different methods and define the properties of the methods. It is instructive to seek a detailed understanding of these choices and how they impact the schemes to appreciate how to address problems and limitations associated with the classic schemes.

### 1.4.1 Finite Difference Method

The Finite Difference Method (FDM) was first introduced by Yee [210] in 1966 for the study of electromagnetic scattering problems. One of the most attracting aspects of FDM is its simplicity. It leads to very efficient semi-discrete spatial schemes. We begin with the simplest and historically oldest method. In this approach, a grid  $x_k$  ( $k = 1, 2 \dots K$ ) is laid down in 1D space as shown in Fig. 1.11

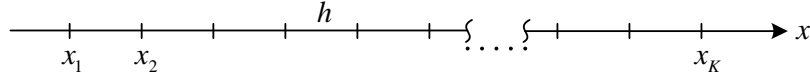


Fig. 1.11 Grid distribution of Finite Difference Method in 1D.

The conservation law is approximated by difference methods as

$$\frac{du_h(x_k, t)}{dt} + \frac{f_h(x_{k+1}, t) - f_h(x_{k-1}, t)}{h_k + h_{k-1}} = g(x_k, t), \quad (1.69)$$

where  $u_h$  and  $f_h$  are the numerical approximations to the solution and the flux, respectively, and  $h_k = x_{k+1} - x_k$  is the local grid size. The construction of a finite difference method requires that, in the neighborhood of each grid point  $x_k$ , the solution and the flux are assumed to be well approximated by local polynomials

$$x \in [x_{k-1}, x_{k+1}]: \quad u_h(x, t) = \sum_{i=0}^2 a_i(t)(x - x_k)^i, \quad \text{and} \quad f_h(x, t) = \sum_{i=0}^2 b_i(t)(x - x_k)^i, \quad (1.70)$$

where the coefficients  $a_i(t)$  and  $b_i(t)$  are found by requiring that the approximate function interpolates at the grid points  $x_k$ . Inserting these local approximations into Eq. (1.68), the residual will be obtained as following

$$x \in [x_{k-1}, x_{k+1}]: \quad \mathfrak{R}_h(x, t) = \frac{\partial u_h}{\partial t} + \frac{\partial f_h}{\partial x} - g(x, t). \quad (1.71)$$

Thus, we need to specify in which way  $u_h(x, t)$  must satisfy the equation, which amounts to a statement about the residual  $\mathfrak{R}_h(x, t)$ . If we have a total of  $K$  grid points and, thus,  $K$  unknown grid point values,  $u_h(x_k, t)$  is a natural choice to require that the residual vanishes exactly at these grid points. This results in exactly  $K$  finite difference equation of the type in Eq. (1.69) for the  $K$  unknowns.

If the equation, which should be solved, is in second order formulation within the time domain, the following second order finite difference formulation can be used

$$\frac{d^2 u_h(x, t_k)}{dt^2} = \frac{u_h(x, t_{k+1}) - 2u_h(x, t_k) + u_h(x, t_{k-1}))}{\Delta t_k^2}, \quad (1.72)$$

where  $\Delta t_k = t_{k+1} - t_k$  is the time step of calculation. For us, to do the simulation of elastic

wave propagating in anisotropic solid medium, described in a second order wave equation, with C-PML absorbing boundary condition, the preceding second order finite difference formulation in time domain has been used [117].

The simplicity is one of the most appealing properties of the FDM method. Moreover, due to its features of robustness and powerfulness, it has been used to many general problems in a wide range of domains, e.g., acoustic [211], [166], elastic wave [60], [61], [43], [48], computational electrodynamics [210], [178], and so on. Furthermore, the explicit semidiscrete form gives flexibility in the choice of timestepping methods, e.g., Runge-Kutta [35] and Adams-Bashforth [76] time integrators can easily be used in the FDM scheme. Finally, extension to higher order approximations by using a local polynomial approximation of higher degree is relatively straightforward.

However, the reliance on the local one-dimensional polynomial approximation that is the Achilles' heel of the method, as that enforces a simple dimension-by-dimension structure in higher dimensions. Additional complications caused by the simple underlying structure are introduced around boundaries and discontinuous internal layers (e.g., discontinuous material coefficients). This makes the native FDM ill-suited to deal with complex geometries, both in terms of general computational domains and internal discontinuities as well as for local order and grid size changes to reflect local features of the solution.

## 1.4.2 Finite Volume Method

The Finite Volume Method (FVM) is a discretization method which is well suited for the numerical simulation of various types (elliptic, parabolic or hyperbolic, for instance) of conservation laws. One important feature of FVM is that it can be used on arbitrary geometries, using structured or unstructured meshes, due to the introduction of an element-based discretization.

Grid distribution for the 1D FVM scheme is shown in Fig. 1.12:

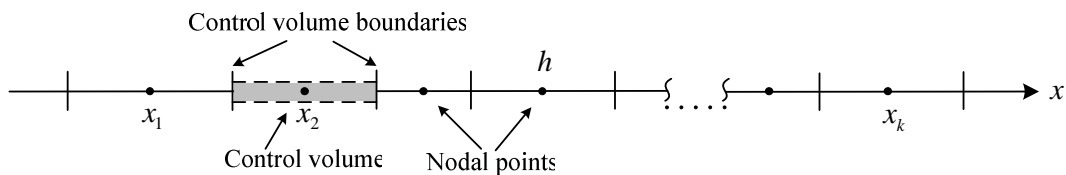


**Fig. 1.12** Control volumes and nodal points of Finite Volume Method in 1D.

Each discretization cell is often called “control volume” and grids point located at the center of each element. In its simplest form, the solution of Eq. (1.68)  $u(x,t)$  is approximated on the element by a constant  $\bar{u}_k(t)$  at the center of the element  $x_k$ . This is introduced into Eq. (1.68) to recover the cellwise residual

$$x \in D_k: \quad \mathfrak{R}_h(x, t) = \frac{\partial \bar{u}_k}{\partial t} + \frac{\partial f(\bar{u}_k)}{\partial x} - g(x, t), \quad (1.73)$$

where the element is defined as  $D_k = [x_{k-1/2}, x_{k+1/2}]$  with  $x_{k+1/2} = (x_k + x_{k+1})/2$ . In the FVM method we require that the cell average of the residual vanishes identically, leading to the scheme:

$$h_k \frac{d\bar{u}_k}{dt} + f_{k+1/2} - f_{k-1/2} = h_k \bar{g}_k, \quad (1.74)$$

for each cell. Note that the approximation and the scheme are purely local and, thus, imposes no conditions on the grid structure. In particular, all cells can have different sizes  $h_k$ . The flux term reduces to a pure surface term by the use of the divergence theorem, or Gauss' theorem. This step introduces the need to evaluate the fluxes at the boundaries. However, since the unknowns are the cell averages of the numerical solution  $u_h$ , the evaluation of these fluxes is not straightforward.

This reconstruction problem and the subsequent evaluation of the fluxes at the interfaces can be addressed in many different ways and the details of this lead to different finite volume methods. For example, a simple solution to the reconstruction problem is to use

$$u_{k+1/2} = (\bar{u}_{k+1} + \bar{u}_k)/2, \quad f_{k+1/2} = f(u_{k+1/2}), \quad (1.75)$$

and likewise for  $f_{k-1/2}$ . The local conservativity of the numerical fluxes is that the numerical flux is conserved from one discretization cell to its neighbor. This feature makes the finite volume method quite attractive when modeling problems for which the flux is of importance, such as in fluid mechanics [196], or elastodynamic [198]. For linear problems and equidistant grids these methods reduce to the finite difference method. However, one easily realizes that the formulation is less restrictive in terms of the grid structure, that is, the reconstruction of solution values at the interfaces is a local procedure and generalizes straightforwardly to unstructured grids in high dimensions, thus ensuring the desired geometric flexibility.

However, if we need to increase the order of accuracy of the method, a fundamental problem emerges. Consider again the problem in one dimension. We wish to reconstruct the solution  $u_h$  at the interface and we seek a local polynomial,  $u_h(x)$  of the form

$$x \in [x_{k-1/2}, x_{k+3/2}]: \quad u_h(x) = a + bx. \quad (1.76)$$

To recover the two coefficients, then, we require

$$\int_{x_{k-1/2}}^{x_{k+1/2}} u_h(x) dx = h_k \bar{u}_k, \quad \int_{x_{k+1/2}}^{x_{k+3/2}} u_h(x) dx = h_{k+1} \bar{u}_{k+1}. \quad (1.77)$$

The reconstructed value of the solution  $u_h$ , and therefore also  $f(u_h(x_{1+1/2}))$  can then be evaluated.

To reconstruct the interface values at a higher accuracy we can continue as above and

seek a local solution of the form

$$u_h(x) = \sum_j^N a_j (x - x_k)^j. \quad (1.78)$$

However, to find the  $N + 1$  unknown coefficients, we will need information from at least  $N + 1$  cells. In the simple one-dimensional case, this can be done straightforwardly, as for the finite difference scheme (i.e., by extending the size of the stencil). However, the need for a high-order reconstruction reintroduces the need for a particular grid structure and thus destroys the geometric flexibility of the finite volume method in higher dimensions. This defeats the initial motivation for considering the finite volume method. On unstructured grids this approach requires a reconstruction based on genuinely multivariate polynomials with general cell center locations which is both complex and prone to stability problems. So, the main limitation of finite volume methods is found in its inability to extend to higher-order accuracy on general unstructured grids.

### 1.4.3 Finite Element Method

From the presentation of Finite Volume Method (FVM), we realize that the problem with the high-order reconstruction is that it must span multiple elements as the numerical approximation  $u_h(x, t)$  is represented by cell averages only. One could be tempted to take a different approach and introduce more degrees of freedom on the element. To pursue this idea, Finite Element Method (FEM) should be present.

As the methods of FDM and FVM, the FEM is also a numerical technique which gives approximate solutions to differential equations that modelize problems arising in physics and engineering. As in simple finite difference schemes, the finite element method requires a problem defined in geometric domain to be subdivided into a finite number of smaller regions (mesh). In finite differences, the mesh consists of rows and columns of orthogonal lines, however, in finite element method, each subdivision is unique and need not be orthogonal. For example, triangles or quadrilaterals can be used in two dimensions and tetrahedrons or hexahedrons in three dimensions. Over each finite element, the unknown variables are approximated using known functions, these functions can be linear or higher-order polynomial expansions that depend on the geometrical locations used to define the finite element shape. In contrast to finite difference procedures (or finite volume method), the governing equations in the finite element method are integrated over each finite element and the solution summed over the entire problem domain. As a consequence of these operations, a set of finite linear equations is obtained in terms of a set of unknown parameters over each element. Solution of these equations is achieved using linear algebra techniques.

For solving the approximate solution of Eq. (1.68) with FEM scheme, we redefine the element  $D_k$  as the interval bounded by the grid points  $[x_k, x_{k+1}]$  and with a total of  $K$  elements and  $K + 1$  grid points as shown in Fig. 1.13.



**Fig. 1.13** Grid distribution of Finite Element Method in 1D.

Note that this is slightly different from the finite volume scheme where the element was defined by staggered grid points as  $[x_k, x_{k+1}]$ . Inside the element, we assume that the local solution is expressed in the form

$$x \in D_k : u_h(x) = \sum_{n=1}^{N_p} b_n \varphi_n(x), \quad (1.79)$$

where we have introduced the use of a locally defined basis function  $\varphi_n(x)$ . In the simplest case, we can take these basis functions to be linear:

$$x \in D_k : u_h(x) = u(x_k) \frac{x - x_{k+1}}{x_k - x_{k+1}} + u(x_{k+1}) \frac{x - x_k}{x_{k+1} - x_k} = \sum_{i=0}^1 u(x_{k+i}) \ell_i^k(x), \quad (1.80)$$

where the linear Lagrange polynomial  $\ell_i^k(x)$  is given as

$$\ell_i^k(x) = \frac{x - x_{k+1-i}}{x_{k+i} - x_{k+1-i}}. \quad (1.81)$$

With this local element-based model, each element shares the nodes with one other element. We have a global representation of  $u_h$  as

$$u_h(x) = \sum_{k=1}^K u(x_k) N_k(x) = \sum_{k=1}^K u_k N_k(x), \quad (1.82)$$

where the piecewise linear shape function,  $N_i(x_j) = \delta_{ij}$  is the basis function and  $u_k = u(x_k)$  remain as the unknowns.

To recover the scheme to solve Eq. (1.68), we define a space of test functions  $V_h$ , and require that the residual is orthogonal to all test functions in this space as

$$\int_{\Omega} \left( \frac{\partial u_h}{\partial t} + \frac{\partial f_h}{\partial x} - g_h \right) \phi_h(x) dx = 0. \quad \forall \phi_h \in V_h. \quad (1.83)$$

The details of the scheme are determined by how this space of test functions is defined. A classic choice, leading to a Galerkin scheme, is to require that spaces spanned by the basis functions and test functions are the same. Since the residual has to vanish for all  $\phi_h \in V_h$ , this amounts to

$$\int_{\Omega} \left( \frac{\partial u_h}{\partial t} + \frac{\partial f_h}{\partial x} - g_h \right) N_j(x) dx = 0, \quad (1.84)$$

for  $j = 1 \dots K$ . Straightforward manipulations yield the scheme

$$M \frac{du_h}{dt} + S f_h = M g_h, \quad (1.85)$$

where

$$M_{ij} = \int_{\Omega} N_i(x) N_j(x) dx, \quad S_{ij} = \int_{\Omega} N_i(x) \frac{dN_j}{dx} dx, \quad (1.86)$$

reflect the globally defined mass matrix and stiffness matrix, respectively.

This approach, which reflects the essence of the classic finite element method [97], clearly allows different element sizes. Furthermore, we recall that a main motivation for considering methods beyond the finite volume approach was the interest in higher-order approximations. Such extensions are relatively simple in the finite element setting and can be achieved by adding additional degrees of freedom to the element while maintaining shared nodes along the faces of the elements [102]. In particular, one can have different orders of approximation in each element, thereby enabling local changes in both size and order, known as hp-adaptivity [54].

However, the above discussion also highlights disadvantages of the classic continuous finite element formulation. First, we see that the globally defined basis functions and the requirement that the residual be orthogonal to the same set of globally defined test functions implies that the semidiscrete scheme becomes implicit and  $M$  must be inverted. For time dependent problems, this is a clear disadvantage compared to finite difference and finite volume methods.

Simulations with FEM scheme, for applications of Convolution Perfectly Matched Layer in isotropic, anisotropic solids [117], piezoelectric media [25], [116], and plate [25], [116], have been implemented within a commercial FEM software (COMSOL Multiphysics) in the frequency domain. Details about this will be presented in Chapter 3.

#### 1.4.4 Pseudo-Spectral Method

The FDM scheme has been used in many researching domains by a huge number of authors who appreciate its simplicity, robustness, and powerfulness. However, numerical examples have indicated that a spatial sampling density of at least 10 to 20 cells per minimum wavelength is necessary to ensure that the FDM produces acceptable results to the calculations of wave propagation on several wavelengths. For such kinds of problem, the bigger the size of the modeled structure, the higher the spatial sampling rate used in order to

reduce the cumulative numerical dispersion error. This makes FDM modeling of large scale problems very challenging.

In order to efficiently solve this kind of problem, Pseudo-Spectral (PS) algorithms have been developed. These methods use either trigonometric functions (Fourier Pseudo-Spectral), [119] or Chebyshev polynomials (Chebyshev Pseudo-Spectral) [216] to approximate spatial derivatives in order to greatly reduce the numerical dispersion error. When applied to single domains having smooth internal media, PS methods based upon these functions have spectral accuracy, meaning that the numerical dispersion error decreases exponentially with the sampling density. Spectral accuracy also can be achieved for problems with multiple inhomogeneity regions when PS algorithms are coupled with appropriate boundary-patching conditions [178].

In this part we will mainly present the Fourier Pseudo-Spectral (PS) method in which a staggered grid will be used. In the Fourier PS scheme, computation of the variables spatial derivatives is accomplished by the *FFT* algorithm. For example, the derivative  $\partial f(x)/\partial x$  in Eq. (1.68) is computed by taking the Fourier transform of  $f(x)$  over  $x$ :

$$\frac{\partial f(x)}{\partial x} = \frac{2\pi}{N_p \Delta x} FFT^{-1}[jk_x FFT[f(x)]], \quad (1.87)$$

where  $N_p$  is the number of grid points,  $\Delta x$  is the spatial step of discretization, *FFT* is a forward Fourier transform, *FFT*<sup>-1</sup> is an inverse Fourier transform,  $k_x$  is the wave number in the  $x$  direction. Eq. (1.87) yields an approximation to the spatial derivatives that has spectral accuracy for which the error decreases exponentially as  $N_p$  increase. The precision of calculation can be satisfied with a discretization of only two grid cells per minimum wavelength. The time-integration in the PS method can be realized with the Runge-Kutta [35] and Adams-Bashforth [76] integrators, as for FDM technique.

### 1.4.5 Discontinuous Galerkin Finite Element Method

The FEM has the properties of geometric flexibility and high-order accuracy, however, its globally defined basis and test functions destroy the locality of the scheme and introduce potential problems of stability for wave-dominated problems. In the following paragraphs, an intelligent combination of the finite element and the finite volume methods, utilizing a space of basis and test functions that mimics the finite element method but satisfying the equation in a sense closer to the finite volume method, appears to offer many of the desired properties. This combination is exactly what leads to the Discontinuous Galerkin Finite Element Method (DG-FEM) which has been proposed first in [152] as a way of solving the steady-state neutron transport equation. The first analysis of this method was presented by Lesaint and Raviart [113].

To achieve the scheme of DG-FEM, we maintain the definition of elements as in the FEM scheme such that  $D_k = [x_k, x_{k+1}]$ . However, to ensure the locality of the scheme, we duplicate the variables located at the nodes  $x_k$ . The sketch of the geometry for DG-FEM in one-dimensional is illustrated in Fig. 1.14.

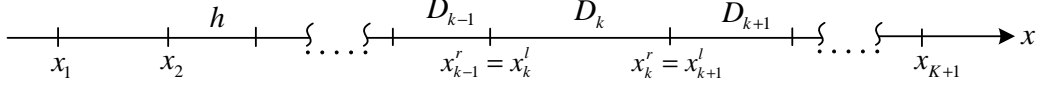


**Fig. 1.14** Geometry sketch of the DG-FEM in 1D.

Hence the vector of unknowns is defined as

$$\mathbf{u}_h = [u_1, u_2, u_2, u_3, \dots, u_{K-1}, u_K, u_K, u_{K+1}]^T, \quad (1.88)$$

and is now  $2K$  long rather than  $K + 1$  as in the finite element method. In each of these elements we assume that the local solution can be expressed as

$$x \in D_k: u_h^k(x) = u_k \frac{x - x_{k+1}}{x_k - x_{k+1}} + u_{k+1} \frac{x - x_k}{x_{k+1} - x_k} = \sum_{i=0}^1 u_{k+i} \ell_i^k(x) \in V_h, \quad (1.89)$$

and likewise for the flux  $f_h^k$ . The space of basis functions is defined as  $V_h = \bigoplus_{k=1}^K \{\ell_i^k\}_{i=0}^1$ , i.e., as the space of piecewise polynomial functions. Note in particular that there is no restrictions on the smoothness of the basis functions between elements.

As in the finite element case, we now assume that the local solution can be well represented by a linear approximation  $u_h \in V_h$  and form the local residual

$$x \in D_k: \mathfrak{R}_h(x, t) = \frac{\partial u_h^k}{\partial t} + \frac{\partial f_h^k}{\partial x} - g(x, t), \quad (1.90)$$

for each element. Going back to the finite element scheme, we recall that the global conditions on this residual are the source of the global nature of the operators  $M$  and  $S$  in Eq. (1.85). To overcome this, we require that the residual is orthogonal to all test functions  $\phi_h \in V_h$ , leading to

$$\int_{D_k} \mathfrak{R}_h(x, t) \ell_j^k(x) dx = 0, \quad (1.91)$$

for all the test functions  $\ell_j^k(x)$ . The strictly local statement is a direct consequence of  $V_h$  being a broken space and the fact that we have duplicated solutions at all interface nodes.

There are two questions that should be considered. First, the locality also appears problematic as this statement does not allow one to recover a meaningful global solution. Second, the points at the ends of the elements are shared by two elements so how does one ensure uniqueness of the solution at these points?

These problems are overcome by observing that the above local statement is very similar to that recovered in the finite volume method. Following this line of thinking, let us use Gauss' theorem to obtain the local statement

$$\int_{D_K} \frac{\partial u_h^k}{\partial t} \ell_j^k - f_h^k \frac{d\ell_j^k}{dx} - g \ell_j^k dx = -[f_h^k \ell_j^k]_{x_k}^{x_{k+1}}. \quad (1.92)$$

For the right-hand side term, it is easy to understand by considering the simplest case where  $\ell_j^k(x)$  is a constant, in which case we recover the finite volume scheme in Eq. (1.74). Hence, the main purpose of the term of the right-hand side is to connect the elements. This is further made clear by observing that both element  $D_K$  and element  $D_{K+1}$  depend on the flux evaluation at the point  $x_{k+1}$ , shared among the two elements. This situation is identical to the reconstruction problem discussed previously for the finite volume method where the interface flux is recovered by combining the information of the two cell averages appropriately.

According to the preceding analysis, it suffices to introduce the numerical flux  $f^*$ , as the unique value to be used at the interface and obtained by combining information from both elements. With this the following scheme will be recovered

$$\int_{D_K} \frac{\partial u_h^k}{\partial t} \ell_j^k - f_h^k \frac{d\ell_j^k}{dx} - g \ell_j^k dx = -[f^* \ell_j^k]_{x_k}^{x_{k+1}}, \quad (1.93)$$

or, by applying Gauss' theorem once again,

$$\int_{D_K} \mathfrak{R}_h(x, t) \ell_j^k(x) dx = [(f_h^k - f^*) \ell_j^k]_{x_k}^{x_{k+1}}. \quad (1.94)$$

These two formulations are the Discontinuous Galerkin Finite Element Method (DG-FEM) schemes for the scalar conservation law in weak and strong form, respectively. Note that the choice of the numerical flux  $f^*$  is a central element of the scheme and is also where one can introduce knowledge of the dynamics of the problem.

To mimic the terminology of the finite element scheme, the following two local element wise schemes are obtained

$$\mathbf{M}_k \frac{du_h^k}{dt} - (\mathbf{S}_k)^T \mathbf{f}_h^k - \mathbf{M}_k \mathbf{g}_h^k = -f^*(x_{k+1}) \ell^k(x_{k+1}) + f^*(x_k) \ell^k(x_k), \quad (1.95)$$

and

$$\mathbf{M}_k \frac{du_h^k}{dt} + \mathbf{S}_k \mathbf{f}_h^k - \mathbf{M}_k \mathbf{g}_h^k = (f_h^k(x_{k+1}) - f^*(x_{k+1})) \ell^k(x_{k+1}) - (f_h^k(x_k) - f^*(x_k)) \ell^k(x_k), \quad (1.96)$$

here we have the vectors of local unknown  $u_h^k$ , of fluxes  $\mathbf{f}_h^k$ , and the source forces  $\mathbf{g}_h^k$ , all given on the nodes in each element. Given the duplication of unknowns at the element interfaces, each vector is  $2K$  long. Furthermore, we have  $\ell^k(x) = [\ell_1^k(x), \dots, \ell_{N_p}^k(x)]^T$  and the local matrices

$$\mathbf{M}_{ij}^k = \int_{D_k} \ell_i^k(x) \ell_j^k(x) dx, \quad \mathbf{S}_{ij}^k = \int_{D_k} \ell_i^k(x) \frac{d\ell_j^k(x)}{dx} dx. \quad (1.97)$$

While the structure of the DG-FEM is very similar to that of the finite element method (FEM), there are several fundamental differences. In particular, the mass matrix is local rather than global and thus can be inverted at very little cost, yielding a semidiscrete scheme that is explicit. Furthermore, by carefully designing the numerical flux to reflect the underlying dynamics, one has more flexibility than in the classic FEM to ensure stability for wavenumber-dominated problems. Compared with the FEM, the DG-FEM overcomes the key limitation on achieving high-order accuracy on general grids by enabling this through the local element-based basis. This is all achieved while maintaining benefits such as local conservation and flexibility in the choice of the numerical flux.

The DG-FEM scheme has been widely used for Maxwell's equations [46], [91], elastic wave equations [103], [148], and piezoelectric equations [27], etc. For realizing the time-integration within DG-FEM construction, the Runge-Kutta [35] and ADER (arbitrary high order derivatives) [103], [148], time integration approaches have been applied.

More details about the DG-FEM method will be presented in Chapter 2, where a numerical software based on it is described for nonlinear elastic wave propagation phenomena.

## 1.5 Pseudo-Spectral Simulation of 1D Nonlinear Propagation in Elastic Media

As described previously, for a large class of elastic heterogeneous solid media, the conventional five-constant elasticity theory is often insufficient to explain anomalous nonlinear behaviors of these media.

In this part, numerical simulations of “classical” and “non-classical” nonlinearities will be presented with a 1D model describing a compressional wave propagating in a heterogeneous medium. The comparisons of nonlinear signatures of these different kinds of nonlinearity for shock wave generation, and rod resonance will be studied. These results are expected to be useful in helping to determine the predominant nonlinear mechanism in specific experiments.

### 1.5.1 The Elastic Wave Solver

In this part, we will first present the Pseudo-Spectral (PS) algorithm used to solve the system of equations Eqs. (1.1)-(1.2), or Eqs. (1.1), (1.35) and (1.38) if attenuation needs to be

included. When needed to simulate unbounded media a Convolution Perfectly Matched Layer (C-PML) is introduced.

### 1.5.1.1 The Pseudo-Spectral Method and the Free-Surface Implementation

The spatial derivatives involved in Eqs. (1.1)-(1.2), are calculated by using a Pseudo-Spectral (PS) method. To reduce numerical artifacts in Pseudo-Spectral simulation in heterogeneous medium a staggered grid implementation is used [76], [143]. For example, the derivative  $\partial\tau/\partial z$  is computed by taking the Fourier transform of  $\tau(z)$  over  $z$ , multiplying each point in the resulting spectrum by  $jk_z e^{jk_z\Delta z/2}$ , and performing the inverse Fourier transform:

$$\frac{\partial\tau(z)}{\partial t} = FT^{-1}\left[jk_z e^{jk_z\Delta z/2} FT[\tau(z)]\right], \quad (1.98)$$

where  $FT$  is a forward Fourier transform,  $FT^{-1}$  is an inverse Fourier transform, and  $k_z$  is the wave number in the  $z$  direction.  $\Delta z$  is the spatial step of the numerical grid.

The solver uses a staggered fourth order Adams–Bashforth method [76] by which stress and particle velocity are updated at alternating half time steps to integrate forward in time. To circumvent wraparound inherent to FFT-based Pseudo-Spectral simulation, a Convolution Perfectly Matched Layers (C-PML) boundary condition is used.

In Pseudo-Spectral simulation the introduction of free-surface is not easy due to the non local behavior of the spatial derivatives, even if this problem has been reduced by the use of staggered grid. In the solver, a method of images, first introduced by Levander [114] and described in details by Robertsson [155] has been used. The idea is as follows: the free surface is chosen such to be located on a  $\tau$  node. On this node  $\tau = 0$ , the spatial derivatives are calculated with particle velocity and stress components mirrored around the free surface as even and odd functions respectively.

In the solver the C-PML zone is suppressed behind a free surface, because no waves are supposed to propagate, and so to be absorbed. Nevertheless, in this case the effects of the domain periodicity inherent in FFT-based calculations reappear. For this reason the stress and the particle velocity are smoothly reduced to zero using an apodization window near the limits of the numerical domain when a stress free boundary is present.

### 1.5.1.2 Application of C-PML Absorbing Boundary

In this part, we introduce the Convolution Perfectly Matched Layer (C-PML), to the 1D nonlinear elastic motion equation. The C-PML method is introduced based on a stretched-

coordinate formulation of Eqs. (1.1)-(1.2). For more details see chapter 3. In the 1D simulation, the choice of the complex stretching variable is given by:

$$s_z = \kappa_z(z) + \frac{\sigma_z(z)}{\alpha_z(z) + j\omega}. \quad (1.99)$$

where the parameters  $\kappa_z$ ,  $\sigma_z$  and  $\alpha_z$  will be described with great details in chapter 3 (Eqs. (3.18)).

In the frequency domain and stretched-coordinate space, we can obtain the following equations:

$$j\omega\hat{v} = \frac{1}{\rho_0} \frac{1}{s_z} \frac{\partial \hat{t}}{\partial z}, \quad (1.100)$$

$$j\omega\hat{t} = \hat{K} \otimes \left[ \frac{1}{s_z} \frac{\partial \hat{v}}{\partial z} \right]. \quad (1.101)$$

where  $\hat{u}$  is the Fourier transform of the variable  $u$  and  $\otimes$  is a convolution. Eqs. (1.100)-(1.101) are next transformed back to the time domain. The final time domain equation, with memory variables, is then:

$$\frac{\partial v}{\partial t} = \frac{1}{\rho_0 \kappa_z} \left( \frac{\partial \tau}{\partial z} + A_z \right), \quad (1.102)$$

$$\frac{\partial \tau}{\partial t} = \frac{K(t)}{\kappa_z} \left( \frac{\partial v}{\partial z} + B_z \right), \quad (1.103)$$

$$\frac{\partial A_z}{\partial t} = -\frac{\sigma_z}{\kappa_z} \frac{\partial \tau}{\partial z} - \left( \frac{\sigma_z}{\kappa_z} + \alpha_z \right) A_z, \quad (1.104)$$

$$\frac{\partial B_z}{\partial t} = -\frac{\sigma_z}{\kappa_z} \frac{\partial v}{\partial z} - \left( \frac{\sigma_z}{\kappa_z} + \alpha_z \right) B_z. \quad (1.105)$$

where  $A_z$  and  $B_z$  are the memory variables and they are zero outside the C-PML zones.

The C-PML offers a number of advantages over the traditional implementation of the PML. First, the application of the C-PML is, as shown in Eqs. (1.102)-(1.103), independent of the host medium. Secondly, this is a nonsplitting PML corresponding to perturbations to the original wave equations where the perturbed equations reduce automatically to the original wave equation outside the PML absorbing layers. So, the fact that the C-PML treats the boundary layers in the same way as the rest of the computational domain, greatly simplify the computer implementation.

Now, the simulation results for different kinds of nonlinearity will be presented, and we will focus on the comparison of nonlinear signatures of these different kinds of nonlinearity for shock wave generation, and rod resonance.

## 1.5.2 Shock Wave Simulation

Now, we will present the results of shock wave simulation, which have been realized using the PS method, for different kinds of nonlinearity. In all the 1D simulations, we assume a bar discretized with 4096 elements, constituted of a material with density  $\rho_0 = 2600 \text{ kg/m}^3$ , modulus  $K_0 = 10 \text{ GPa}$ . A time step  $\Delta t = 2.5 \text{ ns}$  and spatial step  $\Delta z = 0.15625 \text{ mm}$  have been used. The source signal, which will be used at the left side of the bar, is a sinusoid with amplitude  $A_0$  and frequency  $f$ . To simulate a semi-infinite medium a C-PML boundary condition has been used at the right side of the bar.

### 1.5.2.1 Quadratic and Cubic Nonlinearity

First, the results of simulation for “classical” quadratic nonlinearity with  $\Gamma = 40$ ,  $\delta = 0$ ,  $A_0 = 2 \text{ MPa}$  and  $f = 50 \text{ kHz}$  will be presented. In Fig. 1.15(a)-(d), we plot the particle velocity  $v$  at a distance of 2, 6, 10 and 15 wavelengths, respectively. From this figure we can see the process of shock formation: the sinusoidal signal (a) becomes more and more steeper as the wave propagates forward (d). Fig. 1.16 is the corresponding frequency spectrum at the distance of 15 wavelengths, from which we can see the existence of both even and odd harmonics.

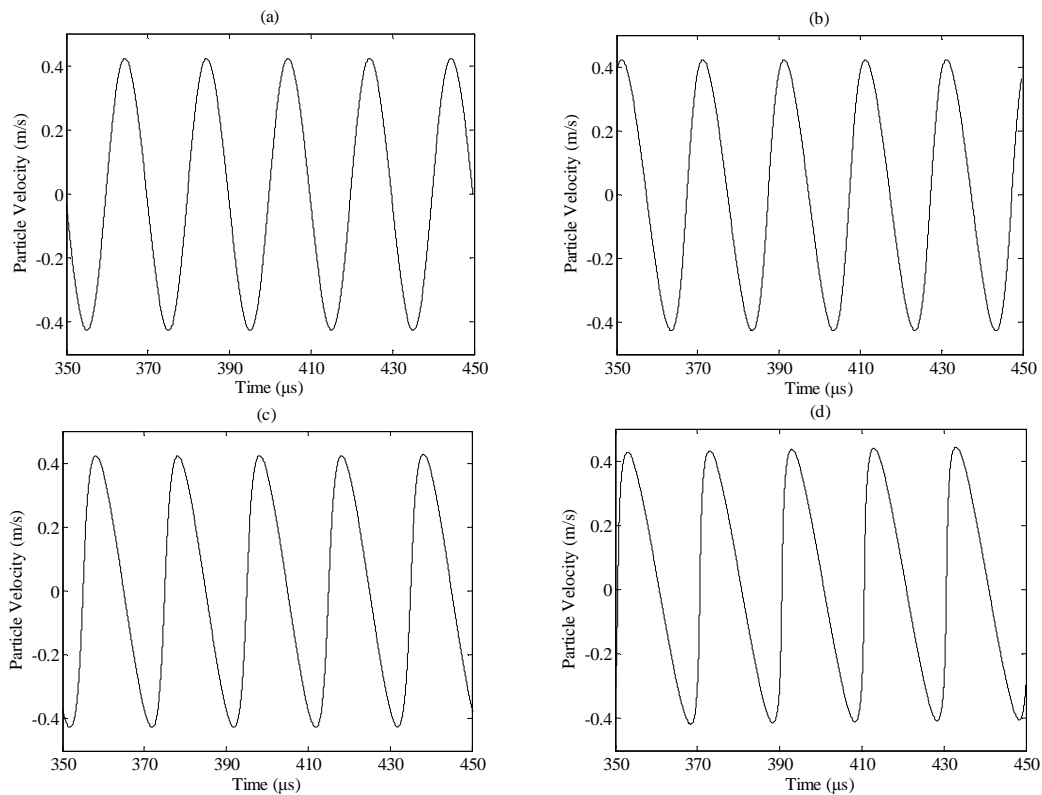


**Fig. 1.15** Particle velocity for “classical” quadratic nonlinearity at a distance of (a) 2, (b) 6, (c) 10 and (d) 15 wavelengths. From these figures we can see the process of shock front formation.

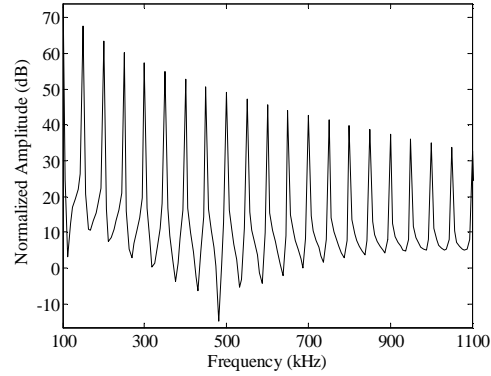


**Fig. 1.16** Corresponding frequency spectrum for “classical” quadratic nonlinearity at a distance of 15 wavelengths. From this figure we can see both even harmonic (100kHz, 200kHz, 300kHz, etc) and odd harmonic (150kHz, 250kHz, 350kHz, etc).

Fig. 1.17 displays the results of simulation for “classical” cubic nonlinearity with  $\Gamma = 0$ ,  $\delta = 5 \times 10^5$ ,  $A_0 = 1$  MPa and  $f = 50$  kHz at the distance of 15 wavelengths. In this case, no shock front appears and only odd harmonics are presents.

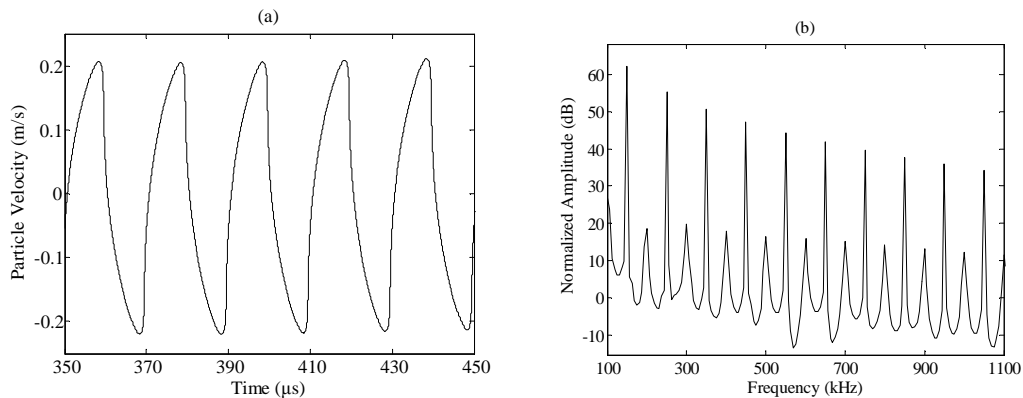


**Fig. 1.17** (a) Particle velocity for “classical” cubic nonlinearity, and (b) the corresponding frequency spectrum at a distance of 15 wavelengths.

### 1.5.2.2 Bi-modular Elasticity

For the “non-classical” Bi-modular nonlinearity simulation, the following parameters,  $E_+ = 10$  GPa and  $E_- = 9.98$  GPa,  $A_0 = 0.1$  MPa and  $f = 50$  kHz have been used. From Fig. 1.18(a), corresponding to the particle velocity at a distance of only 2 wavelengths, we can see already a wave jump. The calculations in such nonlinear medium are very difficult to realize, because contrary to the “classical” quadratic or cubic nonlinearity, here, the harmonic generation is not a cascade process. So, all the harmonics appear simultaneously, as shown on the frequency spectrum of the calculated particle velocity plotted on Fig. 1.18(b). Here, mainly odd harmonics are generated during the wave propagation. These results are in accordance with analytical predictions [135], [142].

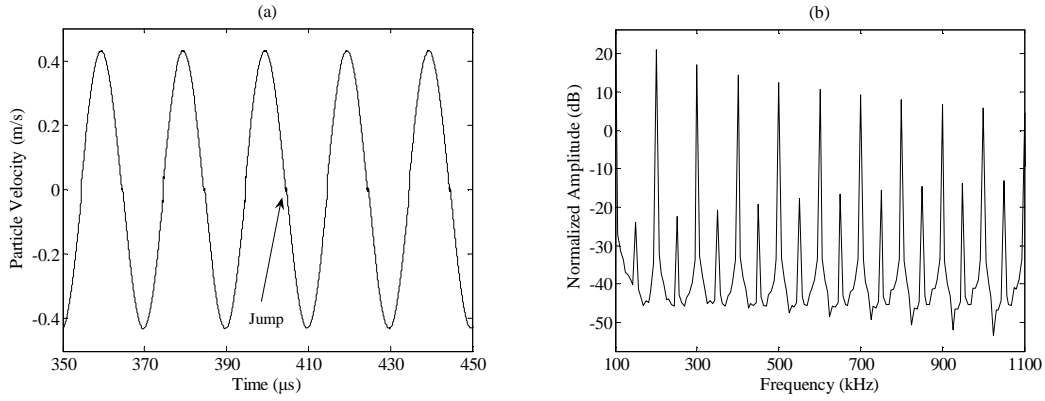


**Fig. 1.18** (a) Particle velocity for “non-classical” Bi-modular nonlinearity, and (b) the corresponding frequency spectrum.

### 1.5.2.3 Nazarov Model of Hysteretic Nonlinearity

Now the results of simulation for “non-classical” Nazarov hysteretic nonlinearity will be presented. The parameters we have used are as follows:  $n = 2$ ,  $\gamma_1 = \gamma_2 = \gamma_3 = \gamma_4 = 2 \times 10^3$ ,  $A_0 = 0.1$  MPa and  $f = 50$  kHz. Fig. 1.19(a)-(d) are the particle velocity at the same distances: 2, 6, 10 and 15 wavelengths. From these figures we can see both a shock front and a triangularisation of the top of the particle velocity, when the wave propagates forward. For the chosen case, where all the four nonlinear parameter are equal, the frequency spectrum displays only odd harmonics as shown on Fig. 1.20. Once again, these results are in perfect accordance with theoretical predictions [137], [138].

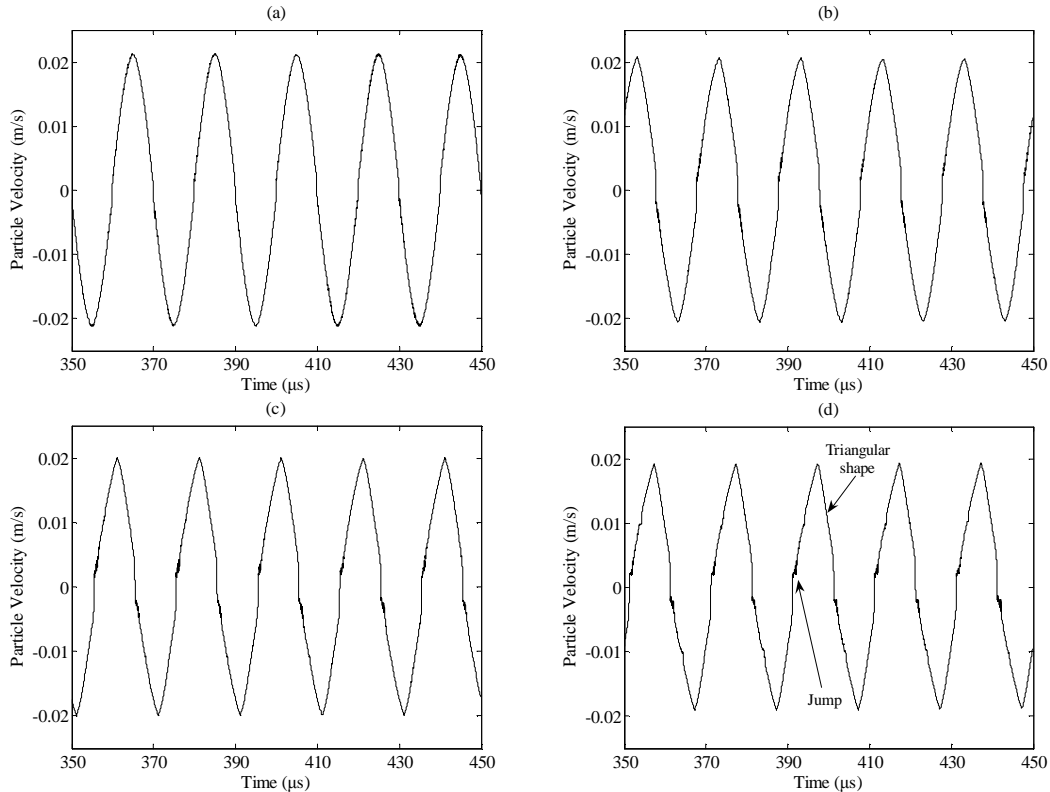


**Fig. 1.19** Particle velocity for “non-classical” Nazarov hysteretic nonlinearity at a distance of (a) 2, (b) 6, (c) 10 and (d) 15 wavelengths.

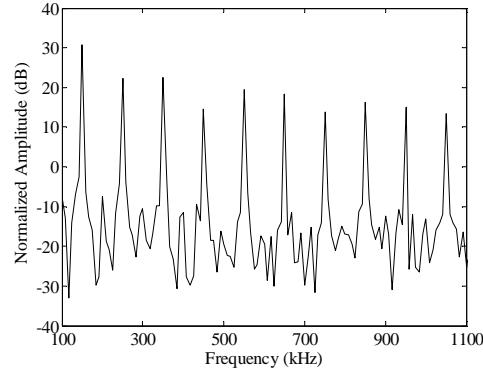


**Fig. 1.20** Frequency spectrum of “non-classical” Nazarov hysteretic nonlinearity at a distance of 15 wavelengths. Only odd harmonics are generated during the propagation.

### 1.5.3 Rod Resonance Simulation

In this part rod resonance simulations will be presented for different kinds of nonlinearity. In this simulation, we assume a bar of length  $L = 250$  mm, constituted of the same material as the one previously used. A uniform spatial step  $\Delta z = 6.1728$  mm has been used and the whole length is discretized into 45 grid points. The time step is chosen as  $\Delta t = 1/(776f)$ . The source signal used in the left side of the bar is a sinusoidal signal where the amplitude  $A$  is increased from 2 to 16384, and the frequency  $f$  is increased from 3859.2 kHz to 3956.5 kHz with a step of 3.1376 Hz. The presented results correspond to the particle velocity measured at the stress free boundary of the rod.

#### 1.5.3.1 Quadratic and Cubic Nonlinearity

First, we present the results of simulation for “classical” quadratic and cubic nonlinearity with  $\Gamma = 4$  and  $\delta = 5 \times 10^5$ . Moreover, relaxation attenuation has been introduced in order to obtain a finite amplitude at the resonance frequency. The selected Q-factor was 80 as described previously in paragraph 1.3.2. On Fig. 1.21(a), we plot the typical resonance curves for the different amplitude of excitation. We can see the frequency shift with the increasing source amplitude. It is important to remind that, contrary to what is believed, both quadratic and cubic nonlinear terms contribute to this frequency shift. Here, as expected the obtained dependence of this shift on the input strain is quadratic. Fig. 1.21(b) is the normalized amplitude of resonance curves, where it is clear that no extra-attenuation is induced by this “classical” nonlinearity.

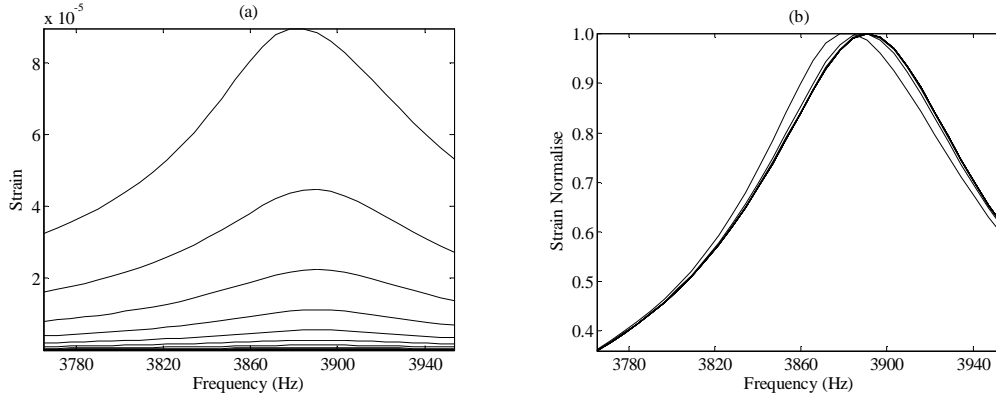


**Fig. 1.21** (a) Resonance curves for “classical” quadratic and cubic nonlinearity with relaxation attenuation, and (b) the corresponding normalized resonance curves showing no extra-attenuation process.

### 1.5.3.2 Bi-modular Elasticity

For the “nonclassical” Bi-modular nonlinearity simulation, relaxation attenuation has also been introduced with the same Q-factor. The following two parameters,  $E_+ = 10$  GPa and  $E_- = 9.98$  GPa have been used. Fig. 1.22(a) is the obtained resonance curves and Fig. 1.22(b) the corresponding normalized strain amplitude. We can see that all the curves are superposed, that means that there is no frequency shift and no extra-attenuation for resonance in a Bi-modular nonlinear medium.

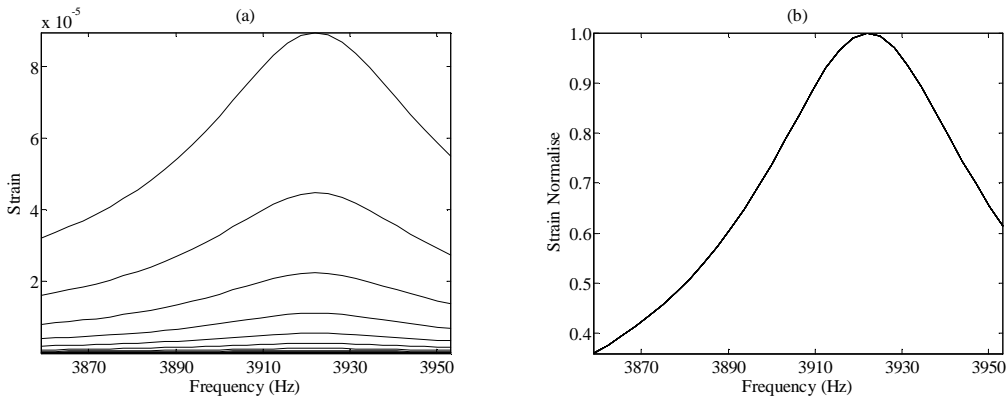


**Fig. 1.22** (a) Resonance curves for “non-classical” Bi-modular nonlinearity with relaxation attenuation, and (b) the corresponding normalized resonance curves, where no frequency shift and extra-attenuation appear.

### 1.5.3.3 Nazarov Model of Hysteretic Nonlinearity

Now, we present the results of resonance simulation for “non-classical” Nazarov hysteretic nonlinearity. The parameters are as before  $n = 2$  and  $\gamma_1 = \gamma_2 = \gamma_3 = \gamma_4 = 2 \times 10^3$ . Fig. 1.23(a) is the resonance curves and Fig. 1.23(b) the corresponding normalized resonance curves. Here, both frequency shift, with a linear dependence on the input strain, and an extra-attenuation also with a linear dependence on the input strain are simultaneously obtained.

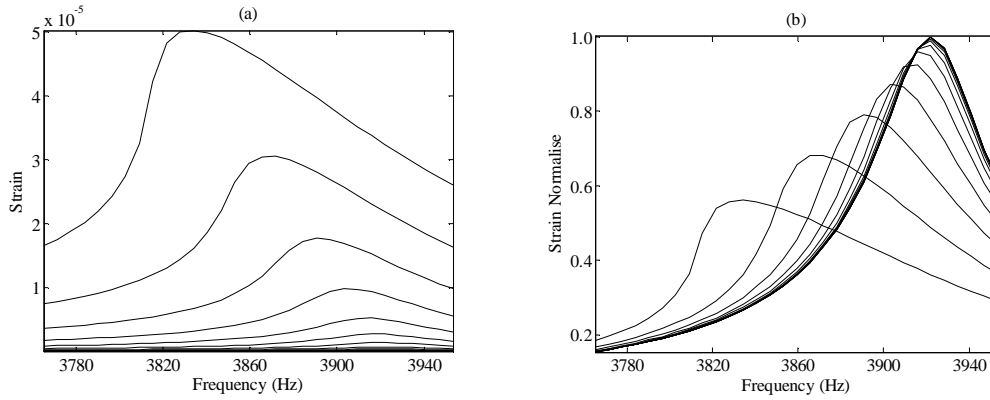


**Fig. 1.23** (a) Resonance curves for “non-classical” Nazarov hysteretic nonlinearity with relaxation attenuation, and (b) the corresponding normalized strain resonance curves.

All the obtained results are summarized in Tab. 1.2.

**Tab. 1.2** Resume of the nonlinear signature of the four considered kinds of nonlinearity.

Kind of nonlinearity	Shock	Even harmonics	Odd harmonics	Frequency shift	Extra attenuation
Quadratic	yes	yes	yes	yes	no
Cubic	no	no	yes	yes	no
Bi-modular	yes immediate	yes	-	no	no
Hysteretic (Nazarov)	yes	no	yes	yes	yes

## 1.6 Conclusion

We have first provided a quick introduction of nonlinear ultrasonic nondestructive testing and imaging and especially the ones which are combined with time reversal process, are reviewed. The nonlinear elastodynamic equations needed in the remainder of the thesis has been introduced. Different kinds of nonlinearity models, including the “classical” conventional five-constant elasticity theory and “non-classical” nonlinearity have been discussed. An overview of the classical numerical methods including Finite Difference Method, Finite Volume Method, Finite Element Method, Pseudo-Spectral method and Discontinuous Galerkin Finite Element Method (DG-FEM), focusing mainly on their advantages and weaknesses is made. Among these methods DG-FEM will be the one chosen to the numerical development made during the thesis, due to its ability to maintain a high degree of accuracy with geometric flexibility.

In order to profoundly understand the nonlinear elastic properties of fatigued solids, 1D simulations of nonlinear propagation of elastic wave in heterogeneous media with different

kinds of nonlinearity have been numerically studied. This study can help in the determination of the predominant nonlinear mechanism in specific experiments. It was a first step in the development of the proposed numerical tools described in the next two chapters and “chaotic cavity transducer” imaging system presented in the last chapter.



# CHAPTER 2: THE NODAL DISCONTINUOUS GALERKIN METHOD

## 2.1 Introduction

As presented in the first Chapter, the Finite Difference Method (FDM), Finite Element Method (FEM) and Finite Volume Method (FVM) have been widely used to solve Partial Differential Equations (PDE) in many computational fields to derive discrete representations of the spatial derivative operators.

For FDM method, it leads to very efficient semi-discrete spatial schemes and its most attracting aspects is its simplicity. Furthermore, the explicit semi-discrete form gives flexibility in the choice of time-stepping methods which are supported by an extensive body of theory [84], and are sufficiently robust and efficient to be used for a large variety of problems. The extensions to higher order approximations can be realized by using a local approximation of the derivation operator of higher degree. However, for the FDM method, additional complications caused by the simple underlying structure are introduced around boundaries and discontinuous internal layers which use different material coefficients. This makes it ill-suited to deal with complex geometries, both in terms of general computational domains and internal discontinuities as well as for local order and grid size changes to reflect local features of the solution.

The FVM is a method closely related to the FDM, but which introduce an element-based discretization and with added geometric flexibility. In this method, we assume that the whole calculation domain is represented by a collection of elements, typically triangles and cubes, organized in an unstructured manner to fill the physical domain. For each cell, the numerical approximation and the scheme are purely local and, thus, impose no conditions on the grid structure. In particular, all cells can have different sizes. By using the divergence theorem, such as Gauss' theorem, the flux term reduces to a pure surface term. There are many different ways to get the evaluation of the fluxes at the interfaces and the details of these methods lead to different finite volume methods [115]. For linear problems and equidistant grids these methods will be reduce to the FDM. If, however, we want to increase the order of accuracy of the FVM method, the need for a high-order reconstruction reintroduces the need for a particular grid structure and thus destroys the geometric flexibility of the FVM in higher dimensions. The main limitation of FVM is its inability to extend to higher-order accuracy on general unstructured grids.

For the FEM method, which use the unstaggered grid point and share nodes along the faces of the elements, by adding additional degrees of freedom to the element, the higher-order accuracy can be realized in higher dimensions. In particular, one can have different orders of approximation in each element, thereby enabling local changes in both size and order, known as hp-adaptivity [54]. However, for FEM method, the globally defined basis functions and the requirement that the residual be orthogonal to the same set of globally defined test functions implies that the semi-discrete scheme becomes implicit and the mass matrix must be inverted. For time dependent problems, this is a clear disadvantage compared to the FDM and FVM methods. From the previous discussion, we realize that to ensure geometric flexibility and support for locally adapted resolution, we must strive for an element based method where high-order accuracy is enabled through the local approximation, as in the FEM method. However, the global statement, which is introduced by the globally defined basis functions and test functions, destroys the locality of the scheme and introduces potential problems with the stability for wave-dominated problems. That is precisely the regime where the FVM method has some attractive features.

An intelligent combination of the FEM and FVM methods, utilizing a space of basis and test functions that mimics the FEM method but satisfying the equation in a sense closer to the FVM method, appears to offer many of the desired properties. This combination is exactly what leads to the Discontinuous Galerkin Finite Element Method (DG-FEM). In the DG-FEM method, the points at the face of the elements are duplicated and shared by two elements. The interface flux connects the elements by combining the information of the two cells. In the structure of DG-FEM, the mass matrix is local rather than global as used in FEM and thus can be inverted at very little cost, yielding an explicit semi-discrete scheme. Compared with the FVM, by using the local element-based basis, the DG-FEM overcomes the key limitation on achieving high-order accuracy on general grids. In contrast to classical FEM, with the DG-FEM framework the solution can be discontinuous across the element interfaces, which allows incorporating the well-established numerical flux functions from the FVM framework.

As we want to simulate nonlinear elastic wave propagation in structures of complex geometry, we need, in order to reduce the number of cells to be used while maintaining a high degree of accuracy, a high-order numerical method with geometric flexibility. This last point will be a great improvement to the Pseudo-Spectral scheme we previously used. Our choice, motivated by the previous discussion on the comparative advantages of the different numerical methods, corresponds to the nodal DG-FEM scheme first introduced by Hesthaven and Warburton [91] for electro-dynamic simulations. Moreover, a numerical scheme based on this method has been developed since then for a large number of fields as Maxwell eigenvalue problem [92], left-handed medium [167], chaotic transport in turbulent flow [160], water-wave and free surface flow [83], Boussinesq type equation [66], and piezoelectric transducer [27]. It is now freely available at the following internet addresses <http://www.caam.rice>.

*edu/~timwar/Software* (Matlab script) or *http://www.nudg.org* (C++ script), and well documented [94], [93].

The introduction of nonlinear elasto-dynamics (including sources) in this software will be now described in details, and validated on a plane wave benchmark simulation.

## 2.2 Discontinuous Galerkin Finite Element Method Scheme in 2D

In this part, how to implement the DG-FEM operators in a general, flexible, and robust manner will be presented in detail. We will discuss how to, in practice, assemble the computational grid and compute all the entities required to enable the implementation of the scheme, both for triangular and quadrilateral grids. Moreover, different choices of numerical fluxes will also be discussed. How this method can be used in numerical schemes approximating the PDEs describing nonlinear elastodynamic is explained. The fundamental elastodynamic equations have been presented in the subsection 1.3.3 of Chapter 1 within a conservative form.

In 2D, the elastodynamic equations Eq. (1.49) can be rewritten as:

$$\frac{\partial \mathbf{Q}(t, \mathbf{x})}{\partial t} = \frac{\partial \mathbf{F}}{\partial x} + \frac{\partial \mathbf{G}}{\partial y}, \quad \mathbf{x} = [x, y] \in \Omega \in \mathbf{R}^2 \quad (2.1)$$

where  $\Omega$  is the global physical domain with boundary  $\partial\Omega$  and

$$\mathbf{Q} = \begin{pmatrix} \rho_0 v_1 \\ \rho_0 v_2 \\ F_{11} \\ F_{22} \\ F_{12} \\ F_{21} \end{pmatrix}, \quad \mathbf{F} = \begin{pmatrix} P_{11} \\ P_{21} \\ v_1 \\ 0 \\ 0 \\ v_2 \end{pmatrix}, \quad \mathbf{G} = \begin{pmatrix} P_{12} \\ P_{22} \\ 0 \\ v_2 \\ v_1 \\ 0 \end{pmatrix}.$$

### 2.2.1 General Formulation of Discontinuous Galerkin Schemes

In the discontinuous scheme, the global domain  $\Omega$  is divided into  $K$  non-overlapping triangular elements  $D^k$

$$\Omega \cong \Omega_h = \bigcup_{k=1}^K D^k. \quad (2.2)$$

In the  $k$ -th element, the numerical solution  $\mathbf{Q}_h^k$  of Eq. (2.1) is approximated through an interpolation

$$\mathbf{Q}(t, \mathbf{x}^k) \equiv \mathbf{Q}_h^k(t, \mathbf{x}) = \sum_{n=1}^{N_p} \hat{\mathbf{Q}}_n^k(t) \psi_n(\mathbf{x}) = \sum_{i=1}^{N_p} \mathbf{Q}_h^k(t, \mathbf{x}_i) \mathbf{l}_i^k(\mathbf{x}) = \sum_{i=1}^{N_p} \mathbf{Q}_{hi}^k(t) \mathbf{l}_i^k(\mathbf{x}). \quad (2.3)$$

In the first formulation, known as the modal form,  $\psi_n(\mathbf{x})$  is a local two-dimensional polynomial basis of order  $N$ . In the alternative form, known as the nodal representation,  $\mathbf{l}_i^k(\mathbf{x})$  are two-dimensional Lagrange interpolation polynomials based on the grid points  $\mathbf{x}_i$ . The connection between these two forms is done through the definition of the expansion coefficients  $\hat{\mathbf{Q}}_n^k$ .  $N_p$  is the number of interpolation grid points in each element, which is equivalent to the number of expansion terms. An interpolation is obtained by connecting these grid points to a set of basis functions.

Multiplying Eq. (2.1) by a test function, the same as the basis function in our case (Galerkin Method), and integrating on each element  $D^k$  yields

$$\begin{aligned} \int_{D^k} \frac{\partial \mathbf{Q}_h^k}{\partial t} \mathbf{l}_i^k(\mathbf{x}) d\mathbf{x} &= \int_{D^k} \left( \frac{\partial \mathbf{F}_h^k}{\partial x} + \frac{\partial \mathbf{G}_h^k}{\partial y} \right) \mathbf{l}_i^k(\mathbf{x}) d\mathbf{x} \\ &= \int_{D^k} \left( \frac{\partial \mathbf{F}_h^k \mathbf{l}_i^k(\mathbf{x})}{\partial x} + \frac{\partial \mathbf{G}_h^k \mathbf{l}_i^k(\mathbf{x})}{\partial y} \right) d\mathbf{x} - \int_{D^k} \left( \frac{\partial \mathbf{l}_i^k(\mathbf{x})}{\partial x} \mathbf{F}_h^k + \frac{\partial \mathbf{l}_i^k(\mathbf{x})}{\partial y} \mathbf{G}_h^k \right) d\mathbf{x} \end{aligned} \quad (2.4)$$

According to the Green theorem, the first term of Eq. (2.4) in the right hand can be written as a curl integral on the edges  $\partial D^k$  of element  $D^k$ , and the following equation is obtained

$$\int_{D^k} \frac{\partial \mathbf{Q}_h^k}{\partial t} \mathbf{l}_i^k(\mathbf{x}) d\mathbf{x} = \int_{\partial D^k} (n_x^k \mathbf{F}_h^k + n_y^k \mathbf{G}_h^k) \mathbf{l}_i^k(\mathbf{x}) d\mathbf{x} - \int_{D^k} \left( \frac{\partial \mathbf{l}_i^k(\mathbf{x})}{\partial x} \mathbf{F}_h^k + \frac{\partial \mathbf{l}_i^k(\mathbf{x})}{\partial y} \mathbf{G}_h^k \right) d\mathbf{x}, \quad (2.5)$$

where  $\partial D^k$  is the edge of the  $D^k$ , and  $\hat{\mathbf{n}}^k = [n_x^k \ n_y^k]$  is the normalized outward pointing normal vector. Since  $\mathbf{Q}_h$  may be discontinuous at an element boundary, we replace the flux  $(n_x^k \mathbf{F}_h^k + n_y^k \mathbf{G}_h^k) = \mathbf{f}^k$  by a numerical flux  $(n_x^k \mathbf{F}_h^k + n_y^k \mathbf{G}_h^k)^* = \mathbf{f}^{k*}$ :

$$\int_{D^k} \frac{\partial \mathbf{Q}_h^k}{\partial t} \mathbf{l}_i^k(\mathbf{x}) d\mathbf{x} = \int_{\partial D^k} (n_x^k \mathbf{F}_h^k + n_y^k \mathbf{G}_h^k)^* \mathbf{l}_i^k(\mathbf{x}) d\mathbf{x} - \int_{D^k} \left( \frac{\partial \mathbf{l}_i^k(\mathbf{x})}{\partial x} \mathbf{F}_h^k + \frac{\partial \mathbf{l}_i^k(\mathbf{x})}{\partial y} \mathbf{G}_h^k \right) d\mathbf{x}, \quad (2.6)$$

or

$$\begin{aligned} \int_{D^k} \frac{\partial \mathbf{Q}_h^k}{\partial t} \mathbf{l}_i^k(\mathbf{x}) d\mathbf{x} &= \int_{\partial D^k} ((n_x^k \mathbf{F}_h^k + n_y^k \mathbf{G}_h^k)^* - (n_x^k \mathbf{F}_h^k + n_y^k \mathbf{G}_h^k)) \mathbf{l}_i^k(\mathbf{x}) d\mathbf{x} \\ &\quad + \int_{D^k} \left( \frac{\partial \mathbf{F}_h^k}{\partial x} + \frac{\partial \mathbf{G}_h^k}{\partial y} \right) \mathbf{l}_i^k(\mathbf{x}) d\mathbf{x} \end{aligned} \quad (2.7)$$

Eqs. (2.6)-(2.7) are the weak and strong formulation, respectively, of the nodal discontinuous Galerkin method in two spatial dimensions. Note that the strong form is derived directly from the weak form through integration by parts. Since the weak form does not allow a space of nonsmooth test functions, we consider the strong form in the following. The last term of the Eq. (2.7) in the right hand is the volume term.

## 2.2.2 Defining Discontinuous Galerkin Operators on Triangular Elements

As in the preceding presentation, the global domain  $\Omega$  is divided into  $K$  non-overlapping triangular elements  $D^k$ . The number of interpolation points  $N_p$ , for each triangular element, has the following relation with the polynomial order  $N$

$$N_p = \frac{(N+1)(N+2)}{2}. \quad (2.8)$$

The grid points, which the Lagrange interpolation is based on, are a set of local grid points belonging to element  $k$ . They define the vectors  $\mathbf{x}_h^k = [x_1^k, x_2^k, \dots, x_{N_p}^k]$  and  $\mathbf{y}_h^k = [y_1^k, y_2^k, \dots, y_{N_p}^k]$ . Here, we consider the case where we interpolate with the same number of grid points  $N_p$ , in all the elements.

As sketched in Fig. 2.1, we introduce a mapping,  $\Psi$ , connecting the general straight-sided triangle,  $\mathbf{x} \in D^k$  with the standard straight-angle triangle, defined as

$$\mathbf{I} = \{\mathbf{r} = (r, s) \mid (r, s) \geq -1; r + s \leq 0\}. \quad (2.9)$$

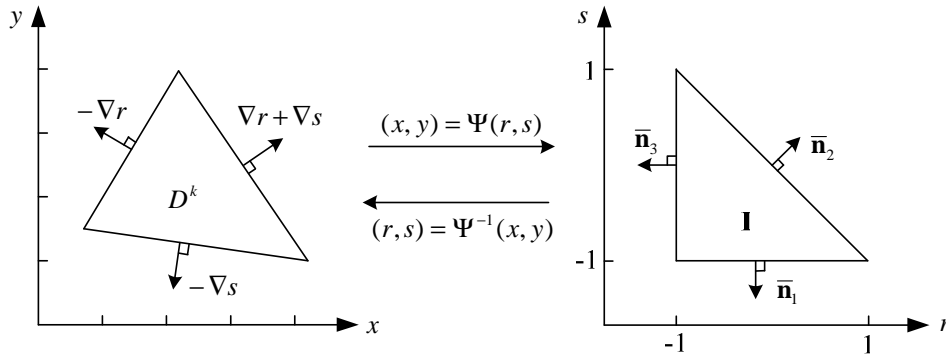


**Fig. 2.1** The mapping between the reference straight-angle triangle element  $\mathbf{I}$  and a general triangular shaped element.

$r$  and  $s$  are the coordinates in a reference standard triangle. Assume that  $D^k$  is spanned by the three vertices,  $(\mathbf{v}_1^k, \mathbf{v}_2^k, \mathbf{v}_3^k)$ , counted counter-clockwise. These vertices are related to the reference triangle  $\mathbf{I}$  through the linear mapping

$$\begin{bmatrix} x^k \\ y^k \end{bmatrix} = -\frac{r+s}{2} \mathbf{v}_1^k + \frac{r+1}{2} \mathbf{v}_2^k + \frac{s+1}{2} \mathbf{v}_3^k. \quad (2.10)$$

It is important that the mapping is linear. This has the consequence that any two straight-sided triangles are connected through an affine mapping. That is, it has a constant transformation Jacobian. The metric for the mapping can be found directly since

$$\frac{\partial x}{\partial r} \frac{\partial r}{\partial x} = \begin{bmatrix} x_r & x_s \\ y_r & y_s \end{bmatrix} \begin{bmatrix} r_x & r_y \\ s_x & s_y \end{bmatrix} = \begin{bmatrix} 1 & 0 \\ 0 & 1 \end{bmatrix}. \quad (2.11)$$

Here, the standard notation of  $a_b$  which means that  $a$  is differentiated with respect to  $b$  has been used. From Eq. (2.10) we can get

$$r_x = \frac{y_s}{J}, \quad r_y = -\frac{x_s}{J}, \quad s_x = -\frac{y_r}{J}, \quad s_y = \frac{x_r}{J}, \quad (2.12)$$

with the Jacobian

$$J = x_r y_s - x_s y_r. \quad (2.13)$$

The  $r_x$ ,  $r_y$ ,  $s_x$ ,  $s_y$  and  $J$  are constants due to the use of triangular elements with straight sides.

In the reference triangle **I**, it's very important how to find exactly  $N_p$  points for interpolation. Several different ways [41], [181] have been done, leading to nodal distributions with very similar behaviour. Here, we use the distributions proposed by *J. S. Hesthaven* [94], [90] (up to order 19), for which the nodes along the edges are the one dimensional Legendre-Guass-Lobatto points. Examples of nodal distributions in the reference triangle are displayed on Fig. 2.2.

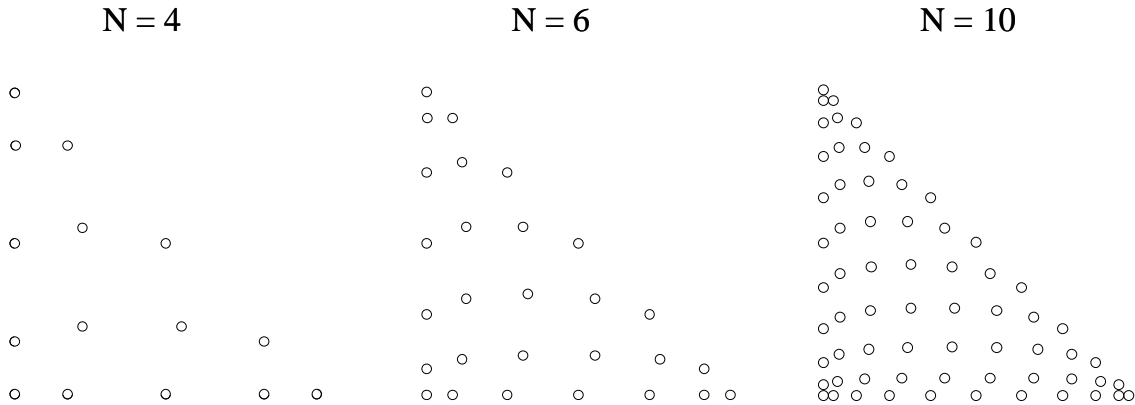


**Fig. 2.2** Nodal distributions in the reference straight-angle triangle element **I** for polynomial order  $N = 4, 6,$  and  $10$ .

Through the mapping, we are back in the position where we can focus on the development of polynomials and operators defined on **I**. To obtain a spectral scheme, we need to define an orthogonal set of basis functions on the reference triangle **I**. One kind of basis functions is [84]

$$\psi_m(r, s) = \sqrt{2} P_i^{(a,b)}(a) P_j^{(2i+1,0)}(b) (1-b)^i, \quad \text{for } (i, j) \geq 0 \text{ and } i + j \leq N, \quad (2.14)$$

where

$$a = 2 \frac{1+r}{1-s} - 1, \quad b = s \quad \text{and} \quad m = i + (N+1)j + 1 - \frac{j}{2}(j-1) \quad (2.15)$$

and  $P_n^{(\alpha,\beta)}(x)$  is the  $n$ -th order Jacobi polynomial. If  $\alpha = \beta = 0$ , then it becomes the Legendre polynomial.

In the reference triangle, by interpolating, the transformation between modal and nodal form can be achieved:

$$\sum_{j=1}^{N_p} \hat{\mathbf{Q}}_j^k \psi_j(r, s) \equiv \sum_{i=1}^{N_p} \left( \sum_{j=1}^{N_p} \hat{\mathbf{Q}}_j^k \psi_j(r_i, s_i) \right) \mathbf{l}_i^k(r, s) = \sum_{i=1}^{N_p} \mathbf{Q}_h^k(r_i, s_i) \mathbf{l}_i^k(r, s). \quad (2.16)$$

From this equation and by interpolating the basis function, the two following relations can be obtained in the matrix form,

$$\mathbf{Q}_h = \mathbf{V} \hat{\mathbf{Q}}, \text{ and } \boldsymbol{\psi}(\mathbf{r}, \mathbf{s}) = \mathbf{V}^T \mathbf{l}(\mathbf{r}, \mathbf{s}), \quad (2.17)$$

where we have defined the vectors  $\mathbf{r} = [r_1, r_2, \dots, r_{N_p}]^T$  and  $\mathbf{s} = [s_1, s_2, \dots, s_{N_p}]^T$ , and introduce the Vandermonde matrix  $\mathbf{V} = \psi_j(r_i, s_i)$ .  $\mathbf{V}^T$  is the transpose of  $\mathbf{V}$ .

Even though we do not have the direct expression of the derivation of the Lagrange interpolation  $\mathbf{l}$  in nodal representation, we can calculate the derivatives in modal space and transform the derivatives back to nodal space, because the derivatives of the basis function  $\psi_j$  can be obtained directly. On the reference element  $\mathbf{I}$ , the differentiation operator can be computed from the following relations

$$\mathbf{D}_r = \left. \frac{\partial \mathbf{l}(r, \mathbf{s})}{\partial r} \right|_{\mathbf{r}} = (\mathbf{V}^T)^{-1} \left. \frac{\partial \boldsymbol{\psi}(r, \mathbf{s})}{\partial r} \right|_{\mathbf{r}}, \text{ and } \mathbf{D}_s = \left. \frac{\partial \mathbf{l}(\mathbf{r}, s)}{\partial s} \right|_{\mathbf{s}} = (\mathbf{V}^T)^{-1} \left. \frac{\partial \boldsymbol{\psi}(\mathbf{r}, s)}{\partial s} \right|_{\mathbf{s}}. \quad (2.18)$$

In the orthogonal basis  $\psi_m$ , the variables  $a$  and  $b$  are functions of  $r$  and  $s$ . From Eq. (2.14), we obtained

$$\frac{\partial \psi_m(r, \mathbf{s})}{\partial r} = \frac{\partial a}{\partial r} \frac{\partial \psi_m(r, \mathbf{s})}{\partial a} \text{ and } \frac{\partial \psi_m(\mathbf{r}, s)}{\partial s} = \frac{\partial a}{\partial s} \frac{\partial \psi_m(\mathbf{r}, s)}{\partial a} + \frac{\partial \psi_m(\mathbf{r}, s)}{\partial b}. \quad (2.19)$$

Using the chain rule, the differentiation matrix is then obtained directly

$$\frac{\partial}{\partial x} = \frac{\partial r}{\partial x} \mathbf{D}_r + \frac{\partial s}{\partial x} \mathbf{D}_s \text{ and } \frac{\partial}{\partial y} = \frac{\partial r}{\partial y} \mathbf{D}_r + \frac{\partial s}{\partial y} \mathbf{D}_s. \quad (2.20)$$

By using the differentiation matrix Eq. (2.20), the calculation of volume term will be obtained as following

$$\frac{\partial \mathbf{F}_h^k}{\partial x} + \frac{\partial \mathbf{G}_h^k}{\partial y} = r_x \mathbf{D}_r \mathbf{F}_h^k + s_x \mathbf{D}_s \mathbf{F}_h^k + r_y \mathbf{D}_r \mathbf{G}_h^k + s_y \mathbf{D}_s \mathbf{G}_h^k. \quad (2.21)$$

The normal vectors belonging to the three faces of the standard triangle  $\mathbf{I}$  are  $\bar{\mathbf{n}}_1 = -\bar{s}$ ,  $\bar{\mathbf{n}}_2 = (\bar{r} + \bar{s})/\sqrt{2}$  and  $\bar{\mathbf{n}}_3 = -\bar{r}$ , where  $\bar{r}$  and  $\bar{s}$  are unit vectors. Hence, the outward pointing vectors at the surface of the elements  $D^k$  follow directly from the properties of the mapping, that are

$$\hat{\mathbf{n}}_1^k = -\frac{\nabla r}{\|\nabla r\|_k}, \quad \hat{\mathbf{n}}_2^k = \frac{\nabla r + \nabla s}{\|\nabla r + \nabla s\|_k} \quad \text{and} \quad \hat{\mathbf{n}}_3^k = -\frac{\nabla s}{\|\nabla s\|_k}. \quad (2.22)$$

Here,  $\|\cdot\|$  is the Euclidian length of the vector. These can be computed directly using the Eq. (2.12) from the physical coordinates  $(x, y)$ . The corresponding edge Jacobian for the mapping is computed as

$$J_{1D}^{k_1} = \|\nabla r^k\|, \quad J_{1D}^{k_2} = \|\nabla r^k + \nabla s^k\| \quad \text{and} \quad J_{1D}^{k_3} = \|\nabla s^k\|. \quad (2.23)$$

With these local Discontinuous Galerkin operators defined on each triangle of the mesh, the scheme in strong form becomes from Eq. (2.7):

$$\begin{aligned} \sum_{j=1}^{N_p} \int_{D^k} \frac{\partial \mathbf{Q}_h^k}{\partial t}(\mathbf{x}_j) \mathbf{l}_j^k(\mathbf{x}) \mathbf{l}_i^k(\mathbf{x}) d\mathbf{x} = \\ \sum_{j=1}^{N_p} \int_{D^k} (r_x \mathbf{D}_r \mathbf{F}_h^k + s_x \mathbf{D}_s \mathbf{F}_h^k + r_y \mathbf{D}_r \mathbf{G}_h^k + s_y \mathbf{D}_s \mathbf{G}_h^k) \mathbf{l}_j^k(\mathbf{x}) \mathbf{l}_i^k(\mathbf{x}) d\mathbf{x} \\ + \int_{\partial D^k} ((n_x^k \mathbf{F}_h^k + n_y^k \mathbf{G}_h^k)^* - (n_x^k \mathbf{F}_h^k + n_y^k \mathbf{G}_h^k)) \mathbf{l}_i^k(\mathbf{x}) d\mathbf{x} \end{aligned} \quad (2.24)$$

Considering the local mass matrix of the  $k$ -th element:

$$\begin{aligned} \mathbf{M}_{ij}^k &= \int_{D^k} l_i^k(x, y) l_j^k(x, y) d\mathbf{x} = J^k \int l_i(r, s) l_j(r, s) dr \\ &= J^k \sum_{m,n=0}^{N_p} (\mathbf{V}_{in}^T)^{-1} (\mathbf{V}_{jm}^T)^{-1} \int l_n(r, s) l_m(r, s) dr = J^k (\mathbf{M})_{ij} \end{aligned} \quad (2.25)$$

where  $\mathbf{M} = (\mathbf{V}\mathbf{V}^T)^{-1}$  is the mass matrix on the standard triangle  $\mathbf{I}$ , we obtain:

$$\begin{aligned} \frac{\partial \mathbf{Q}_h^k}{\partial t} &= r_x \mathbf{D}_r \mathbf{F}_h^k + s_x \mathbf{D}_s \mathbf{F}_h^k + r_y \mathbf{D}_r \mathbf{G}_h^k + s_y \mathbf{D}_s \mathbf{G}_h^k \\ &+ \frac{M^{-1}}{J^k} \int_{\partial D^k} ((n_x^k \mathbf{F}_h^k + n_y^k \mathbf{G}_h^k)^* - (n_x^k \mathbf{F}_h^k + n_y^k \mathbf{G}_h^k)) \mathbf{l}_i^k(\mathbf{x}) d\mathbf{x} \end{aligned} \quad (2.26)$$

To calculate the surface integral over  $\partial D^k$ , the integral over the faces  $f_i^k$  ( $i=1, 2, 3$ ) of the triangle are evaluated with the use of a 1D interpolation  $l^{k,1D}$ :

$$\oint_{f_i^k} (n_x^k \mathbf{F}_h^k + n_y^k \mathbf{G}_h^k) \mathbf{l}_m^k d\mathbf{x} = \sum_{n=0}^{N+1} (n_x^{ki} \mathbf{F}_{hm}^{ki} + n_y^{ki} \mathbf{G}_{hn}^{ki}) \oint_{f_i^k} l_n^{k,1D} l_m^k d\mathbf{x} = \mathbf{f}^{ki} \mathbf{M}_{1D}^{ki}. \quad (2.27)$$

Here,  $\mathbf{x}$  is assumed to be the trace along the edge where there are exactly  $N+1$  nodal points, and  $M_{1D}^{ki}$  is the edge-mass matrix

$$\mathbf{M}_{1D}^{ki} = \oint_{f_i^k} l_n^{k,1D} l_m^k d\mathbf{x} = \oint_{f_i^k} l_n^{k,1D} l_m^{k,1D} d\mathbf{x} = J_{1D}^{ki} (\mathbf{V}_{1D} \mathbf{V}_{1D}^T)^{-1}, \quad (2.28)$$

where  $J_{1D}$  is the transformation Jacobian along the face, the ratio between the length of the face in  $D_k$  and in  $\mathbf{I}$ , respectively. In this numerical scheme, the surface integral is an array with the  $3(N+1)K$  elements.

Finally, we obtain the following local scheme on each triangle of the mesh:

$$\frac{\partial \mathbf{Q}_h^k}{\partial t} = r_x \mathbf{D}_r \mathbf{F}_h^k + s_x \mathbf{D}_s \mathbf{F}_h^k + r_y \mathbf{D}_r \mathbf{G}_h^k + s_y \mathbf{D}_s \mathbf{G}_h^k + \sum_{i=1}^3 \frac{J_{1D}^k}{J^k} M^{-1} M^{1D} (\mathbf{f}^{ki*} - \mathbf{f}^{ki}). \quad (2.29)$$

As the operators, in the DG-FEM scheme, work purely on each local element, we should recover the global solution from the  $k$  local solutions. As in FVM the fluxes, called numerical fluxes  $\mathbf{f}^*$ , can be used to transfer information between the elements. The numerical fluxes, used in the DG-FEM, are founded upon a theory which was developed in the FVM and aims at solving hyperbolic problems on conservative form [115].

### 2.2.3 Numerical Fluxes in the Discontinuous Galerkin Method

In the discontinuous method, we have two possibilities to represent the  $\mathbf{Q}_h$  at a coordinate point  $\mathbf{x}_p$ , belonging to an interface between two elements. The local flux  $\mathbf{f}^k$ , in the element  $k$ , is only a function of the local values  $\mathbf{Q}_{h-}^k = \mathbf{Q}^k(\mathbf{x}_p)$ . The external value, at the same spatial coordinate of an external boundary in the neighbouring element  $n$ , is given as  $\mathbf{Q}_{h+}^k = \mathbf{Q}^n(\mathbf{x}_p)$ . The numerical fluxes are typically functions of the information about the both,  $\mathbf{f}^{k*}(\mathbf{Q}_{h-}^k, \mathbf{Q}_{h+}^k)$ . There are many different numerical fluxes that have been suggested in the literature [94], [196], [115].

For example one can consider a numerical flux like

$$\begin{aligned} \mathbf{f}^{k*}(\mathbf{Q}_{h-}^k, \mathbf{Q}_{h+}^k) &= \frac{\mathbf{f}^k(\mathbf{Q}_{h-}^k) + \mathbf{f}^k(\mathbf{Q}_{h+}^k)}{2} \\ &= \frac{n_x(\mathbf{F}(\mathbf{Q}_{h-}^k) + \mathbf{F}(\mathbf{Q}_{h+}^k)) + n_y(\mathbf{G}(\mathbf{Q}_{h-}^k) + \mathbf{G}(\mathbf{Q}_{h+}^k))}{2}, \end{aligned} \quad (2.30)$$

which corresponds to a purely central flux. In this case, we do not get any contributions from the internal boundaries, which give a stable scheme for linear hyperbolic problems. That is, for a periodic case, the energy is constant as for the original equation.

An another kind of numerical flux is the Lax-Freidrich flux, which has the following formulation

$$\begin{aligned} \mathbf{f}_{LF}^{k*}(\mathbf{Q}_{h-}^k, \mathbf{Q}_{h+}^k) &= \frac{\mathbf{f}^k(\mathbf{Q}_{h-}^k) + \mathbf{f}^k(\mathbf{Q}_{h+}^k)}{2} + \frac{C}{2} \hat{\mathbf{n}}^k \cdot (\mathbf{Q}_{h-}^k - \mathbf{Q}_{h+}^k) \\ &= \frac{n_x(\mathbf{F}(\mathbf{Q}_{h-}^k) + \mathbf{F}(\mathbf{Q}_{h+}^k)) + n_y(\mathbf{G}(\mathbf{Q}_{h-}^k) + \mathbf{G}(\mathbf{Q}_{h+}^k))}{2} + \frac{C}{2} \hat{\mathbf{n}}^k \cdot (\mathbf{Q}_{h-}^k - \mathbf{Q}_{h+}^k), \end{aligned} \quad (2.31)$$

where  $C$  is the local maximum of the directional flux Jacobian

$$C = \max_{\mathbf{Q} \in [\mathbf{Q}_{h-}, \mathbf{Q}_{h+}]} \left| n_x \frac{\partial \mathbf{F}}{\partial \mathbf{Q}} + n_y \frac{\partial \mathbf{G}}{\partial \mathbf{Q}} \right|. \quad (2.32)$$

$C$  corresponds to maximal value of all the velocities of the waves propagating in the medium. The Lax-Freidrich flux ensures a monotone solution and can therefore be used in non-linear hyperbolic problems [94].

The third considered numerical flux is a Godunov type of flux. It is generally based on the resolution of the normal Riemann problem at each cell edge. Such kind of numerical flux has been introduced in the framework of a modal DG-FEM scheme for the simulation of linear elastic or viscoelastic waves in isotropic and anisotropic solids by Käser *et al.* in a series of papers [103], [148], [104], [63], [64]. In this case, the numerical flux always takes information from where the waves are coming from, that corresponds to an upwind flux expressed on a local coordinate system defined by the vector,  $\bar{\mathbf{n}} = (n_x, n_y)$ , normal to the considered interface between the current element and one of the three neighbouring triangles and the corresponding tangential vectors. To do this, one needs to rotate both the variable vector  $\mathbf{Q}$  and the Hooke's matrix with components  $C_{ijkl}$ . To rotate  $\mathbf{Q}$  to the local coordinate system, it is multiplied by the inverse of the rotation matrix  $\mathbf{T}^{-1}$  which reads as:

$$\mathbf{T}^{-1} = \begin{bmatrix} n_x & n_y & 0 & 0 & 0 & 0 \\ -n_y & n_x & 0 & 0 & 0 & 0 \\ 0 & 0 & n_x^2 & n_y^2 & n_x n_y & n_x n_y \\ 0 & 0 & n_y^2 & n_x^2 & -n_x n_y & -n_x n_y \\ 0 & 0 & -n_x n_y & n_x n_y & n_x^2 & -n_y^2 \\ 0 & 0 & -n_x n_y & n_x n_y & -n_y^2 & n_x^2 \end{bmatrix}. \quad (2.33)$$

The rotation of the Hooke's matrix  $\mathbf{C}$  to this local coordinate system is done by applying the so-called Bond's matrix method [6], [139]. The Hooke's matrix  $\tilde{\mathbf{C}}$  in the local system is given by:

$$\tilde{\mathbf{C}} = \mathbf{N}\mathbf{C}\mathbf{N}^T, \quad (2.34)$$

where  $\mathbf{N}$  is the Bond's matrix:

$$\mathbf{N} = \begin{bmatrix} n_x^2 & n_y^2 & 2n_x n_y \\ n_y^2 & n_x^2 & -2n_x n_y \\ -n_x n_y & n_x n_y & n_x^2 - n_y^2 \end{bmatrix}. \quad (2.35)$$

The numerical Godunov type flux, if only the flux normal to the interface is considered, is then given by:

$$\mathbf{f}^{k*}(\mathbf{Q}_{h-}^k, \mathbf{Q}_{h+}^k) = \mathbf{T}^k \tilde{\mathbf{A}} (\mathbf{T}^{-1})^k \hat{\mathbf{Q}}^k, \quad (2.36)$$

where  $\tilde{\mathbf{A}}$  is the matrix  $\mathbf{A}$  of Eq. (1.52) in which the components  $C_{ij}$  are rotated, and where for upwind  $\hat{\mathbf{Q}}^k$  is defined as:

$$\begin{aligned}
 \hat{\mathbf{Q}}^k &= \mathbf{Q}_{h+}^k & \text{if } \mathbf{f}^k > 0 \\
 \hat{\mathbf{Q}}^k &= \mathbf{Q}_{h-}^k & \text{if } \mathbf{f}^k < 0. \\
 \hat{\mathbf{Q}}^k &= 0 & \text{if } \mathbf{f}^k = 0
 \end{aligned} \tag{2.37}$$

This leads to the following numerical flux:

$$\begin{aligned}
 \mathbf{f}^{k*}(\mathbf{Q}_{h-}^k, \mathbf{Q}_{h+}^k) &= \frac{1}{2}(\mathbf{T}^k \tilde{\mathbf{A}}(\mathbf{T}^{-1})^k + \mathbf{T}^k |\tilde{\mathbf{A}}|(\mathbf{T}^{-1})^k) \mathbf{Q}_{h+}^k + \frac{1}{2}(\mathbf{T}^k \tilde{\mathbf{A}}(\mathbf{T}^{-1})^k - \mathbf{T}^k |\tilde{\mathbf{A}}|(\mathbf{T}^{-1})^k) \mathbf{Q}_{h-}^k \\
 &= \frac{1}{2}(\mathbf{T}^k \tilde{\mathbf{A}}(\mathbf{T}^{-1})^k + \mathbf{T}^k |\tilde{\mathbf{A}}|(\mathbf{T}^{-1})^k)(\mathbf{Q}_{h+}^k - \mathbf{Q}_{h-}^k) + \mathbf{f}^k(\mathbf{Q}_{h-}^k).
 \end{aligned} \tag{2.38}$$

So, the term  $\mathbf{f}^{k*} - \mathbf{f}^k$  encountered in the numerical DG-FEM scheme can be expressed as:

$$\mathbf{f}^{k*} - \mathbf{f}^k = \frac{1}{2} \mathbf{T}^k (\tilde{\mathbf{A}} + |\tilde{\mathbf{A}}|)(\mathbf{T}^{-1})^k (\mathbf{Q}_{h+}^k - \mathbf{Q}_{h-}^k). \tag{2.39}$$

The main advantages of this flux are first the possibility to extend it to a flux of higher order of precision, using a wave-propagation approach as described in the book of Le Veque [115], and second to offer a simple way to implement open boundary condition. This last possibility will be described in paragraph 2.3.1.

## 2.2.4 Discontinuous Galerkin Operators on Quadrilateral Element

In the preceding part, the DG-FEM scheme has been presented for triangular cell elements. This involved the introduction of the mapping between the general triangular element and the straight-angle reference triangle, the nodal sets for the triangle and an orthonormal polynomial basis that has been used as a reference basis for interpolation and differentiation. Here, we will go further and consider the use of quadrilateral mesh elements in substitution to the triangular mesh elements, that to say the whole computational physical domain,  $\Omega$ , is decomposed into quadrilateral cell elements  $D_q^k$ .

In this case, for solving the system of Eq. (2.1) in the discontinuous scheme, we assume that  $\Omega$  can be tiled using non-overlapping  $K$  quadrilateral elements  $D_q^k$ :

$$\Omega \cong \Omega_h = \bigcup_{k=1}^K D_q^k. \tag{2.40}$$

In the  $k$ -th quadrilateral element, the numerical solution  $\mathbf{Q}_h^k$  of Eq. (2.1) can be approximated through an interpolation as in the triangular element with the same representation as Eq. (2.3). In this case, the number of grid points  $N_p$  in the local expansion has the following relation with the order of interpolation polynomial  $N$

$$N_p = (N + 1)(N + 1), \tag{2.41}$$

As for triangular elements, we introduce a mapping,  $\Psi$ , which connects the general straight-sided quadrilateral,  $x \in D_q^k$ , with the standard quadrilateral, defined by

$$\mathbf{I} = \{\mathbf{r} = (r, s) \mid (r, s) \geq -1; (r, s) \leq 1\}, \quad (2.42)$$

as sketched in Fig. 2.3.

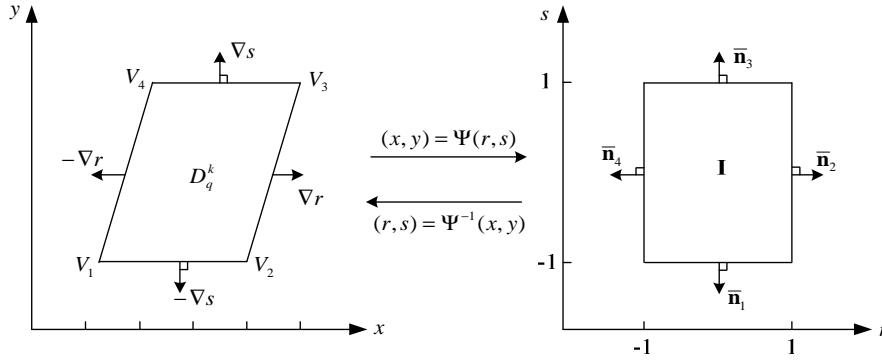


**Fig. 2.3.** The mapping between the standard reference quadrilateral element  $\mathbf{I}$  and a general quadrilateral shaped element.

The mapping relation between the standard quadrilateral and the general quadrilateral is then given as

$$\begin{bmatrix} x^k \\ y^k \end{bmatrix} = \frac{(1-r)(1-s)}{2} \mathbf{v}_1^k + \frac{(1+r)(1-s)}{2} \mathbf{v}_2^k + \frac{(1+r)(1+s)}{2} \mathbf{v}_3^k + \frac{(1-r)(1+s)}{2} \mathbf{v}_4^k, \quad (2.43)$$

in which  $(\mathbf{v}_1^k, \mathbf{v}_2^k, \mathbf{v}_3^k, \mathbf{v}_4^k)$  are the vertex coordinates of the  $k$ -th general quadrilateral element. In the standard quadrilateral, for interpolation the vectors  $\mathbf{r} = [r_1, r_2, \dots, r_{N_p}]^T$  and  $\mathbf{s} = [s_1, s_2, \dots, s_{N_p}]^T$  have been defined and the positions of these grid using the Legendre-Gauss-Lobatto points as in the case of reference triangular element. This choice leaves the possibility to combine the two different types of elements. Examples of nodal distributions in the reference quadrilateral are shown on Fig. 2.4.

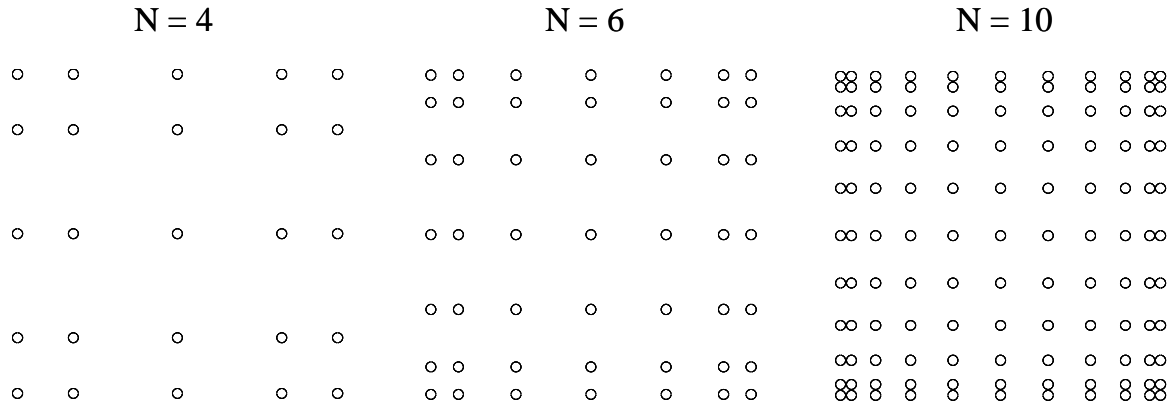


**Fig. 2.4** Nodal distributions in the reference straight-angle quadrilateral element  $\mathbf{I}$  for polynomial order  $N = 4, 6,$  and  $10$ .

The  $r_x$ ,  $r_y$ ,  $s_x$ ,  $s_y$  and the transformation Jacobian  $J$  are given by the same expressions Eqs. (2.12)-(2.13) as for triangular elements and are also constants due to the use of quadrilateral elements with straight sides. In the reference standard quadrilateral, we use the following orthonormal interpolation basis function [167]

$$\psi_q(r, s) = P_i^{(0,0)}(r)P_j^{(0,0)}(s)/\sqrt{\gamma_{i,j}}, \text{ for } (i, j) \geq 0 \text{ and } i + j \leq N, \quad (2.44)$$

with

$$\gamma_{i,j} = \left(\frac{2}{2i+1}\right)\left(\frac{1}{2j+1}\right).$$

The  $P_i^{(0,0)}(r)$  and  $P_j^{(0,0)}(s)$  are the  $i$ -th and  $j$ -th order Legendre polynomials, respectively. The Vandermonde matrix is constructed by the basis function  $\mathbf{V}_q = \psi_{qj}(r_i, s_i)$ . The differentiation operator and the differentiation matrix have the same formulations as Eq. (2.18) and Eq. (2.20), respectively. But because the interpolation function  $\psi_q$  is function of variables  $r$  and  $s$  directly, its derivatives are simply given, for the reference quadrilateral, by

$$\frac{\partial \psi_q(r, s)}{\partial r} = \frac{\partial P_i^{(0,0)}(r)}{\partial r} P_j^{(0,0)}(s) \text{ and } \frac{\partial \psi_q(\mathbf{r}, s)}{\partial s} = P_i^{(0,0)}(\mathbf{r}) \frac{\partial P_j^{(0,0)}(s)}{\partial r}. \quad (2.45)$$

In the reference standard quadrilateral  $\mathbf{I}$ , the normal vectors belonging to its four faces are  $\bar{\mathbf{n}}_1 = -\bar{\mathbf{s}}$ ,  $\bar{\mathbf{n}}_2 = \bar{\mathbf{r}}$ ,  $\bar{\mathbf{n}}_3 = \bar{\mathbf{s}}$  and  $\bar{\mathbf{n}}_4 = -\bar{\mathbf{r}}$ , where  $\bar{\mathbf{r}}$  and  $\bar{\mathbf{s}}$  are unit vectors. Hence, the outward pointing vectors at the surface of the elements  $D_q^k$  have the following formulations

$$\hat{\mathbf{n}}_1^k = -\frac{\nabla r}{\|\nabla r\|_k}, \quad \hat{\mathbf{n}}_2^k = \frac{\nabla s}{\|\nabla s\|_k}, \quad \hat{\mathbf{n}}_3^k = \frac{\nabla r}{\|\nabla r\|_k} \text{ and } \hat{\mathbf{n}}_4^k = -\frac{\nabla s}{\|\nabla s\|_k}. \quad (2.46)$$

Here,  $\|\cdot\|$  is the Euclidian length of the vector. The corresponding edge Jacobian for the mapping is computed as

$$J_{1D}^{k_1} = J_{1D}^{k_3} = \|\nabla r^k\|, \text{ and } J_{1D}^{k_2} = J_{1D}^{k_4} = \|\nabla s^k\|. \quad (2.47)$$

For the numerical flux, local flux and volume terms, the results are analogous to the one already described in the case of triangular mesh elements.

## 2.2.5 Time-Stepping and Discrete Stability

A semi-discrete DG-FEM form has been obtained on the spatial dimension from the above analysis, that is, we have discretized in space domain but kept continuous in time domain. This means that in the used approach we discretize the space and time domain separately. Standard techniques can be used to solve the semi-discrete DG-FEM scheme for the time discretization. The quadrature-free Runge-kutta Discontinuous Galerkin approach developed for the semi-discrete equation by Atkins & Shu [4] which used a three-stage TVD

Runge-Kutta time integration method [168]. An Arbitrary high order DERivatives (ADER) [103], [148], [104], [63], [64] approach has been applied to the semi-discrete form of the DG-FEM scheme in order to achieve an arbitrarily accurate time discretization. Bordal *et al.* [27] use a fourth-order low storage explicit Runge-Kutta (LSERK) method [35] to discretize the DG-FEM in time domain for piezoelectric material.

For us, in the following, the same fourth-order low storage explicit Runge-Kutta (LSERK) method will be used for discretization the DG-FEM scheme in time domain. Now, we make the notation of Eq. (2.1) as following

$$\frac{\partial \mathbf{Q}_h}{\partial t} = \mathfrak{R}_h(\mathbf{Q}_h, t), \quad (2.48)$$

where  $\mathfrak{R}_h(\mathbf{Q}_h, t)$  represents the right hand side of Eq. (2.1). The LSERK scheme has the form

$$\begin{aligned} \mathbf{p}^{(0)} &= \mathbf{Q}_h^n, \\ i \in [1, \dots, 5]: & \begin{cases} \mathbf{k}^{(i)} = a_i \mathbf{k}^{(i-1)} + \Delta t \mathfrak{R}_h(\mathbf{p}^{(i-1)}, t^n + c_i \Delta t), \\ \mathbf{p}^{(i)} = \mathbf{p}^{(i-1)} + b_i \mathbf{k}^{(i)}, \end{cases} \\ \mathbf{Q}_h^{n+1} &= \mathbf{p}^{(5)}. \end{aligned} \quad (2.49)$$

This scheme has five stages and one extra storage level in each time-step  $\Delta t$ , while a standard explicit fourth-order RK scheme uses four stages and has four additional storage levels. The LSERK scheme will therefore require less memory, but increase the number of computations in each step, as it has five stages. However, the additional stage will give the LSERK scheme a larger stability region. That is, it is more stable and we can use larger time-steps, which will reduce the number of computations. The time-step is chosen from the following formula

$$\Delta t = \frac{2}{3} \min_{i=1}^N(\Delta r_i) \min_{\Omega} \left( \frac{r_D}{|v_l|} \right), \quad (2.50)$$

with  $r_D = A/s$  the radius of the inscribed circle in the triangular elements, where  $A$  is the area of the triangle and  $s$  is half the triangle perimeter. The  $v_l$  is the longitudinal wave speed and  $\Delta r_i = r_{i+1} - r_i$ , which is the distance between the neighbouring grid points on the legs in the standard triangle **I**. The coefficients needed in the LSERK are given in Tab. 2.1.

**Tab. 2.1** Coefficients for the low-storage five-stage fourth-order explicit Runge-Kutta method (LSERK)

$i$	$a_i$	$b_i$	$c_i$
1	0	$\frac{1432997174477}{9575080441755}$	0
2	$-\frac{567301805773}{1357537059087}$	$\frac{5161836677717}{13612068292357}$	$\frac{1432997174477}{9575080441755}$

3	$-\frac{2404267990393}{2016746695238}$	$\frac{1720146321549}{2090206949498}$	$\frac{2526269341429}{6820363962896}$
4	$-\frac{3550918686646}{2091501179385}$	$\frac{3134564353537}{4481467310338}$	$\frac{2006345519317}{3224310063776}$
5	$-\frac{1275806237668}{842570457699}$	$\frac{2277821191437}{14882151754819}$	$\frac{2802321613138}{2924317926251}$

## 2.3 Boundary Conditions

A large variety of physically meaningful boundary conditions exists for an elastic medium. However, the three most important kinds of boundaries are: open boundaries, stress free surface boundaries and fixed surface boundaries.

### 2.3.1 Open Boundaries

At the open boundaries, no waves are supposed to reflect back into the computational domain and those waves that are travelling out should be able to pass the boundary without reflections. There is a whole scientific community dealing with non-reflective boundary conditions, however, in this section we present only a very simple approach that so far yielded satisfactory results, at least for our purposes in the Discontinuous Galerkin Scheme. It is a strict upwind method, i.e. outgoing waves at an element interface are only influenced by the state in the element itself and not by the state in the neighbour. Indeed, since incoming waves are not allowed, the respective flux contribution must vanish. Thus, a very simple implementation of open boundary conditions can be derived using a Godunov type numerical flux, and is given by:

$$(\mathbf{f}^{k*}(\mathbf{Q}_{h-}^k, \mathbf{Q}_{h+}^k))^{OpenBC} = \frac{1}{2} \mathbf{T}^k (\tilde{\mathbf{A}} - |\tilde{\mathbf{A}}|)(\mathbf{T}^{-1})^k \mathbf{Q}_{h-}^k \quad (2.51)$$

This leads to a term  $\mathbf{f}^{k*} - \mathbf{f}^k$  encountered in the numerical DG-FEM scheme written as:

$$(\mathbf{f}^{k*} - \mathbf{f}^k)^{OpenBC} = -\frac{1}{2} \mathbf{T}^k (\tilde{\mathbf{A}} + |\tilde{\mathbf{A}}|)(\mathbf{T}^{-1})^k \mathbf{Q}_{h-}^k \quad (2.52)$$

This method, although giving satisfactory results for bulk waves, is generally less efficient in absorbing surface waves. To circumvent this problem a Perfectly Matched Layer well adapted to the DG-FEM method has been developed as it will be described in Chapter 3.

### 2.3.2 Stress Free and Fixed Surface Boundaries

On the free surface of an elastic medium, the normal stress and the shear stresses with respect to the boundary are determined by physical constraints. At the outside of the elastic

medium, there are no external forces that retract the particles into their original position. Therefore,

$$T_1 = P_{11}n_x + P_{12}n_y = 0, \quad (2.53)$$

$$T_2 = P_{21}n_x + P_{22}n_y = 0, \quad (2.54)$$

where  $T_i$  are the components of the traction acting on the surface. Equivalently, the normal stress and the shear stress values at the free surface have to be zero:

$$P_{\xi\xi} = 0, \quad (2.55)$$

$$P_{\xi\eta} = 0, \quad (2.56)$$

where  $\xi$  and  $\eta$  indicates the normal and tangential directions, respectively.

On the fixed surface of an elastic medium, all the components of the displacement (or the particle velocity) have to be zero.

In contrast to classical continuous FE methods we have no direct control on the values at the boundaries within the Discontinuous Galerkin framework. However, the boundary values can be imposed via the numerical flux, as in the Finite Volume framework.

### Lax-Freidrich and Central Flux

On the six components of the numerical flux only the first two are imposed (equal to zero) in the case of a stress-free boundary. We have chosen to calculate the four remaining components with the image method [114], [155]. So, for the other components we just copy the inside values to the virtual outside neighbour. For the free surface boundary condition the resulting Lax-Freidrich numerical flux function in Eq. (2.31) can be then formulated as follows:

$$\mathbf{f}_{LF}^{k*}(\mathbf{Q}_{h-}^k, \mathbf{Q}_{h+}^k) = \frac{n_x(\mathbf{F}(\mathbf{Q}_{h-}^k) + \Gamma_{FreeBC}\mathbf{F}(\mathbf{Q}_{h-}^k)) + n_y(\mathbf{G}(\mathbf{Q}_{h-}^k) + \Gamma_{FreeBC}\mathbf{G}(\mathbf{Q}_{h-}^k))}{2} + \frac{C}{2}\hat{\mathbf{n}}^k \cdot (\mathbf{Q}_{h-}^k - \mathbf{Q}_{h+}^k), \quad (2.57)$$

with the matrix  $\Gamma_{FreeBC} = \mathbf{diag}(-1, -1, 1, 1, 1, 1)$ . For the fixed-surface boundary condition the resulting Lax-Freidrich numerical flux is the same as Eq. (2.57) just replacing  $\Gamma_{FreeBC}$  by  $\Gamma_{FixedBC} = \mathbf{diag}(1, 1, -1, -1, -1, -1)$ . In the case of a central flux  $C = 0$  in Eq. (2.57).

### Godunov Flux

Considering that the numerical flux is based on the solution of a Riemann-Problem at an element interface and given some boundary extrapolated values from inside the computational

domain on a fixed surface, we must search corresponding virtual neighbour values outside the computational domain. We prescribe a virtual component outside the domain that has the same magnitude but opposite sign. For the other components we use the image method. Then, the stress-free boundary in the case of Godunov type numerical flux can be obtained with:

$$(\mathbf{f}^{k*} - \mathbf{f}^k)_{FreeBC} = \frac{1}{2} \mathbf{T}^k (\tilde{\mathbf{A}} + |\tilde{\mathbf{A}}|) \Gamma_{FreeBC} (\mathbf{T}^{-1})^k \mathbf{Q}_h^k, \quad (2.58)$$

where  $\Gamma_{FreeBC} = \mathbf{diag}(0, 0, -2, 0, -2, -2)$ . Note that in this case, contrary to what happens for the Lax-Friedrich flux, the matrix  $\Gamma_{FreeBC}$  acts on the rotated components of the  $\mathbf{Q}$  vector. In the case of a fixed boundary  $\Gamma$  becomes  $\Gamma_{FixedBC} = \mathbf{diag}(-2, -2, 0, 0, 0, 0)$ .

## 2.4 Sources

The consideration of source terms in numerical simulation is often a difficult task, but indispensable when realistic simulation of an experiment is expected. Here, two different cases of source terms have been considered: continuous sources in space and point sources that are characterized by a Delta distribution in space. In both cases the source time function is continuous. The used method is able to deal with point sources at any position in the computational domain that does not necessarily need to coincide with a grid point. Indeed, an interpolation is performed by evaluation of the test functions at the source locations.

When considering a source term  $\mathbf{S}$ , the system of equations that need to be resolved becomes:

$$\frac{\partial \mathbf{Q}(t, \mathbf{x})}{\partial t} = \frac{\partial \mathbf{F}}{\partial x} + \frac{\partial \mathbf{G}}{\partial y} + \mathbf{S}, \quad \mathbf{x} = [x, y] \in \Omega \in \mathbf{R}^2. \quad (2.59)$$

As for the variable  $\mathbf{Q}$ , the source in the  $k$ -th element is approximated through an interpolation

$$\mathbf{S}(t, \mathbf{x}^k) \cong \mathbf{S}_h^k(t, \mathbf{x}) = \sum_{i=1}^{N_p} \mathbf{S}_{hi}^k(t) \mathbf{I}_i^k(\mathbf{x}). \quad (2.60)$$

Multiplying Eq. (2.59) by the basis function and integrating on each element  $D^k$  yields for the source term:

$$\int_{D^k} \mathbf{S}_h^k \mathbf{I}_i^k(\mathbf{x}) d\mathbf{x} = J^k M \mathbf{S}_h^k, \quad (2.61)$$

Then following the steps described in the paragraph 2.2.2 or 2.2.4 we obtain the following local scheme on each triangle (or quadrilateral) of the mesh:

$$\frac{\partial \mathbf{Q}_h^k}{\partial t} = r_x \mathbf{D}_r \mathbf{F}_h^k + s_x \mathbf{D}_s \mathbf{F}_h^k + r_y \mathbf{D}_r \mathbf{G}_h^k + s_y \mathbf{D}_s \mathbf{G}_h^k + \sum_{i=1}^3 \frac{J_{1D}^{k_i}}{J^k} M^{-1} M^{1D} (\mathbf{f}^{ki*} - \mathbf{f}^{ki}) + \mathbf{S}_h^k. \quad (2.62)$$

Eq. (2.61) has been obtained because the source term was discretized on the nodes of the grid. But, when a point source, not placed on a nodal point, is introduced the calculation of the integral of Eq. (2.61) needs to be reconsidered. Now, we have

$$\int_{D^k} \mathbf{S}_h^k \mathbf{l}_i^k(\mathbf{x}) d\mathbf{x} = J^k \int_I \mathbf{S}(t) \delta(r - r_0, s - s_0) \mathbf{l}_i^k(\mathbf{x}) d\mathbf{x} = J^k \mathbf{S}(t) \mathbf{l}_i^k(r_0, s_0), \quad (2.63)$$

where  $(r_0, s_0)$  are the coordinates of the point source in the reference triangle. Using the relation between the modal and nodal form of DG-FEM, the value of the Lagrange interpolation polynomials at  $(r_0, s_0)$  is calculated as

$$\mathbf{l}_i^k(r_0, s_0) = (V^{-1})^T \boldsymbol{\psi}(r_0, s_0). \quad (2.64)$$

Therefore, for the introduction of a point source it is necessary to first find the triangle containing the source, and then to find in the corresponding reference triangle its coordinates  $(r_0, s_0)$ .

Frequently, one needs to introduce sources directly on boundaries, for example in the case of an impact or when a transducer is glued on the sample. As for the boundary conditions in a DG-FEM scheme these source terms are introduced via the numerical flux. In our simulations, we often need to consider the case when a stress was imposed normally to a part of a surface of the sample. For a surface with a normal given by  $\mathbf{n} = (n_x, n_y)$  the components of the traction are:

$$T_1 = P_{11}n_x + P_{12}n_y = S_1 = n_x \mathbf{S}(t), \quad (2.65)$$

$$T_2 = P_{21}n_x + P_{22}n_y = S_2 = n_y \mathbf{S}(t), \quad (2.66)$$

Here,  $\mathbf{S}(t)$  is the time source function at the considered point. This simply corresponds to a normal stress and a shear stress values at the free surface given by:

$$P_{\xi\xi} = \mathbf{S}(t), \quad (2.67)$$

$$P_{\xi\eta} = 0. \quad (2.68)$$

## 2.5 Numerical Validation: Comparison with Analytical Solutions

In this section, several simulations will be presented to demonstrate the performance of the proposed DG-FEM scheme for the two kinds of grid elements (triangle and quadrilateral). Applications of DG-FEM will be made for both isotropic and anisotropic solid medium and for linear and nonlinear elastic waves. For each situation the result of simulation will be compared with an analytical solution to valid the implementation of DG-FEM.

### 2.5.1 Linear Isotropic Simulation of Lamb's Problem

Here, for the application of DG-FEM scheme to isotropic medium, we present a classical test case which uses a vertical force in a homogeneous elastic half-space with a free surface. This test is called Lamb's Problem (Lamb 1904), consisting in a vertical point force acting on the free surface. The solution of Lamb's Problem for a plane surface can be computed analytically and can hence be used for comparison with the DG-FEM framework results meshed with triangular elements. We use the FORTRAN code EX2DDIR of Berg [18] to compute the exact solution of the seismic 2D response from a vertical directional point source in an elastic half space. The code EX2DDIR is based on the Cagniard-de Hoop [51] technique and allows the use of an arbitrary source time function for displacements or velocities.

The numerical model is as follows: the physical domain has its origin (0, 0) at the left upper corner and is 4000 m wide and has a height of 2000 m. The tilt angle of the free surface is  $\phi = 10^\circ$ . A directional point source, acting as a force perpendicular to this tilted surface, is located at the free surface (1720.00, -2303.28). Two receivers are located at (2557.1, -2450.9) and (2901.8, -2511.7) such that the distances from the source along the surface are 850 m and 1200 m, respectively. The whole calculation domain consists of 4007 triangular mesh elements. For the homogeneous elastic medium, the parameters of simulation were: the mass density  $\rho_0 = 2200 \text{ kg/m}^3$ , the velocities of *P*-wave and *S*-wave  $c_p = 3200 \text{ m/s}$  and  $c_s = 1847.5 \text{ m/s}$ , respectively. The source time function that specifies the temporal variation of the point source is a Ricker wavelet given by the following form:

$$s(t) = (0.5 + a_1(t - t_D)^2) \cdot e^{a_1(t - t_D)^2}, \quad (2.69)$$

where  $t_D = 0.16 \text{ s}$  is the source delay time and  $a_1 = -(\pi f_c)^2$  is the constant determining the amplitude, and the central frequency of the Ricker wavelet is  $f_c = 7.25 \text{ Hz}$ . By considering the tilt angle  $\phi$ , the final resulting source vector  $s_p(x, y, t)$  acting on the governing Eq. (2.1) is

$$s_p(x, y, t) = (-\sin(\phi), \cos(\phi), 0, 0, 0, 0)' \cdot s(t) \cdot \delta(x - x_0). \quad (2.70)$$

In this simulation, a fifth order RK-DG-FEM O5 scheme has been used with a triangular elements mesh. The wave propagation has been simulated until time  $T = 1.0 \text{ s}$  when all the waves have already passed the two receivers. We use the Lax-Freidrich numerical flux and stress free surface boundary condition. The snapshot of the velocity component of the wave field at  $t = 0.7 \text{ s}$  is presented in Fig. 2.5, from which we can see the propagation of the bulk waves in the medium and the Rayleigh wave at the surface. In Fig. 2.6, we present the results from the numerical simulations, as recorded by receiver 1 and receiver 2, respectively, together with the analytical solution provided by EX2DDIR. For the first receiver, the analytical and numerical solutions match well for the two vertical and horizontal particle

velocities, while for the second receiver, the match of horizontal particle velocity is not as good.

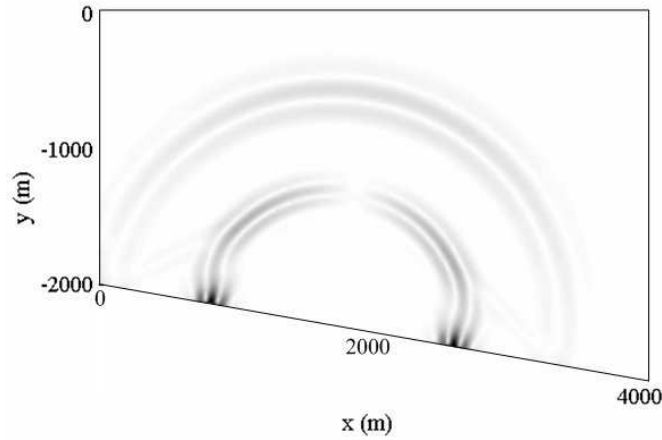


**Fig. 2.5** Amplitude of the velocity  $v$  at  $t = 0.7$  s calculated within RK-DG-FEM O5 scheme meshed on triangular element.

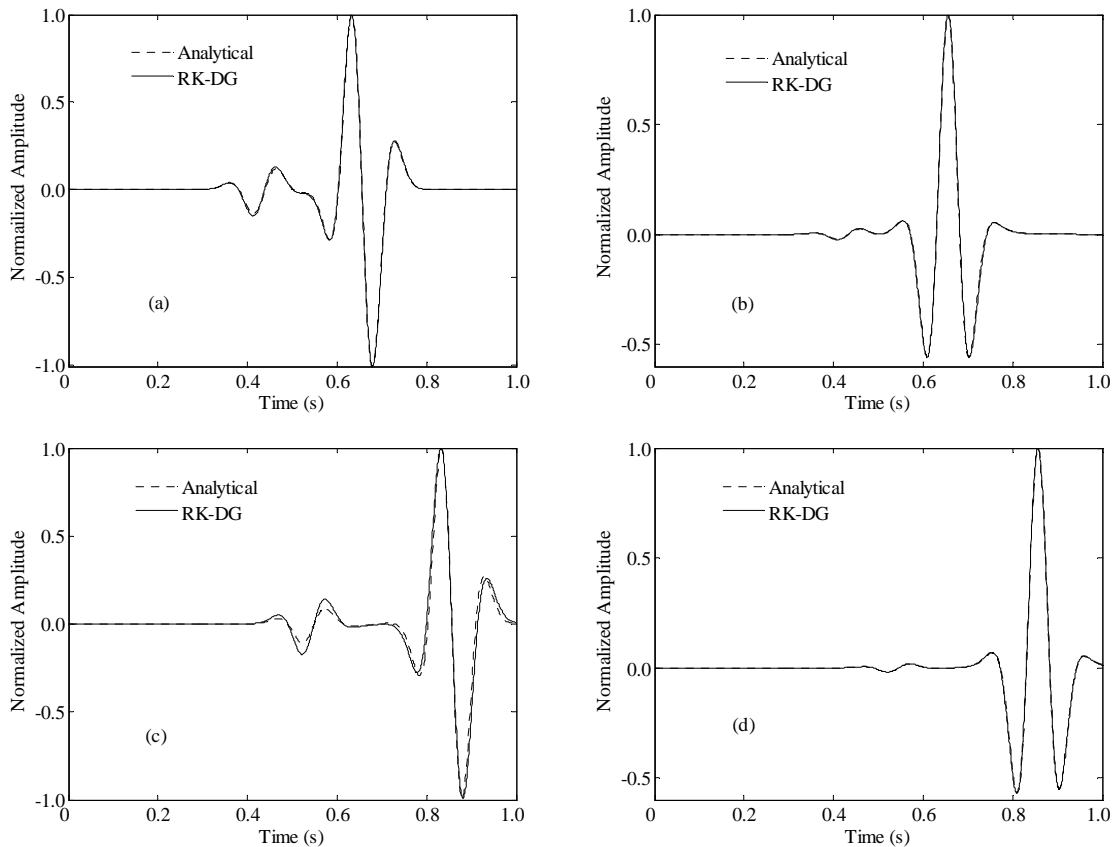


**Fig. 2.6** Comparison of the analytical reference solution with simulation results at the two receivers obtained within the five order RK-DG-FEM O5 scheme meshed on triangular element. The first row (a) and (b) are for receiver 1 and the second row (c) and (d) are for receiver 2. In each row the right hand figure displays the horizontal particle velocity and the left hand figure is the vertical particle velocity.

In Fig. 2.7 we present the results of simulation made with a seven order RK-DG-FEM with the same number of total mesh element. We can see that the analytical and numerical match well for the two receivers. This means that by increasing the order of interpolation, we will get better result.

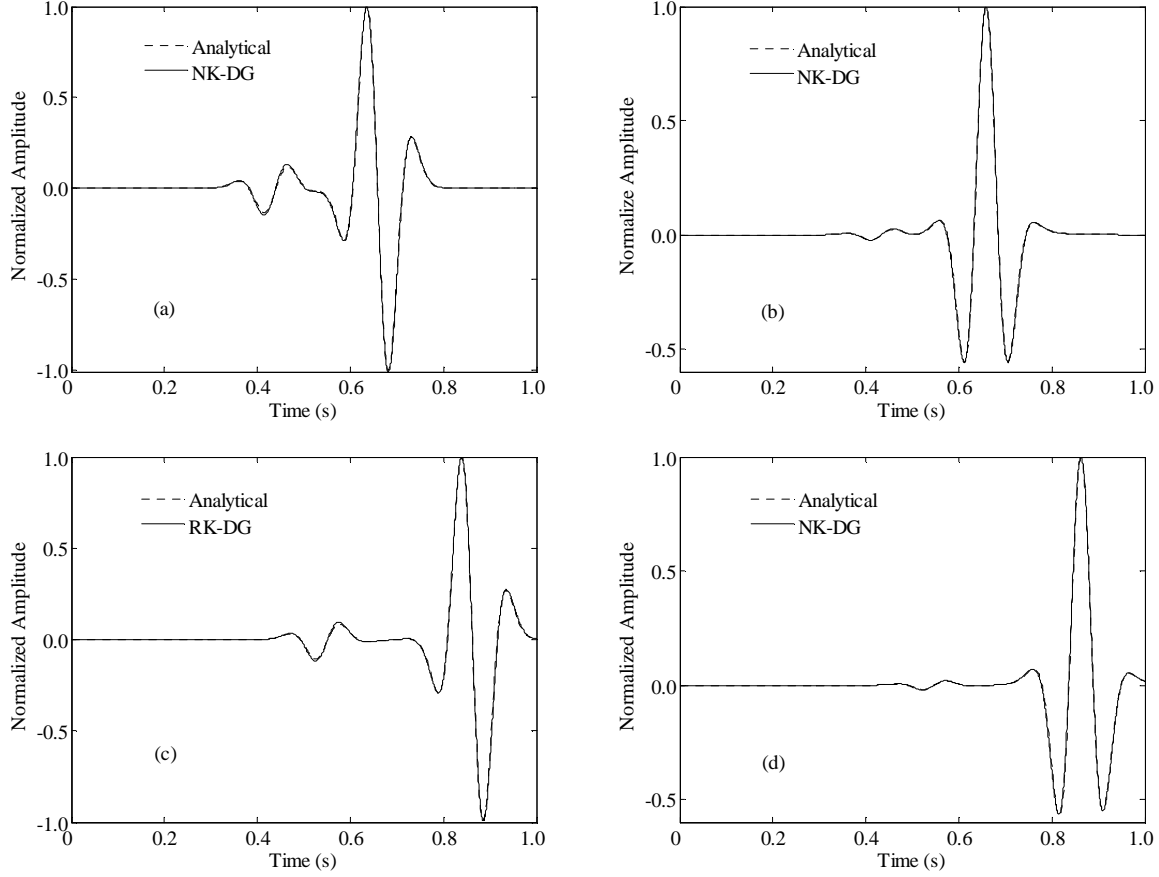


**Fig. 2.7** Comparison of the analytical reference solution with simulation results at the two receivers obtained within the seven order RK-DG-FEM O7 scheme meshed on triangular element. The first row (a) and (b) are for receiver 1 and the second row (c) and (d) are for receiver 2. In each row the right hand figure displays the horizontal particle velocity and the left hand figure is the vertical particle velocity.

In the following paragraphs, we present the results of the simulation of Lamb's Problem obtained with a quadrilateral elements mesh. The numerical model is a rectangular zone (4000 m wide and 2500 m height) with origin (0, 0) at the left upper corner. The vertical directional point source is located at the centre position of the underside stress free surface (2000.0, -2500.0). One receiver is located at (2800.0, -2500.0) such that the distance from the source along the surface is 800 m. The same material and source function Eq. (2.69) have been used with the same parameters as the one use in the case of triangular elements. In this case, no tilt angle  $\phi$  has been used. The source vector  $s_p(x, y, t)$  acting on the governing Eq. (2.1) is then

$$s_p(x, y, t) = (0, 1, 0, 0, 0, 0)' \cdot s(t) \cdot \delta(x - x_0). \quad (2.71)$$

In this simulation, the time  $T = 1.0$  s and the whole physical domain has been meshed with 4000 quadrilateral elements. The Lax-Freidrich numerical flux and stress free surface boundary condition have been used. The snapshot of the velocity component of the wave field at  $t = 0.8$  s presented in Fig. 2.8, obtained with a seven order RK-DG-FEM O7, shows the propagation of both the bulk waves and the Rayleigh wave. In Fig. 2.9, the results of numerical simulations, as recorded by the receiver, together with the analytical solution provided by EX2DDIR have been plotted. The analytical and numerical solutions match well for the vertical and horizontal particle velocities.

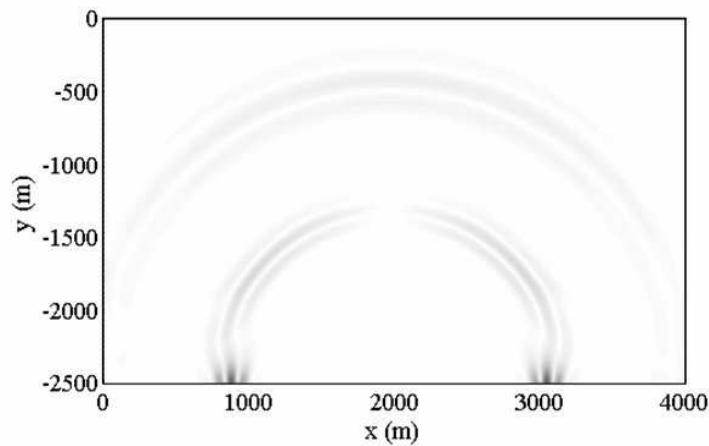


**Fig. 2.8** Amplitude of the velocity  $v$  at  $t = 0.8$  s within RK-DG-FEM O7 scheme meshed on quadrilateral element.

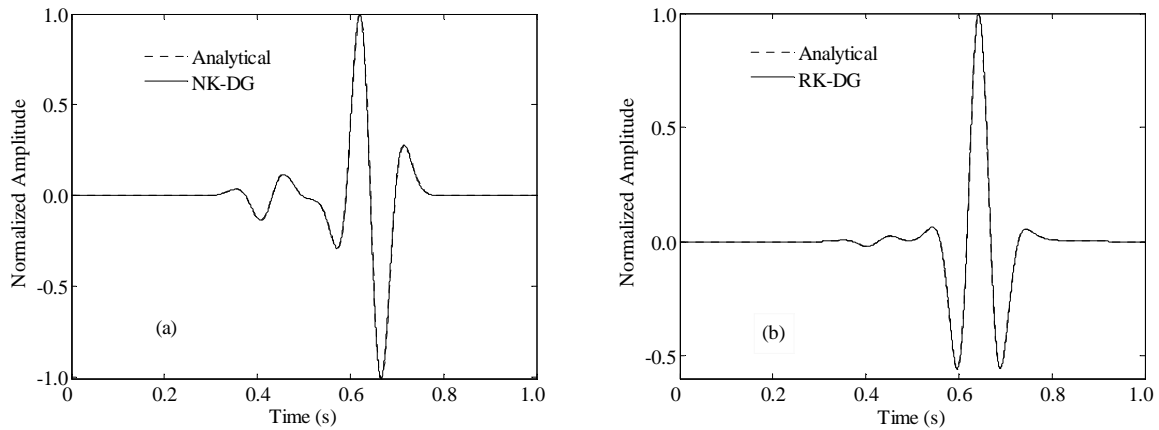


**Fig. 2.9** Comparison of the analytical reference solution with results of simulation at the receiver within the seven order RK-DG-FEM O7 scheme meshed on quadrilateral element. The right hand figure displays the horizontal particle velocity and the left hand figure displays the vertical particle velocity.

## 2.5.2 Linear Simulation of Elastic Waves Propagation in Anisotropic Apatite Material

In the preceding subsection, the simulation with the DG-FEM scheme for Lamb's problem has been presented, demonstrating the good performance of the DG-FEM method for isotropic materials. In this subsection, the results of simulation with anisotropic material will be presented, and compared with an analytical reference solution.

A computational domain of  $33 \times 33$  cm with the origin  $(0.0, 0.0)$  at the centre point is meshed with 6802 triangular elements. The point source, acting in the  $y$ -direction, located at the centre  $(0.0, 0.0)$  of the physical domain, is a shifted zero-phase pulse defined by

$$s(t) = e^{(-0.5f_0^2(t-t_0)^2)} \cos(\pi f_0(t-t_0)), \quad (2.72)$$

with  $t_0 = 7 \mu\text{s}$  and a high cut-off frequency  $f_0 = 0.5$  MHz. The anisotropic solid is apatite with the following properties:  $C_{11} = 167$  GPa,  $C_{12} = 66$  GPa,  $C_{22} = 140$  GPa,  $C_{66} = 66.3$  GPa and density  $\rho_0 = 3200$  kg/m<sup>3</sup>. The two receivers are located at  $(2.6, 0.0)$  and  $(7.8, 0.0)$  (cm) for receiving the signal to make compare with analytical solution.

First, the results of simulation, which has been realized with a five order RK-DG-FEM O5 scheme using triangular elements, will be presented. In this simulation, the total calculation time has been chosen equal to  $T = 32.0 \mu\text{s}$  in order that all the waves have propagated through the two receivers. We use the Lax-Freidrich numerical flux and a stress free boundary condition on the four boundaries. Fig. 2.10 is the snapshot of the velocity component of the wave field at  $t = 27.5 \mu\text{s}$ . It displays the form of wave-front curves in the apatite material. In Fig. 2.11, we present the vertical particle velocities, as recorded by receiver 1 and receiver 2, respectively, together with the analytical solution which has been proposed by Carcione *et al.* [34] (see Annexe A). As the figures show, the comparison between numerical and analytical solution is excellent.

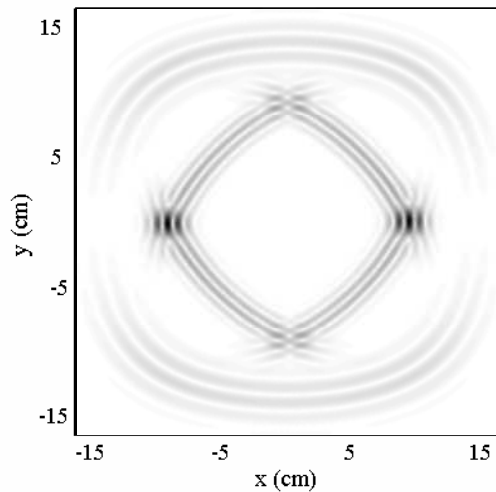


**Fig. 2.10** Amplitude of the velocity  $v$  at  $t = 27.5 \mu\text{s}$  within RK-DG-FEM O5 scheme with triangular mesh element.

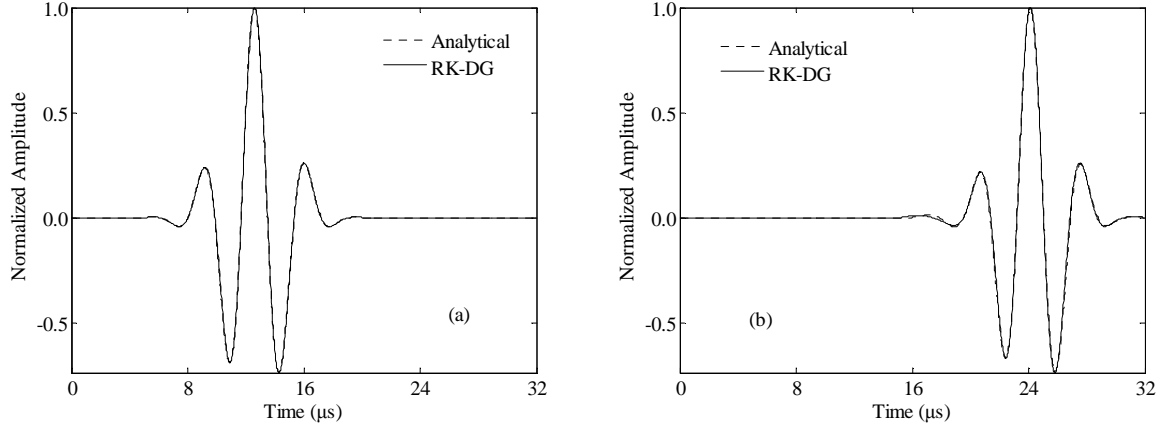


**Fig. 2.11** Comparison of the analytical reference solution with results of simulation at the receivers within the five order RK-DG-FEM O5 scheme meshed on triangle element. The two figures (a) and (b) represent the vertical particle velocity at the receiver 1 and 2, respectively.

The same simulation has been reproduced with a five order DG-FEM scheme using 6400 quadrilateral elements. Fig. 2.12 shows the vertical particle velocity obtained at the two receivers, compared with the analytical reference solution. These two figures show a good match result between the simulation result and the analytical solution, validating the implementation of the DG-FEM scheme with quadrilateral elements for anisotropic solid.

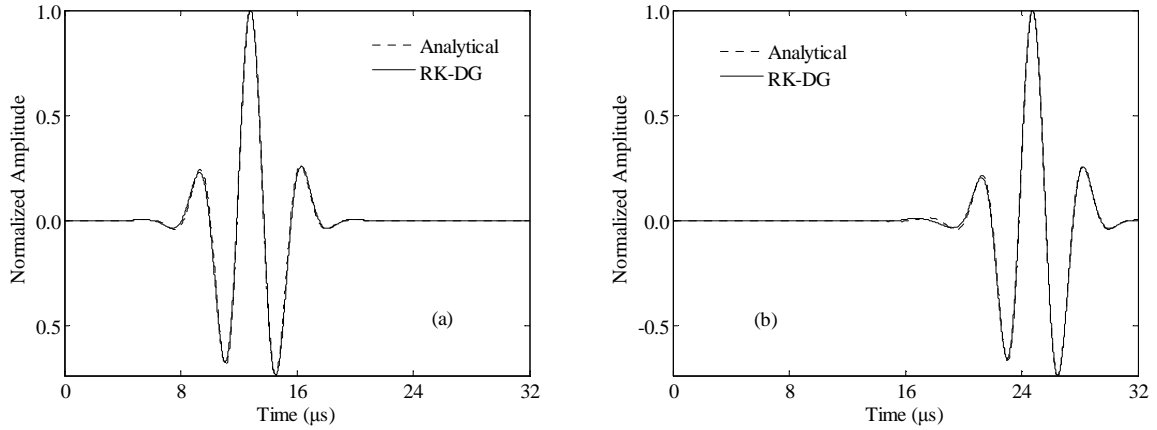


**Fig. 2.12** Comparison of the analytical reference solution with results of simulation at the receivers within the five order RK-DG-FEM O5 scheme meshed on quadrilateral element. The two figures (a) and (b) represent the vertical particle velocity at the receiver 1 and 2, respectively.

### 2.5.3 Attenuation

In order to introduce thermo-viscous attenuation in the scheme, only the stress-strain relationship needs to be modified. In this case, Eq. (1.47) is replaced by:

$$P_{ij} = \tau_{ij} = C_{ijkl}\epsilon_{kl} + \eta_{ijkl} \frac{\partial \epsilon_{kl}}{\partial t}, \quad (2.73)$$

where  $\eta_{ijkl}$  are viscosity coefficients. As the attenuation is considered small enough, only the linear part of the strain component is used in the attenuation term. This leads to:

$$P_{ij} = \tau_{ij} = C_{ijkl} \varepsilon_{kl} + \eta_{ijkl} \frac{\partial F_{kl}}{\partial t} = C_{ijkl} \varepsilon_{kl} + \eta_{ijkl} \frac{\partial v_k}{\partial x_l}. \quad (2.74)$$

Unfortunately, the spatial derivative appearing now in the stress-strain relationship needs to be considered carefully. Indeed, instability can appear if only Eq. (2.74) is used in place of Eq. (1.47) without any other modification of the scheme [94]. In order to stabilize the scheme, it has been pruned to introduce a numerical flux contribution. Following the methodology used in the case of the heat equation [94], [9], each component of the stress tensor is calculated with:

$$P_{ij}^k = C_{ijkl} F_{klh}^k + \eta_{ijkl} D_k^k v_{lh}^k - \sum_{n=1}^3 \frac{J_{1D}^{k_n}}{J^k} M^{-1} M^{1D} \eta_{ijkl} n_{k_n}^k (v_{lh}^{k_i} - v_{lh}^{*k_i}), \quad (2.75)$$

where  $v_l^*$  is a numerical flux term associated with the  $l$ -th particle velocity component. This introduction of the thermoviscuous attenuation needs only a modification of the DG-FEM scheme in the flux term calculations.

We consider plane wave propagation in the  $x$  direction in an isotropic attenuating elastodynamic medium. The thermoviscuous model leads, in this case, to a quadratic dependence of the attenuation parameter of both longitudinal  $\alpha_l$  and transverse  $\alpha_t$  waves as a function of frequency:

$$\alpha_l = \frac{2\pi^2 \eta_{11}}{\rho_0 c_l^3} f^2, \quad (2.76)$$

$$\alpha_t = \frac{2\pi^2 \eta_{66}}{\rho_0 c_t^3} f^2, \quad (2.77)$$

Here, the Voigt notations have been used for the viscosity coefficients, and  $c_l$  and  $c_t$  are the longitudinal and transversal wave velocity, respectively.

In the numerical simulation, a homogenous medium with the following parameters,  $\rho_0 = 2000 \text{ kg/m}^3$ ,  $\lambda = 4.96 \text{ GPa}$ ,  $\mu = 13.52 \text{ GPa}$ ,  $\eta_{11} = 17.1 \text{ MN s/m}^2$ , and  $\eta_{66} = 4.7 \text{ MN s/m}^2$ , is considered. A  $3000 \times 200 \text{ m}$  computational domain, with its origin  $(0.0, 0.0)$  at the centre point, is meshed with 240 quadrilateral elements. A source, consisting of compressional and shear forces, is applied along a line located at  $x = -1000 \text{ m}$  in order to generate a plane wave:

$$s_x(t) = A_x \sin(2\pi f t) e^{-(t-6T/2T)^2} \delta(x), \quad (2.78)$$

$$s_y(t) = A_y \sin(2\pi f t) e^{-(t-6T/2T)^2} \delta(y), \quad (2.79)$$

where  $A_x = 1000$  and  $A_y = 2000$  are the amplitudes of the sources in directions  $x$  and  $y$ ,  $f = 1/T = 20 \text{ Hz}$  is the source frequency and  $\delta$  is the Dirac function. Three receivers  $R_1$ ,  $R_2$ ,  $R_3$  are positioned at the positions  $(-400, 0)$ ,  $(200, 0)$  and  $(1000, 0)$ , respectively. The distances between the source and the three receivers are 3, 6 and 10 longitudinal wavelengths. In this simulation, the Lax-Freidrich numerical flux has been used in the 5 order DG-FEM scheme.

The total calculation time is 2 s. Symmetric boundary conditions on the upper and bottom borders, and 500 m thickness Nearly Perfectly Matched Layer (NPML) boundary condition on the left and right sides have been used. The NPML absorbing boundary layer used here will be presented in detail in part 3.4.

The horizontal  $V_x$  and vertical  $V_y$  particle velocity components calculated at the three receiver positions are displayed on Fig. 2.13. From these time evolution curves, the attenuation parameter evolution as a function of frequency can be calculated with:

$$\alpha = -\frac{1}{x_3 - x_1} \ln\left(\frac{S_3(f)}{S_1(f)}\right), \quad (2.80)$$

where  $S_i(f)$  is the spectrum of the considered particle velocity component,  $V_x$  for longitudinal wave and  $V_y$  for transverse wave, and  $x_i$  the position of the  $i^{\text{th}}$  receiver. A comparison the attenuation parameter evolution as a function of frequency, calculated with Eq. (2.80), and the expected value of the thermoviscous model given by Eq. (2.76), is shown on Fig. 2.13(b) for the longitudinal wave. Excellent agreement is found, validating the implementation of thermoviscous attenuation in the DG-FEM scheme. Similar results have been obtained for the transverse wave, as shown on Fig. 2.13(d).

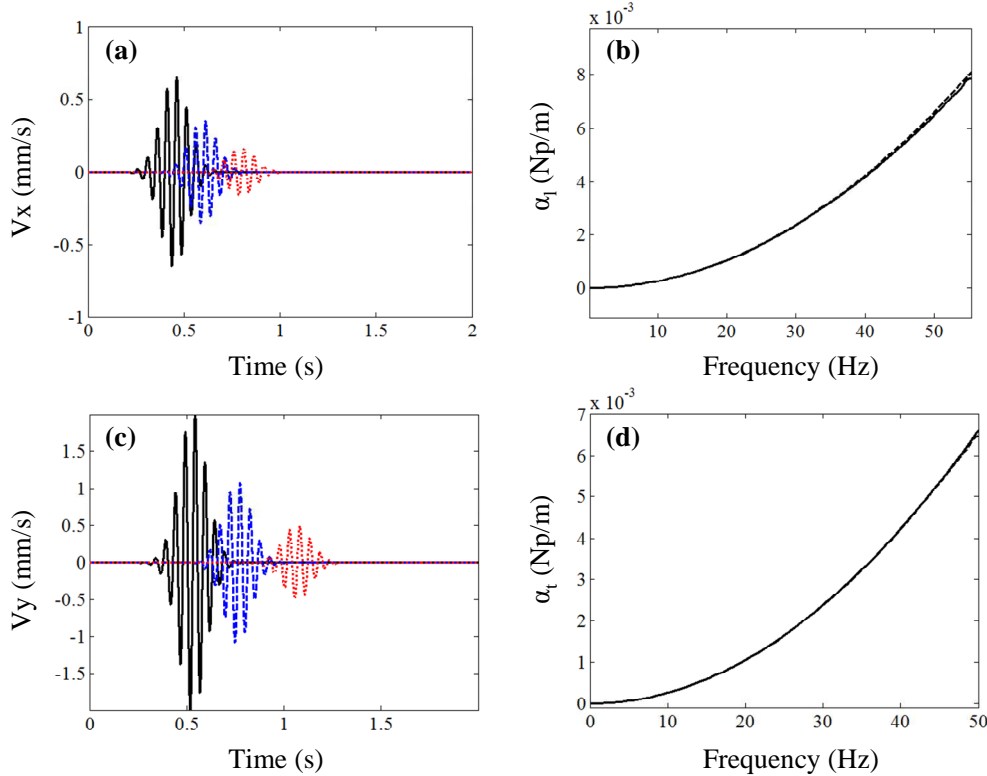


**Fig. 2.13** (a) Horizontal and (c) vertical particle velocities of the attenuated elastic plane wave at the receiver  $R_1$  (dark solid line),  $R_2$  (blue dashed line), and  $R_3$  (red dotted line). (b) Comparison of the frequency dependence of the longitudinal attenuation parameter  $\alpha_l$  (Np/m) obtained by numerical simulation (solid line) and desired (dashed line). (d) Comparison of the frequency dependence of the transverse attenuation parameter  $\alpha_t$  (Np/m) obtained by numerical simulation (solid line) and desired (dashed line).

## 2.5.4 Simulation of Wave Propagation in “Classical” Nonlinear Elastodynamic Material

The simulations with the DG-FEM scheme for isotropic Lamb’s problem and anisotropic apatite media have been presented in the preceding subsections, demonstrating the good performance of the DG-FEM method for linear elastic wave propagation in solids. In this subsection, the simulation of nonlinear elastic elastodynamic material with DG-FEM scheme will be presented.

Up to now, only a few studies have been devoted to the 2D or 3D numerical simulation of elastic wave propagation in nonlinear media. Kosik used the FDTD method to calculate nonlinear spherical wave propagation. An extension of this method with flux-corrected transport technique have been proposed to deal with steep gradients and shocks or reduce unphysical oscillations appearing during the calculations due to the introduction of nonlinearity in Ref. [218]. The FDTD method has also been used for the simulation of propagation of waves in pre-stressed materials [42]. Due to its efficiency in solving large scale problem a PS has been developed for active [22] or nonlinear hysteretic media [207], [208], [209]. During the AERONEWS European Strep 6 project, several numerical methods, FDTD [193], [186], [194], Local Interaction Simulation Approach (LISA) [77], [162], [53], [163], [78], PS [23], [24], [79], [80], FEM [219], [220], and mesh-free FEM Galerkin [8], have been used to simulate hysteretic nonlinear elastic wave propagation in 2D and 3D, mainly using the PM-space formalism.

### 2.5.4.1 Nonlinear Elastic Stress Tensor

For nonlinear elastodynamic solid media, the stress tensor  $P_{ij}$  in Eq. (2.1) can be expressed as follows:

$$P_{ij} = (C_{ijkl} + \frac{1}{2} M_{ijklmn} \frac{\partial u_m}{\partial x_n}) \frac{\partial u_k}{\partial x_l}, \quad (2.81)$$

where  $x_n$  is the  $n$ -th component of the position vector,  $u_m$  is the  $m$ -th component of displacements,  $C_{ijkl}$  and  $M_{ijklmn}$  ( $i, j, k, l, m, n = 1, 2, 3$ ) are the components of the fourth-rank or second-order elastic (SOE) linear tensor and nonlinear elastic tensor,  $M_{ijklmn}$  can be expressed as:

$$M_{ijklmn} = C_{ijklmn}^{(NLphysical)} + C_{ijklmn}^{(NLgeometrical)}, \quad (2.82)$$

with

$$C_{ijklmn}^{(NLphysical)} = C_{ijklmn} \quad \text{and} \quad C_{ijklmn}^{(NLgeometrical)} = C_{ijlm} \delta_{kn} + C_{ilmn} \delta_{jk} + C_{iklm} \delta_{jn}, \quad (2.83)$$

where  $\delta$  is the Kronecker delta symbol, and  $C_{ijklmn}$  the sixth-rank or third-order elastic (TOE) nonlinear tensor. There are two types of nonlinearity represented in Eq. (2.81), one is called

geometrical nonlinearity which is expressed by  $C_{ijklmn}^{(NLgeometrical)}$ , and accounts for the nonlinear relationship between strain and displacement when finite deformations are taken into account. The other type of nonlinearity,  $C_{ijklmn}^{(NLphysical)}$ , is “physical”, and corresponds to a nonlinear stress-strain relationship of the medium. The Voigt notation will be used for simplicity. For example,  $C_{1122}$  and  $C_{112222}$  can be simply replaced by  $C_{12}$  and  $C_{126}$ , respectively.

For 2D nonlinear transversely isotropic medium, the constitutive stress tensor Eq. (2.81) is given by:

$$\begin{bmatrix} P_{11} \\ P_{22} \\ P_{12} \\ P_{21} \end{bmatrix} = \begin{bmatrix} C_{11}^e & C_{12}^e & C_{13}^e & C_{14}^e \\ C_{21}^e & C_{22}^e & C_{23}^e & C_{24}^e \\ C_{31}^e & C_{32}^e & C_{33}^e & C_{34}^e \\ C_{41}^e & C_{42}^e & C_{43}^e & C_{44}^e \end{bmatrix} \begin{bmatrix} F_{11} \\ F_{22} \\ F_{12} \\ F_{21} \end{bmatrix}, \quad (2.84)$$

where  $F_{ij}$  are the strains (displacement gradient) and  $C_{ij}^e$  are the effective nonlinear elastic tensor which include the SOE linear tensor  $C_{ijkl}$  and TOE nonlinear tensor, and  $C_{ijklmn}^{(NLgeometrical)}$ . According to Ref. [218] they can be expressed as:

$$C_{11}^e = C_{11} + (C_{111} + 3C_{11})F_{11} + (C_{112} + C_{12})F_{22}, \quad (2.85)$$

$$C_{12}^e = C_{12} + (C_{112} + C_{66})F_{11} + (C_{122} + C_{12})F_{22}, \quad (2.86)$$

$$C_{13}^e = (C_{166} + C_{66} + 2C_{12})F_{21} + (C_{166} + C_{66})F_{12}, \quad (2.87)$$

$$C_{14}^e = (C_{166} + C_{66})F_{21} + (C_{166} + C_{11})F_{12}, \quad (2.88)$$

$$C_{21}^e = C_{12} + (C_{112} + C_{12})F_{11} + (C_{122} + C_{66})F_{22}, \quad (2.89)$$

$$C_{22}^e = C_{22} + (C_{122} + C_{12})F_{11} + (C_{222} + 3C_{22})F_{22}, \quad (2.90)$$

$$C_{23}^e = (C_{266} + C_{22})F_{21} + (C_{266} + C_{66})F_{12}, \quad (2.91)$$

$$C_{24}^e = (C_{266} + C_{66})F_{21} + (C_{266} + C_{66} + 2C_{12})F_{12}. \quad (2.92)$$

$$C_{31}^e = (C_{166} + C_{66})F_{21} + (C_{166} + C_{11})F_{12}, \quad (2.93)$$

$$C_{32}^e = (C_{266} + C_{66})F_{21} + (C_{266} + 3C_{66})F_{12}, \quad (2.94)$$

$$C_{33}^e = C_{66} + (C_{166} + C_{66})F_{11} + (C_{266} + C_{12})F_{22}, \quad (2.95)$$

$$C_{34}^e = C_{66} + (C_{166} + C_{11})F_{11} + (C_{266} + C_{12} + 2C_{66})F_{22}, \quad (2.96)$$

$$C_{41}^e = (C_{166} + 3C_{66})F_{21} + (C_{166} + C_{66})F_{12}, \quad (2.97)$$

$$C_{42}^e = (C_{266} + C_{22})F_{21} + (C_{266} + C_{66})F_{12}, \quad (2.98)$$

$$C_{43}^e = C_{66} + (C_{166} + 2C_{66} + C_{12})F_{11} + (C_{266} + C_{22})F_{22}, \quad (2.99)$$

$$C_{44}^e = C_{66} + (C_{166} + C_{12})F_{11} + (C_{266} + C_{66})F_{22}, \quad (2.100)$$

These effective elastic nonlinear coefficients, which depend on strains, will be used in the following numerical simulation.

### 2.5.4.2 Simulation of Nonlinear Elastic Plane Wave Propagation

First, a validation of the nonlinear elastic wave DG-FEM scheme will be presented. As only a few analytical results are available in the case of nonlinear elastic waves, we consider plane wave propagation in the  $x$  direction in a nonlinear elastodynamic medium, in which the stress and strain relationships are explicitly given by [209]:

$$P_{11} = C_{11}F_{11} + \beta C_{11}F_{11}^2 + 4\gamma C_{11}F_{21}^2, \quad (2.101)$$

$$P_{12} = (2C_{66} + 4\gamma C_{11}F_{11})F_{21}. \quad (2.102)$$

Here  $C_{11} = \lambda + 2\mu$ ,  $C_{66} = \mu$  and  $C_{12} = \lambda$  where  $\lambda$  and  $\mu$  are the Lamé constants, and  $\beta = C_{111}/C_{11}$  and  $\gamma = C_{166}/C_{11}$  are two nonlinear parameters.

The numerical simulation is identical to the one used for the validation of the attenuation implementation. The nonlinear parameters  $\beta$  and  $\gamma$  are equal to 5000 and 4000, respectively. A snapshot of the particle velocity component of the wave field at  $t = 0.48$  s is plotted on Fig. 2.14. This figure shows the plane character of the propagating wave-front and the absorption by the NPML of left going wave generated by the source.

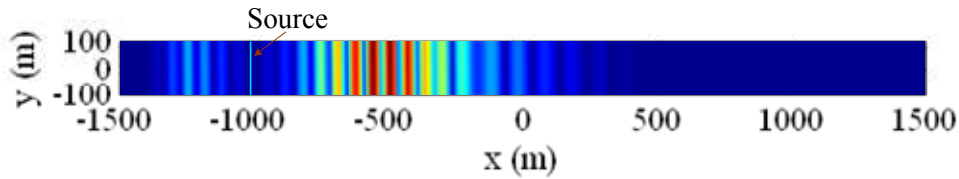


**Fig. 2.14** Velocity amplitude of the plane wave at  $t = 0.48$  s obtained with RK-DG-FEM O5 scheme using quadrilateral elements.

In Fig 2.15 we plot the horizontal and vertical particle velocities of the nonlinear elastic plane wave received at the second receiver  $R_2$ . Normally, without nonlinearity the  $x$  component contains only a compressional wave, while the  $y$  component contains only a shear wave. Because of the nonlinearity, the  $x$  component includes not only a wave with a compressional wave speed but also a wave with a shear wave speed, as shown on the upper right plot of Fig. 2.15. This is typical of nonlinear elastic wave propagation and indicates mode crossing [15]. In Fig 2.16, the spectra of the horizontal and vertical particle velocities received at the three different receivers are plotted. Since there is no attenuation, the amplitude of the spectral peak at the source frequency remains nearly unchanged with distance, as expected. However, for the harmonic waves (right spectra on Fig. 2.16), the evolution as a function of distance is more complex than the linear increase predicted for a plane wave in a fluid. All the obtained results are perfectly identical to the one presented in figure 2a and 2b of Ref. [209]. As their results have been successfully compared to an analytical prediction [123], this simulation validates our nonlinear implementation.

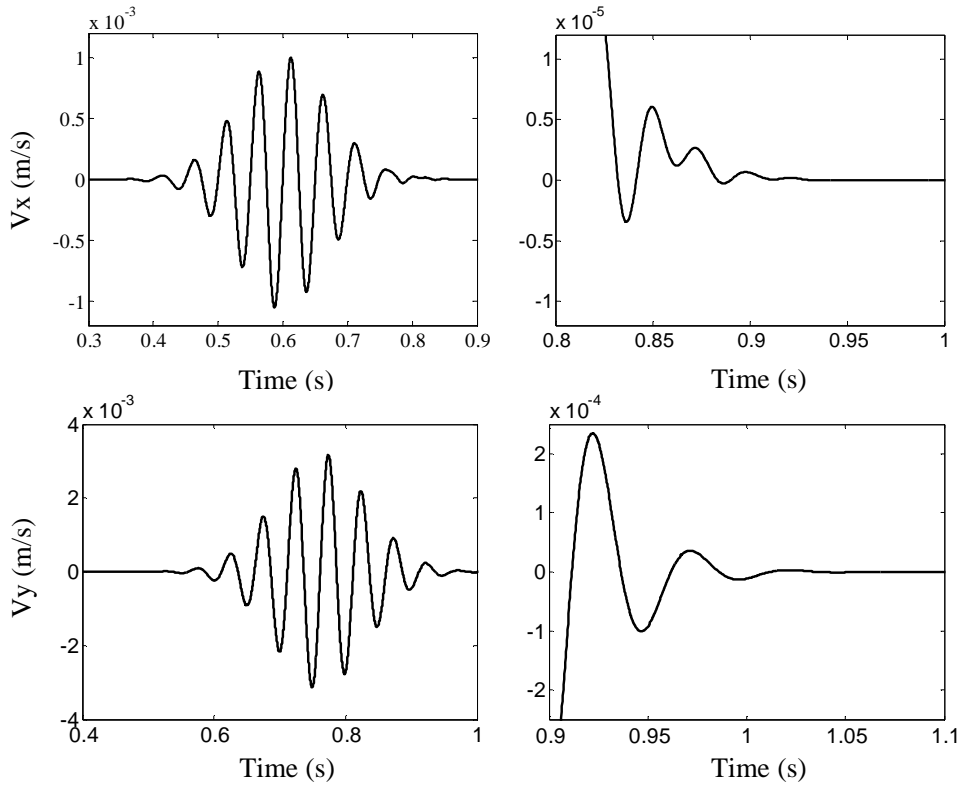


**Fig. 2.15** Horizontal (first line) and vertical (second line) particle velocities of the nonlinear elastic plane wave at the receiver  $R_2$ . The expanded scale on the right shows the mode crossing process induced by nonlinearity.

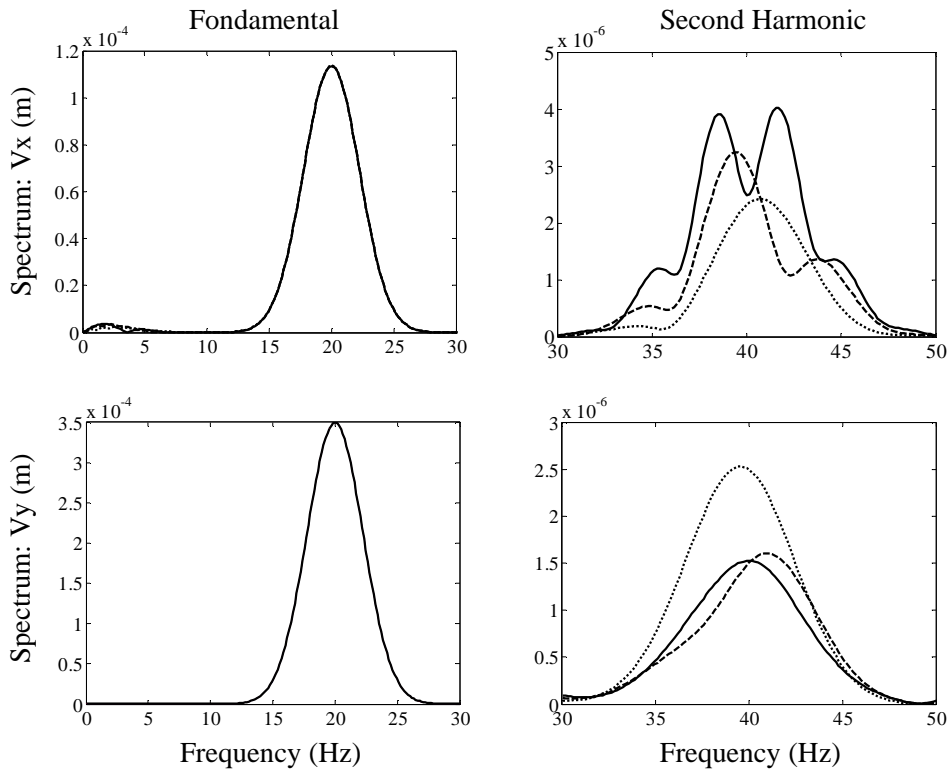


**Fig. 2.16** Spectra of the horizontal  $V_x$  (first line) and vertical  $V_y$  (second line) particle velocities of the numerical solutions of the propagation of an elastic plane wave at distances of 3 (dotted line), 6 (dashed line) and 10 (solid line) longitudinal wavelengths.

### 2.5.4.3 Nonlinear Pulse Propagation

In the following numerical experiments, a computational domain of  $1100 \times 1100$  m with the origin  $(0.0, 0.0)$  at the centre point is meshed with quadrilateral elements. The point source time function is a Richer wavelet expressed in Eq. (2.69), acting in the  $x$  and  $y$  directions, and located at the centre  $(0.0, 0.0)$  of the computational domain. The amplitude factor is 5000, the source delay time  $t_D = 0.02$  s and  $a_1 = -(2\pi f_c)^2$  with a peak frequency  $f_c = 30$  Hz. The receiver is located at the point  $(200, 0)$ .

The properties of the simulated solid media are represented by the following SOE and TOE constants:

- For the isotropic nonlinear medium (called BMIN):  $C_{11} = C_{22} = 28.5$  GPa,  $C_{12} = C_{66} = 9.5$  GPa,  $C_{111} = C_{222} = -780$  GPa,  $C_{112} = C_{122} = -180$  GPa and  $C_{166} = C_{266} = -150$  GPa;
- For the transversely isotropic nonlinear medium (called BMAIN):  $C_{11} = 28.5$  GPa,  $C_{12} = 6$  GPa,  $C_{22} = 30$  GPa,  $C_{66} = 9.5$  GPa,  $C_{111} = -780$  GPa,  $C_{222} = -850$  GPa,  $C_{112} = -16$  GPa,  $C_{122} = -90$  GPa,  $C_{166} = -108$  GPa,  $C_{266} = -154$  GPa.

The densities for both the isotropic and transversely isotropic nonlinear medium are given by  $\rho_0 = 2.75$  kg/m<sup>3</sup>.

First, a simulation for the isotropic nonlinear media was realized with a six order RK-DG-FEM scheme meshed with 3600 quadrilateral elements. In this simulation, the total calculation time was  $T = 0.18$  s. The Lax-Freidrich numerical flux and surface free boundary condition have also been used. Fig. 2.17 shows two snapshots of the velocity component of the wave field at  $t = 0.15$  s and  $t = 0.18$  s, respectively. From these snapshots we can see the form of wave-front curves in the BMIN isotropic nonlinear material. The corresponding received horizontal and vertical particle velocities are plotted in Fig. 2.18.

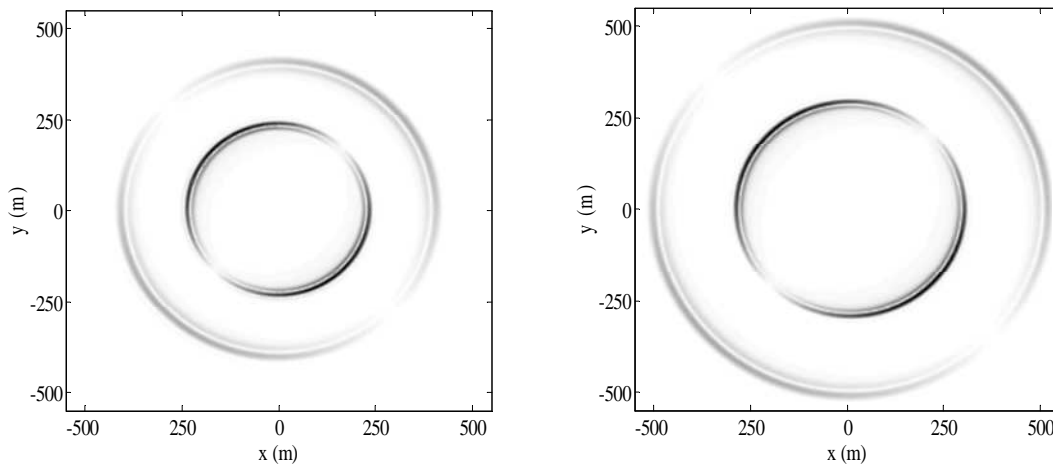


**Fig. 2.17** Amplitude of the particle velocity  $v$  at  $t = 0.15$  s (left) and  $t = 0.18$  s (right) calculated with a RK-DG-FEM O6 scheme using quadrilateral elements, for the isotropic nonlinear media.

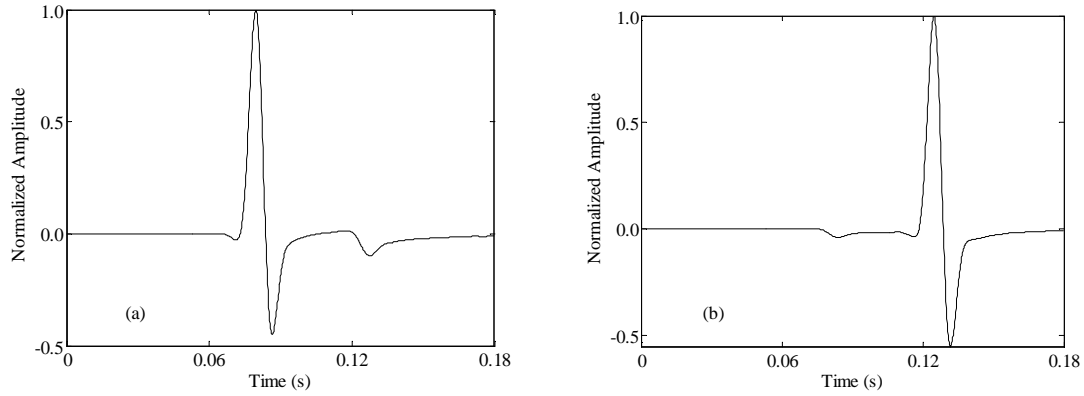


**Fig. 2.18** Received signals for (a) the horizontal particle velocity and (b) vertical particle velocity calculated with a six order RK-DG-FEM scheme for the isotropic nonlinear media.

A second simulation has been made with the same six order RK-DG-FEM scheme and the same number of quadrilateral elements, but this time, for transversely isotropic nonlinear medium. The snapshots of the velocity component of the wave field at  $t = 0.15$  s and  $t = 0.18$  s are plotted in the Fig. 2.19. From these snapshots we can see the form of wave-front curves in the BMAIN transversely isotropic nonlinear material. The corresponding received horizontal and vertical particle velocities are plotted in the Fig. 2.20.

The obtained results are in perfect accordance with the one obtained in Ref. [218] but without the need of using a flux-transport correction in order to limit spurious oscillation induced by nonlinear effects. Nevertheless, it can be noted that these examples show in fact only a very low level of nonlinearity as the sent wave is very short.

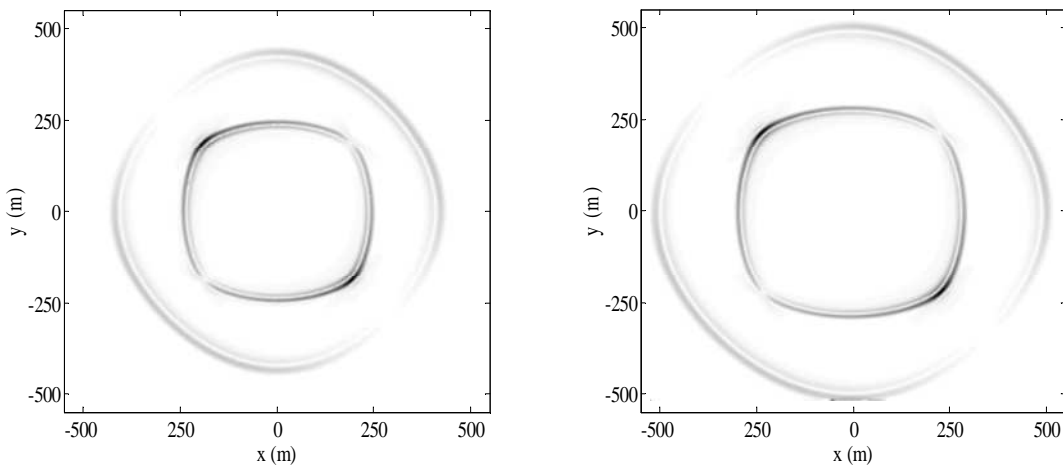


**Fig. 2.19** Amplitude of the particle velocity  $v$  at  $t = 0.15$  s (left) and  $t = 0.18$  s (right) calculated with a RK-DG-FEM O6 scheme using quadrilateral elements, for the transversely isotropic nonlinear media.

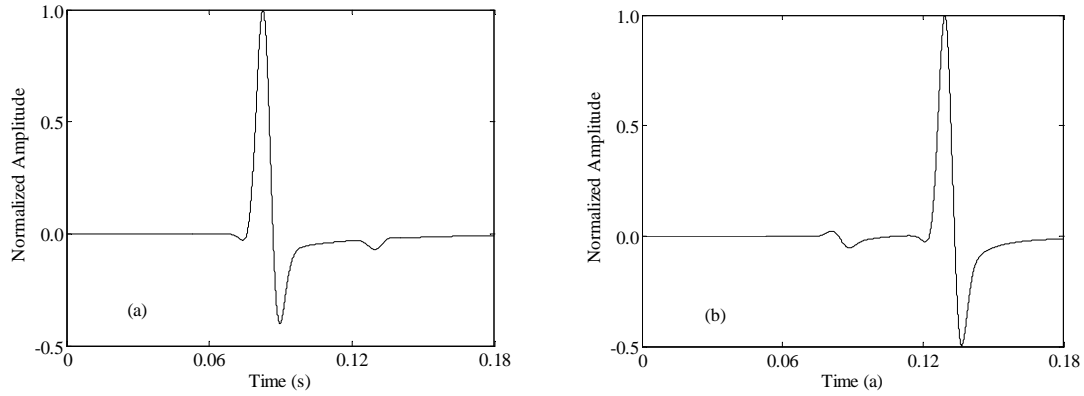


**Fig. 2.20** Received signals for (a) the horizontal particle velocity and (b) vertical particle velocity calculated with a six order RK-DG-FEM scheme for the transversely isotropic nonlinear media.

## 2.6 Conclusion

In this chapter, a nodal Discontinuous Galerkin Finite Element Method (DG-FEM) scheme, which is an intelligent combination of the FEM and FVM methods, has been presented. Two kinds of operators, based on triangular or quadrilateral mesh element, respectively, have been developed for the weak and strong form Discontinuous Galerkin formulations. Different numerical fluxes, as the central and Lax-Freidrich fluxes, have been used. Open boundary, surface-free boundary and fixed boundary conditions have also been discussed in this chapter. To realize time domain discretization the DG-FEM scheme, a fourth-order low storage explicit Runge-Kutta (LSERK) method has been used.

The results of simulations for isotropic Lamb's problem and elastic wave propagation in apatite, an anisotropic medium, have authorized a validation of the DG-FEM scheme, by comparison to known analytical solutions.

As only a few analytical results are available in the case of nonlinear elastic waves, a plane wave propagation has been considered. The obtained results compare perfectly to previously published numerical calculations and approximate analytical solutions.

The main contributions of the present PhD thesis to this numerical scheme was to extend it to nonlinear elasto-dynamic including source terms, and to introduce the possibility to use quadrilateral elements. Moreover a Perfectly Matched Layer (PML) type of absorbing boundary condition well adapted to the DG-FEM scheme, called Nearly Perfectly Matched Layer (NPML), was also developed. This point will be discussed in the next chapter. Finally, a sub-domain implementation was developed to increase the efficiency of the scheme when PML are used. It will also enable to easily implement, in the future, multiphysics problems.



# CHAPTER 3: PML ABSORBING BOUNDARY CONDITION

## 3.1 Introduction

Numerical solutions of Partial Differential Equations (PDE) for wave propagation require the truncation of an unbounded media to fit into computers with a limited memory and computation time. For such problems, an Absorbing Boundary Conditions (ABC) is needed at the truncated boundary to eliminate the reflections from this boundary to the computational domain. Many kinds of ABCs have been found, for example, the ABCs of Clayton and Engquist [45], Peng and Toksoz [144] and Mur [133], etc. These ABCs, although successful in many fields, provide only limited absorption to waves within a limited range of incidence angles and limited frequencies [171].

In 1994, an implementation of Perfectly Matched Layer (PML) media [16] has introduced by Berenger for electromagnetic waves. Since then, it has been proven to be one of the most robust and efficient technique for the termination of unbounded domain [74]. In addition to be useful for electromagnetism simulation [73], [206], it was demonstrated to be very efficient for acoustic [118,] [211] and elastic waves in isotropic [43], [88] and anisotropic solids [48]. It has been proven that theoretically, before discretization, at the interface between a computational medium and a perfectly matched medium no reflection occurs, and the incident waves from the computational medium are completely absorbed, regardless of their incidence angle and frequency [16], [43]. Nevertheless, this property is lost when a discretization is needed for numerical implementation, especially in the case of oblique incidence. One then needs to optimise the PML parameters in order to decrease parasitic reflections [111], [47].

Convolution Perfectly Matched Layer (C-PML), first presented in electromagnetism by Roden and Gedney [156], and applied in the simulation of elastic wave propagation [60], [61], [22], [107], has been shown to improve the behaviour of the discrete PML for grazing angles encountered in the case of surface waves. The main advantage of C-PML over the classical PML layer is that it is based on the un-split components of the wave field, and lead to a more stable scheme. Moreover, it is highly effective at absorbing signals of long time-signature [12], surface waves [107] or in elongated domains of calculation [61]. Classically, C-PML has been introduced in first-order formulation of both electromagnetism and elastodynamic. In this chapter, we propose first to extend the C-PML absorbing layer to the second-order system

describing elastic waves in displacement formulation in anisotropic solids, as it was done for classical split PML [106]. This second-order formulation will be described in frequency and time domains both for elastic solid [117] and piezoelectric medium [25], [116]. In frequency domain, this technique is easy to implement in commercial software based on Finite Element Method (FEM). The efficiency of this second-order perfectly matched layer is then demonstrated based upon 2D benchmarks both for isotropic and anisotropic solids, and for bulk and surface wave propagation. The simulations are realized with the commercially available software Comsol Multiphysics in frequency domain, and with a Pseudo-Spectral (PS) method in time domain.

Another kind of PML called the Nearly Perfectly Matched Layer (NPML) [49], [95] will be introduced. In electromagnetism, the domain in which this PML has been first developed, analytical and numerical results show that the NPML is equivalent to the standard PML in Cartesian coordinates and performs identically to them as an ABC while simpler implementation [49].

In some anisotropic media, numerical instabilities appear in the C-PML [10], limiting the use of this absorbing layer. In order to stabilize the absorbing layer, another PML has been proposed by Meza-Fajardo *et al.* [126] and referred to as the “Multiaxial Perfectly Matched Layer” (“MPML”). A study of the matching and stability properties of this last PML will be presented. A similar idea was previously proposed in the case of guided waves for frequencies where “inverse modes” with group and phase velocities of opposite signs are excited [25], where split field PML or C-PML don’t work satisfactorily. Examples of stabilized absorbing layers will also be presented for such guided waves case.

## 3.2 C-PML for Second-Order Elastodynamic Wave Equations

### 3.2.1 Wave Equations for Anisotropic Solid in 2D

Consider the propagation of 2D plane strain elastic waves in an anisotropic elastic solid medium. With Einstein’s convention of summation, the equation of motion can be written:

$$\frac{\partial^2 u_i}{\partial t^2} = \frac{1}{\rho_0} \frac{\partial \tau_{ij}}{\partial x_j}, \quad (3.1)$$

where  $i, j = 1, 2$ ,  $\rho_0$  is the density,  $x_j$  are the components of the position vector,  $t$  is the time,  $u_i$  are the components of the particle displacement vector, and  $\tau_{ij}$  are the components of the stress tensor. For a linear elastic solid, the constitutive relation is given by the Hooke’s law:

$$\tau_{ij} = C_{ijkl} \epsilon_{kl}, \quad (3.2)$$

where  $C_{ijkl}$  are the elastic constants, and the linear approximation of the strain tensor  $\epsilon$  is:

$$\varepsilon_{kl} = \frac{1}{2} \left( \frac{\partial u_k}{\partial x_l} + \frac{\partial u_l}{\partial x_k} \right). \quad (3.3)$$

In the case of a transverse isotropic medium (the lowest symmetry which can be considered in 2D), the following second-order system of equation is obtained:

$$\frac{\partial^2 u_1}{\partial t^2} = \frac{1}{\rho_0} \left( \frac{\partial \tau_{11}}{\partial x} + \frac{\partial \tau_{12}}{\partial y} \right), \quad (3.4a)$$

$$\frac{\partial^2 u_2}{\partial t^2} = \frac{1}{\rho_0} \left( \frac{\partial \tau_{12}}{\partial x} + \frac{\partial \tau_{22}}{\partial y} \right), \quad (3.4b)$$

$$\tau_{11} = C_{11} \frac{\partial u_1}{\partial x} + C_{12} \frac{\partial u_2}{\partial y}, \quad (3.4c)$$

$$\tau_{22} = C_{12} \frac{\partial u_1}{\partial x} + C_{22} \frac{\partial u_2}{\partial y}, \quad (3.4d)$$

$$\tau_{12} = C_{66} \left( \frac{\partial u_1}{\partial y} + \frac{\partial u_2}{\partial x} \right). \quad (3.4e)$$

Here we have considered that  $x_1 = x$  and  $x_2 = y$ . This system will be used as the starting point in the remainder of the chapter when considering anisotropic solids.

### 3.2.2 C-PML Elastic Wave Equations in Frequency Domain

Here, the methodology used for the introduction of C-PML zones for axisymmetric active solid media [22], is used for the system of Eqs. (3.4). First, taking Fourier transform of the system, it is rewritten in the frequency domain. Then, the following complex coordinate's transformation [44] is used:

$$\tilde{x} = \int_0^x s_x(x') dx', \quad (3.5a)$$

$$\tilde{y} = \int_0^y s_y(y') dy', \quad (3.5b)$$

where  $s_x$  and  $s_y$  are the Complex Frequency Shifted (CFS) stretched-coordinate metrics proposed by Kuzuoglu and Mittra [109]:

$$s_x(x) = \kappa_x(x) + \frac{\sigma_x(x)}{\alpha_x(x) + j\omega}, \quad (3.6a)$$

$$s_y(y) = \kappa_y(y) + \frac{\sigma_y(y)}{\alpha_y(y) + j\omega}, \quad (3.6b)$$

where,  $\alpha_x$ ,  $\sigma_x$ ,  $\alpha_y$  and  $\sigma_y$  are assumed to be positive and real, and  $\kappa_x$  and  $\kappa_y$  are real and  $\geq 1$ . The  $\sigma_{x,y}$  and  $\kappa_{x,y}$  are the so-called [74] attenuation factor used for the attenuation of propagating

waves, and scaling factor used for the attenuation of evanescent waves, respectively. The choice of the optimum spatial variation of these variables has been discussed in the literature [178], [47]. Our choice will be described for each example in the numerical simulations parts of the chapter. The  $\alpha_{x,y}$  are frequency-dependent terms that implement a Butterworth-type filter in the layer. The original split PML, introduced for isotropic elastic waves propagation by Chew and Liu [43] and for anisotropic solid by Collino and Tsogka [48], is retrieved imposing  $\alpha_{x,y} = 0$  and  $\kappa_{x,y} = 1$ . Using the complex coordinate variables  $\tilde{x}$  and  $\tilde{y}$  to replace  $x$  and  $y$  in Eqs. (3.4), and noting that  $\partial/\partial\tilde{x} = (1/s_x)\partial/\partial x$  and  $\partial/\partial\tilde{y} = (1/s_y)\partial/\partial y$ , we obtain the following frequency-domain equations in Cartesian coordinates:

$$-\omega^2 \rho_0 \hat{u}_1 = \frac{1}{s_x} \frac{\partial \hat{\tau}_{11}}{\partial x} + \frac{1}{s_y} \frac{\partial \hat{\tau}_{12}}{\partial y}, \quad (3.7a)$$

$$-\omega^2 \rho_0 \hat{u}_2 = \frac{1}{s_x} \frac{\partial \hat{\tau}_{12}}{\partial x} + \frac{1}{s_y} \frac{\partial \hat{\tau}_{22}}{\partial y}, \quad (3.7b)$$

$$\hat{\tau}_{11} = C_{11} \frac{1}{s_x} \frac{\partial \hat{u}_1}{\partial x} + C_{12} \frac{1}{s_y} \frac{\partial \hat{u}_2}{\partial y}, \quad (3.7c)$$

$$\hat{\tau}_{22} = C_{12} \frac{1}{s_x} \frac{\partial \hat{u}_1}{\partial x} + C_{22} \frac{1}{s_y} \frac{\partial \hat{u}_2}{\partial y}, \quad (3.7d)$$

$$\hat{\tau}_{12} = C_{66} \left( \frac{1}{s_y} \frac{\partial \hat{u}_1}{\partial y} + \frac{1}{s_x} \frac{\partial \hat{u}_2}{\partial x} \right), \quad (3.7e)$$

where  $\hat{u}$  represents the Fourier transform of the variable  $u$ .

### 3.2.3 Interpretation of C-PML as an Anisotropic Solid Medium

In order to implement these C-PML in a commercial FEM software (COMSOL Multiphysics), the resulting second-order C-PML wave equations are interpreted as an anisotropic medium, as it has already been done for PML [217]. Multiplying Eqs. (3.7) by  $s_x s_y$  and introducing new stress tensor  $\hat{\tau}'_{ij}$  and density  $\rho'_0$  (given by  $\rho_0 s_x s_y$ ), we get the following equations:

$$-\omega^2 \rho'_0 \hat{u}_1 = \frac{\partial \hat{\tau}'_{11}}{\partial x} + \frac{\partial \hat{\tau}'_{12}}{\partial y}, \quad (3.8a)$$

$$-\omega^2 \rho'_0 \hat{u}_2 = \frac{\partial \hat{\tau}'_{21}}{\partial x} + \frac{\partial \hat{\tau}'_{22}}{\partial y}, \quad (3.8b)$$

$$\hat{\tau}'_{11} = \hat{\tau}_{11} s_y = C_{11} \frac{s_y}{s_x} \frac{\partial \hat{u}_1}{\partial x} + C_{12} \frac{\partial \hat{u}_2}{\partial y}, \quad (3.8d)$$

$$\hat{\tau}'_{22} = \hat{\tau}_{22} s_x = C_{12} \frac{\partial \hat{u}_1}{\partial x} + C_{22} \frac{s_x}{s_y} \frac{\partial \hat{u}_2}{\partial y}, \quad (3.8e)$$

$$\hat{\tau}'_{12} = \hat{\tau}_{12} s_x = C_{66} \left( \frac{s_x}{s_y} \frac{\partial \hat{u}_1}{\partial y} + \frac{\partial \hat{u}_2}{\partial x} \right), \quad (3.8f)$$

$$\hat{\tau}'_{21} = \hat{\tau}_{12} s_y = C_{66} \left( \frac{\partial \hat{u}_1}{\partial y} + \frac{s_y}{s_x} \frac{\partial \hat{u}_2}{\partial x} \right). \quad (3.8g)$$

This system of equation corresponds to the propagation of elastic waves in a “fictious” anisotropic medium and can be written in the matrix form as:

$$\begin{bmatrix} \hat{\tau}'_{11} \\ \hat{\tau}'_{22} \\ \hat{\tau}'_{12} \\ \hat{\tau}'_{21} \end{bmatrix} = \begin{bmatrix} C'_{11} & C_{12} & 0 & 0 \\ C_{12} & C'_{22} & 0 & 0 \\ 0 & 0 & C'_{66} & C_{66} \\ 0 & 0 & C_{66} & C''_{66} \end{bmatrix} \begin{bmatrix} \hat{u}_{1x} \\ \hat{u}_{2y} \\ \hat{u}_{1y} \\ \hat{u}_{2x} \end{bmatrix}, \quad (3.9)$$

with  $\hat{u}_{1x} = \partial \hat{u}_1 / \partial x$ ,  $\hat{u}_{2y} = \partial \hat{u}_2 / \partial y$ ,  $\hat{u}_{1y} = \partial \hat{u}_1 / \partial y$  and  $\hat{u}_{2x} = \partial \hat{u}_2 / \partial x$ , the new effective elastic stiffness constants are  $C'_{11} = C_{11} s_y / s_x$ ,  $C'_{22} = C_{22} s_x / s_y$ ,  $C''_{66} = C_{66} s_y / s_x$  and  $C'_{66} = C_{66} s_x / s_y$ . It should be noted that this fictious anisotropic medium have a non symmetric stress tensor ( $\hat{\tau}'_{ij} \neq \hat{\tau}'_{ji}$  when  $i \neq j$ ), and the complex-valued tensor of elastic constants conserves minor symmetry properties, but not the major one.

We can easily extend this description of C-PML in anisotropic solid to 3D. In this case, the general form of the propagation of elastic waves can be described as:

$$-\omega^2 \rho'_0 \hat{u}_i = \frac{\partial \hat{\tau}'_{ij}}{\partial x_j}, \quad (3.10a)$$

$$\hat{\tau}'_{ij} = C'_{ijkl} \frac{\partial \hat{u}_l}{\partial x_k}, \quad (3.10b)$$

where  $i, j, k, l = 1, 2$  or  $3$ . The effective elastic tensor  $C'$  and the density  $\rho'_0$  are given by:

$$C'_{ijkl} = C_{ijkl} \frac{s_x s_y s_z}{s_i s_k}, \quad (3.11a)$$

$$\rho'_0 = \rho_0 s_x s_y s_z. \quad (3.11b)$$

The effective constants already obtained for 2D situation can be easily derived from Eq. (3.11) by considering  $s_z = 1$  and  $i, j, k, l = 1$  or  $2$ . Moreover, this “fictious” anisotropic interpretation of C-PML or PML can be extended to piezoelectric solids [25], [7], [122].

### 3.2.4 C-PML Elastic Wave Equations in Time Domain

Now, to be able to obtain a C-PML formulation in time domain, the resulting equations are transformed back to time domain by inverse Fourier transform. Due to the frequency dependence of the CFS stretched-coordinate metrics, a convolution appears in the resulting equations, as shown for example for Eq. (3.7a):

$$\frac{\partial^2 u_1}{\partial t^2} = \frac{1}{\rho_0} \left[ F^{-1} \left[ \frac{1}{s_x} \right] \otimes \frac{\partial \tau_{11}}{\partial x} + F^{-1} \left[ \frac{1}{s_y} \right] \otimes \frac{\partial \tau_{12}}{\partial y} \right], \quad (3.12)$$

where  $\otimes$  and  $F^{-1}[\cdot]$  are respectively the convolution and inverse Fourier transform operators. In order to eliminate the convolutions appearing in Eq. (3.12), we use the methodology introduced by Roden and Gedney [156] in electromagnetism, and extended by Bou Matar *et al.* [22] for elastic wave propagation in active (or nonlinear) media, by introducing memory variables. The time evolution of each of these memory variables is realized by a first order differential equation. The obtained result can be rewritten as:

$$\frac{\partial^2 u_1}{\partial t^2} = \frac{1}{\rho_0} \left( \frac{1}{\kappa_x} \frac{\partial \tau_{11}}{\partial x} + \frac{1}{\kappa_y} \frac{\partial \tau_{12}}{\partial y} + \frac{A_x}{\kappa_x} + \frac{B_y}{\kappa_y} \right), \quad (3.13a)$$

where the memory variables  $A_x$  and  $B_y$  are given by:

$$\frac{\partial A_x}{\partial t} = -\delta_x \frac{\partial \tau_{11}}{\partial x} - \beta_x A_x, \quad (3.13b)$$

$$\frac{\partial B_y}{\partial t} = -\delta_y \frac{\partial \tau_{12}}{\partial y} - \beta_y B_y, \quad (3.13c)$$

with  $\delta_{x,y} = \sigma_{x,y}/k_{x,y}$ ,  $\beta_{x,y} = \sigma_{x,y}/k_{x,y} + \alpha_{x,y}$ . Making the same calculation for Eqs. (3.7b)-(3.7e), we obtain the following system equations of C-PML in time domain for elastic wave propagation in anisotropic solid:

$$\frac{\partial^2 u_1}{\partial t^2} = \frac{1}{\rho_0} \left( \frac{1}{\kappa_x} \frac{\partial \tau_{11}}{\partial x} + \frac{1}{\kappa_y} \frac{\partial \tau_{12}}{\partial y} + \frac{A_x}{\kappa_x} + \frac{B_y}{\kappa_y} \right), \quad (3.14a)$$

$$\frac{\partial^2 u_2}{\partial t^2} = \frac{1}{\rho_0} \left( \frac{1}{\kappa_x} \frac{\partial \tau_{12}}{\partial x} + \frac{1}{\kappa_y} \frac{\partial \tau_{22}}{\partial y} + \frac{C_x}{\kappa_x} + \frac{D_y}{\kappa_y} \right), \quad (3.14b)$$

$$\tau_{11} = \frac{C_{11}}{\kappa_x} \frac{\partial u_1}{\partial x} + \frac{C_{12}}{\kappa_y} \frac{\partial u_2}{\partial y} + \frac{C_{11}}{\kappa_x} E_x + \frac{C_{12}}{\kappa_y} F_y, \quad (3.14c)$$

$$\tau_{22} = \frac{C_{12}}{\kappa_x} \frac{\partial u_1}{\partial x} + \frac{C_{22}}{\kappa_y} \frac{\partial u_2}{\partial y} + \frac{C_{12}}{\kappa_x} E_x + \frac{C_{22}}{\kappa_y} F_y, \quad (3.14d)$$

$$\tau_{12} = \frac{C_{66}}{\kappa_x} \frac{\partial u_2}{\partial x} + \frac{C_{66}}{\kappa_y} \frac{\partial u_1}{\partial y} + \frac{C_{66}}{\kappa_x} G_x + \frac{C_{66}}{\kappa_y} H_y, \quad (3.14e)$$

where the memory variables  $A_x$ ,  $B_y$ ,  $C_x$ ,  $D_y$ ,  $E_x$ ,  $F_y$ ,  $G_x$ , and  $H_y$  are obtained by a first order differential equations of the form (Appendix B):

$$\frac{\partial A_x}{\partial t} = -\delta_x \frac{\partial \tau_{11}}{\partial x} - \beta_x A_x, \quad (3.15)$$

The memory variables will be zero outside the C-PML zones, so the first order differential equations of memory variables need only to be solved in a small part of the calculation domain. After introduction of Eqs. (3.14c)-(3.14e) into Eqs. (3.14a)-(3.14b), the resulting system of wave equations can be written as:

$$\rho_0 \frac{\partial^2 u_1}{\partial t^2} - \left( \frac{\partial}{\partial x} \left( C_{11} \frac{\partial u_1}{\partial x} + C_{12} \frac{\partial u_2}{\partial y} \right) + \frac{\partial}{\partial y} \left( C_{66} \frac{\partial u_2}{\partial x} + C_{66} \frac{\partial u_1}{\partial y} \right) \right) = f_1, \quad (3.16a)$$

$$\rho_0 \frac{\partial^2 u_2}{\partial t^2} - \left( \frac{\partial}{\partial x} \left( C_{66} \frac{\partial u_2}{\partial x} + C_{66} \frac{\partial u_1}{\partial y} \right) + \frac{\partial}{\partial y} \left( C_{12} \frac{\partial u_1}{\partial x} + C_{22} \frac{\partial u_2}{\partial y} \right) \right) = f_2, \quad (3.16b)$$

where  $f_1$  and  $f_2$  are:

$$f_1 = \left( \begin{array}{l} -\frac{\kappa'_x}{\kappa_x} \frac{\partial}{\partial x} \left( \frac{C_{11}}{\kappa_x} \frac{\partial u_1}{\partial x} + \frac{C_{12}}{\kappa_y} \frac{\partial u_2}{\partial y} + \frac{C_{11}}{\kappa_x} E_x + \frac{C_{12}}{\kappa_y} F_y \right) \\ -\frac{\kappa'_y}{\kappa_y} \frac{\partial}{\partial y} \left( \frac{C_{66}}{\kappa_x} \frac{\partial u_2}{\partial x} + \frac{C_{66}}{\kappa_y} \frac{\partial u_1}{\partial y} + \frac{C_{66}}{\kappa_x} G_x + \frac{C_{66}}{\kappa_y} H_y \right) \\ -\frac{\partial}{\partial x} \left( \frac{\kappa'_x C_{11}}{\kappa_x} \frac{\partial u_1}{\partial x} + \frac{\kappa'_y C_{12}}{\kappa_y} \frac{\partial u_2}{\partial y} - \frac{C_{11}}{\kappa_x} E_x - \frac{C_{12}}{\kappa_y} F_y \right) \\ -\frac{\partial}{\partial y} \left( \frac{\kappa'_x C_{66}}{\kappa_x} \frac{\partial u_2}{\partial x} + \frac{\kappa'_y C_{66}}{\kappa_y} \frac{\partial u_1}{\partial y} - \frac{C_{66}}{\kappa_x} G_x - \frac{C_{66}}{\kappa_y} H_y \right) + \frac{A_x}{\kappa_x} + \frac{B_y}{\kappa_y} \end{array} \right), \quad (3.16c)$$

$$f_2 = \left( \begin{array}{l} -\frac{\kappa'_x}{\kappa_x} \frac{\partial}{\partial x} \left( \frac{C_{66}}{\kappa_x} \frac{\partial u_2}{\partial x} + \frac{C_{66}}{\kappa_y} \frac{\partial u_1}{\partial y} + \frac{C_{66}}{\kappa_x} G_x + \frac{C_{66}}{\kappa_y} H_y \right) \\ -\frac{\kappa'_y}{\kappa_y} \frac{\partial}{\partial y} \left( \frac{C_{12}}{\kappa_x} \frac{\partial u_1}{\partial x} + \frac{C_{22}}{\kappa_y} \frac{\partial u_2}{\partial y} + \frac{C_{12}}{\kappa_x} E_x + \frac{C_{22}}{\kappa_y} F_y \right) \\ -\frac{\partial}{\partial x} \left( \frac{\kappa'_x C_{66}}{\kappa_x} \frac{\partial u_2}{\partial x} + \frac{\kappa'_y C_{66}}{\kappa_y} \frac{\partial u_1}{\partial y} - \frac{C_{66}}{\kappa_x} G_x - \frac{C_{66}}{\kappa_y} H_y \right) \\ -\frac{\partial}{\partial y} \left( \frac{\kappa'_x C_{12}}{\kappa_x} \frac{\partial u_1}{\partial x} + \frac{\kappa'_y C_{22}}{\kappa_y} \frac{\partial u_2}{\partial y} - \frac{C_{12}}{\kappa_x} E_x - \frac{C_{22}}{\kappa_y} F_y \right) + \frac{C_x}{\kappa_x} + \frac{D_y}{\kappa_y} \end{array} \right), \quad (3.16d)$$

where we have introduced the notation  $\kappa'_{x,y} = \kappa_{x,y} - 1$ . This results shows that the C-PML zone can be interpreted as the same anisotropic medium as the one in the calculation domain, but in which volumetric sources ( $f_1$  and  $f_2$ ) are present.

It is important to note that in time domain the number of equations needed to be solved increases in the C-PML zones. This can considerably increase the burden of calculation. Nevertheless, when active (or nonlinear) media are considered, then time domain formulations are needed [22], and Eqs. (3.16) have to be used.

### 3.2.5 Numerical Simulations

In this section, the excellent absorbing behaviours of both formulations (frequency and time domains) are demonstrated. The frequency domain formulation has been implemented in

a commercial FEM software (COMSOL Multiphysics), and a PS code has been developed for the time domain formulation. The choice of these numerical schemes has been motivated by the compromise in obtaining both efficient and accurate methods for the two different formulations. Here, the DG-FEM scheme has not been used because as explained later the C-PML, even in first order formulation, is not well adapted to this scheme.

### 3.2.5.1 Elastic Wave Propagation in an Unbounded Isotropic Solid

The numerical simulation presented in this subsection was made for the elastic wave propagation in an unbounded isotropic medium. The scale of computational domain and the C-PML layer are given in Fig. 3.1. The simulation has been performed over a  $80 \times 80$  grid, which was surrounded by a C-PML layer having a thickness of  $d = 10$  cells, with  $\Delta x = \Delta y = 0.6$  mm.

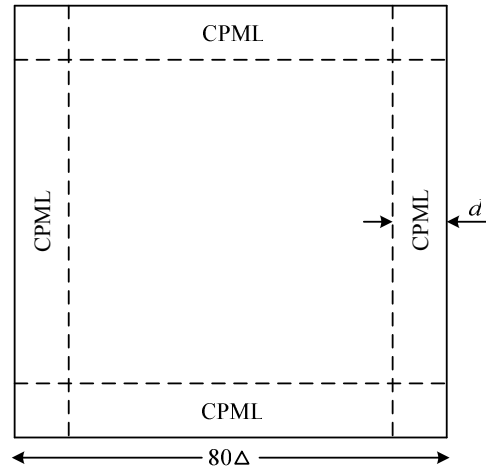


**Fig. 3.1** 2D physical domain  $48 \times 48$  mm surrounded by a  $10\Delta$  C-PML layer.

The parameters for the simulation were as follows: the density is  $\rho_0 = 2500 \text{ kg/m}^3$ , the elastic constants are  $C_{11} = 85 \text{ GPa}$ ,  $C_{12} = 25 \text{ GPa}$ ,  $C_{22} = 85 \text{ GPa}$ ,  $C_{66} = 30 \text{ GPa}$ . A 2D point source with a  $0.5 \text{ mm}$  diameter was set up at the point  $(0, 0)$  with a time function given by Ricker wavelet expressed as:

$$s(t) = (0.5 + a_1(t - t_D)^2) \cdot e^{a_1(t - t_D)^2}. \quad (3.17)$$

where  $t_D = 0.5 \mu\text{s}$  is the source delay time,  $a_1 = (\pi f_c)^2$ , and  $f_c = 1 \text{ MHz}$  is the central frequency.

In the stretched-coordinate metrics, the following spatial coordinates dependences are used for the parameters of the C-PML layers in the  $x$  direction:

$$\kappa_x = 1 + \kappa_{\max} \left( \frac{x - x_0}{d_x} \right)^{n_1}, \quad (3.18a)$$

$$\sigma_x = \sigma_{\max} \left( \frac{x - x_0}{d_x} \right)^{n_1 + n_2}, \quad (3.18b)$$

$$\alpha_x = \alpha_{\max} \left( \frac{d_x - x + x_0}{d_x} \right)^{n_3}, \quad (3.18c)$$

with  $\alpha_{\max} = 2\pi f_c$  and:

$$\sigma_{\max} = (1 + n_1 + n_2) \cdot \sqrt{C_{11}/\rho_0} \cdot \log(1/R_0)/(2d), \quad (3.18d)$$

where the  $R_0$  is the theoretical desired reflection coefficient and  $x_0$  and  $d$  are respectively the starting position and thickness of the C-PML layer.  $\kappa_y$ ,  $\sigma_y$  and  $\alpha_y$  have the same form as  $\kappa_x$ ,  $\sigma_x$  and  $\alpha_x$ , respectively, just replacing  $x$  by  $y$ . In the considered cases, as no evanescent waves are presents, we use  $\kappa_{\max} = 0$ . Moreover,  $\kappa_{x,y} = 1$  and  $\sigma_{x,y} = 0$  in the computational domain, outside the C-PML zone. In the presented results a C-PML thickness of ten grid elements around the boundaries,  $R_0 = 5 \times 10^{-5}$ ,  $n_1 = 3$ ,  $n_2 = 0$  and  $n_3 = 1$  have been chosen.

For characterizing the performance of the C-PML layer quantitatively, here, Eqs. (3.8) have been solved with COMSOL Multiphysics FEM software in frequency domain. Indeed, as demonstrated by Castaings *et al.* [37], very efficient simulations of linear pulse propagation in solids can be obtained with only a limited number of frequency calculations. The time evolution of the point source Eq. (3.17) is first Fourier transformed, and Eqs. (3.8) are then solved for forty frequencies equally spaced in the source spectrum. Then the inverse Fourier transform will be done within the Matlab software to get the result in time domain. The resulting snapshots are presented in Fig. 3.2 for four different times: 3.13  $\mu\text{s}$ , 4.10  $\mu\text{s}$ , 8.01  $\mu\text{s}$  and 11.92  $\mu\text{s}$ . They show that there is no visible reflection at the boundaries on a 50 dB dynamic range, and illuminate the effective absorbing ability of C-PML for the outgoing energy.

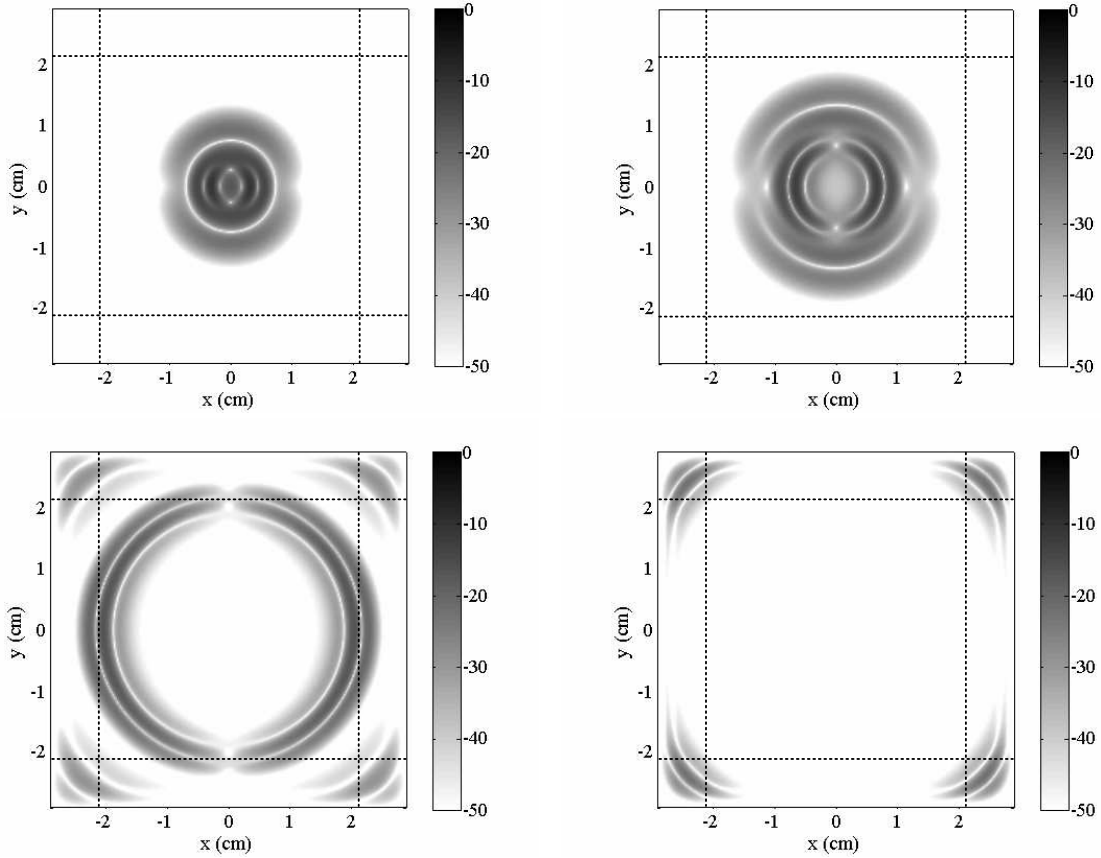


**Fig. 3.2** Propagation of elastic waves in an unbounded isotropic solid medium with a  $10\Delta$  C-PML layer. In the first row the times of the two figures are  $3.13 \mu\text{s}$  (left) and  $4.10 \mu\text{s}$  (right), and in the second row the times are  $8.01 \mu\text{s}$  (left) and  $11.92 \mu\text{s}$  (right). The displayed dynamic range is 50 dB.

### 3.2.5.2 Lamb's Problem Simulation

In order to further demonstrate the performance of the C-PML, here a classical test case (Lamb's Problem), which has been presented for DG-FEM in the subsection 2.5.1 of chapter 2, will be applied using a vertical force in a homogeneous elastic half-space with a free surface. The analytical solution can be obtained with the same FORTRAN code EX2DDIR, to make the comparison with the simulation results.

The same size of numerical model has been considered as in the subsection 2.5.1 of chapter 2. The calculation domain and C-PML layer are given in Fig. 3.3, with origin  $(0, 0)$  at the left upper corner and the width and height of left boundary are 4000 m and 2000 m, respectively, and the tilt angle of the free surface is  $\phi = 10^\circ$ . The directional point source, acting as a force perpendicular to this tilted surface, is located at the free surface  $(1720.00, -2303.28)$ . One receiver is located at  $(2670.33, -2470.85)$  and the distance from the source along the surface is 965 m. The same Ricker wavelet source, Eq. (3.17), has been used with the following parameters: delay time  $t_D = 0.32$  s, amplitude  $a_1 = (\pi f_c)^2$  and central frequency  $f_c = 3.625$  Hz. For the homogeneous elastic medium, the parameters of simulation are:

$\rho_0 = 2200 \text{ kg/m}^3$ , velocity of  $P$ -wave  $c_p = 3200 \text{ m/s}$  and velocity  $S$ -wave  $c_s = 1847.5 \text{ m/s}$ . The same spatial coordinates dependences Eqs. (3.18) are used for the C-PML parameters with now  $\alpha_{\max} = 5\pi f_c$ ,  $n_1 = 3$ ,  $n_2 = 0$ ,  $n_3 = 1$  and

$$\sigma_{\max} = (1 + n_1 + n_2) \cdot c_p \cdot \log(1/R_0)/(2d), \quad (3.19)$$

where  $R_0 = 10^{-5}$ .

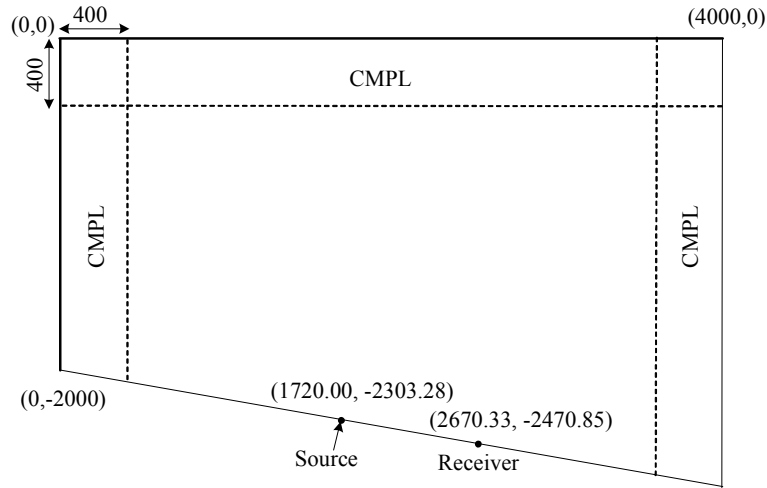


**Fig. 3.3** Computational domain and C-PML layer used for the Lamb's Problem.

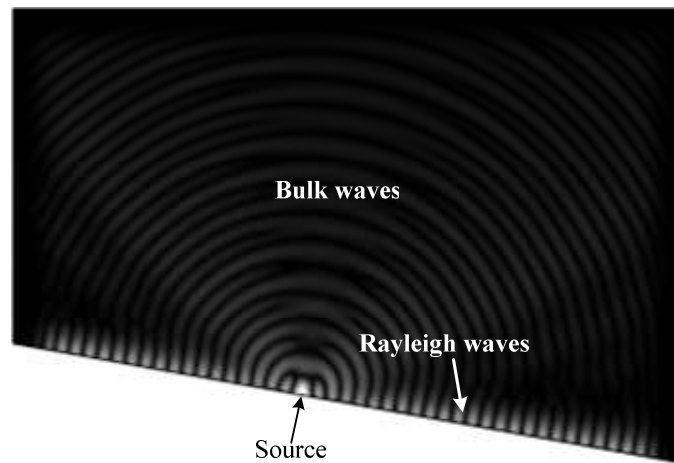


**Fig. 3.4** Bulk waves and Rayleigh waves propagating in the Lamb's Problem.

In this simulation, we solved Eqs. (3.8) again with COMSOL Multiphysics FEM software in frequency domain. After Fourier transform of the source function in frequency domain, Eqs. (3.8) is then solved for sixty frequencies equally spaced in the source spectrum. The result obtained at one frequency (10 Hz) is shown in Fig. 3.4, from which we can see the propagation of the Bulk waves in the computational domain and the Rayleigh waves on the free surface boundary. For testing the efficiency of C-PML layer, in Fig. 3.5 the time evolutions of the normal (a) and tangential displacement (b) components reconstructed by

inverse Fourier transform of the sixty frequency responses at the receiver, positioned at the free surface, in the case of both C-PML (dashed line) and PML (dotted line) layers for absorbing the surface wave, are displayed and compared to the analytical solution (solid line). We remind that the PML case corresponds to  $\alpha_{\max} = 0$ .

The obtained results clearly demonstrated the increase efficiency of the C-PML in comparison of the PML in order to absorb the Rayleigh wave. This is in perfect accordance with previous results obtained with the C-PML first-order velocity-stress formulation implementation [60], [61], [107].

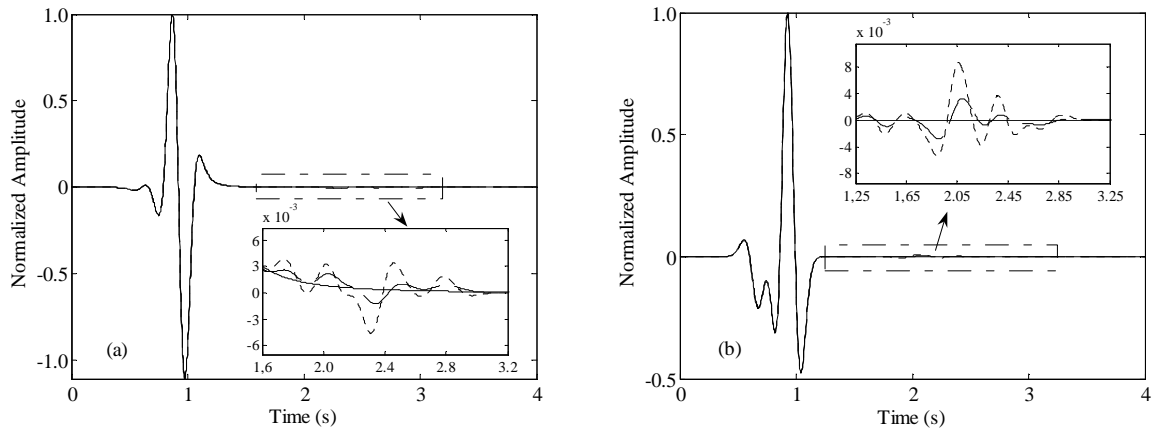


**Fig. 3.5** Comparison of C-PML results (dashed lines) with analytical solution (solid line) and PML results (dotted line) of Lamb's problem, (a) The normal displacement component, and (b) the tangential displacement component.

### 3.2.5.3 Efficiency of C-PML for Elongated Domain of Simulation

In order to demonstrate the improvement induced by the use of C-PML, instead of classical PML, numerical simulations of elastic wave propagation in an elongated half space of homogeneous isotropic medium, similar to the ones proposed by Drossaert *et al.* [60], are presented. The sketch of the used elongated calculation domain (3750 m wide and 375 m height, including the C-PML layers and corresponding to  $200 \times 20$  grid elements) is given in Fig. 3.6, where the origin (0, 0) is at the left upper corner. The properties of the elastic medium have been chosen as follows:  $\rho_0 = 2000 \text{ kg/m}^3$  and the Lamé constants are  $\lambda = 0.6 \text{ GPa}$  and  $\mu = 0.3 \text{ GPa}$ . A directional point source, acting as a force perpendicular to the upper free surface, is located at (2870.0, 0.0). Four receiving positions  $R_1$ ,  $R_2$ ,  $R_3$  and  $R_4$  are chosen at the following locations: (2800.0, -187.5), (1120.0, -42.5), (168.75, -18.75) and (562.5, 0), respectively. The choice of these receiving positions has been realized in order to demonstrate typical behaviour of the C-PML. The source time function that specifies the temporal variation of the point source is a Ricker wavelet given by Eq. (3.17) with  $t_D = 1.0 \text{ s}$ ,

$a_1 = (\pi f_c)^2$  and  $f_c = 1.0$  Hz. The C-PML parameters which have been used are as follows:  
 $\alpha_{\max} = 5\pi f_c$ ,  $n_1 = 3$ ,  $n_2 = 0$ ,  $n_3 = 1$  and

$$\sigma_{\max} = (1 + n_1 + n_2) \cdot \sqrt{(\lambda + 2\mu)/\rho_0} \cdot \log(1/R_0)/(2d), \quad (3.20)$$

where  $R_0 = 5 \times 10^{-5}$ .

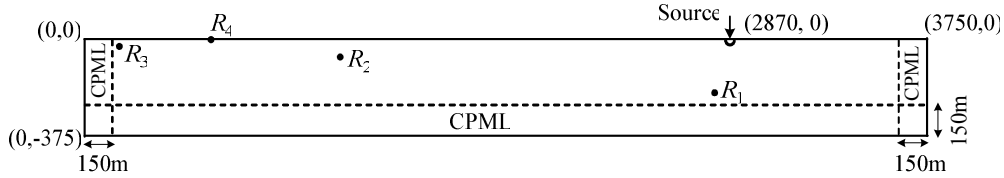


**Fig. 3.6** Schematic of the model used in the example of surface wave in an elongated homogeneous isotropic medium. The C-PML terminations are positioned at the left, right and bottom side of the simulation domain. The top boundary is a stress free boundary. The source and four receivers ( $R_1$ ,  $R_2$ ,  $R_3$ ,  $R_4$ ) positions are also depicted.

The time evolution of the point source Eq. (3.17) is first Fourier transformed, and Eqs. (3.8) is then solved for forty frequencies equally spaced in the source spectrum. The result obtained at one frequency (3 Hz) is shown on Fig. 3.7, where both bulk waves in the physical domain and Rayleigh waves on the free surface boundary can be seen. In Fig. 3.8, the time evolutions of the horizontal (a), (c) and vertical displacements (b), (d) reconstructed by inverse Fourier transform of the forty frequency responses at the fourth receiver, positioned at the free surface, in the case of both C-PML (dashed line) and PML (dotted line) layers for absorbing the surface wave, are displayed and compared to an analytical solution (solid line). The FORTRAN code EX2DDIR of Berg *et al.* [18] has been used, as for the previous example, to compute this exact solution of the 2D response from a vertical directional point source in an isotropic elastic half space with a free surface. The obtained results clearly demonstrated the increase efficiency of the C-PML in comparison of the PML in order to absorb the Rayleigh wave, even when a zoom (Fig. 3.8 (c), (d)) is made around the end of this surface wave. This is again in perfect accordance with previous results obtained with the C-PML first-order velocity-stress formulation implementation [60], [22], [107].

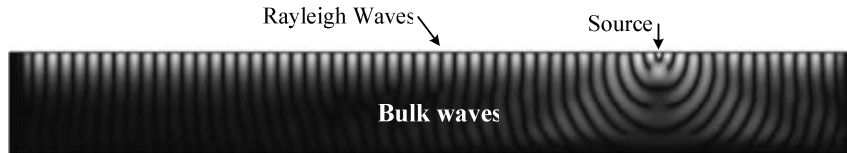


**Fig. 3.7** Displacement amplitude snapshot at frequency 3 Hz for the model depicted on Fig. 3.6, showing the propagation and absorption in the C-PML terminations of both bulk and Rayleigh waves.

The time evolutions of the horizontal (a), (c), (e) and vertical displacements (b), (d), (f) for the three others receivers ( $R_1$ ,  $R_2$  and  $R_3$ ) in the case of FEM simulation with C-PML

(dashed line) are plotted on Fig. 3.9, and compared, as before, with a FEM simulation with PML (dotted line) and an analytical solution (solid line). As in Fig. 3.8, it clearly appears on Fig. 3.9 that the use of C-PML greatly improves the surface wave absorption efficiency of the absorbing layer (see  $R_2$  signal, where spurious oscillations of the horizontal displacement component is observed in the case of PML), even if the receiver is positioned close to the absorbing layer, as for the  $R_3$  receiver. In the case of the first receiver, placed in the bulk of the sample where the contribution of surface wave is negligible, the C-PML and PML have the same absorbing efficiency and the overall agreement with the analytical solution is almost perfect.

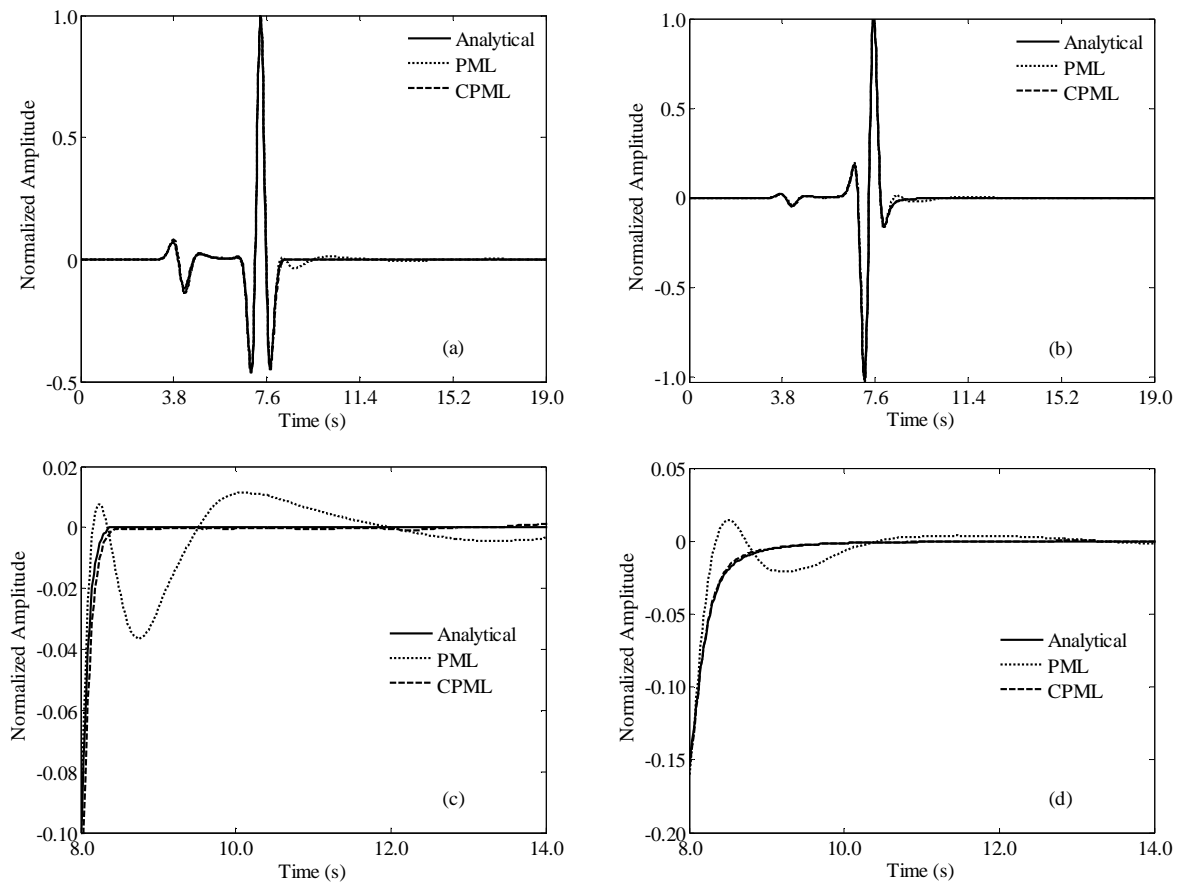


**Fig. 3.8** Time evolution of the horizontal  $u_1$  (a) and the vertical  $u_2$  (b) components of the displacement vector at the fourth receiver  $R_4$  of the analytical solution of the problem (solid line) and the numerical solution with C-PML (dashed line) and PML (dotted line). (c) and (d) are zoom of (a) and (b) respectively, showing the benefit of using C-PML instead of PML.

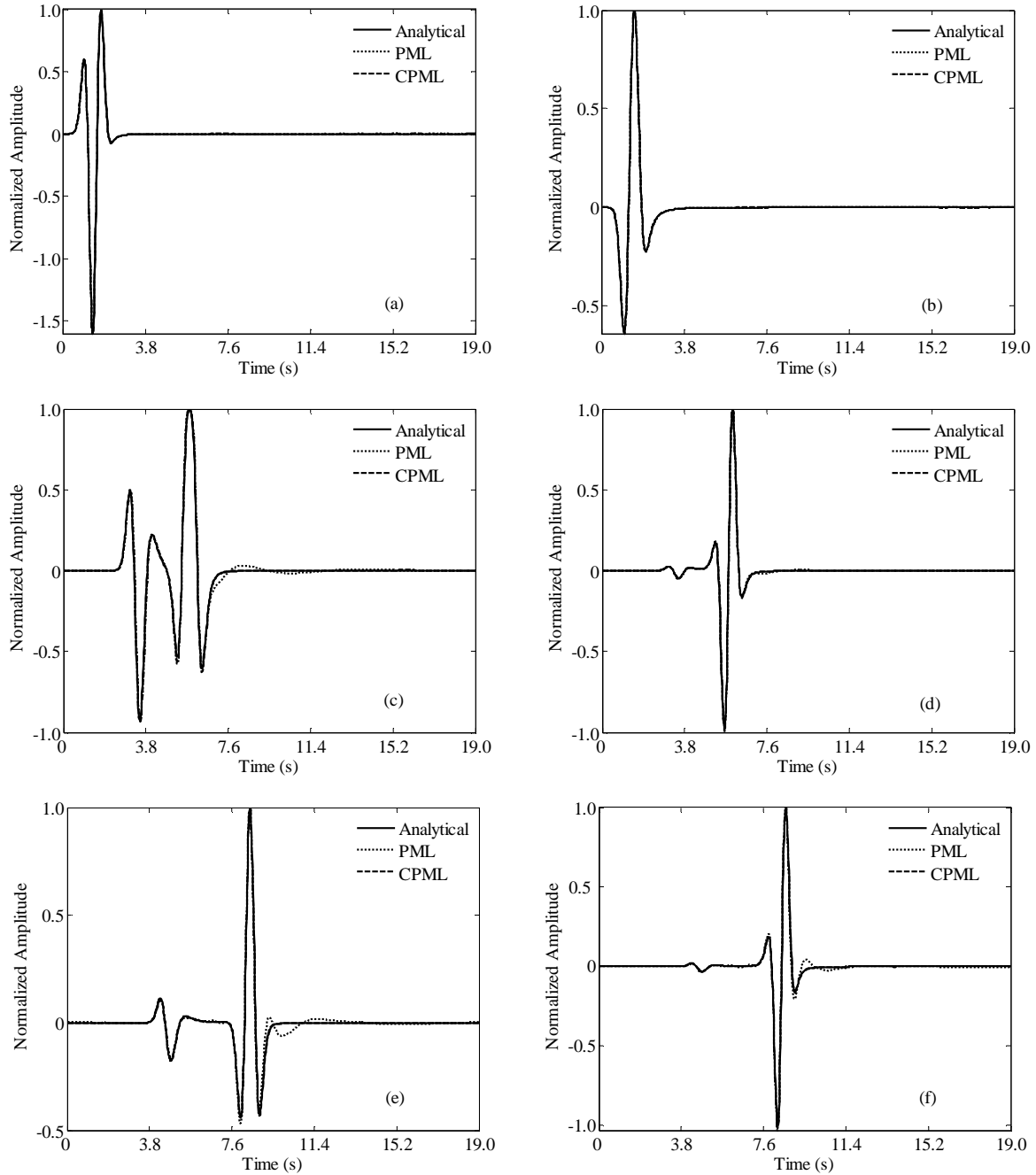


**Fig. 3.9** Time evolution of the horizontal  $u_1$  (left) and the vertical  $u_2$  (right) components of the displacement vector at the first (top), second (middle), and third (bottom) receiver of the analytical solution of the problem (solid line) and the numerical solution with C-PML (dashed line) and PML (dotted line).

### 3.3 C-PML Formulation for Piezoelectric Solid

Although not directly linked to the main objective of the thesis, the previous second order C-PML formulation can be extended to the case of piezoelectric solid. This choice has been motivated, in part, by the interest aroused in other IEMN groups, as Microfluidique and Ultrasons groups, for their own applications.

Only few works are available in the literature on the use of PML for elastic wave propagation in piezoelectric solids. Split field PML, as the one introduced by Berenger [16], has been first derived for angular spectrum [200] and FDTD [38] methods. In both papers, instabilities appear in the PML for some of the presented simulations. This problem will be addressed in more detail in parts 3.4 and 3.5. Here, we propose to improve these first formulations by using un-split C-PML in stead of split PML. This idea has been developed simultaneously by other groups [7], [122], but only in frequency domain calculations.

### 3.3.1 Wave Equations for Piezoelectric Solid in 2D

Consider the propagation of 2D plane strain elastic waves in a heterogeneous piezoelectric solid media. In time domain, equations of motion, Hooke's law and Maxwell equations in the quasi-static approximation are given by:

$$\frac{\partial^2 u_1}{\partial t^2} = \frac{1}{\rho_0} \left( \frac{\partial \tau_{11}}{\partial x} + \frac{\partial \tau_{13}}{\partial z} \right), \quad (3.21a)$$

$$\frac{\partial^2 u_3}{\partial t^2} = \frac{1}{\rho_0} \left( \frac{\partial \tau_{13}}{\partial x} + \frac{\partial \tau_{33}}{\partial z} \right), \quad (3.21b)$$

$$\frac{\partial D_1}{\partial x} + \frac{\partial D_3}{\partial z} = 0, \quad (3.21c)$$

$$\tau_{11} = C_{11} \frac{\partial u_1}{\partial x} + C_{13} \frac{\partial u_3}{\partial z} + e_{31} \frac{\partial \phi}{\partial z}, \quad (3.21d)$$

$$\tau_{13} = C_{44} \left( \frac{\partial u_1}{\partial z} + \frac{\partial u_3}{\partial x} \right) + e_{15} \frac{\partial \phi}{\partial x}, \quad (3.21e)$$

$$\tau_{33} = C_{13} \frac{\partial u_1}{\partial x} + C_{33} \frac{\partial u_3}{\partial z} + e_{33} \frac{\partial \phi}{\partial z}, \quad (3.21f)$$

$$D_1 = -\varepsilon_{11} \frac{\partial \phi}{\partial x} + e_{15} \left( \frac{\partial u_1}{\partial z} + \frac{\partial u_3}{\partial x} \right), \quad (3.21g)$$

$$D_3 = -\varepsilon_{33} \frac{\partial \phi}{\partial z} + e_{31} \frac{\partial u_1}{\partial x} + e_{33} \frac{\partial u_3}{\partial z}. \quad (3.21h)$$

where  $u_i$  is the particle displacement,  $\tau_{ij}$  is the stress tensor,  $\phi$  is the electric potential and  $D_i$  is the electric displacement.  $C_{ij}$ ,  $e_{ij}$  and  $\varepsilon_{ij}$  are respectively the elastic stiffness constants, the piezoelectric strain constants and the permittivity constants (not confuse with the strain notation used in chapter 2).

### 3.3.2 Formulation of C-PML in Frequency Domain

First, taking the Fourier transform of the system, then using the complex coordinates transformation and stretched-coordinate metrics as for anisotropic elastic solid, the following equations are obtained in the frequency domain:

$$-\omega^2 \rho_0 \hat{u}_1 = \frac{1}{s_x} \frac{\partial \hat{\tau}_{11}}{\partial x} + \frac{1}{s_z} \frac{\partial \hat{\tau}_{13}}{\partial z}, \quad (3.22a)$$

$$-\omega^2 \rho_0 \hat{u}_3 = \frac{1}{s_x} \frac{\partial \hat{\tau}_{13}}{\partial x} + \frac{1}{s_z} \frac{\partial \hat{\tau}_{33}}{\partial z}, \quad (3.22b)$$

$$\frac{1}{s_x} \frac{\partial \hat{D}_1}{\partial x} + \frac{1}{s_z} \frac{\partial \hat{D}_3}{\partial z} = 0, \quad (3.22c)$$

$$\hat{\tau}_{11} = C_{11} \frac{1}{s_x} \frac{\partial \hat{u}_1}{\partial x} + C_{13} \frac{1}{s_z} \frac{\partial \hat{u}_3}{\partial z} + e_{31} \frac{1}{s_z} \frac{\partial \hat{\phi}}{\partial z}, \quad (3.22d)$$

$$\hat{\tau}_{13} = C_{44} \left( \frac{1}{s_z} \frac{\partial \hat{u}_1}{\partial z} + \frac{1}{s_x} \frac{\partial \hat{u}_3}{\partial x} \right) + e_{15} \frac{1}{s_x} \frac{\partial \hat{\phi}}{\partial x}, \quad (3.22e)$$

$$\hat{\tau}_{33} = C_{13} \frac{1}{s_x} \frac{\partial \hat{u}_1}{\partial x} + C_{33} \frac{1}{s_z} \frac{\partial \hat{u}_3}{\partial z} + e_{33} \frac{1}{s_z} \frac{\partial \hat{\phi}}{\partial z}, \quad (3.22f)$$

$$\hat{D}_1 = -\varepsilon_{11} \frac{1}{s_x} \frac{\partial \hat{\phi}}{\partial x} + e_{15} \left( \frac{1}{s_z} \frac{\partial \hat{u}_1}{\partial z} + \frac{1}{s_x} \frac{\partial \hat{u}_3}{\partial x} \right), \quad (3.22g)$$

$$\hat{D}_3 = -\varepsilon_{33} \frac{1}{s_z} \frac{\partial \hat{\phi}}{\partial z} + e_{31} \frac{1}{s_x} \frac{\partial \hat{u}_1}{\partial x} + e_{33} \frac{1}{s_z} \frac{\partial \hat{u}_3}{\partial z}. \quad (3.22h)$$

As for the anisotropic solid, multiplying by  $s_x s_z$  and introducing the new variables  $\hat{\tau}'_{ij}$  and  $\rho'_0$  (given by  $\rho_0 s_x s_z$ ), we get the following equations which show that C-PML can be interpreted as an anisotropic piezoelectric medium:

$$-\omega^2 \rho'_0 \hat{u}_1 = \frac{\partial \hat{\tau}'_{11}}{\partial x} + \frac{\partial \hat{\tau}'_{13}}{\partial z}, \quad (3.23a)$$

$$-\omega^2 \rho'_0 \hat{u}_3 = \frac{\partial \hat{\tau}'_{31}}{\partial x} + \frac{\partial \hat{\tau}'_{33}}{\partial z}, \quad (3.23b)$$

$$\frac{\partial \hat{D}'_1}{\partial x} + \frac{\partial \hat{D}'_3}{\partial z} = 0, \quad (3.23c)$$

$$\hat{\tau}'_{11} = \hat{\tau}_{11} s_z = C_{11} \frac{s_z}{s_x} \frac{\partial \hat{u}_1}{\partial x} + C_{13} \frac{\partial \hat{u}_3}{\partial z} + e_{31} \frac{\partial \hat{\phi}}{\partial z}, \quad (3.23d)$$

$$\hat{\tau}'_{13} = \hat{\tau}_{13} s_x = C_{44} \frac{s_x}{s_z} \frac{\partial \hat{u}_1}{\partial z} + C_{44} \frac{\partial \hat{u}_3}{\partial x} + e_{15} \frac{\partial \hat{\phi}}{\partial x}, \quad (3.23e)$$

$$\hat{\tau}'_{31} = \hat{\tau}_{13} s_z = C_{44} \frac{\partial \hat{u}_1}{\partial z} + C_{44} \frac{s_z}{s_x} \frac{\partial \hat{u}_3}{\partial x} + e_{15} \frac{s_z}{s_x} \frac{\partial \hat{\phi}}{\partial x}, \quad (3.23f)$$

$$\hat{\tau}'_{33} = \hat{\tau}_{33} s_x = C_{13} \frac{\partial \hat{u}_1}{\partial x} + C_{33} \frac{s_x}{s_z} \frac{\partial \hat{u}_3}{\partial z} + e_{33} \frac{s_x}{s_z} \frac{\partial \hat{\phi}}{\partial z}, \quad (3.23g)$$

$$\hat{D}'_1 = -\varepsilon_{11} \frac{s_z}{s_x} \frac{\partial \hat{\phi}}{\partial x} + e_{15} \left( \frac{\partial \hat{u}_1}{\partial z} + \frac{s_z}{s_x} \frac{\partial \hat{u}_3}{\partial x} \right), \quad (3.23h)$$

$$\hat{D}'_3 = -\varepsilon_{33} \frac{s_x}{s_z} \frac{\partial \hat{\phi}}{\partial z} + e_{31} \frac{\partial \hat{u}_1}{\partial x} + e_{33} \frac{s_x}{s_z} \frac{\partial \hat{u}_3}{\partial z}. \quad (3.23i)$$

Eqs. (3.23d)-(3.23i) can be written in a matrix form as follows:

$$\begin{bmatrix} \hat{\tau}'_{11} \\ \hat{\tau}'_{13} \\ \hat{\tau}'_{31} \\ \hat{\tau}'_{33} \\ \hat{D}'_1 \\ \hat{D}'_3 \end{bmatrix} = \begin{bmatrix} C'_{11} & C_{13} & 0 & 0 & 0 & e_{31} \\ 0 & 0 & C'_{44} & C_{44} & e_{15} & 0 \\ 0 & 0 & C_{44} & C''_{44} & e'_{15} & 0 \\ C_{13} & C'_{33} & 0 & 0 & 0 & e'_{33} \\ 0 & 0 & e_{15} & e'_{15} & -\varepsilon'_{11} & 0 \\ e_{31} & e'_{33} & 0 & 0 & 0 & -\varepsilon'_{33} \end{bmatrix} \begin{bmatrix} \hat{u}_{1x} \\ \hat{u}_{3z} \\ \hat{u}_{1z} \\ \hat{u}_{3x} \\ \hat{\phi}_x \\ \hat{\phi}_z \end{bmatrix},$$

with  $\hat{u}_{1x} = \partial \hat{u}_1 / \partial x$ ,  $\hat{u}_{3z} = \partial \hat{u}_3 / \partial z$ ,  $\hat{u}_{1z} = \partial \hat{u}_1 / \partial z$ ,  $\hat{u}_{3x} = \partial \hat{u}_3 / \partial x$ ,  $\hat{\phi}_x = \partial \hat{\phi} / \partial x$  and  $\hat{\phi}_z = \partial \hat{\phi} / \partial z$ . The new effectives elastic stiffnesses, piezoelectric strain and permittivities constant are  $C'_{11} = C_{11} s_z / s_x$ ,  $C'_{33} = C_{33} s_x / s_z$ ,  $C'_{44} = C_{44} s_x / s_z$ ,  $C''_{44} = C_{44} s_z / s_x$ ,  $e'_{15} = e_{15} s_z / s_x$ ,  $e'_{33} = e_{33} s_x / s_z$ ,  $\varepsilon'_{11} = \varepsilon_{11} s_z / s_x$ ,  $\varepsilon'_{33} = \varepsilon_{33} s_x / s_z$ .

For 3D, following the same procedure, it can be demonstrated that in this case, the propagation of elastic waves is described in C-PML by:

$$-\omega^2 \rho'_0 \hat{u}_i = \frac{\partial \hat{\tau}'_{ij}}{\partial x_j}, \quad (3.24a)$$

$$\frac{\partial \hat{D}'_i}{\partial x_i} = 0, \quad (3.24b)$$

$$\hat{\tau}'_{ij} = C'_{ijkl} \frac{\partial \hat{u}_l}{\partial x_k} + e'_{kij} \frac{\partial \hat{\phi}}{\partial x_k}, \quad (3.24c)$$

$$\hat{D}'_i = -\varepsilon'_{ij} \frac{\partial \hat{\phi}}{\partial x_j} + e'_{ijk} \frac{\partial \hat{u}_j}{\partial x_k}, \quad (3.24d)$$

where  $i, j, k, l = 1, 2$  or  $3$ . The effective elastic tensor  $C'$ , piezoelectric strain matrix  $e'$ , permittivity matrix  $\varepsilon'$  and density  $\rho'_0$  are given by:

$$C'_{ijkl} = C_{ijkl} \frac{s_x s_y s_z}{s_i s_k}, \quad (3.25a)$$

$$e'_{kij} = e_{kij} \frac{s_x s_y s_z}{s_i s_k}, \quad (3.25b)$$

$$\varepsilon''_{ij} = \varepsilon_{ij} \frac{s_x s_y s_z}{s_i s_j}, \quad (3.25c)$$

$$\rho'_0 = \rho_0 s_x s_y s_z. \quad (3.25d)$$

### 3.3.3 Formulation of C-PML in Time Domain

By using an inverse Fourier transform, we can translate the system of equations Eqs. (3.22) back to time domain. As for anisotropic solids a convolution appears. It can be

eliminated by introducing memory variables, and then replaced by a first order differential equation for each of these memory variables. The resulting second-order system equations of C-PML in time domain are given by:

$$\frac{\partial^2 u_1}{\partial t^2} = \frac{1}{\rho_0} \left( \frac{1}{\kappa_x} \frac{\partial \tau_{11}}{\partial x} + \frac{1}{\kappa_z} \frac{\partial \tau_{13}}{\partial z} + \frac{A_x}{\kappa_x} + \frac{B_z}{\kappa_z} \right), \quad (3.26a)$$

$$\frac{\partial^2 u_3}{\partial t^2} = \frac{1}{\rho_0} \left( \frac{1}{\kappa_x} \frac{\partial \tau_{13}}{\partial x} + \frac{1}{\kappa_z} \frac{\partial \tau_{33}}{\partial z} + \frac{C_x}{\kappa_x} + \frac{D_z}{\kappa_z} \right), \quad (3.26b)$$

$$\frac{1}{\kappa_x} \frac{\partial \hat{D}_1}{\partial x} + \frac{1}{\kappa_z} \frac{\partial \hat{D}_3}{\partial z} + \frac{K_x}{\kappa_x} + \frac{L_z}{\kappa_z} = 0, \quad (3.26c)$$

$$\tau_{11} = \frac{C_{11}}{\kappa_x} \frac{\partial u_1}{\partial x} + \frac{C_{13}}{\kappa_z} \frac{\partial u_3}{\partial z} + \frac{e_{31}}{\kappa_z} \frac{\partial \phi}{\partial z} + \frac{E_x}{\kappa_x} + \frac{F_z}{\kappa_z} + \frac{J_x}{\kappa_z}, \quad (3.26d)$$

$$\tau_{13} = \frac{C_{44}}{\kappa_x} \frac{\partial u_3}{\partial x} + \frac{C_{44}}{\kappa_z} \frac{\partial u_1}{\partial z} + \frac{e_{15}}{\kappa_x} \frac{\partial \phi}{\partial x} + \frac{G_x}{\kappa_x} + \frac{H_z}{\kappa_z} + \frac{I_x}{\kappa_x}, \quad (3.26e)$$

$$\tau_{33} = \frac{C_{13}}{\kappa_x} \frac{\partial u_1}{\partial x} + \frac{C_{33}}{\kappa_z} \frac{\partial u_3}{\partial z} + \frac{e_{33}}{\kappa_z} \frac{\partial \phi}{\partial z} + \frac{E_x}{\kappa_x} + \frac{F_z}{\kappa_z} + \frac{J_z}{\kappa_z}, \quad (3.26f)$$

$$D_1 = -\frac{\varepsilon_{11}}{\kappa_x} \frac{\partial \phi}{\partial x} + \frac{e_{15}}{\kappa_z} \frac{\partial u_1}{\partial z} + \frac{e_{15}}{\kappa_x} \frac{\partial u_3}{\partial x} - \frac{I_x}{\kappa_x} + \frac{H_z}{\kappa_z} + \frac{G_x}{\kappa_x}, \quad (3.26g)$$

$$D_3 = -\frac{\varepsilon_{33}}{\kappa_z} \frac{\partial \phi}{\partial z} + \frac{e_{31}}{\kappa_x} \frac{\partial u_1}{\partial x} + \frac{e_{33}}{\kappa_z} \frac{\partial u_3}{\partial z} - \frac{J_z}{\kappa_z} + \frac{E_x}{\kappa_x} + \frac{F_z}{\kappa_z}. \quad (3.26h)$$

with each of the 12 introduced memory variables corresponds a first order differential equation of the form (Appendix B):

$$\frac{\partial A_x}{\partial t} = -\delta_x \frac{\partial \tau_{11}}{\partial x} - \beta_x A_x, \quad (3.27)$$

Here the memory variables will be zero outside the C-PML zones. Then, introducing Eqs. (3.26d)-(3.26h) into Eqs. (3.26a)-(3.26c), the system of equations to be solved becomes:

$$\frac{\partial^2 u_1}{\partial t^2} = \frac{1}{\rho_0} \left( \frac{\partial \tau_{11}}{\partial x} + \frac{\partial \tau_{13}}{\partial z} + f_{p1} \right), \quad (3.28a)$$

$$\frac{\partial^2 u_3}{\partial t^2} = \frac{1}{\rho_0} \left( \frac{\partial \tau_{13}}{\partial x} + \frac{\partial \tau_{33}}{\partial z} + f_{p2} \right), \quad (3.28b)$$

$$\frac{\partial D_1}{\partial x} + \frac{\partial D_3}{\partial z} = f_{p3}, \quad (3.28c)$$

which is equivalent to the system of Eqs.(3.21a)-(3.21c) with source terms  $f_{pi}$ . These source terms are given by the following expressions:

$$f_{p1} = \left( \begin{array}{l} -\frac{\kappa'_x}{\kappa_x} \frac{\partial}{\partial x} \left( \frac{C_{11}}{\kappa_x} \left( \frac{\partial u_1}{\partial x} + E_x \right) + \frac{C_{13}}{\kappa_z} \left( \frac{\partial u_3}{\partial z} + F_z \right) + \frac{e_{31}}{\kappa_z} \left( \frac{\partial \phi}{\partial z} + J_z \right) \right) \\ -\frac{\kappa'_z}{\kappa_z} \frac{\partial}{\partial z} \left( \frac{C_{44}}{\kappa_x} \left( \frac{\partial u_3}{\partial x} + G_x \right) + \frac{C_{44}}{\kappa_z} \left( \frac{\partial u_1}{\partial z} + H_z \right) + \frac{e_{15}}{\kappa_x} \left( \frac{\partial \phi}{\partial x} + I_x \right) \right) \\ -\frac{\partial}{\partial x} \left( \frac{C_{11}}{\kappa_x} \left( \kappa'_x \frac{\partial u_1}{\partial x} - E_x \right) + \frac{C_{13}}{\kappa_z} \left( \kappa'_z \frac{\partial u_3}{\partial z} - F_z \right) + \frac{e_{31}}{\kappa_z} \left( \kappa'_z \frac{\partial \phi}{\partial z} - J_z \right) \right) \\ -\frac{\partial}{\partial z} \left( \frac{C_{44}}{\kappa_x} \left( \kappa'_x \frac{\partial u_3}{\partial x} - G_x \right) + \frac{C_{44}}{\kappa_z} \left( \kappa'_z \frac{\partial u_1}{\partial z} - H_z \right) + \frac{e_{15}}{\kappa_x} \left( \kappa'_x \frac{\partial \phi}{\partial x} - I_x \right) \right) \\ + \frac{A_x}{\kappa_x} + \frac{B_z}{\kappa_z} \end{array} \right), \quad (3.29a)$$

$$f_{p2} = \left( \begin{array}{l} -\frac{\kappa'_x}{\kappa_x} \frac{\partial}{\partial x} \left( \frac{C_{44}}{\kappa_x} \left( \frac{\partial u_3}{\partial x} + G_x \right) + \frac{C_{44}}{\kappa_z} \left( \frac{\partial u_1}{\partial z} + H_z \right) + \frac{e_{15}}{\kappa_x} \left( \frac{\partial \phi}{\partial x} + I_x \right) \right) \\ -\frac{\kappa'_z}{\kappa_z} \frac{\partial}{\partial z} \left( \frac{C_{13}}{\kappa_x} \left( \frac{\partial u_1}{\partial x} + E_x \right) + \frac{C_{33}}{\kappa_z} \left( \frac{\partial u_3}{\partial z} + F_z \right) + \frac{e_{33}}{\kappa_z} \left( \frac{\partial \phi}{\partial z} + J_z \right) \right) \\ -\frac{\partial}{\partial x} \left( \frac{C_{44}}{\kappa_x} \left( \kappa'_x \frac{\partial u_3}{\partial x} - G_x \right) + \frac{C_{44}}{\kappa_z} \left( \kappa'_z \frac{\partial u_1}{\partial z} - H_z \right) + \frac{e_{15}}{\kappa_x} \left( \kappa'_x \frac{\partial \phi}{\partial x} - I_x \right) \right) \\ -\frac{\partial}{\partial z} \left( \frac{C_{13}}{\kappa_x} \left( \kappa'_x \frac{\partial u_1}{\partial x} - E_x \right) + \frac{C_{33}}{\kappa_z} \left( \kappa'_z \frac{\partial u_3}{\partial z} - F_z \right) + \frac{e_{33}}{\kappa_z} \left( \kappa'_z \frac{\partial \phi}{\partial z} - J_z \right) \right) \\ + \frac{C_x}{\kappa_x} + \frac{D_z}{\kappa_z} \end{array} \right), \quad (3.29b)$$

$$f_{p3} = \left( \begin{array}{l} \frac{\kappa'_x}{\kappa_x} \frac{\partial}{\partial x} \left( \frac{e_{15}}{\kappa_x} \left( \frac{\partial u_3}{\partial x} + G_x \right) + \frac{e_{15}}{\kappa_z} \left( \frac{\partial u_1}{\partial z} + H_z \right) - \frac{\varepsilon_{11}}{\kappa_x} \left( \frac{\partial \phi}{\partial x} + I_x \right) \right) \\ + \frac{\kappa'_z}{\kappa_z} \frac{\partial}{\partial z} \left( \frac{e_{31}}{\kappa_x} \left( \frac{\partial u_1}{\partial x} + E_x \right) + \frac{e_{33}}{\kappa_z} \left( \frac{\partial u_3}{\partial z} + F_z \right) - \frac{\varepsilon_{33}}{\kappa_z} \left( \frac{\partial \phi}{\partial z} + J_z \right) \right) \\ -\frac{\partial}{\partial x} \left( \frac{e_{15}}{\kappa_x} \left( -\kappa'_x \frac{\partial u_3}{\partial x} + G_x \right) + \frac{e_{15}}{\kappa_z} \left( -\kappa'_z \frac{\partial u_1}{\partial z} + H_z \right) + \frac{\varepsilon_{11}}{\kappa_x} \left( \kappa'_x \frac{\partial \phi}{\partial x} - I_x \right) \right) \\ -\frac{\partial}{\partial z} \left( \frac{e_{31}}{\kappa_x} \left( -\kappa'_x \frac{\partial u_1}{\partial x} + E_x \right) + \frac{e_{33}}{\kappa_z} \left( -\kappa'_z \frac{\partial u_3}{\partial z} + F_z \right) + \frac{\varepsilon_{33}}{\kappa_z} \left( \kappa'_z \frac{\partial \phi}{\partial z} - J_z \right) \right) \\ - \frac{K_x}{\kappa_x} - \frac{L_z}{\kappa_z} \end{array} \right), \quad (3.29c)$$

where, as it was done previously, we have introduced the notation  $\kappa'_{x,z} = \kappa_{x,z} - 1$ .

We can verify that if there is no piezoelectricity Eqs. (3.29) become the ones obtained for anisotropic solid.

### 3.3.4 Numerical Simulations

#### 3.3.4.1 Simulation of Elastic Wave in an Unbounded Piezoelectric Medium

The simulation presented in this section was made for elastic wave propagation across a (0, 0, 0) cut of a bismuth germanium oxide ( $\text{Bi}_{12}\text{GeO}_{20}$ ) unbounded substrate. For this cubic material the non zero constants are:  $C_{11} = C_{22} = 128$  GPa,  $C_{44} = 25.5$  GPa,  $C_{13} = 30.5$  GPa,  $e_{14} = e_{36} = 0.99$  C/m<sup>2</sup>,  $\epsilon_{11} = \epsilon_{33} = 38\epsilon_0$  and  $\rho_0 = 9200$  kg/m<sup>3</sup>.  $\epsilon_0 = 1/36\pi \cdot 10^{-9}$  F/m is the electric permittivity of vacuum. The simulation has been performed over a  $80 \times 80$  grid, which was surrounded by a C-PML layer having a thickness of 10 cells, with  $\Delta x = \Delta z = 0.5$   $\mu\text{m}$ . A 2D circular source with a  $0.15$   $\mu\text{m}$  diameter and  $0.8$  GHz centre frequency was set up at the point (0,0) with a time evolution corresponding to a Ricker wavelet expressed as in Eq. (3.17) with parameters  $t_D = 2$  ns,  $a_1 = (\pi f_c)^2$ , and  $f_c = 0.8$  GHz. In this simulation, the C-PML parameters in the stretched-coordinate metrics are given by:  $\alpha_{\max} = 2\pi f_c$ ,  $n_1 = 3$ ,  $n_2 = 0$ ,  $n_3 = 1$  and  $\sigma_{\max}$  has the same expression as Eq. (3.18d), in which we have used  $R_0 = 10^{-6}$ .

For characterizing the absorbing ability of the C-PML layer, here, Eqs. (3.23) have been solved with COMSOL Multiphysics FEM software in frequency domain. Here sixty frequencies equally spaced in the source spectrum have been used. Then an inverse Fourier transform has been done with Matlab software to get the result in time domain. The snapshots for four different times, 3.25 ns, 5.86 ns, 9.12 ns and 13.02 ns, are displayed on Fig. 3.10. They show the wave propagating away from the source and being absorbed by the C-PML layer, demonstrating the efficiency of the method. It has to be noted that, for certain kinds of piezoelectric substrates, instabilities can appear in PML [38]. In fact, these instabilities correspond to waves entering with group and phase velocities of opposite signs [10]. The stability problem of C-PML will be discussed in this chapter in parts of 3.5.

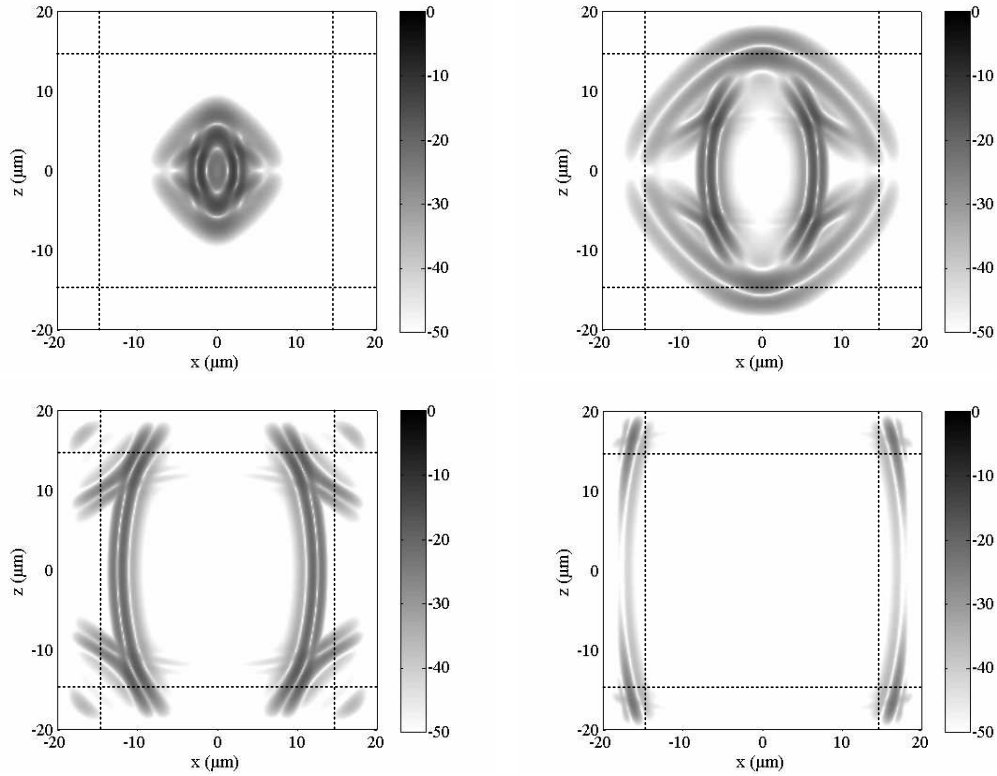


**Fig. 3.10** Propagation of elastic waves in an unbounded  $\text{Bi}_{12}\text{GeO}_{20}$  sample. In the first row the times of the two figures are 3.25 ns (left) and 5.86 ns (right), and in the second row the times are 9.12 ns (left) and 13.02 ns (right). The displayed dynamic range is 50 dB.

### 3.3.4.2 Surface Acoustic Wave Streaming System

In this subsection, the simulation of an integrated Surface Acoustic Wave (SAW) streaming system will be presented. In this system (Fig. 3.11), a Rayleigh SAW is generated using an interdigital transducer (IDT) source laid on a X-cut  $\text{LiNbO}_3$  substrate, with an interdigit of  $50\ \mu\text{m}$ . Such waves are radiated on one half of the studied micro-chambers consisting in microlitre droplets situated between a hydrophobic substrate and a glass cover. The simulated system corresponds to a real one developed in our laboratory by E. Galopin (Micro-fluidic group) and O. Ducloux (previously at LEMAC) [62]. The aim of this simulation was to confirm the link between streaming pattern obtained experimentally and the acoustic standing wave pattern created in the water droplet.

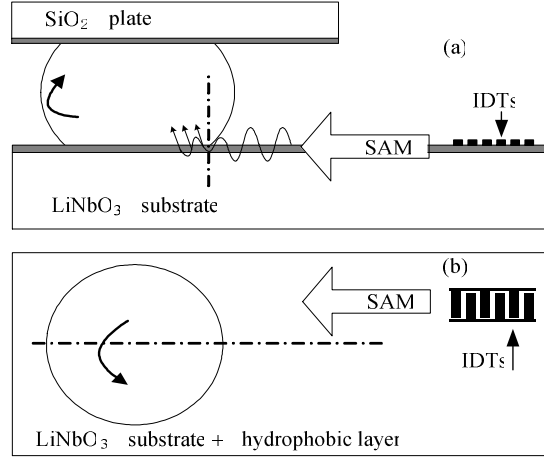


**Fig. 3.11** SAW streaming system developed by E. Galopin and O. Ducloux at IEMN, (a) Side view, (b) Top view.

This SAW streaming system has been modeled in frequency domain, using the General Form Modes of COMSOL Multiphysics, by a model with three domains: the piezoelectric substrate, the water droplet and the glass plate. The piezoelectric substrate has been modeled using Eqs. (3.23). Eqs. (3.8) has been used for the glass plate, but with no C-PML. In the water droplet, the system of equations of linear acoustic in fluids has been used:

$$\frac{\partial \mathbf{v}}{\partial t} = -\frac{1}{\rho_0} \nabla p, \quad (3.30a)$$

$$\frac{\partial p}{\partial t} = -\rho_0 c_0^2 \nabla \cdot \mathbf{v}, \quad (3.30b)$$

where  $\mathbf{v}$  is the particle velocity vector,  $p$  is the pressure field and  $\rho_0$ ,  $c_0$  are the density and sound speed respectively. The boundary conditions used between the model and the surrounding ambient air are stress free conditions. Between the solid and the water droplet continuity of the normal stress and displacement have been assumed.

The pressure field inside the water droplet, which is the component  $-\tau_{33}$  of the stress field inside the piezoelectric solids, obtained for a continuous wave excitation at 20.5 MHz is shown on Fig. 3.12. The propagation of the Rayleigh wave in the piezoelectric substrate can easily be seen.

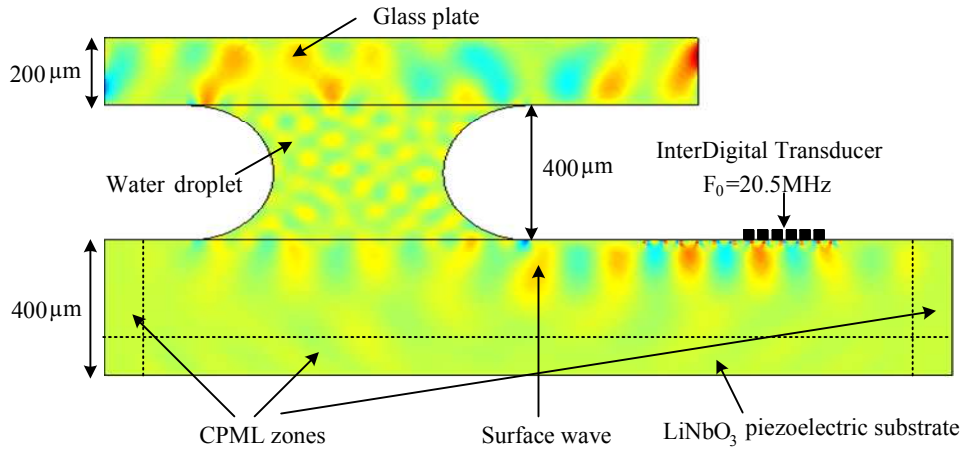


**Fig. 3.12** Pressure field created in a water droplet in contact with a piezoelectric substrate where a Rayleigh wave propagates.

This wave created in the water droplet a stationary wave pattern with a characteristic length given by the sound wavelength in water at the corresponding frequency. In this case, it corresponds to  $75 \mu\text{m}$  as shown on Fig. 3.13. Moreover, the form of this pattern is linked to the form of the water droplet and the critical angle of Rayleigh wave emission between the  $\text{LiNbO}_3$  substrate and water (dashed lines on Fig. 3.13). This qualitatively corresponds to the observations made by fluorescence microscopy on the experimental set-up, as it was done in our laboratory, by Olivier Ducloux and Elisabeth Galopin [62], as shown on Fig. 3.14.

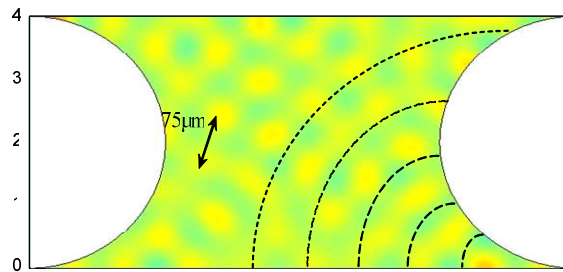


**Fig. 3.13** Zoom on the pressure field created in the water droplet showing the stationary waves pattern.

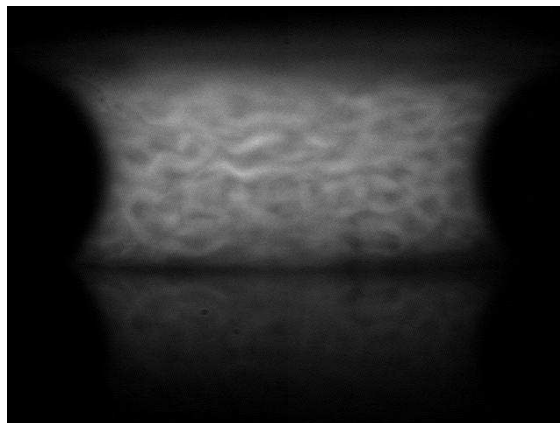


**Fig. 3.14** Side view of the pattern induced in the water droplet by a 20.5 MHz surface wave and observed by fluorescence with an optical microscope [62].

### 3.4 Nearly Perfectly Matched Layer (NPML) for Elastic Solid

In the preceding two parts, the applications of C-PML for anisotropic elastic solids and piezoelectric media have been presented. The results demonstrate the efficient ability of C-PML for absorbing the outgoing energy of bulk waves and surface waves. But in all presented implementations of C-PML supplementary PDE are introduced to actualize the C-PML variables. These PDE, as they contain spatial derivative terms, are cumbersome and difficult to introduce in our Discontinuous Galerkin scheme. This is particularly true when a flux based on physical considerations, like Godunov type flux, is used.

In this subsection, an another kind of PML named Nearly Perfectly Matched Layer (NPML), which has been proposed by Cummer *et al.* [49], [95] for electromagnetism and then extended to acoustic [96], and which can overcome these problems (as it will be shown), will be extended for nonlinear elastodynamic.

#### 3.4.1 Formulation of NPML for Elastic Wave Propagation

Here, the methodology introduced by Cummer *et al.* [49], [95] in electromagnetism is used for the system of Eq. (2.1). First, it is rewritten in the frequency domain by taking its Fourier transform. Then, the same complexes coordinates transformation with the same stretched-coordinate metrics, as the one used in C-PML implementation, is introduced. Eq. (2.1) becomes:

$$j\omega\hat{\mathbf{Q}} = \frac{1}{s_x} \frac{\partial \hat{\mathbf{F}}}{\partial x} + \frac{1}{s_y} \frac{\partial \hat{\mathbf{G}}}{\partial y}. \quad (3.31)$$

Here ( $\hat{\bullet}$ ) denotes the frequency domain of the considered vector. Neglecting the  $x$ -dependence of  $s_x$  and the  $y$ -dependence of  $s_y$  Eq. (3.31) is rewritten as:

$$j\omega\hat{\mathbf{Q}} = \frac{\partial \hat{\mathbf{F}}'}{\partial x} + \frac{\partial \hat{\mathbf{G}}'}{\partial y}, \quad (3.32)$$

where the following stretched fluxes have been introduced:

$$\hat{\mathbf{F}}' = \frac{\hat{\mathbf{F}}}{s_x} \quad \text{and} \quad \hat{\mathbf{G}}' = \frac{\hat{\mathbf{G}}}{s_y}. \quad (3.33)$$

It is noted that the NPML performance is not affected by the approximation used during its derivation, due to the fact that NPML is really a perfectly matched layer [17]. Finally, the resulting equations are transformed back to the time domain by inverse Fourier transform and the system to be solved becomes:

$$\frac{\partial \mathbf{Q}}{\partial t} = \frac{\partial \mathbf{F}'}{\partial x} + \frac{\partial \mathbf{G}'}{\partial y}, \quad (3.34)$$

with

$$\frac{\partial \mathbf{F}'}{\partial t} + \left( \frac{\sigma_x}{\kappa_x} + \alpha_x \right) \mathbf{F}' = \frac{1}{\kappa_x} \frac{\partial \mathbf{F}}{\partial t} + \frac{\alpha_x}{\kappa_x} \mathbf{F}, \quad (3.35a)$$

$$\frac{\partial \mathbf{G}'}{\partial t} + \left( \frac{\sigma_y}{\kappa_y} + \alpha_y \right) \mathbf{G}' = \frac{1}{\kappa_y} \frac{\partial \mathbf{G}}{\partial t} + \frac{\alpha_y}{\kappa_y} \mathbf{G}. \quad (3.35b)$$

In the case where Eqs. (3.35) are not solved by a Finite Difference (FD) method, it can be interesting to use an equivalent formulation where the time derivative of both stretched fluxes  $\mathbf{F}'$  and unstretched fluxes  $\mathbf{F}$  are not needed in the same equation. So, introducing the change of variables  $\mathbf{F}'' = \kappa_x \mathbf{F}' - \mathbf{F}$  and  $\mathbf{G}'' = \kappa_y \mathbf{G}' - \mathbf{G}$  we arrive at the following equivalent system, which needs to be solved in the NPML:

$$\frac{\partial \mathbf{Q}}{\partial t} = \frac{\partial \left( \frac{\mathbf{F}'' + \mathbf{F}}{\kappa_x} \right)}{\partial x} + \frac{\partial \left( \frac{\mathbf{G}'' + \mathbf{G}}{\kappa_y} \right)}{\partial y}, \quad (3.36)$$

with

$$\frac{\partial \mathbf{F}''}{\partial t} = -\alpha_x \mathbf{F}'' - \frac{\sigma_x}{\kappa_x} (\mathbf{F}'' + \mathbf{F}), \quad (3.37a)$$

$$\frac{\partial \mathbf{G}''}{\partial t} = -\alpha_y \mathbf{G}'' - \frac{\sigma_y}{\kappa_y} (\mathbf{G}'' + \mathbf{G}). \quad (3.37b)$$

The main advantage of this formulation is linked to the fact that (i) the obtained system of equations (Eq. (3.34) or Eq. (3.36)) is in exactly the same form as the original system and so strongly hyperbolic, and (ii) the introduced stretched fluxes are linked by Ordinary Differential Equations (ODEs) to the physical fluxes. This last advantage can be particularly interesting for Discontinuous Galerkin scheme, preserving the highly parallelisable capabilities of this numerical method.

The 3D extension of the proposed NPML formulation is straight forward, and is given by:

$$\frac{\partial \mathbf{Q}}{\partial t} = \frac{\partial \left( \frac{\mathbf{F}_x'' + \mathbf{F}_x}{\kappa_x} \right)}{\partial x} + \frac{\partial \left( \frac{\mathbf{F}_y'' + \mathbf{F}_y}{\kappa_y} \right)}{\partial y} + \frac{\partial \left( \frac{\mathbf{F}_z'' + \mathbf{F}_z}{\kappa_z} \right)}{\partial z}, \quad (3.38)$$

where

$$\mathbf{Q} = \begin{pmatrix} \rho_0 v_1 \\ \rho_0 v_2 \\ \rho_0 v_3 \\ F_{11} \\ F_{22} \\ F_{33} \\ F_{23} \\ F_{32} \\ F_{13} \\ F_{31} \\ F_{12} \\ F_{21} \end{pmatrix}, \quad \mathbf{F}_x = \begin{pmatrix} P_{11} \\ P_{21} \\ P_{31} \\ v_1 \\ 0 \\ 0 \\ 0 \\ 0 \\ 0 \\ v_3 \\ 0 \\ v_2 \end{pmatrix}, \quad \mathbf{F}_y = \begin{pmatrix} P_{12} \\ P_{22} \\ P_{32} \\ 0 \\ v_2 \\ 0 \\ 0 \\ v_3 \\ 0 \\ 0 \\ v_1 \\ 0 \end{pmatrix}, \quad \mathbf{F}_z = \begin{pmatrix} P_{13} \\ P_{23} \\ P_{33} \\ 0 \\ 0 \\ v_3 \\ v_2 \\ 0 \\ v_1 \\ 0 \\ 0 \\ 0 \end{pmatrix},$$

represent the state vector and the three components of the flux, respectively. The stretched fluxes  $\mathbf{F}_x''$  are updated by:

$$\frac{\partial \mathbf{F}_x''}{\partial t} = -\alpha_x \mathbf{F}_x'' - \frac{\sigma_x}{\kappa_x} (\mathbf{F}_x'' + \mathbf{F}_x). \quad (3.39)$$

Similar equations are used for the up dating of  $\mathbf{F}_y''$  and  $\mathbf{F}_z''$ , just replacing the index  $x$  by  $y$  and  $z$  respectively.

### 3.4.2 Comparison of NPML with C-PML

To demonstrate the efficiency of the proposed NPML, we will first compare it to C-PML. The comparison has been made on the following test case: propagation in a homogeneous orthotropic solid medium. The properties, density and elasticity coefficients, of the different orthotropic materials, used in the simulations presented in this, and in the following paragraphs, are shown in Tab. 3.1. The choice of the material name has been made, following Bécache *et al.* [10], in order to simplify the comparison of our results with previous ones [2], [10], [126]. Moreover, as only the NPML has been implemented in the DG-FEM scheme, the calculation has been made with a Pseudo-Spectral code [79], [22].

In all cases, a  $25 \times 25$  cm portion of an infinite solid has been discretized on a  $128 \times 128$  elements grid (including the 10 elements NPML or C-PML placed on each side), and a 5 ns time step was used.

**Tab. 3.1** Properties of the orthotropic materials used in the time domain simulations.

Material	$\rho$ (kg/m <sup>3</sup> )	$C_{11}$ (GPa)	$C_{22}$ (GPa)	$C_{12}$ (GPa)	$C_{66}$ (GPa)
I	4000	40	200	38	20
III	4000	40	200	75	20
V	4000	300	60	99	15
Isotropic	1000	20	20	16	2

The following source term  $s(x, y, t)$  is added in the right hand side of Eq. (3.36):

$$s(x, y, t) = (0.5 + a_1(t - t_D)^2) \cdot e^{a_1(t-t_D)^2} \cdot (e^{-7(x^2+y^2)/r_0^2} / r_0^2), \quad (3.40)$$

where  $a_1 = (\pi f_c)^2$ ,  $f_c = 150$  KHz is the central frequency,  $t_D = 1/f_c$  is the source delay time, and  $r_0 = 5$  mm. It corresponds to a Gaussian spatial distribution around the (0, 0) point which is placed at the centre in all the simulations, and to a Ricker wavelet time evolution. The same spatial coordinate dependence (Eqs. 3.18) are used for the NPML parameters with now  $\alpha_{\max} = 20\pi$ ,  $n_1 = 2$ ,  $n_2 = 1$ ,  $n_3 = 1$  and:

$$\sigma_{\max} = (1 + n_1 + n_2) \cdot \sqrt{C_{11}/\rho_0} \cdot \log(1/R_0)/(2d), \quad (3.41)$$

where  $R_0 = 10^{-12}$ .

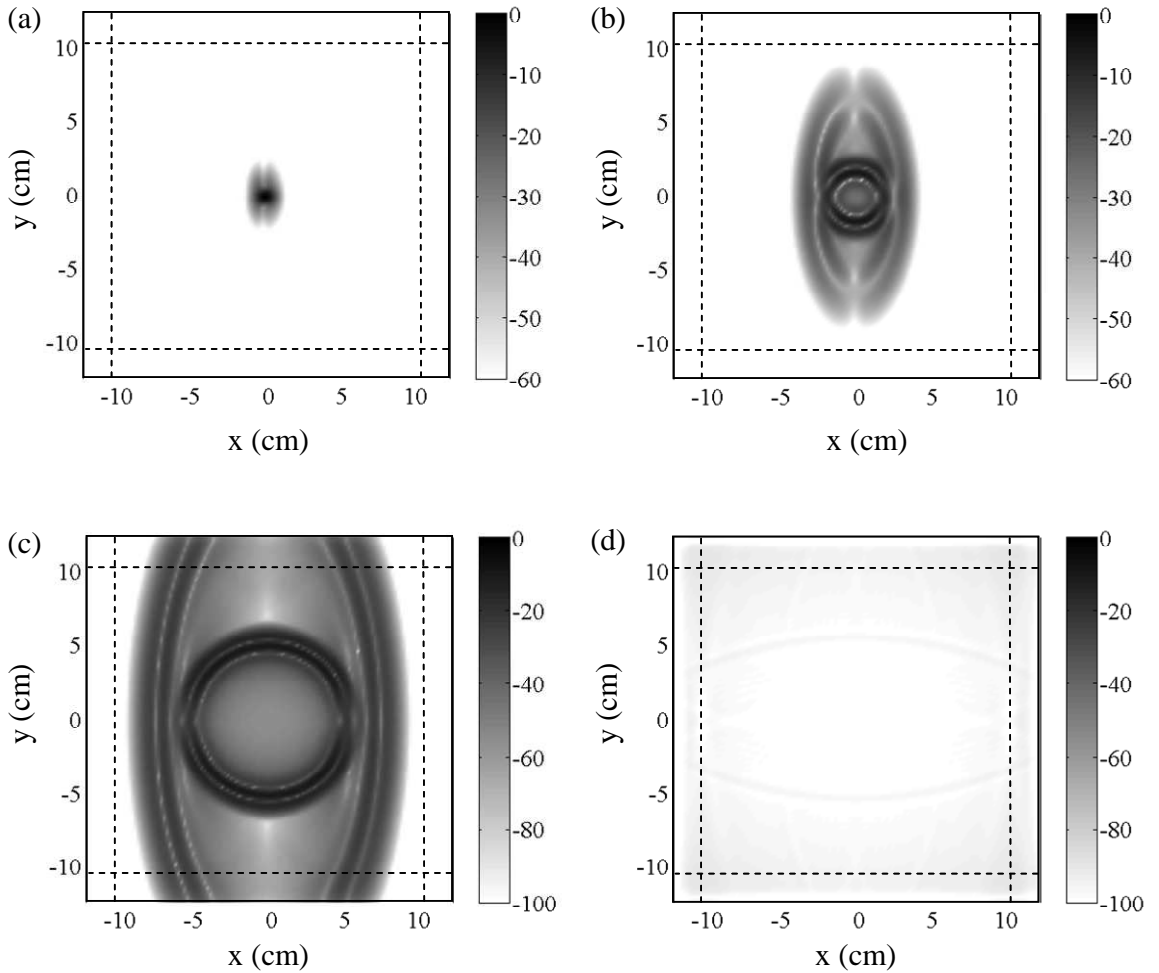


**Fig. 3.15** Snapshots of propagation of the displacement magnitude in an orthotropic elastic medium, model I, at (a)  $t = 5 \mu\text{s}$ , (b)  $t = 15 \mu\text{s}$ , (c)  $t = 30 \mu\text{s}$ , and (d)  $t = 125 \mu\text{s}$ . The snapshots are in dB scale with a reference displacement amplitude of 10 nm.

The obtained snapshots, for elastic waves propagation in an orthotropic medium (model I) are displayed on Fig. 3.15 for four different times  $5 \mu\text{s}$ ,  $15 \mu\text{s}$ ,  $30 \mu\text{s}$  and  $125 \mu\text{s}$  in dB scale

with a reference displacement of 10 nm. The results show that the NPML work well for this anisotropic medium and the level of spurious reflection is very small, only a -90 dB reflected pulse can be seen at the later time (Fig. 3.15(d)).

In order to quantify the efficiency of absorption of NPML method, the evolution of the total energy stored in the physical domain during the simulation has been investigated. The total energy at each time instant is computed according to the following expression:

$$E = \frac{1}{2} \int_{\Omega} \rho \|\mathbf{v}\|^2 d\Omega + \frac{1}{2} \int_{\Omega} \tau_{ij} \varepsilon_{ij} d\Omega, \quad (3.42)$$

where  $\Omega$  is the volume corresponding to the physical domain,  $\|\mathbf{v}\|$  is magnitude of the velocity vector,  $\tau_{ij}$  are the components of the stress tensor, and  $\varepsilon_{ij}$  are the components of the strain tensor. Fig. 3.16 displays the energy decay in the physical domain for the proposed C-PML and NPML models. The wave field has left the physical domain at about 60  $\mu\text{s}$  here. This figure not only confirms that at later time the energy has decayed by a factor  $10^{12}$ , but also demonstrates that no significant spurious reflection appears before. Moreover, the same

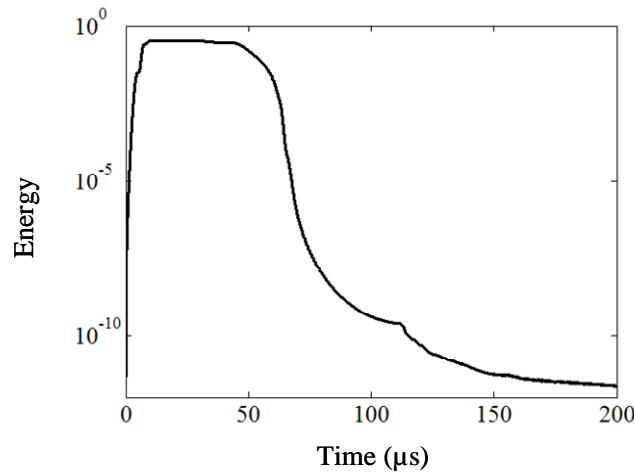


**Fig. 3.16** Energy decay in computational domain for C-PML (dashed line) and NPML (solid line) for the orthotropic elastic medium, model I, in the same conditions as the ones used to obtain the snapshots of Fig. 3.15.

ability of energy absorption has been obtained with the two methods for this anisotropic media, confirming the fact that NPML is a true perfectly matched layer.

Snapshots of the propagation of the amplitude of the displacement in the medium III are displayed for 4 different times (5, 15, 30 and 50  $\mu\text{s}$ ) on Fig. 3.17. As in the case of the others PML or C-PML implementations, some instabilities appear (Fig. 3.17(c)-(d)) in the absorbing layers. The energy decay in the computational domain for this simulation is shown on Fig. 3.18. When the quasi-transversal wave penetrates in the NPML (at time  $t = 35 \mu\text{s}$ ) the energy begins to increase with time, corresponding to an instable behaviour of the NPML.

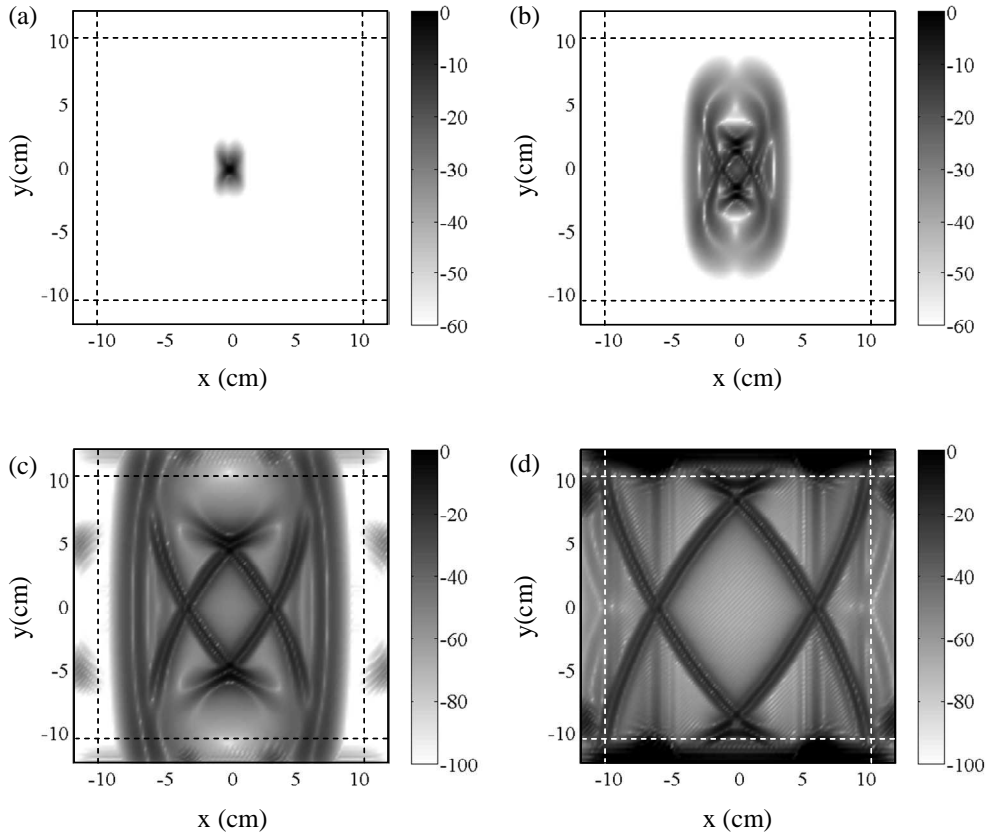


**Fig. 3.17** Snapshots of propagation of the displacement magnitude in an orthotropic elastic medium, model III, at (a)  $t = 5 \mu\text{s}$ , (b)  $t = 15 \mu\text{s}$ , (c)  $t = 30 \mu\text{s}$ , and (d)  $t = 50 \mu\text{s}$ . The snapshots are in dB scale with a reference displacement amplitude of 10 nm. Instabilities are observed for the NPML terminations used in the simulation.

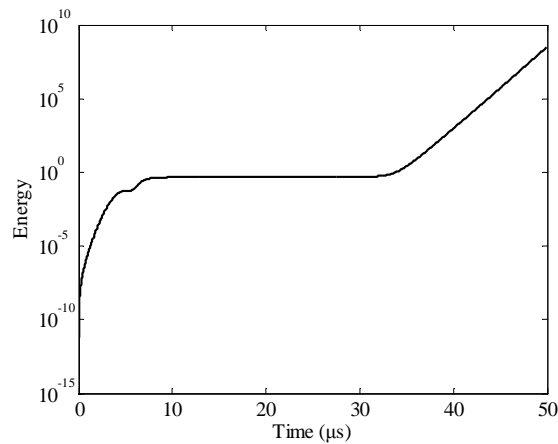


**Fig. 3.18** Time evolution of the energy in the computational domain for NPML for the orthotropic elastic medium, model III, in the same conditions as the ones used to obtain the snapshots of Fig. 3.17.

As explained by Bécache *et al.* [10], one of the incident elastic waves arrives with the components of the group velocity and the slowness vector, in the NPML direction, of opposite signs. The slowness curves for the considered orthotropic medium are represented in Fig. 3.19. There are some wave vectors  $\mathbf{k}$  (whose extremities describe the purple line) for which the component in the  $x$  direction of the group velocity has an opposite direction than the

component in the  $x$  direction of the phase velocity. In these directions the NPML are not stable. Similarly, there are some wave vectors  $\mathbf{k}$  (whose extremities describe the blue line) for the component in the  $y$  direction of the group velocity has an opposite direction than the component in the  $y$  direction of the phase velocity.

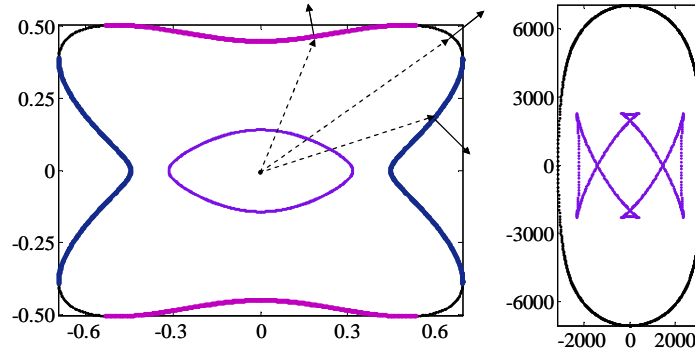


**Fig. 3.19** Slowness curves (left) and wave front (right) for the orthotropic anisotropic medium (III). Purple lines correspond to incident wave direction for which the NPLM in the  $x$  direction is unstable. Blue lines correspond to incident wave direction for which the NPLM in the  $y$  direction is unstable.

These instabilities are one of the major limitations in the use of PML for elastic waves propagating in anisotropic solids and in plates, even in the case of an isotropic medium [11]. For anisotropic solids an absorbing layer called “MPML”, showing no instabilities, has recently been developed [126]. But, contrary to what is claimed by the authors their “MPML” is not perfectly matched to the physical domain and corresponds in fact to a mixture of classical PML and of sponge layer [39], with a controllable ratio of these two kinds of absorbing layers. This mixture can easily be extended to the case where C-PML or NPML is used in place of PML. More details on the behaviour of these combined absorbing layers will be given in the next part.

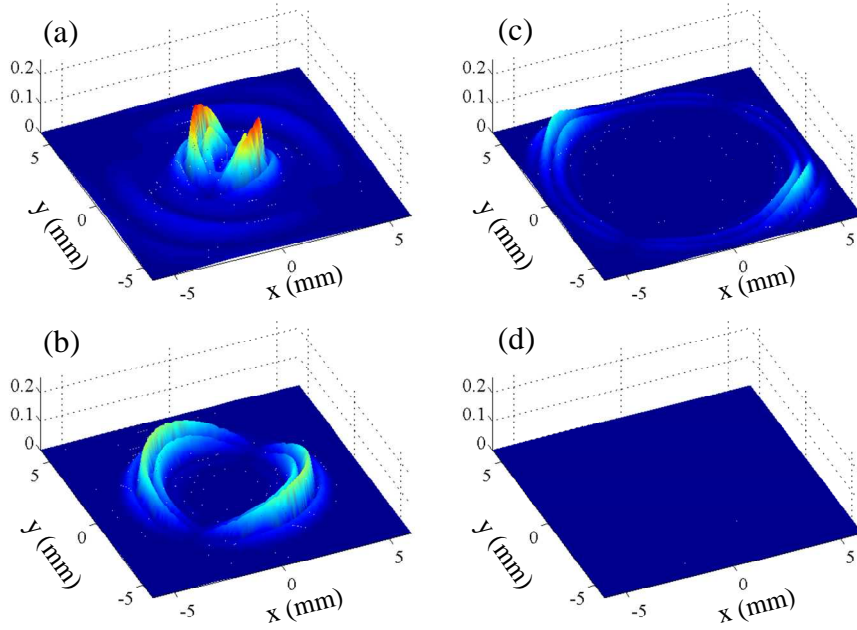


**Fig. 3.20** Snapshots of propagation of the particle velocity magnitude in an isotropic elastic medium, at (a)  $t = 2 \mu\text{s}$ , (b)  $t = 3.5 \mu\text{s}$ , (c)  $t = 5 \mu\text{s}$ , and (d)  $t = 10 \mu\text{s}$  obtained with the RK-DG-FEM O4 scheme using quadrilateral elements.

To conclude this part, an example of results obtained with the proposed NPML formulation introduced in the DG-FEM scheme is presented. The NPML has been introduced using a block implementation, each block corresponding to a set of equations. This method is very useful in configuration where one want to simulate a multi-physics problem. The interface between the two blocks is considered as an exterior boundary for each block, on which specific boundary conditions depending on results obtained in the other block need to be applied. In the considered case, in one block (physical domain) only Eq. (2.1) is solved, and both Eqs. (3.36) and (3.37) in the second one (NPML domain). A  $12 \times 12$  mm portion of an infinite solid has been discretized on a  $24 \times 24$  quadrilateral elements grid including the 4 NPML elements placed on each side. The material properties of the simulated isotropic medium are given in Tab. 3.1. The source is as before a Ricker wavelet with a central frequency of 900 kHz. The snapshots of the particle velocity magnitude at  $t = 2 \mu\text{s}$ ,  $t = 3.5 \mu\text{s}$ ,  $t = 5 \mu\text{s}$ , and  $t = 10 \mu\text{s}$  obtained with a RK-DG-FEM O4 scheme are displayed on Fig. 3.20. No reflection can be noticed on the last snapshot demonstrating the validity of the NPML implementation. The time evolution of the particle velocity components shown on Fig. 3.21 at a receiver position (3.8, 0) (mm) close to the NPML / physical domain interface, confirms the excellent absorbing behaviour of the proposed absorbing layer.

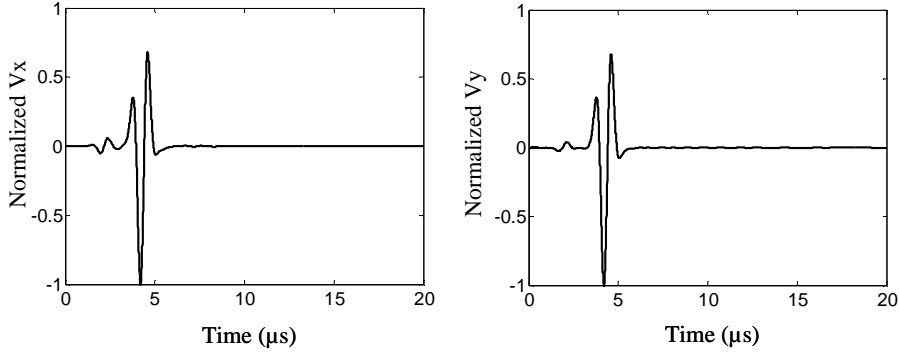


**Fig. 3.21** Time evolution of the normalized (a)  $V_x$  and (b)  $V_y$  particle velocity components calculated at the receiver position (3.8, 0) (mm).

### 3.5 Stabilized Absorbing Boundary Layer

In the preceding subsections, we have seen that for anisotropic solid medium the PML are not always stable. This problem is the main limitation of PML in elastodynamic applications. In this part, the Multiaxial Perfectly Matched Layer (“MPML”) [126] proposed to stabilize PML will be first presented. We will then show that this “MPML” is not perfectly matched to the physical domain and corresponds in fact to a mixture of classical PML and of sponge layer. The stability of this MPML is studied with the help of the method introduced by Bécache *et al.* [10] for PML. This analysis allows giving a physical interpretation of the stability criteria obtained by Meza-Fajardo and Papageorgiou [126]. All this theoretical work is finally validated by numerical examples.

#### 3.5.1 Formulation of Stabilized Absorbing Boundary Layer

The introduction of the stabilized absorbing boundary layer, the so-called “MPML”, is in all points similar to the one of other PML, as C-PML or NPML. However, in the “MPML” the attenuation parameters  $\sigma_x$  and  $\sigma_y$  of the stretching parameter  $s_x$  and  $s_y$  are now a function of the two space variables  $x$  and  $y$ . Considering, as for NPML, Eq. (2.1) in frequency domain, and moving to the stretched coordinates we arrive to:

$$j\omega\hat{Q} = \frac{1}{s_x(x, y)} \frac{\partial \hat{F}}{\partial x} + \frac{1}{s_y(x, y)} \frac{\partial \hat{G}}{\partial y}. \quad (3.43)$$

Coming back to time domain using an inverse Fourier transform, and introducing memory variables we obtain:

$$\frac{\partial Q}{\partial t} = \frac{1}{\kappa_x} \frac{\partial F}{\partial x} + \frac{1}{\kappa_y} \frac{\partial G}{\partial y} + \frac{1}{\kappa_x} F_1 + \frac{1}{\kappa_y} G_2, \quad (3.44)$$

where

$$\frac{\partial F_1}{\partial t} = -\frac{\sigma_x(x, y)}{\kappa_x} \frac{\partial F}{\partial x} - \left( \frac{\sigma_x(x, y)}{\kappa_x} + \alpha_x \right) F_1, \quad (3.45a)$$

$$\frac{\partial G_2}{\partial t} = -\frac{\sigma_y(x, y)}{\kappa_y} \frac{\partial G}{\partial y} - \left( \frac{\sigma_y(x, y)}{\kappa_y} + \alpha_y \right) G_2. \quad (3.45b)$$

Eq. (3.44) is exactly the same equation as the one obtained for C-PML. The only difference is the definition of the  $\sigma_x$  and  $\sigma_y$  parameters.

First, to compare our results to the formulation of Ref. [126], we consider the linear elastodynamic case ( $F = AQ$  and  $G = BQ$ ), with  $\kappa_{x,y} = 1$  and  $\alpha_{x,y} = 0$ . Then Eq. (3.44) and Eqs. (3.45) become:

$$\frac{\partial Q}{\partial t} = A \frac{\partial Q}{\partial x} + B \frac{\partial Q}{\partial y} + AQ_1 + BQ_2, \quad (3.46)$$

with

$$\frac{\partial Q_1}{\partial t} = -\sigma_x(x, y) \left( \frac{\partial Q}{\partial x} + Q_1 \right), \quad (3.47a)$$

$$\frac{\partial Q_2}{\partial t} = -\sigma_y(x, y) \left( \frac{\partial Q}{\partial y} + Q_2 \right). \quad (3.47b)$$

Letting  $\sigma_x(x, y)Q_1' = -AQ_1$  and  $\sigma_y(x, y)Q_2' = -BQ_2$ , we arrive to a set of equations equivalent to the one obtained by Meza-Fajardo and Papagiorgiou [126] for their ‘‘MPML’’:

$$\frac{\partial Q_1'}{\partial t} + \sigma_x(x, y)Q_1' = A \frac{\partial Q}{\partial x}, \quad (3.48a)$$

$$\frac{\partial Q_2'}{\partial t} + \sigma_y(x, y)Q_2' = B \frac{\partial Q}{\partial y}, \quad (3.48b)$$

and  $Q = Q_1' + Q_2'$ . In fact, as it will be demonstrated later, this so-called ‘‘MPML’’ does not correspond to a perfectly matched layer.

In order to give a new interpretation of these ‘‘MPML’’ the attenuation parameters  $\sigma_{x,y}$  are split up in  $x$  and  $y$  dependent components:  $\sigma_x(x, y) = \sigma_{xx}(x) + \sigma_{xy}(y)$  and  $\sigma_y(x, y) = \sigma_{yx}(x) + \sigma_{yy}(y)$ . Introducing these parameters, Eqs. (3.48) are re-written as:

$$\frac{\partial Q_1'}{\partial t} + d(x, y)Q_1' + d_1(x)Q_1' = A \frac{\partial Q}{\partial x}, \quad (3.49a)$$

$$\frac{\partial Q_2'}{\partial t} + d(x, y)Q_2' + d_2(y)Q_2' = B \frac{\partial Q}{\partial y}, \quad (3.49b)$$

where  $d(x, y) = \sigma_{xy}(y) + \sigma_{yx}(x)$ ,  $d_1(x) = \sigma_{xx}(x) - \sigma_{yx}(x)$  and  $d_2(y) = \sigma_{yy}(y) - \sigma_{xy}(y)$  have been introduced. When  $d_1(x) = 0$ , e.g.  $\sigma_{xx}(x) = \sigma_{yx}(x)$ , and  $d_2(y) = 0$ , e.g.  $\sigma_{yy}(y) = \sigma_{xy}(y)$ , Eqs. (3.49) lead to the equations of the sponge layers introduced by Israeli and Orszag [100]. Now, when  $d(x, y) = 0$ , e.g.  $\sigma_{xy}(y) = \sigma_{yx}(x) = 0$ , Eqs. (3.49) become the equations obtained for split

PML. This shows that “MPML” is a mixture of PML and sponge layer, where the respective ratios of the two types of absorbing layers are  $p^x = \sigma_{yx}(x)/\sigma_{xx}(x)$  and  $p^y = \sigma_{xy}(y)/\sigma_{yy}(y)$ , in the  $x$  and  $y$  direction respectively. As the sponge layers are not perfectly matched to the physical domain, the obtained “MPML” are not perfectly matched layers. This conclusion agrees with the fact that to obtain a perfectly matched layer for elastic wave, the projection of the wave vector  $\mathbf{k}$  in the direction perpendicular to the PML need to be the same in the PML and in the physical domain, as demonstrated by Chew and Liu [43]. So, no modification (attenuation term) can be introduced in this component as it was the case in the “MPML”.

Eq. (3.44) is a generalisation of the “MPML” which includes all the benefit of using C-PML in place of “classical” PML. A similar idea has been developed by Martin *et al.* [120] and implemented in a spectral-element scheme [105]. The same stabilization procedure can be introduced in the proposed NPML, leading to:

$$\frac{\partial \mathbf{Q}}{\partial t} = \frac{\partial \left( \frac{\mathbf{F}'' + \mathbf{F}}{\kappa_x} \right)}{\partial x} + \frac{\partial \left( \frac{\mathbf{G}'' + \mathbf{G}}{\kappa_y} \right)}{\partial y}, \quad (3.50)$$

with

$$\frac{\partial \mathbf{F}''}{\partial t} = -\alpha_x \mathbf{F}'' - \frac{\sigma_x(x, y)}{\kappa_x} (\mathbf{F}'' + \mathbf{F}), \quad (3.51a)$$

$$\frac{\partial \mathbf{G}''}{\partial t} = -\alpha_y \mathbf{G}'' - \frac{\sigma_y(x, y)}{\kappa_y} (\mathbf{G}'' + \mathbf{G}). \quad (3.51b)$$

As all these stabilized absorbing boundary layers are not truly matched to the physical domain and correspond to a mixture of PML and sponge layer, the ratio between the two kinds of absorbing layer need to be carefully chosen. Indeed, the proportion of sponge layer need to be as small as possible, but enough to stabilize the PML. A stability analysis will give us a mean to determine the optimum choice of the ratio between the two kinds of absorbing layer.

### 3.5.2 Stability Analysis

To analyse the stability of these “MPML”, we use the method introduced for PML by Bécache *et al.* [10], and used by Appelö and Kreiss [2] for C-PML. In an anisotropic solid, the dispersion equation can be written as:

$$F_0(\omega, \mathbf{k}) = \det(\Gamma(\mathbf{k}) - \rho_0 \omega^2 I) = 0, \quad (3.52)$$

where in the case of an orthotropic medium,  $\Gamma(\mathbf{k})$  the Christoffel’s tensor in 2D is given by:

$$\Gamma(\mathbf{k}) = \begin{pmatrix} C_{11}k_1^2 + C_{66}k_2^2 & (C_{12} + C_{66})k_1k_2 \\ (C_{12} + C_{66})k_1k_2 & C_{66}k_1^2 + C_{22}k_2^2 \end{pmatrix}, \quad (3.53)$$

and  $I$  is the identity tensor. Using the same notation as Meza-Fajardo and Papagiorgiou [126]:

$$c_1 = \frac{C_{66}C_{11}}{\rho_0^2}, \quad c_2 = \frac{C_{66}C_{22}}{\rho_0^2}, \quad c_3 = \frac{C_{11} + C_{66}}{\rho_0}, \quad c_4 = \frac{C_{22} + C_{66}}{\rho_0}, \quad \text{and} \quad c_5 = \frac{C_{11}C_{22} - C_{12}^2 - 2C_{12}C_{66}}{\rho_0^2},$$

the dispersion equation becomes:

$$F_0(\omega, \mathbf{k}) = \rho_0^2[\omega^4 - \omega^2(k_1^2 c_3 + k_2^2 c_4) + (c_1 k_1^4 + c_2 k_2^4 + c_5 k_1^2 k_2^2)], \quad (3.54)$$

The four solutions of this dispersion equation are  $\omega(\mathbf{k}) = \pm\omega_{QP}(\mathbf{k})$  and  $\omega(\mathbf{k}) = \pm\omega_{QS}(\mathbf{k})$  where

$$\omega_{QP}(\mathbf{k}) = \sqrt{\frac{1}{2}\left(k_1^2 c_3 + k_2^2 c_4 + \sqrt{(k_1^2 c_3 + k_2^2 c_4)^2 - 4(k_1^4 c_1 + k_2^4 c_2 + k_1^2 k_2^2 c_5)}\right)}, \quad (3.55a)$$

and

$$\omega_{QS}(\mathbf{k}) = \sqrt{\frac{1}{2}\left(k_1^2 c_3 + k_2^2 c_4 - \sqrt{(k_1^2 c_3 + k_2^2 c_4)^2 - 4(k_1^4 c_1 + k_2^4 c_2 + k_1^2 k_2^2 c_5)}\right)}, \quad (3.55b)$$

corresponding to quasi-longitudinal ( $QP$ ) and quasi-transversal ( $QS$ ) waves propagating in  $\pm\mathbf{k}$  directions.

The dispersion equation of ‘‘MPML’’ in the  $x$  direction can be obtained from Eq. (3.54) by replacing  $k_1$  by  $k_1/s_x^x$  and  $k_2$  by  $k_2/s_y^x$ :

$$F_{MPMLx}(\omega, \mathbf{k}) = F_0\left(\omega, \frac{k_1}{s_x^x}, \frac{k_2}{s_y^x}\right). \quad (3.56)$$

Multiplying this equation by  $(\omega - j\sigma_x - j\alpha_x)$  we arrive at:

$$F_{MPMLx}(\omega, \mathbf{k}) = F_0\left(\omega(\omega - j\sigma_x - j\alpha_x), k_1(\omega - j\alpha_x), k_2 \frac{(\omega - j\alpha_x)}{(\omega - jp^x\sigma_x - j\alpha_x)}(\omega - j\sigma_x - j\alpha_x)\right). \quad (3.57)$$

Introducing the following notations,  $V_p = \frac{\omega}{|\mathbf{k}|}$  the phase velocity,  $\varepsilon = \frac{\sigma_x}{|\mathbf{k}|}$  and  $\delta = \frac{\alpha_x}{|\mathbf{k}|}$  the normalized attenuation and frequency shift parameters, respectively, of the C-PML, and  $\mathbf{K} = \frac{\mathbf{k}}{|\mathbf{k}|}$ , the dispersion equation becomes:

$$\begin{aligned} F_{MPMLx}(V_p, \mathbf{K}, \varepsilon) &= F_0\left(V_p(V_p - j\varepsilon - j\delta), K_1(V_p - j\delta), \frac{K_2(V_p - j\delta)}{(V_p - jp^x\varepsilon - j\delta)}(V_p - j\varepsilon - j\delta)\right) \\ &= F_0\left(V_p, K_1\left(1 - \frac{j\varepsilon}{V_p - j\delta}\right)^{-1}, K_2\left(1 - \frac{jp^x\varepsilon}{V_p - j\delta}\right)^{-1}\right) \end{aligned} \quad (3.58)$$

The stability of the ‘‘MPML’’ system can be analysed by a perturbation analysis for  $\varepsilon \ll 1$ . We expand, for the C-PML case,  $V_p$  in power of the attenuation parameter  $\varepsilon$ :

$$V_p(\mathbf{K}, \varepsilon) = V_p(\mathbf{K}, 0) + \varepsilon \alpha(\mathbf{K}) + O(\varepsilon^2). \quad (3.59)$$

This is equivalent to expanding the angular frequency  $\omega$  in power of the PML attenuation coefficient  $\sigma$ :

$$\omega(k, \sigma) = \omega(k) + \sigma \alpha(\mathbf{K}) + O((\sigma/\omega)^2). \quad (3.60)$$

To understand the physical interpretation of the stability condition we will obtain by the perturbation analysis, we consider a plane wave expansion:

$$D e^{j(\omega(k, \sigma)t - k_1 x - k_2 y)} = D e^{j(\omega(k)t - k_1 x - k_2 y)} e^{j\sigma \alpha(\mathbf{K})t}. \quad (3.61)$$

So, if  $\text{Im}\{\alpha(\mathbf{K})\} < 0$ , then  $j\sigma \alpha(\mathbf{K})$  becomes positive and the PML amplifies the incoming wave, and so becomes instable.

Now, we expand Eq. (3.58) in power of  $\varepsilon$  around  $\varepsilon = 0$ :

$$F_{MPMLx}(V_p, \mathbf{K}) + \varepsilon \alpha(\mathbf{K}) \frac{\partial F_0}{\partial \omega} + \frac{\partial F_0}{\partial K_1} j \varepsilon \frac{K_1}{V_p - j\delta} + \frac{\partial F_0}{\partial K_2} j p^x \varepsilon \frac{K_2}{V_p - j\delta} + O(\varepsilon^2) = 0. \quad (3.62)$$

The first term is equal to 0 due to Eq. (3.52), and then Eq. (3.62) leads, for the attenuation of a plane wave propagating along the direction  $\mathbf{k}$  in the ‘‘MPML’’, to:

$$\alpha(\mathbf{K}) = - \left( \frac{\partial F_0}{\partial \omega} \right)^{-1} \frac{\partial F_0}{\partial K_1} j \frac{K_1}{V_p - j\delta} - \left( \frac{\partial F_0}{\partial \omega} \right)^{-1} \frac{\partial F_0}{\partial K_2} j p^x \frac{K_2}{V_p - j\delta}. \quad (3.63)$$

To give a physical interpretation of the stability condition, we need to link all the terms to a physical quantity. In fact, in Eq. (3.63) only two physical quantities appear: the slowness vector  $\mathbf{S}$  and the group velocity  $\mathbf{V}_g$ , which are given by:

$$\mathbf{S}(\mathbf{K}) = \frac{\mathbf{K}}{V_p}, \quad (3.64)$$

and

$$\mathbf{V}_g(\mathbf{K}) = \frac{\partial \omega(\mathbf{K})}{\partial \mathbf{K}} = \begin{vmatrix} \frac{\partial \omega(\mathbf{K})}{\partial K_1} \\ \frac{\partial \omega(\mathbf{K})}{\partial K_2} \end{vmatrix} = - \left( \frac{\partial F_0}{\partial \omega} \right)^{-1} \begin{vmatrix} \frac{\partial F_0}{\partial K_1} \\ \frac{\partial F_0}{\partial K_2} \end{vmatrix}, \quad (3.65)$$

respectively. So,  $\alpha(\mathbf{K})$  can be expressed in function of the components of the group velocity and the slowness vector:

$$\alpha(\mathbf{K}) = (j S_1 V_{g1} + j p^x S_2 V_{g2}) \frac{V_p}{V_p - j\delta}. \quad (3.66)$$

It follows that:

$$\text{Im}\{\alpha(\mathbf{K})\} = (S_1 V_{g1} + p^x S_2 V_{g2}) \frac{V_p^2}{V_p^2 + \delta^2}, \quad (3.67)$$

leading finally to the ‘‘MPML’’ stability condition:

$$(S_1 V_{g1} + p^x S_2 V_{g2}) > 0 \text{ or } p^x > \max\left(-\frac{S_1 V_{g1}}{S_2 V_{g2}}, 0\right). \quad (3.68)$$

First, when  $p^x = 0$ , in the pure C-PML or NPML case, the absorbing layer is stable when the slowness (or phase velocity) and the group velocity of the wave incoming in the PML are of the same sign:

$$S_1 V_{g1} > 0. \quad (3.69)$$

Unfortunately, this condition is not always verified for all the angle of incidence of the wave impinging on the boundary between the physical domain and the PML in an anisotropic solid, as shown on Fig. 3.22 for the orthotropic medium III. In this example, the waves arriving on the PML with an angle of incidence higher than about  $40^\circ$  will be amplified, instead of being absorbed. Moreover, Fig 3.22 is perfectly similar to the PML eigenderivatives of  $QS$  modes plotted on figure 7 of Ref. [126]. This shows that the different stability analysis used by these authors leads to exactly the same stability criteria. Here, a clear physical interpretation is given.

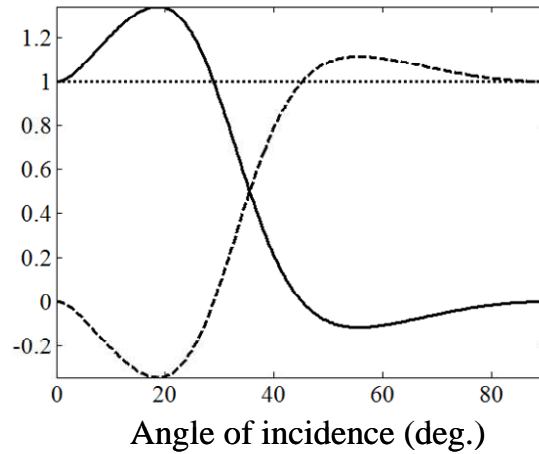


**Fig. 3.22** Evolution as a function of the angle of the incident plane wave of  $S_1 V_{g1}$  (solid line),  $S_2 V_{g2}$  (dashed line), and  $S_1 V_{g1} + S_2 V_{g2}$  (dotted line) for the orthotropic medium III.

Secondly, when  $p^x = 1$ , in the sponge layer case, as  $S_1 V_{g1} + S_2 V_{g2} = 1$ , the absorbing layer is always stable. This also leads to the fact that if  $S_1 V_{g1} < 0$ , *e.g.* the PML is unstable, it exists always a positive value of  $p^x$  such as  $S_1 V_{g1} + p^x S_2 V_{g2} = 0$ . This value of  $p^x$  corresponds to the minimal value needed to stabilize the PML. In the preceding example, medium III, this value is 0.25. So, when it is used in the ‘‘MPML’’,  $S_1 V_{g1} + p^x S_2 V_{g2}$  becomes positive for all angles of incidence, as demonstrated on Fig. 3.23(a), and the absorbing layer is stable. All these

results are also true for PML in the  $y$  direction, just replacing  $x$  by  $y$  and 1 by 2 in the previous formula. Evidently higher value of  $p^x$  can be used, as for example 0.6 as shown on Fig. 3.23(b), but at the expense of an increase of the reflection of incident wave on the layer, as it will become clear now through the numerical examples of the next section.

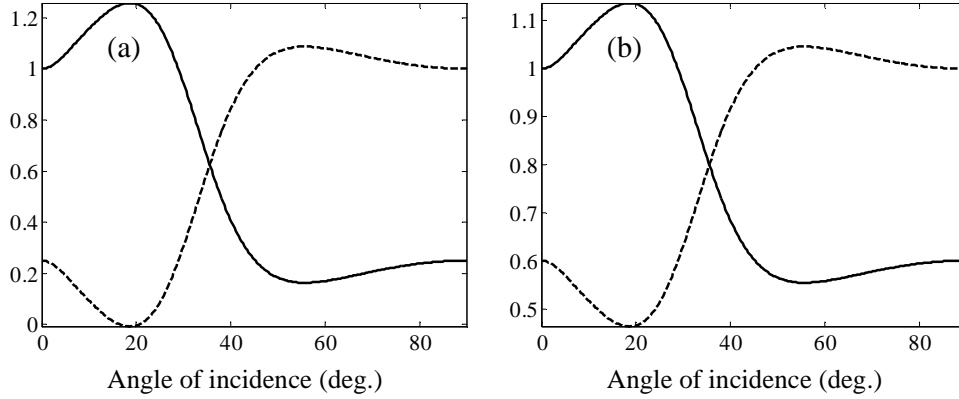


**Fig. 3.23** Evolution as a function of the angle of the incident plane wave of (a)  $S_1V_{g1} + 0.25 S_2V_{g2}$  (solid line) and  $0.25 S_1V_{g1} + S_2V_{g2}$  (dashed line), and (b)  $S_1V_{g1} + 0.6 S_2V_{g2}$  (solid line) and  $0.6 S_1V_{g1} + S_2V_{g2}$  (dashed line) for the orthotropic medium III.

### 3.5.3 Numerical Simulations of MPML for Anisotropic Solid Medium

All simulations presented in this subsection are identical to the ones described in part 3.4.2, only the orthotropic medium, in which the waves propagate, changes.

Snapshots of the propagation of the amplitude of the displacement obtained for medium III with a ratio of 0.25 between the amplitude of the maximal absorption of the sponge layer and the C-PML ( $p^x = p^y = 0.25$ ) are displayed for 4 different times (5, 15, 30 and 125  $\mu\text{s}$ ) on Fig. 3.24. Here and in all the following figures, the snapshots presented are in dB scale with a reference displacement of 10 nm. The instabilities, as expected, have completely disappeared, in comparison to Fig. 3.17, but at the expense of a stronger reflection of the waves impinging the absorbing layer with a grazing angle (Fig. 3.24(d)). This increase of the reflection is in perfect accordance with the non perfectly matched character of the fraction of sponge layer introduced to stabilize the C-PML.

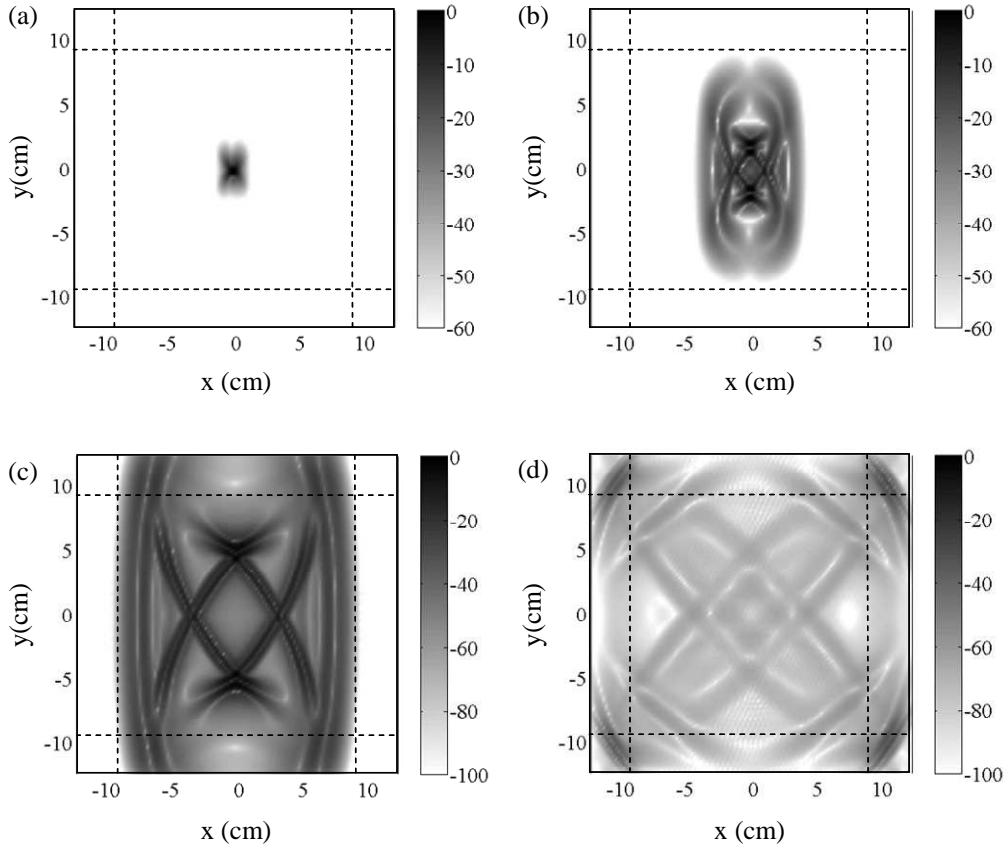


**Fig. 3.24** Snapshots of propagation of the displacement magnitude in an orthotropic elastic medium, model III, at (a)  $t = 5 \mu\text{s}$ , (b)  $t = 15 \mu\text{s}$ , (c)  $t = 30 \mu\text{s}$ , and (d)  $t = 125 \mu\text{s}$ . The snapshots are in dB scale with a reference displacement amplitude of 10 nm. No instability is observed for the “MPML” terminations used in the simulation.

The energy decay in the computational domain for this simulation is shown on Fig. 3.25. For  $p^x = p^y = 0.25$  the level of spurious reflection is around  $10^{-5}$ . The obtained level of reflection is higher than expected (chosen  $R_0$  value) and increase when  $p^x$  and/or  $p^y$  are increased, as shown on the same figure for  $p^x = p^y = 0.6$  (solid line). All these behaviour are in perfect agreement with the theoretical analysis presented in the previous section.

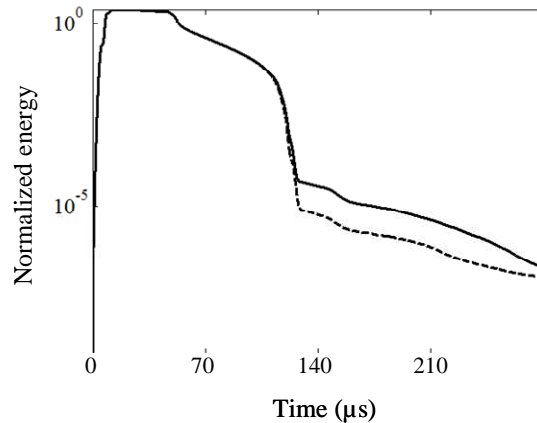


**Fig. 3.25** Energy decay in computational domain for “MPML” for the orthotropic elastic medium (III), with  $p^x = p^y = 0.25$  (dashed line) and  $p^x = p^y = 0.6$  (solid line). The energy is normalized with respect to its maximum value.

To complete this study, we now look at a case where the C-PML is stable, in order to make a direct quantification of the imperfections introduced by the addition of a fraction of sponge layer. On Fig. 3.26, snapshots of the propagation of the amplitude of the displacement in the medium V are displayed for the same 4 different times as in medium I, when C-PML are used. From the point of view of the stability analysis, made with the perturbation method, the application of PML to the medium V seems to have no reason to be unstable (Fig. 3.27). But numerical experiments have demonstrated [10] that for this medium split PML implementation are in fact not stable.

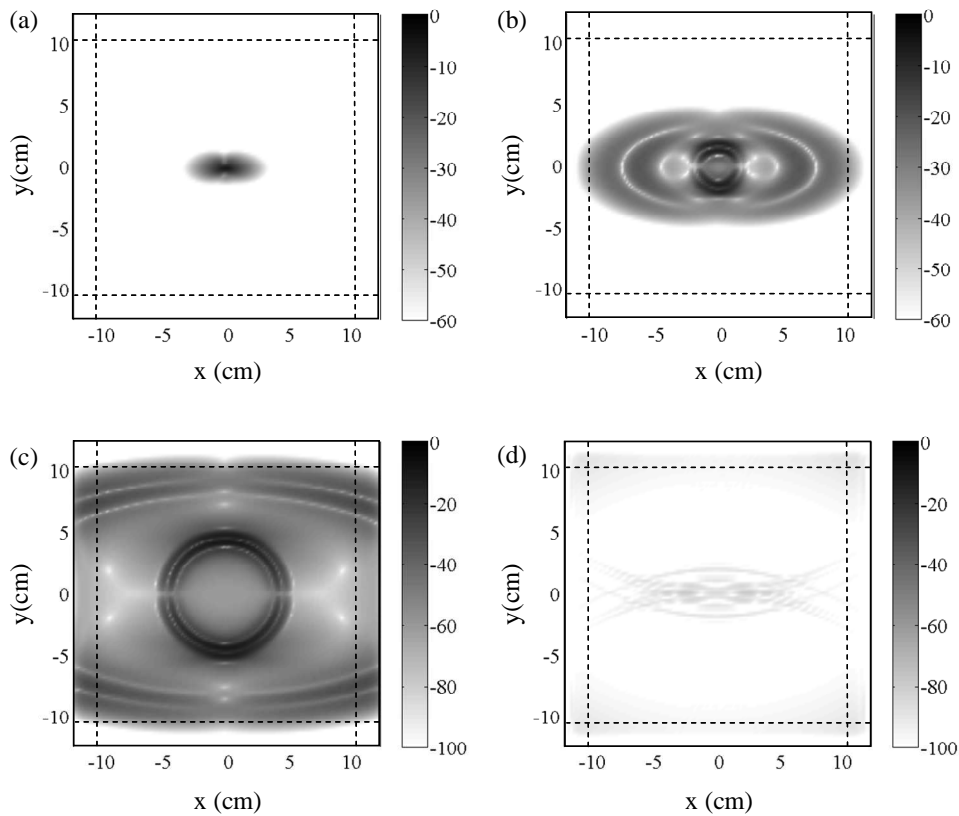


**Fig. 3.26** Snapshots of propagation of the displacement magnitude in an orthotropic elastic medium, model V, at (a)  $t = 5 \mu\text{s}$ , (b)  $t = 15 \mu\text{s}$ , (c)  $t = 30 \mu\text{s}$ , and (d)  $t = 125 \mu\text{s}$ . The snapshots are in dB scale with a reference displacement amplitude of 10 nm.

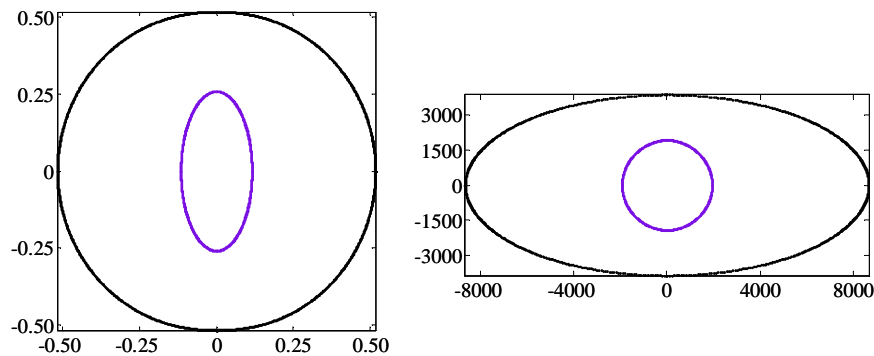


**Fig. 3.27** Slowness curves (left) and wave front (right) for the orthotropic anisotropic medium (V).

Here, contrary to the case of PML, no instabilities appear, even at longer time. This improved stability of the C-PML over the PML has already been demonstrated theoretically by Appelö and Kreiss [2]. In fact, the “new absorbing layer” they proposed, is nothing else than a new derivation of the C-PML introduced for elastic waves in Ref. [22]. It can be noted that it has also been proven that the C-PML is efficient in the case of nonlinear wave absorption [22], [3].

Energy decay in the physical domain has been plotted in Fig. 3.28 for C-PML (solid line) and “MPML” (dashed line), with  $p^x = p^y = 0.25$ . In this example the spurious reflection increases from  $10^{-6}$  when  $p^x = p^y = 0$  (C-PML) to  $10^{-4}$  when  $p^x = p^y = 0.25$ .

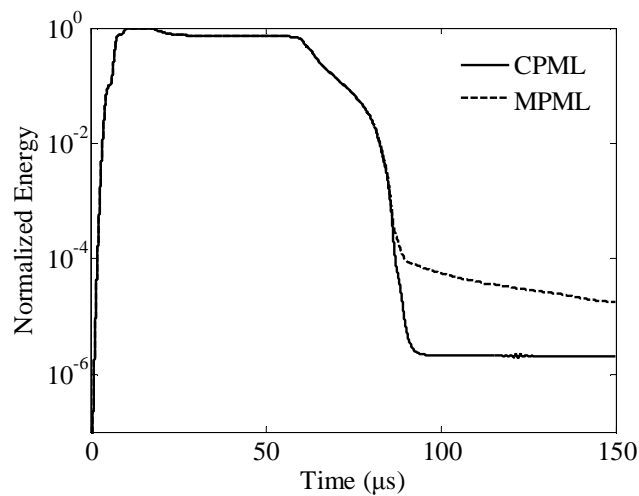


**Fig. 3.28** Energy decay in the physical domain of anisotropic medium (V) for C-PML (solid line) and “MPML” (dashed line). The energy is normalized with respect to its maximum value.

### 3.5.4 Application to Propagation in Isotropic and Piezoelectric Plate

In this part, we will present the use of the stabilized absorbing boundary layer formulation for isotropic solid and piezoelectric plates. It has been found that “classical” implementations of PML (or C-PML) absorbing regions don’t work satisfactorily for guided waves for frequencies where “inverse modes” with group and phase velocities of opposite signs are excited [11]. In frequency domain simulation, this lead to an erroneous selection of the outgoing wave by the C-PML. This corresponds to the existence of numerical instabilities in time domain simulations [10]. One solution proposed to overcome this problem has been to introduce complex elastic moduli, as in viscoelastic materials, with an imaginary part, representing attenuation, increasing with the distance to the absorbing regions boundary [37]. This method, which can be used only in frequency domain simulation, corresponds to a kind of “sponge layer” as already proposed in geophysics [39], but at the expense of an increased length of the absorbing zone [25], [116], [37]. An elegant way of preserving the use of short

length PML has been introduced by Skelton *et al.* [170], but at the expense of having now one different PML for each propagating mode.

For overcoming the “inverse mode” problem, we simply propose to use the stabilized absorbing layer with  $p^x = 1$ , which corresponds, for a C-PML in the  $x$  direction, to the following complex coordinate’s transformation [25], [116] in the plate medium:

$$\tilde{x} = \int_0^x s_x(x') dx', \quad (3.70a)$$

$$\tilde{y} = s_y(x)y. \quad (3.70b)$$

### 3.5.4.1 Single Mode Propagation in a Solid Waveguide

In order to validate the absorption efficiency of the stabilized absorbing layer, a single mode Lamb wave (A0) pulse propagation in an aluminium plate with a thickness jump was simulated. The physic model is described in Fig. 3.29. The considered excitation pulse is a Hanning windowed sinusoid:

$$s(t) = 0.5 \cdot \sin(2\pi f_c t) \cdot \left(1 + \cos\left(\frac{2\pi t}{T}\right)\right) \cdot \text{rect}\left(\frac{t}{T}\right), \quad (3.71)$$

with  $f_c = 200$  kHz and  $T = 50$   $\mu$ s.

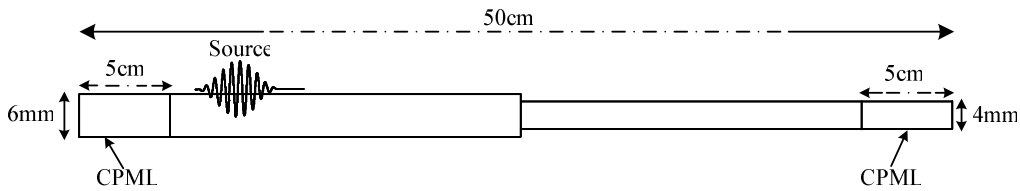


**Fig. 3.29** The model definition for the simulation of a single mode A0 propagation in an aluminum plate with a thickness jump.

Before the thickness jump, the normal displacement at the surface of the plate at 114 mm showing the direct A0 pulse and the reflected wave of A0 pulse by the jump is presented on Fig. 3.30(a). After the thickness jump (at the 364 mm), the transmitted pulse is shown on Fig. 3.30(b). No mode conversion can be noticed in this example. The results are in excellent agreement with the ones obtained by direct Finite Element Time Domain simulation [13], [14], but with a considerable diminution of the needed calculation time. Indeed, here the calculation takes around 15 minutes for 50 frequencies on a computer with a 2.4 GHz CPU.

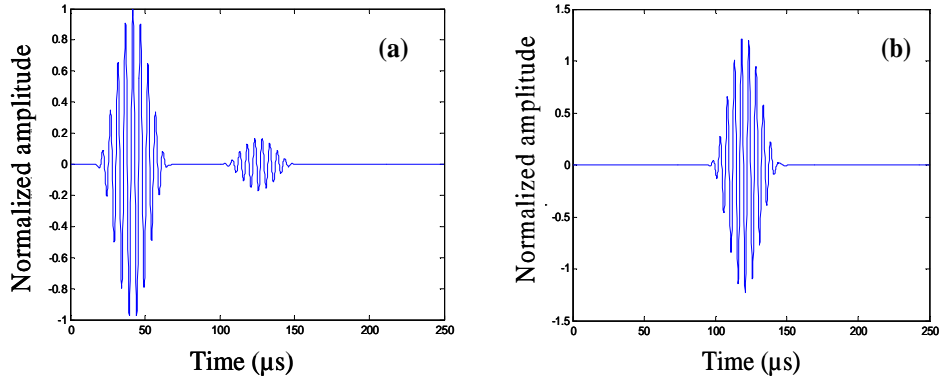


**Fig. 3.30** Normal displacements at the surface of the plate shown in Fig 3.29 at (a)  $l_1 = 114$  mm and (b)  $l_2 = 364$  mm from the source, when only the A0 mode has been excited.

### 3.5.4.2 Multimode Propagation in a Solid Waveguide

In this subsection, 2D simulation of elastic guided waves in a 8 mm thick aluminum plate has been done. In Fig. 3.31 the dispersion curves calculated, in the frequency range [50-550] kHz, with COMSOL Multiphysics compare favorably with the ones obtained by an analytical method.

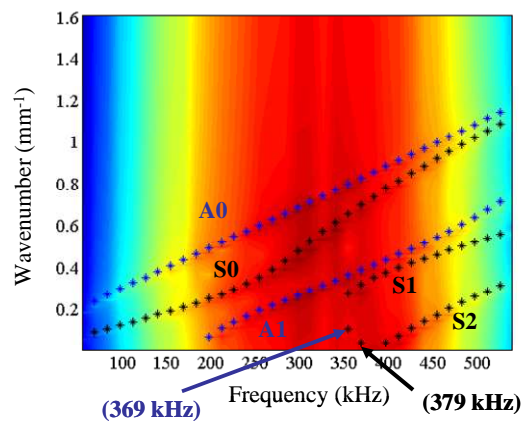


**Fig. 3.31** Comparison of the dispersion curves, for a 8 mm thick aluminum plate, obtained by FEM simulations and an analytical method (blue and black stars).

We consider now two frequencies (369 kHz and 379 kHz) for which the excited S2 mode is an inverse one. The wavenumber spectrum, obtained from signals measured at the surface of the plate between the S2 source and the stabilized absorbing layer zone, are shown respectively on Fig. 3.32 and Fig. 3.33.

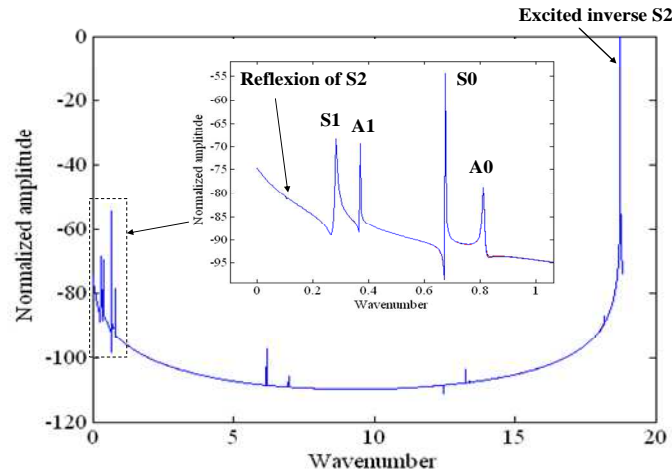


**Fig. 3.32** Wavenumber spectrum obtained from signals calculated at the surface of the plate between the 369 kHz S2 source and the stabilized absorbing layer.

In both case the same absorbing layer, with a length taken to be two times the longest wavelength in the model, has been used. The chosen parameters are:  $\sigma_{\max} = 3.2 \times 10^5$ ,  $\alpha_{\max} = 2\pi \times 10^4$  and  $k_{\max} = 0$ . The results show a reflection of the inverse S2 mode -80 dB smaller than the incident energy. When the same absorbing layer length and parameters are used with other modes excitations and/or different frequencies similar results are always obtained.

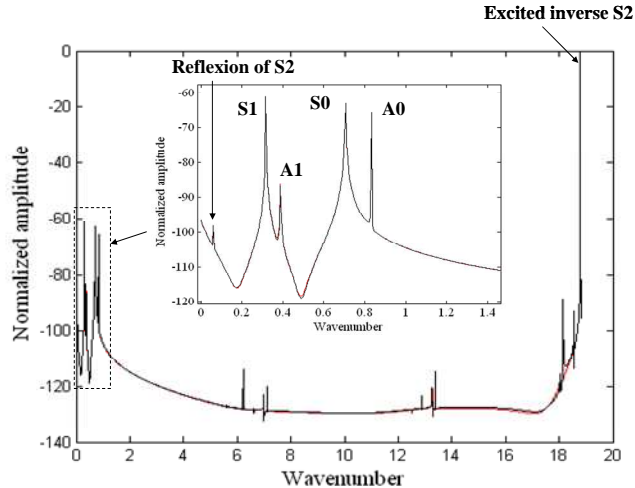


**Fig. 3.33** Wavenumber spectrum obtained from signals calculated at the surface of the plate between the 379 kHz S2 source and the stabilized absorbing layer.

### 3.5.4.3 Elastic Wave Propagation in a Piezoelectric Solid Waveguide

To show the efficiency of the proposed stabilized absorbing layer in 2D simulation of elastic guided waves in piezoelectric medium, an 8 mm thick  $\text{LiNbO}_3$  piezoelectric plate is considered. As in the preceding considered case, the used absorbing layers must have, at least, a length of two times the maximum wavelength of the waves existing in the plate in the

frequency range investigated. In Fig. 3.34 the dispersion curves calculated, in the frequency range [100-500] kHz, with COMSOL Multiphysics are displayed. The inverse part of the S2 mode has, as expected, a negative wavenumber as shown in the wavenumber versus frequency graph of Fig. 3.34.

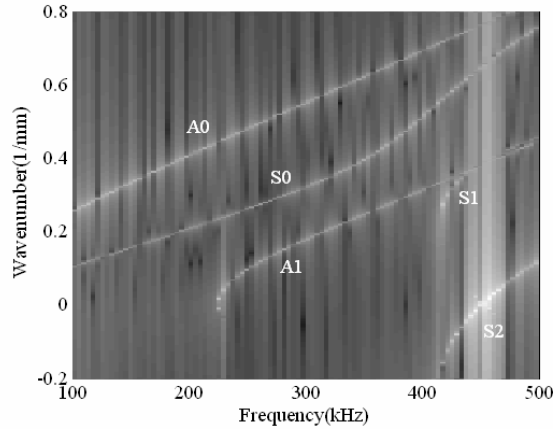


**Fig. 3.34** Dispersion curves for an 8 mm thick LiNbO<sub>3</sub> plate obtained by FEM simulations.

### 3.6 Conclusion

In this chapter, we extended the C-PML implementation, previously made for the first-order velocity-stress formulation, to a second-order elastic wave equation written in term of displacements, both in frequency and time domains. This new formulation has been implemented in a commercial FEM software (Comsol Multiphysics) and in an home made PS code. The results of the simulations, in anisotropic and piezoelectric solids, demonstrate that C-PMLs have more absorbing efficiency in the cases of oblique incidence and surface wave than PMLs. But in all presented implementations of C-PML supplementary PDE are introduced to actualize the C-PML variables. These PDE, as they contain spatial derivative terms, are cumbersome and difficult to introduce in our DG-FEM scheme when a Godunov type flux is used.

To overcome this difficulty, the concept of Nearly Perfectly Matched Layer (NPML) has been applied to the elastic wave propagating in an anisotropic medium. The main advantages of this formulation is linked to the fact that the obtained system of equations is in exactly the same form as the original system, and so strongly hyperbolic, and the introduced stretched fluxes are linked by ODEs to the physical fluxes. This last point reduces the burden and time of calculation. Moreover, comparison of energy decay shows that the NPML has the same absorbing ability than C-PML.

In the case of orthotropic material stability problems have appeared, as in the first-order velocity-stress implementation. Following the “MPML” implementation of Meza-Fajardo and Papageorgiou [126], we have introduced a mixture of C-PML and of sponge layer, with a controllable ratio of these two kinds of absorbing layers, in order to stabilize the C-PML or NPML, and shown that this stabilized C-PML is in fact not perfectly matched to the physical domain. A stability analysis, based on the method proposed by Becache *et al.* [10], has been made. It gives a physical interpretation of the stability criteria obtained by Meza-Fajardo and Papageorgiou [126]: the slowness (or phase velocity) and the group velocity of the wave incoming in the PML need to be of the same sign.

Moreover for Lamb waves simulations, this absorbing layer can absorb “inverse modes” both in non-piezoelectric and piezoelectric plates at the expense to have, at least, a length of two times the maximum wavelength of the waves existing in the plate in the frequency range investigated. In this case the reflection induced by the C-PML is -80 dB smaller than the incident energy.

Although not directly linked to the main objectives of the thesis, the second-order equation C-PML implementation has opened the opportunity to begin fruitful collaborations both in our laboratory and outside. For example, the good agreement between simulations and experimental results for the integrated Surface Acoustic Wave (SAW) streaming system, open to us the opportunity to optimize the system developed by the Microfluidic group. A numerical study of an integrated high frequency (around 1 GHz) ultrasonic system for a unique cell characterization has begun in collaboration with the Ultrasons group. Finally, the optimization for linear imaging application of a “chaotic cavity transducer”, a concept we will describe in the last chapter, is undertaken with the Koen Van Den Abeele group in Kortrijk.



# CHAPTER 4: APPLICATION OF CHAOTIC CAVITY TRANSDUCER TO LINEAR AND NONLINEAR ELASTIC IMAGING

## 4.1 Introduction

Time Reversal Acoustic (TRA) provides the ability to focus ultrasonic waves in time and space, regardless of the position of the initial source and of the heterogeneity of the medium in which the wave propagates [68]-[70]. This technique has attracted great scientific and technological interests in different fields including medical therapy, diagnostic, nondestructive testing (NDT), and underwater acoustics [71]. In a standard TRA experiment, waves generated by an acoustic source are firstly measured by an array of reversible piezoelectric transducers located around the source, and then time reversed and reemitted by the same transducers array. To improve the quality of the focalization the transducers should cover a closed surface around the medium in order to obtain the wave front information coming from all directions [36]. However, this is difficult to realize in practice, and time reversal operation is usually performed on a limited angular area, thus adversely affecting the reversal and focusing quality. In contrast, it has been observed that multiple scattering [55] and multiple reflections, as in the case of a waveguide [128], [158], [159] or a cavity [57], [58], [59], tend to enhance the focusing quality both in resolution and in amplitude. As a consequence, the number of channels participating in the time reversal process can be reduced, even to only one channel as demonstrated by Draeger *et al.* [57], [58], [59] and Fink *et al.* [72] in a silicon wafer chaotic cavity. This astonishing behavior has been linked to the ergodic property of the chaotic cavity, bearing the possibility to collect all information in only one point. In addition, the amplitude at the focal spot can be increased not only by an amplification of the emitted signal, but also by the emission of a longer recording of the time reversed signal. Similar experiments in multiple scattering media have been done by Derode *et al.* [55], [56] and the observed resolution was one-sixth of the theoretical limit for the mirror's aperture. Indeed in this case, the effective focusing aperture is widened due to the increase of the length of paths involved in the experiment. After the time reversal operation, the whole multiple scattering properties of the media behave as a coherent focusing source with a large angular aperture, improving the focalization.

Recently, innovative ultrasonic methods have been developed to probe the existence of damage (e.g., delaminations, micro-cracks or weak adhesive bonds) by investigating various

nonlinear signatures such as the generation of harmonics, the inter-modulation of frequency components, the amplitude dependent shift in resonance frequencies, the slow dynamic conditioning, etc [192]. Such approaches are termed Nonlinear Elastic Wave Spectroscopy (NEWS) techniques. The basis of all NEWS techniques is to measure and analyze macroscopic signatures resulting from a local violation of the linear stress-strain relation at the microscale [85]-[86]. Tests performed on a wide variety of materials subjected to different micro-damage mechanisms of mechanical, chemical and thermal origin, have shown that the sensitivity of such nonlinear methods to the detection of micro-scale features is far greater than what can be obtained with linear acoustical methods. NEWS methods have at first been applied for the global determination of the fatigue state of a structure, and recently extended to visualization techniques for imaging defect's nonlinearity distributions using laser vibrometry [174], airborne ultrasound [175] or shearography [161]. In the last five years, the concept of merging the benefits of both NEWS and TRA has been proposed in order to realize images of defects in solid samples [67], [77], [79], [81], [177], [185]. In most NDT applications of this combination, a one channel TRA experiment has been used in which a piezoelectric (PZT) ceramic is glued directly to a sample. The sample is generally small enough to be considered as multi-reverberant in the frequency range of interest [177], [185]. Non-reverberant samples such as composite plates for instance are difficult to work with, and for systems with a high degree of symmetry, simple reverberating properties may lead to the concentration of virtual sources on a pattern with dimensions correlated to size of the sample (or the transducer) resulting in spatial diffraction figures and "phantom" images [79], [185]. In order to overcome the "phantom" image problem and to extend the method to non-reverberating sample, we propose to use a "chaotic cavity transducer", consisting of a combination of a PZT ceramic glued to a cavity of chaotic shape on the hardware side with the time reversal principle on the software side. Here, we apply it for elastic waves in solids, and demonstrate that a transducer glued on a chaotic cavity can be used as an array of transducers, as it has been done recently for 3D imaging in fluid [149], [129], but for imaging applications in solid medium, and more precisely to nonlinear imaging of defects such as cracks.

## 4.2 Principle of Chaotic Cavity Transducer

### 4.2.1 Principle of One Channel Time Reversal Acoustic

Draeger *et al.* [57], [58], [59] have shown that in a chaotic cavity only one transducer is needed in order to focus an elastic wave every where inside a cavity. This astonishing behavior has been linked to the ergodic property of the chaotic cavity.

The experimental protocol classically used in order to focalise an acoustic wave in a chaotic solid sample is shown on Fig. 4.1. The first step of the experiment is the emission of a

pulse source signal by the transducer. Then the particle velocity at one position on the surface of the sample is measured with a laser vibrometer, and time reversed before reemission by the transducer. The elastic wave generated then focuses at the position where the particle velocity has been measured by the laser vibrometer both in time, called time recompression, and space.

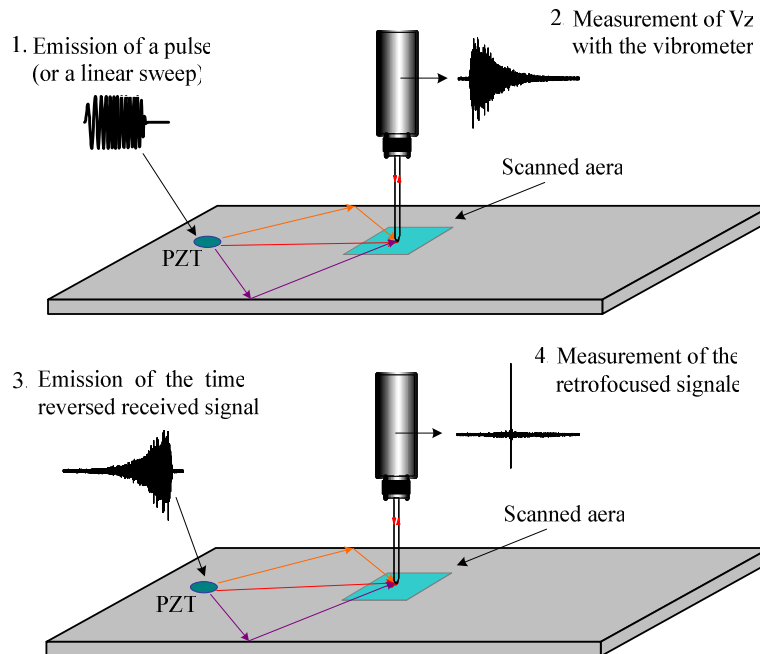


**Fig. 4.1** Principle of one channel Time Reversal (TR) focalization in a reverberant solid sample.

An example of signals measured during the process is shown in Fig. 4.2. In this example a 2 periods sinusoidal signal at frequency 500 kHz is emitted by a piezoelectric ceramic transducer, and the signal measured by a laser vibrometer is displayed on Fig. 4.2(a). This signal clearly corresponds to a long-lasting reverberating wave field, with a duration of 3 ms, corresponding to 1500 periods at the centre frequency of the initial pulse. The retro-focused signal measured at the same point, but after time reversal process and reemission, is shown on Fig. 4.2 (b). A zoom displaying the time recompression quality obtained is presented on Fig. 4.2(c).

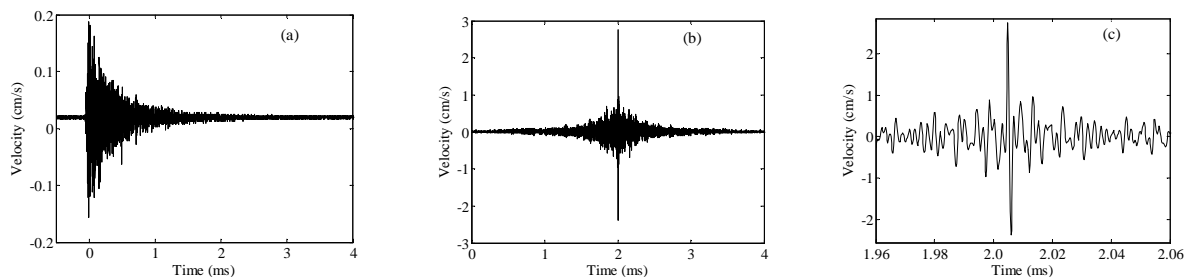


**Fig. 4.2** (a) Direct multi-reverberant signal, (b) retro-focalized signal, and (c) zoom of the time recompression.

The shape of the obtained time-reversed signal at the target position can be explained in the following way: at the focusing time and at this position all the frequency components of

the signal add up coherently, whereas they add up incoherently at other times or other places. In a chaotic cavity, the wave field  $\varphi$  can be expressed as a superposition of eigenmodes  $\psi_n(x)$  which form an orthogonal basis:

$$\varphi(\mathbf{x}, t) = \sum_n \psi_n(\mathbf{x}) \varphi_n(t). \quad (4.1)$$

In this case, a modal decomposition of the impulse response  $h_{AB}(t)$  on the eigenmodes of the cavity with eigenfrequency  $\omega_n$  is given by [57]:

$$h_{AB}(t) = \sum_n \psi_n(A) \psi_n(B) \frac{\sin(\omega_n t)}{\omega_n} = h_{BA}(t) \quad \text{if } t > 0. \quad (4.2)$$

As shown on Fig. 4.3, where the spectrum of the direct multi-reverberant signal of Fig. 4.2(a) is displayed, a large number of eigenmodes are used in the experiment. In a chaotic cavity, the eigenmodes are generally not degenerated (*e.g.*  $\omega_m = \omega_n$  if and only if  $m = n$ ) because for neighbouring eigenfrequencies  $\omega_m - \omega_n$  tends to be small, but in chaotic cavity next neighbours tend to repulse each other. In this case, Draeger [59] has shown that, using this modal decomposition, the following equation is verified in a chaotic cavity when the duration  $\Delta T$  of the time-reversed signal tends to infinity:

$$h_{AB}(t) \otimes h_{BA}(-t) = h_{AA}(t) \otimes h_{BB}(-t), \quad (4.3)$$

and called it the cavity equation. Here  $\otimes$  corresponds to a time domain convolution. Eq. (4.3) demonstrates that the perfect time-reversal process, expressed by  $h_{BB}(-t)$ , is perturbed by a simple convolution by the backscattering impulse response  $h_{AA}(t)$  of the source A. Due to this, the TR is not perfect here, and the retro-focused pulse is surrounded by sidelobes.

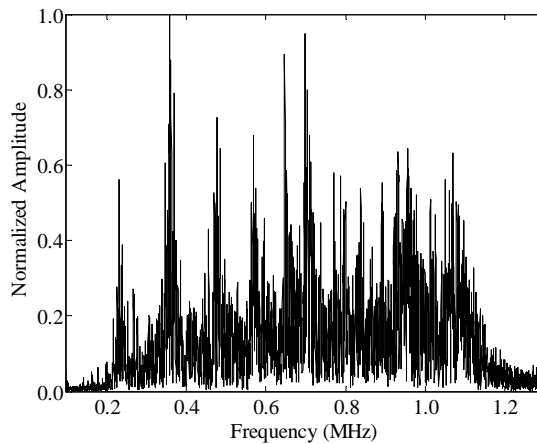


**Fig. 4.3** Normalized spectrum of the long-lasting reverberant signal of Fig. 4.2(a).

Now, when measuring the particle velocity around the position where the direct reverberant signal has been measured, a focal spot appears. A 2D scan of the maximum amplitude measured around this focal spot during the retro-focalisation process is displayed

on Fig. 4.4. It can be shown that the shape of the obtained directivity gives a statistical estimator of the spatial field correlation function, due to the fact that TR process can be interpreted as a spatial correlator [72].

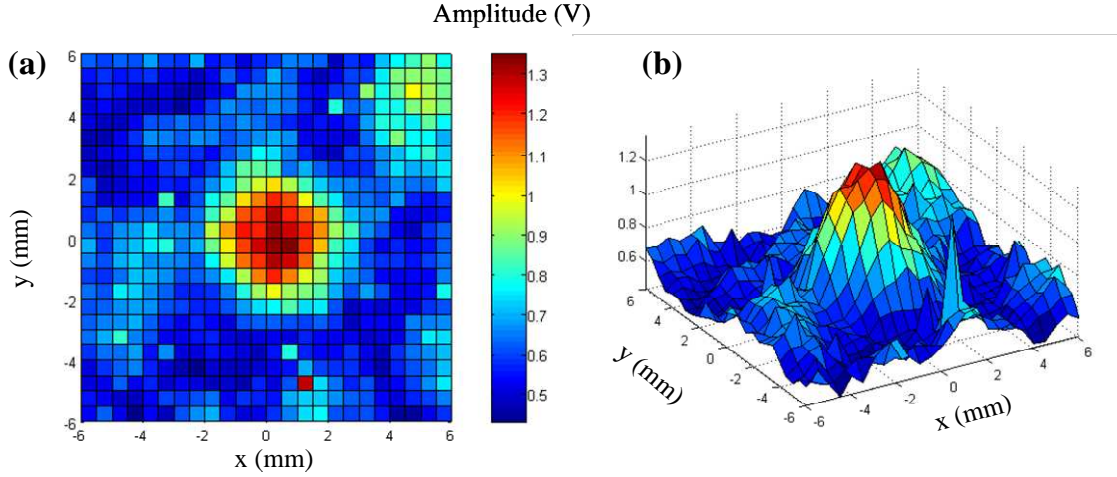


**Fig. 4.4** 2D scan of the maximum amplitude measured around the focal point during the retro-focalisation process in a reverberant steel plate. (a) Intensity plot and (b) surface plot.

Noting  $h_{AB'}(t)$  the impulse response from point  $A$  to an observation point  $B'$  different from the point  $B$ , where the interferometric measurement has been made, the time-reversed signal recreated at  $B'$  at time  $t_1 = 0$  can be written as:

$$s_{tr}(B', 0) = \int h_{AB}(t) h_{AB'}(-t) dt. \quad (4.4)$$

Thus, the obtained directivity pattern of the time-reversed wave field is given by the cross correlation of the Green's functions, developed on the eigenmodes of the cavity:

$$s_{tr}(B', 0) = \sum_n \psi_n^2(A) \psi_n(B) \psi_n(B') \frac{1}{\omega_n^2} E(\omega_n). \quad (4.5)$$

The summation is limited to a finite number of modes, as shown on Fig. 4.3, but as we do not know the exact eigenmode distribution for each chaotic cavity, we use a statistical approach and consider the average over different realizations just summing over different cavity realizations. So we replace in Eq. 4.5 the eigenmodes product by their expectation values:

$$\langle s_{tr}(B', 0) \rangle = \sum_n \langle \psi_n^2(A) \psi_n(B) \psi_n(B') \rangle \frac{1}{\omega_n^2} E(\omega_n). \quad (4.6)$$

If  $B$  and  $B'$  are sufficiently far apart from  $A$ , not to be correlated, then:

$$\langle \psi_n^2(A) \psi_n(B) \psi_n(B') \rangle = \langle \psi_n^2(A) \rangle \langle \psi_n(B) \psi_n(B') \rangle. \quad (4.7)$$

Considering the random plane wave approximation [19], [108], [125], [203] that is the amplitude of the eigenmodes has a Gaussian distribution,  $\langle \psi_n^2 \rangle = \sigma^2$  where  $\sigma$  is a constant, and a short range isotropic correlation function given in 2D by a Bessel function:

$$\langle \psi_n(B)\psi_n(B') \rangle = J_0(2\pi|r_{B'} - r_B|/\lambda_n), \quad (4.8)$$

where  $\lambda_n$  is the wavelength corresponding to  $\omega_n$ , we obtain:

$$\langle s_r(B',0) \rangle = \sum_n J_0(2\pi|r_{B'} - r_B|/\lambda_n) \frac{\sigma^2}{\omega_n^2} E(\omega_n). \quad (4.9)$$

So, the spatial resolution obtained with the TR process is simply an estimate of the correlation length of the scattered wave field. So, it should become independent of the array's aperture. It is to be noted that in 3D, the short range isotropic correlation function is given by a sinus cardinal function:

$$\langle \psi_n(B)\psi_n(B') \rangle = \frac{\sin(2\pi|r_{B'} - r_B|/\lambda_n)}{2\pi|r_{B'} - r_B|/\lambda_n}. \quad (4.10)$$

## 4.2.2 An Instructive Experiment

In most application of one channel time reversal acoustic experiment applied to non-destructive testing a PZT ceramic is glued directly on a sample, small enough to be considered as multi-reverberant in the considered frequencies range. Obviously, the combination of traditional (or reciprocal) single channel TRA for systems with a high degree of symmetry, simple reverberating properties may result in spatial diffraction maxima and “phantom” images [79], [185]. This limitation will be now demonstrated through a first one channel time reversal nonlinear experiment and a 3D numerical simulation.

The experimental set-up used for this “classical” one channel time reversal experiment in a reverberant sample is shown in Fig. 4.5. A PZT ceramic is glued with salol on the sample (10×2.5×1.2 cm steel plate fabricated by the society ASCO during the European Strep project AERONEWS), and a BMI heterodyne interferometer (SH-130) is used to detect the out of plane particle velocity ( $v_z$ ). The PZT ceramic is driven by a pulse (a rectangular pulse of 2  $\mu$ s duration and 50 Hz of repetition frequency) generated by an Agilent 33220A function generator and amplified by an ENI 325 LA RF power amplifier. The mean frequency of the system is around 250 kHz, which is the low frequency limit of the power amplifier.

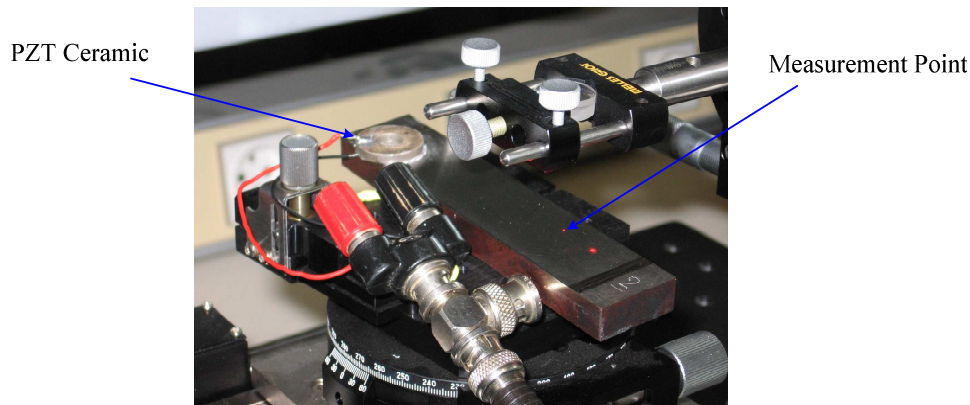


**Fig. 4.5** Set-up for a “classical” one channel time reversal experiment in a reverberant sample. Here, a PZT ceramic is directly glued on a rectangular  $10 \times 2.5 \times 1.2$  cm steel plate, and the vibration measurements are made with a heterodyne interferometer.

The objective of this first experiment was to image a crack on the surface of the sample, obtained by a three point bending fatigue technique, with the method proposed by Sutin *et al.* [176], [184]. A one channel time reversal technique is used to focus an elastic wave on different points of the surface of the sample around the crack. The amplitude of the signal at the second harmonic frequency is then extracted, and an image of the nonlinear response of the sample is made. The 2D map of the second harmonic amplitude obtained around the crack is displayed on Fig. 4.6. On the right of the figure a measurement made along a width of the sample, and crossing the crack is also shown. The crack can easily be seen on this image, but a symmetric image and an increase of the signal on the boundaries are obtained.

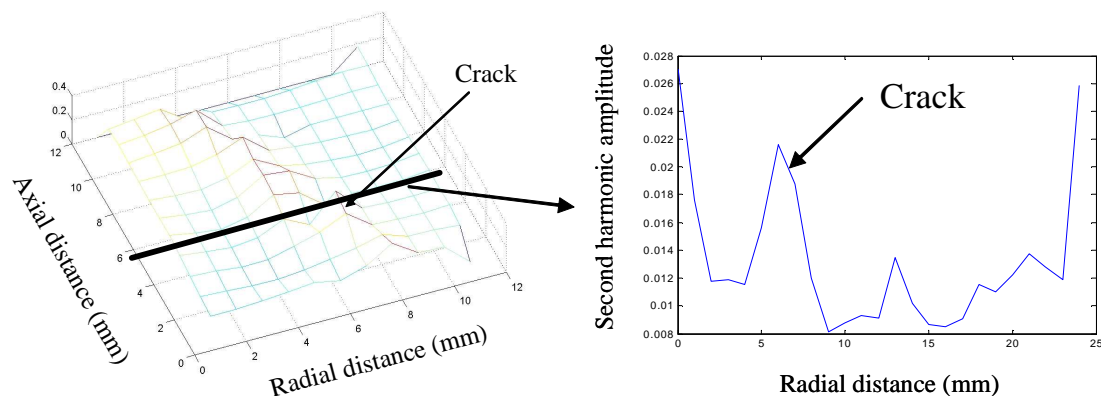


**Fig. 4.6** Part of a 2D map of the second harmonic amplitude measured after focusing of an elastic wave in different points around a crack at the surface of a fatigued steel plate using a one channel TR method, and one slice along a width of the sample.

To understand if the “phantom” image and the increase of the signal on the stress free boundaries are linked to experimental uncertainty or correspond to intrinsic physical problems a 3D linear simulation of the experiments has been made. The geometry of the simulation is shown in Fig. 4.7. It corresponds to wave propagation in a  $2.5 \times 1.2 \times 10$  cm steel sample with

stress free boundaries. A point force  $T_{zz}$  (stress) is applied on the bottom free surface of the sample ( $Y = 1.2$  cm) at the position ( $X = 1$  cm,  $Y = 1.2$  cm,  $Z = 1$  cm). This point force has the following time evolution:

$$T_{zz}(t) = A \sin(2\pi f(t - t_0)) e^{-\frac{1}{p} \left[ \frac{t - t_c}{w} \right]^p} \left( 1 - e^{-\left( \frac{t}{sw} \right)^2} \right), \quad (4.11)$$

with the following parameters:  $f = 250$  kHz,  $t_0 = 0$ ,  $A = 0.05$  MPa,  $p = 2$ ,  $t_c = 0$ ,  $sw = 3/f$ ;  $w = 2/f$ . The sample is an isotropic steel with density  $\rho = 8000$  kg/m<sup>3</sup>, Young modulus  $E = 184$  GPa, and Poisson coefficient  $\nu = 0.3$ . In the first phase of the process corresponding to the propagation of the direct wave generated by the point source at the surface of the sample, the normal particle velocity  $v_z$  on a point of the same free surface is recorded during several ms. The point coordinates are:  $X = 0.7$  cm,  $Y = 1.2$  cm and  $Z = 6$  cm.

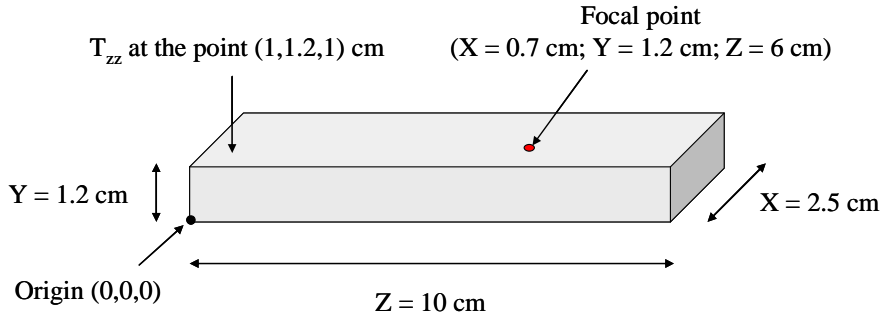


**Fig. 4.7** Geometry of simulation domain with characteristics of source, receivers and material.

The calculated 2D map of the maximum amplitude for the retro-focusing process is shown on Fig. 4.8. Although the focal spot clearly emerges of the 2D map, a slice obtained along a width and crossing the focus displays the same imperfections: increase of the signal on the stress free boundaries and a small amplitude “phantom” image.

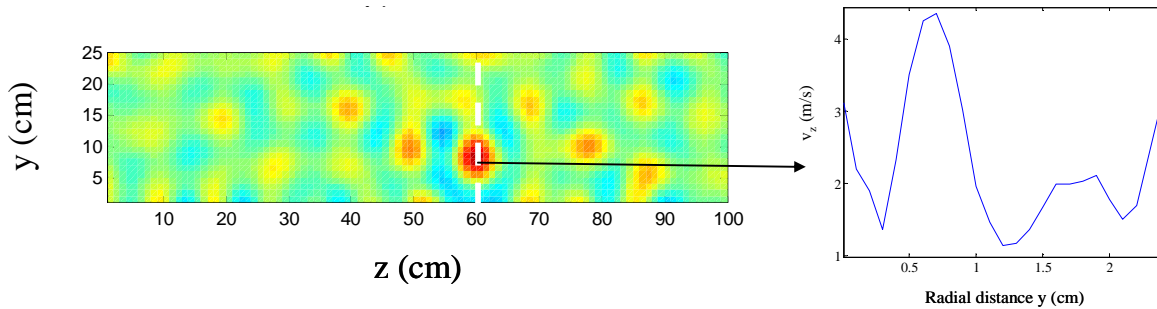


**Fig. 4.8** 2D map of the maximum amplitude for retro-focusing at the surface of the sample (left), and a slice along a width (right).

### 4.2.3 Chaotic Cavity Transducer

In order to overcome the “phantom” image problem and to extend the method to non-reverberating sample, we propose to use a “chaotic cavity transducer”, consisting of a combination of a PZT ceramic glued to a cavity of chaotic shape on the hardware side with the time reversal principle on the software side. An applied source signal to the PZT ceramic generates a wave propagating in the cavity and the sample medium. Each time the propagating wave in the cavity arrives at the boundary between the cavity and the sample, part of the incident energy is reflected and continues to engender multiple reflections on the other boundaries of the cavity, whereas the other part of the energy is transmitted in the sample as shown on Fig. 4.9.

A similar idea has been developed for 3D imaging in fluids [129]. Here, we apply it for elastic waves in solids [26].

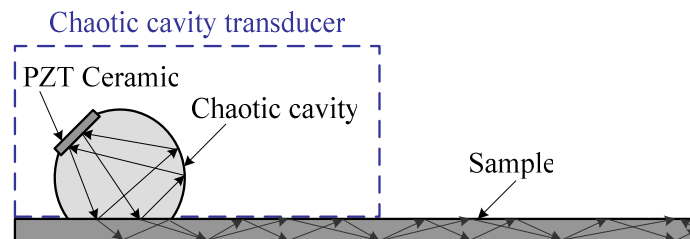


Fig. 4.9 Principle of “chaotic cavity transducer”.

### 4.2.4 Signal Processing Methodology

As we have seen time reversal provides the possibility to focus elastic waves in solid samples with only one channel when used in (or with) a multi-reverberant cavity. But, different kinds of signal processing methods can be used in order to improve both the Signal to Noise Ratio (SNR) and the quality of the focalization. In our study, three techniques have been tested: Chirped excitation, Inverse Filter and 1 bit process.

#### 4.2.4.1 Chirp Excitation

Experimentally, due to the low energy in the pulse, the use of sinusoidal pulse signal for impulse response measurement does not provide strong received signal, leading to a poor signal to noise ratio. So, for more robust measurement of the impulse response and to improve the quality of focalization a pulse compression technique with a linear sweep signal has been used instead of the short sinusoidal pulse. Pulse compression is accomplished by taking the intercorrelation of the measured waveform with the time reversed input signal (chirp). There are three primary reasons why pulse compression is potentially a useful technique:

- improvement of available bandwidth of the imaging system;
- coded waveform has the advantage of being detectable using cross-correlation techniques, even when the received signal is well below the noise;
- high energy levels can be transferred into the test sample.

This last reason is particularly interesting in nonlinear imaging of defect due to the fact that the nonlinear crack response has generally a threshold behaviour, and a quadratic increase when this threshold has been overcome. Various types of swept-frequency signals with large Time-Bandwidth Product (TBP) have been proposed, as for example chirp signal, Barker and Golay codes, but it was found that the linear Frequency Modulated (FM) signal has the best performances in view of SNR improvement and robustness versus attenuation effects [127]. So, the pulse code we used is a chirp with linear increasing or decreasing instantaneous frequency:

$$s(t) = \cos(2\pi f_0 t + \pi \frac{B}{T} t^2), \quad -\frac{T}{2} \leq t \leq \frac{T}{2}, \quad (4.12)$$

where  $f_0$  is the center frequency,  $T$  is the signal duration and  $B$  is the total bandwidth that is swept. Its instantaneous frequency is:

$$f(t) = f_0 + \frac{B}{T} t. \quad (4.13)$$

which is function of time and indicates the spectral band in which the signal energy is concentrated at the time instant  $t$ . The parameter  $k = B/T$  is referred to as the frequency modulated slope or the rate of the frequency modulated sweep. The signal sweeps linearly the frequencies in the interval  $[f_0 - B/2, f_0 + B/2]$ . Moreover, if needed, a time domain window apodization  $A(t)$  can be used in order to reduce time domain sidelobes which can appear in the pulse compression process. Indeed rectangular shaped window leads to Fresnel ripples at the frequency band edges.

The same process, as the one use for the sinusoidal source signal, has been used with a linear sweep source signal, with the following parameters  $T = 100 \mu\text{s}$ ,  $f_1 = 200 \text{ kHz}$ ,  $f_2 = 1000 \text{ kHz}$  ( $B = f_2 - f_1$ ). Comparison of the direct wave recorded signal and the retro-focalized signal obtained by using the sinusoidal pulse and the linear sweep source signal are plotted on Fig. 4.10. It appears that the use of linear sweep source signal improves time recompression quality and signal to noise ratio.

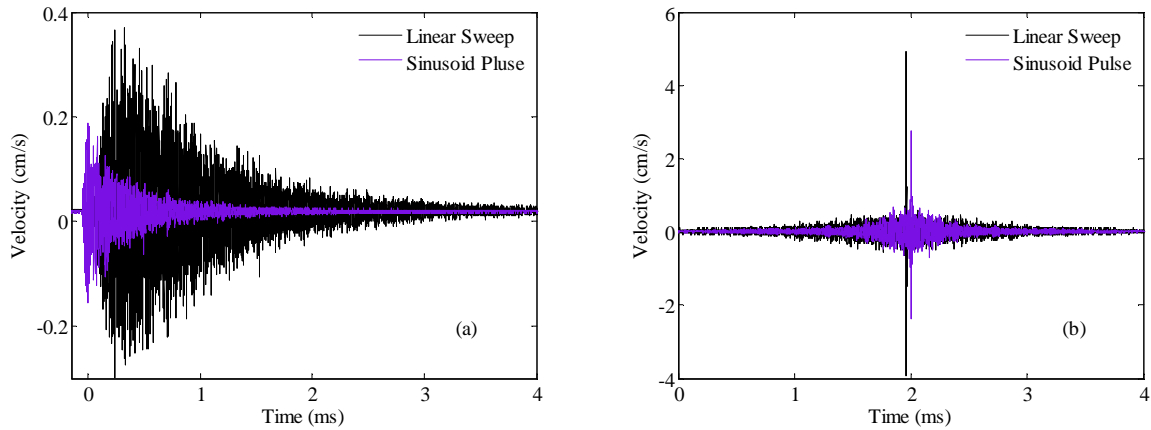


**Fig. 4.10** Comparison of (a) the direct wave recorded signal and (b) the time recompressed signal at the focus for two kinds of source signal: a sinusoidal pulse (purple line) and a linear sweep (black line).

In nonlinear methods such as harmonic generation, or even parametric interactions, signals of a few periods of duration are needed in stead of pulse. But as shown on Fig. 4.11(a), when 60 periods of a 600 kHz sinusoidal signal is used as the source signal, the signal to noise ratio of the obtained time recompressed signal is quite low. This is linked to the small numbers of eigenmodes used due to the limited frequency range of the source. Chirp excitation can also here be a solution. Indeed, when a sweep, of 100  $\mu$ s duration and  $f_{\min} = 200$  kHz and  $f_{\max} = 1.2$  MHz, is used as the source signal, the time recompressed signal although of 100  $\mu$ s duration presents a higher signal to noise ratio (Fig. 4.11(b)). Moreover, by taking the intercorrelation of this signal with the time reversed input signal, a pulse can again be obtained.

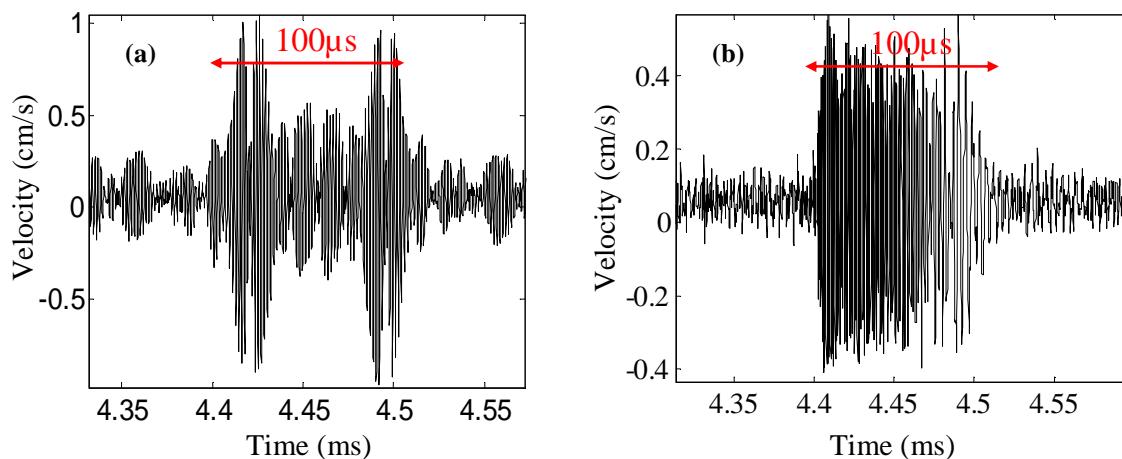


**Fig. 4.11** Time recompressed signal obtained with (a) 50 periods of a 600 kHz sinusoidal signal, and (b) a sweep of 100  $\mu$ s duration and  $f_{\min} = 200$  kHz and  $f_{\max} = 1.2$  MHz.

#### 4.2.4.2 Time Reversal and Inverse Filter

The spatio-temporal inverse filter approach has been used by Tanter *et al.* [180] and Aubry *et al.* [5], and shown to improve the focusing quality. Indeed, if linearity and spatial reciprocity assumptions are valid in the medium, the preceding time reversal process corresponds to a spatial and temporal matched filter [179] of the propagation. That is to say, the time reversal process maximizes the output amplitude received signal at a given location and a given time, and corresponds in our case to the signal amplitude received at the focus at a given time, for a given input energy.

The classical inverse filter is based on the inversion of the propagation operator relating an array of transducers to a set of control point [180]. This technique allows calculation, both in space and time, of the set of temporal signals to be emitted in order to optimally focus on a chosen control point. The broadband inversion process takes advantage of the singular value decomposition of the propagation operator in the Fourier domain.

In our case, the Inverse Filter (IF) approach with a single transducer coupled to a chaotic and reverberant cavity consists in the inversion of the eigenmode energy [150]. The IF approach performs an inversion of the energy of the eigenmodes, and constructs the re-emitted signal as a linear combination of all the eigenmodes of the cavity, weighted by this inversion. Doing so, the focusing process takes advantage of all the modes including those with the weakest energy which are poorly exploited in the time reversal focusing process.

On Fig. 4.12, a comparison between the time recompressed signal obtained with Time Reversal (TR) and Inverse Filter (IF) methods are displayed. As predicted, the amplitude of the pulse obtained by IF is lower than with TR, but at the expense of a better signal to noise ratio and a shorter duration. These properties are linked, as expected, to the fact that the number of eigenmodes used with IF method is higher than with TR (Fig. 4.13).

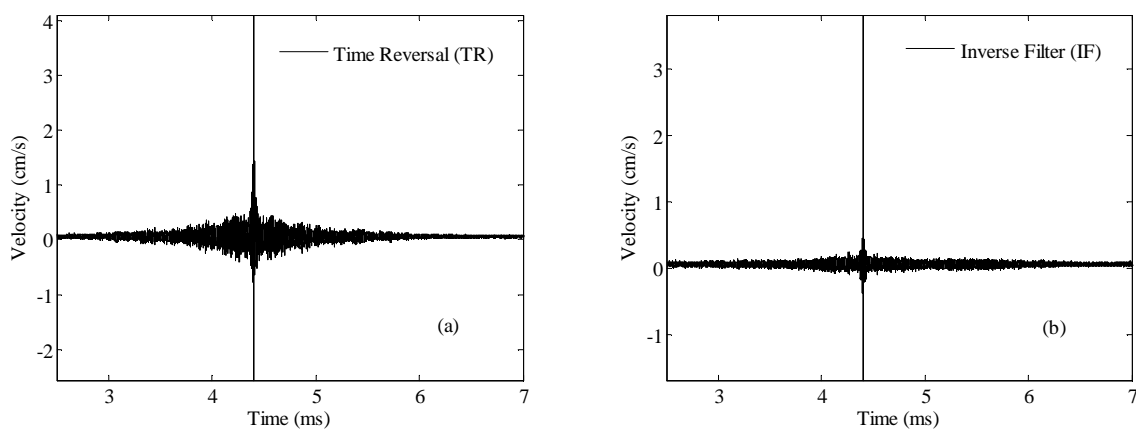


**Fig. 4.12** Comparison of the time-recompression signal obtained at the focus for (a) Time Reversal (TR), (b) Inverse Filter (IF).

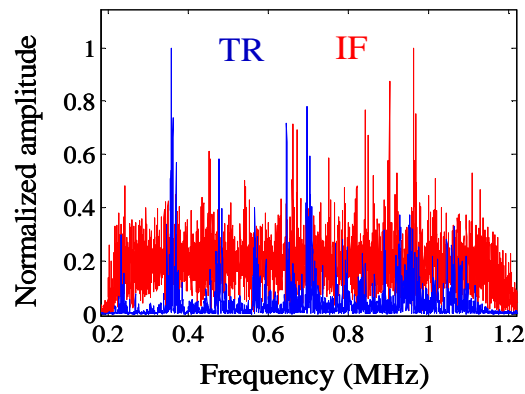


**Fig. 4.13** Comparison of the spectra of the time-recompression signal obtained with Time Reversal (TR) and Inverse Filter (IF) methods.

#### 4.2.4.3 1-bit Process

As demonstrated, a 1-bit process can be used in order to increase the amplitude of the retro-focalized wave. During classical time reversal or inverse filter experiments, both the instantaneous phase and amplitude information of the received signal are sent back. For a 1-bit method, the time reversed or inverse filtered signal will be set to  $\pm 1$  depending on the sign of signal: +1 amplitude is set if the sign is positive, otherwise,  $-1$  amplitude is set. This means that the instantaneous phase information present in the zero crossing of the signal is time reversed while the instantaneous amplitude information is ignored.

The previous experiment has been repeated with a 1-bit inverse filter with the same parameter as for the inverse filter method. Comparing Fig. 4.14(a) and Fig. 4.12(b), a 2.5dB gain is obtained by using the 1-bit method. The spectrum of the signal measured with the 1-bit inverse filter is displayed on Fig. 4.14(b). As for TR, only some eigenmodes are privileged in the 1-bit process, leading to an increase of the correlation noise.

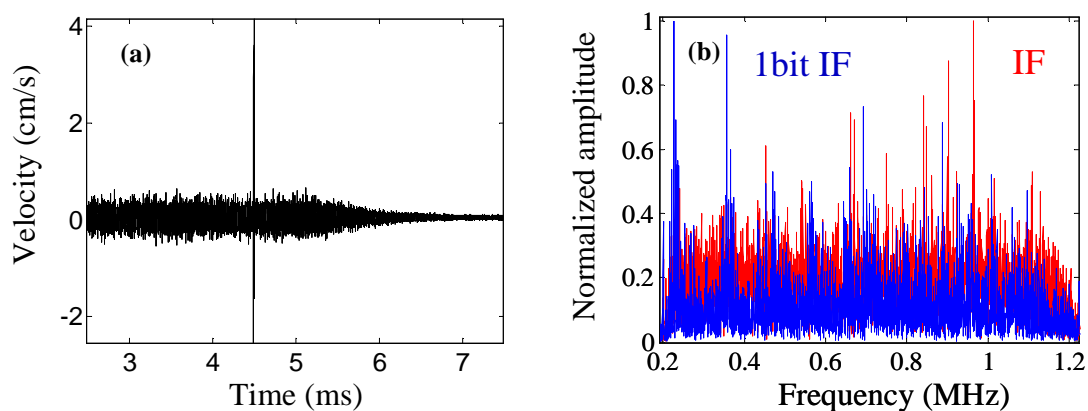
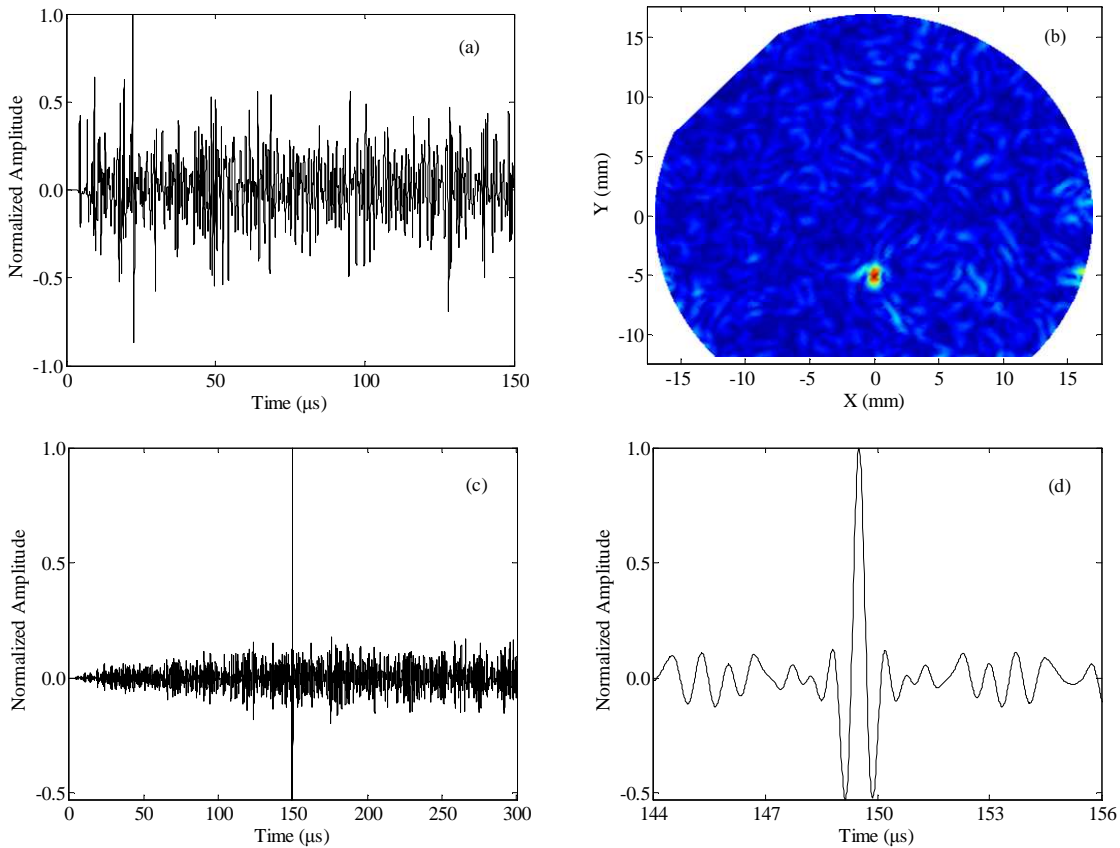


**Fig. 4.14** (a) Velocity at the focus point as a function of time for 1-bit Inverse Filter. (b) Comparison of the spectra of the signals obtained with 1-bit Inverse Filter (1bit IF) and Inverse Filter (IF) methods.

### 4.2.5 Numerical Simulations of Chaotic Cavity Transducer

To demonstrate and give a better understanding of the “chaotic cavity transducer” concept, a numerical simulation study has been first made with the developed DG-FEM scheme, and will now be presented.

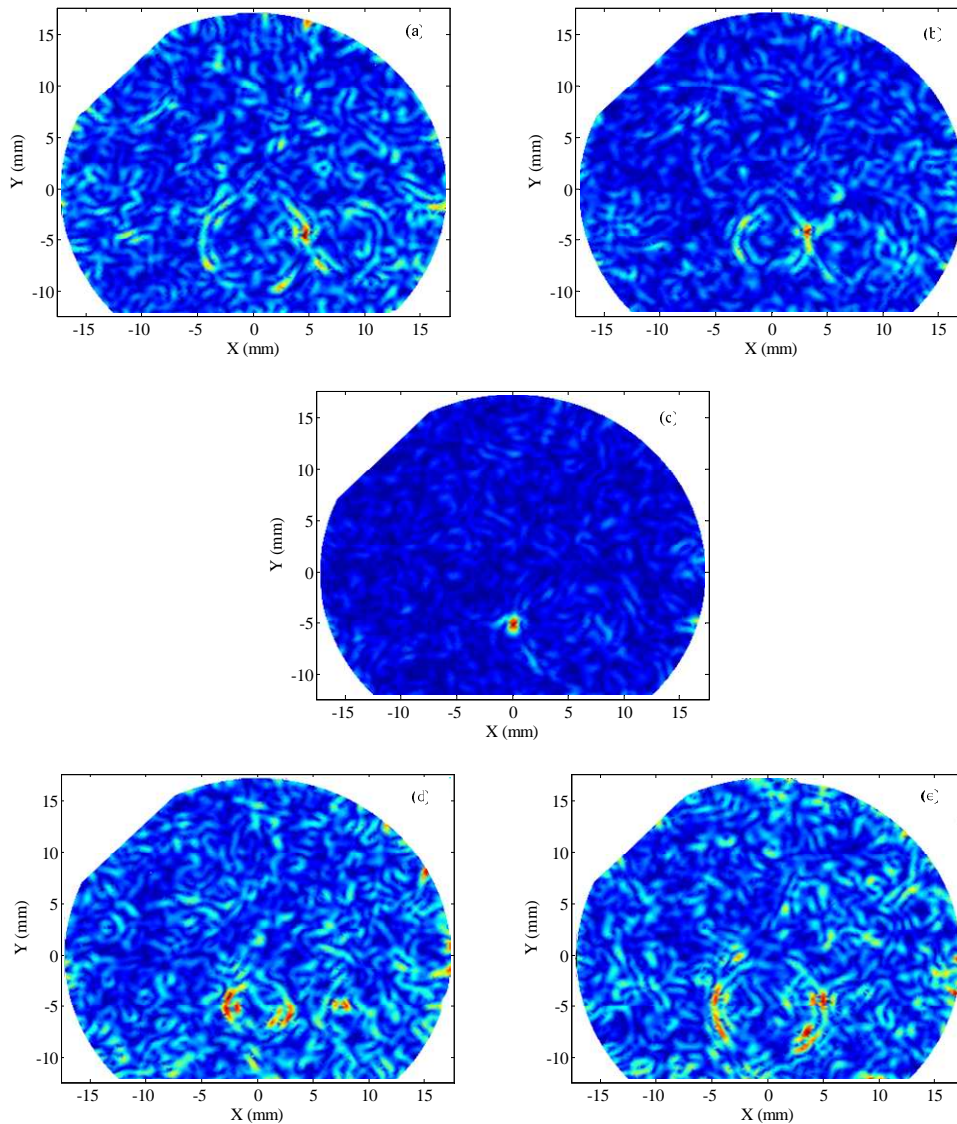
The form and size of the chaotic cavity simulated is displayed in Fig. 4.15(b). It corresponds to a 2D version of the cavity used in the experiments presented later in the chapter. The source signal is the Ricker wavelet given in Eq. (2.69) with  $t_D = 0.5 \mu\text{s}$ ,  $a_1 = (\pi f_c)^2$  and  $f_c = 800 \text{ kHz}$  and located in the middle of the tilted upper side border. The cavity material used in the experiments is copper with stress-free boundary condition on all the cavity boundaries. So the following parameters have been used in the numerical simulation:  $\rho_0 = 8930 \text{ kg/m}^3$ ,  $C_{11} = C_{22} = 224.1 \text{ GPa}$ ,  $C_{12} = 132.1 \text{ GPa}$  and  $C_{66} = 46.0 \text{ GPa}$ .



**Fig. 4.15** (a) Received direct signal at the chosen focal point, (b) snapshot of the particle velocity at the instant of time recompression, (c) retro-focalized signal, and (d) zoom of (c) around the instant of time recompression calculated, for a copper chaotic cavity, with a RK-DG-FEM O4 scheme.

The chosen point of focalization is first positioned at (0.0, -5.0) (mm) inside the cavity in order to verify the chaotic behavior of the designed cavity. The received particle velocity signal at the focal point calculated with a RK-DG-FEM scheme of order 4 is shown on Fig. 4.15(a). It corresponds to a long-lasting reverberant signal. The total simulation time is 150  $\mu\text{s}$

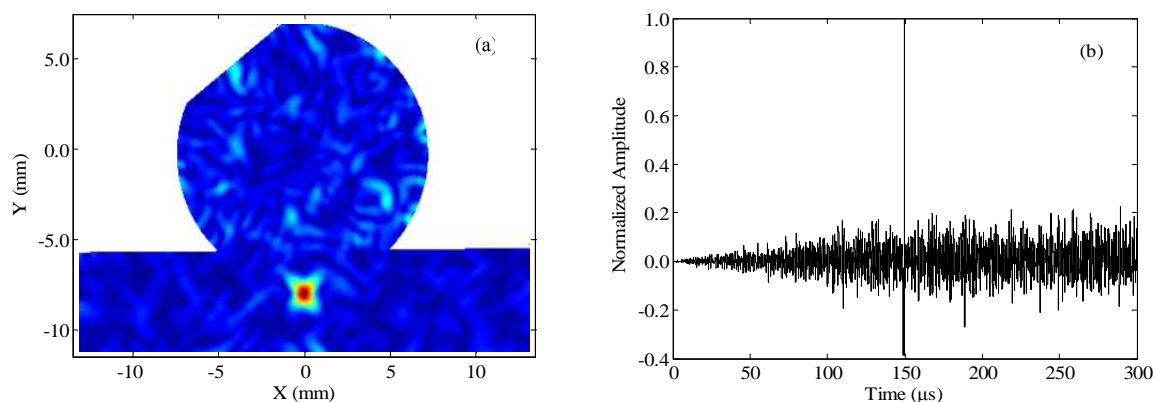
for this first step of the retro-focalization procedure. Here the reflections on the stress-free boundaries of the cavity continue until the end of the simulation as no attenuation has been introduced. Then, a time reversed version of this signal is reemitted by a source located as before in the middle of the tilted upper side border. We can see, on the snapshot of the particle velocity at the instant of time recompression (Fig. 4.15(b)), that the spatial focalization point is at the position where the direct signal was received, confirming that a one channel time reversal process focuses back exactly at the source. The chaotic behaviour of the designed cavity seems to be adequate, as no “phantom” image can be seen on Fig. 4.15(b). The retro-focalized signal, calculated at the focal position, is displayed on Fig. 4.15(c). It confirms the time recompression and correlation noise inherent to the one channel time reversal process. Indeed, in this numerical experiment this noise cannot be attributed to “thermal noise” or experimental errors. The zoom of Fig. 4.15(d) shows the quality of the time recompression.



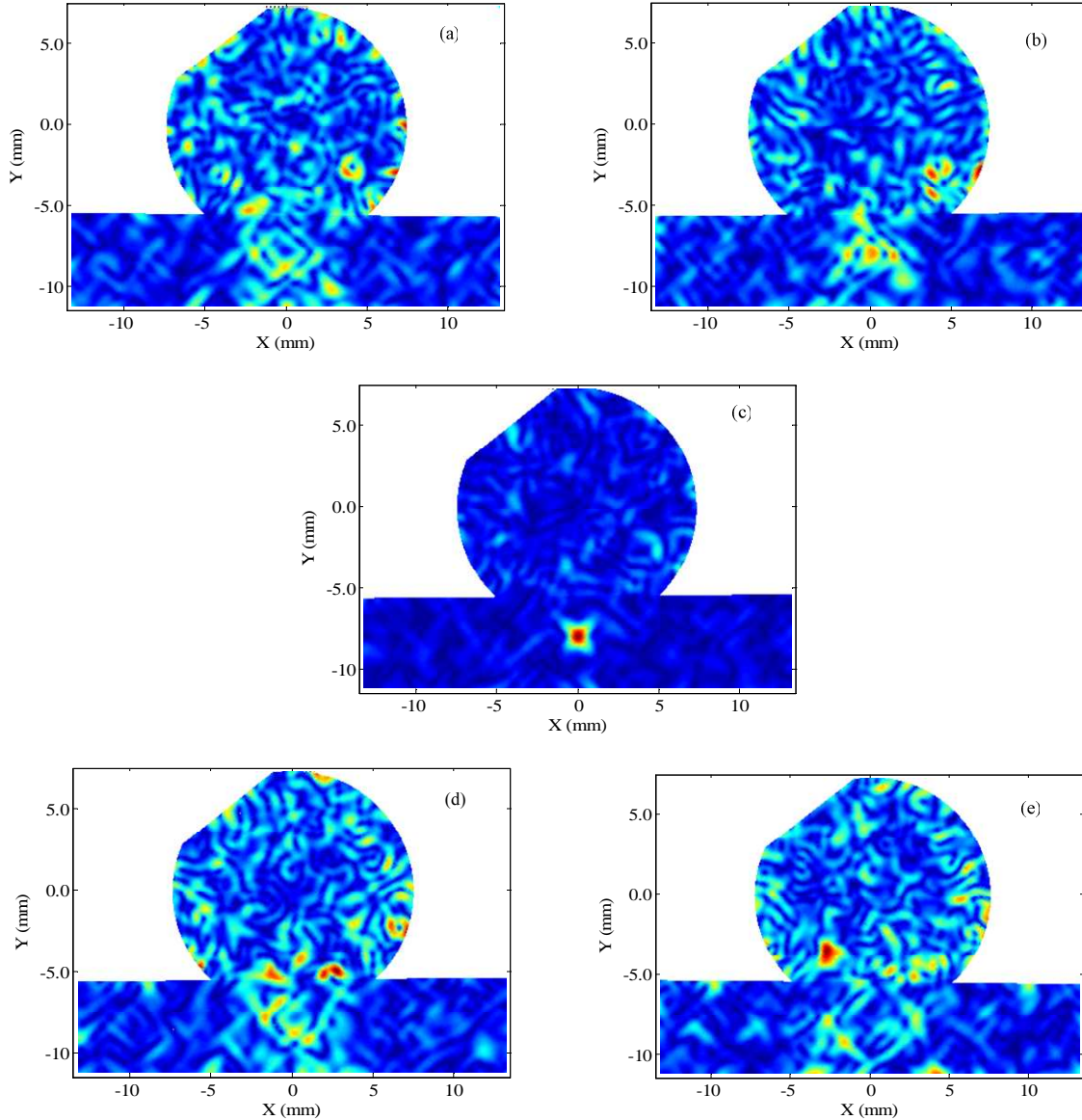
**Fig. 4.16** Snapshots of the particle velocity at five instants around the time recompression, for a copper chaotic cavity, calculated with a RK-DG-FEM O4 scheme. (a)  $t = 149 \mu\text{s}$ , (b)  $t = 149.3 \mu\text{s}$ , (c)  $t = 149.6 \mu\text{s}$ , (d)  $t = 149.9 \mu\text{s}$ , and (e)  $t = 150.5 \mu\text{s}$ .

Fig. 4.16 shows snapshots of the particle velocity at five instants around the time recompression for the copper chaotic cavity. These snapshots display the retro-focusing process, showing that the focusing waves come from every direction around the focal spot, and diverge after passing through it.

Now, the preceding copper chaotic cavity is considered to be glued on a  $27 \times 6$  mm reverberating plate. The plate is first considered to be made of steel:  $\rho_0 = 7870 \text{ kg/m}^3$ ,  $C_{11} = C_{22} = 237 \text{ GPa}$ ,  $C_{12} = 141 \text{ GPa}$  and  $C_{66} = 116 \text{ GPa}$ . The same retro-focusing process is simulated using a fourth order RK-DG-FEM, but with the focusing point chosen in the steel plate at a position with coordinates  $(0.0, -8.0)$  (mm). As in the previous numerical example, the total calculation time, in the first step of the TR retro-focalization process, is  $150 \mu\text{s}$ . The obtained snapshot of the particle velocity at the instant of time recompression, Fig 4.17(a) demonstrates the possibility of focusing in a sample with a one channel TR method combined with a chaotic cavity. It is to be noted that in this case the reflection at the interface between the cavity and the steel plate is rather small because their constituting materials are very similar. Fig. 4.17(b) shows that the quality of the time recompression is nearly as good as the one obtained directly inside the cavity. Only the level of the correlation noise is slightly bigger when the cavity is glued on the steel sample. In this case, the sample contributes to the focusing process and the waves come from every direction around the focal spot as shown on Fig. 4.18 which displays snapshot of the particle velocity at five instants around the time recompression.



**Fig. 4.17** (a) Snapshot of the particle velocity at the instant of time recompression, and (b) retro-focalized signal calculated, for a copper chaotic cavity glued on a reverberating steel plate, with a RK-DG-FEM O4 scheme.



**Fig. 4.18** Snapshots of the particle velocity at five instants around the time recompression, for a copper chaotic cavity glued on reverberating steel plate, calculated with a RK-DG-FEM O4 scheme. (a)  $t = 149 \mu\text{s}$ , (b)  $t = 149.3 \mu\text{s}$ , (c)  $t = 149.6 \mu\text{s}$ , (d)  $t = 149.9 \mu\text{s}$ , and (e)  $t = 150.5 \mu\text{s}$ .

Next, we want to see the influence of a higher impedance mismatch between the cavity and the sample on the retro-focusing process. So, we consider the case where the cavity is still made in copper, but glued this time on a composite plate with the following material parameters:  $\rho_0 = 1400 \text{ kg/m}^3$ ,  $C_{11} = 20.28 \text{ GPa}$ ,  $C_{22} = 20.52 \text{ GPa}$ ,  $C_{12} = 5.59 \text{ GPa}$  and  $C_{66} = 5.87 \text{ GPa}$ . In this simulation, the receiver is located at the point  $(0.0, -7.0) \text{ (mm)}$ , and the total calculation time for the first step is  $100 \mu\text{s}$ . With the same procedure as in the two preceding calculations, we obtain the results plotted on Fig. 4.19. These figures show that it is possible to get a retro-focalization even on this medium with a high impedance mismatch.

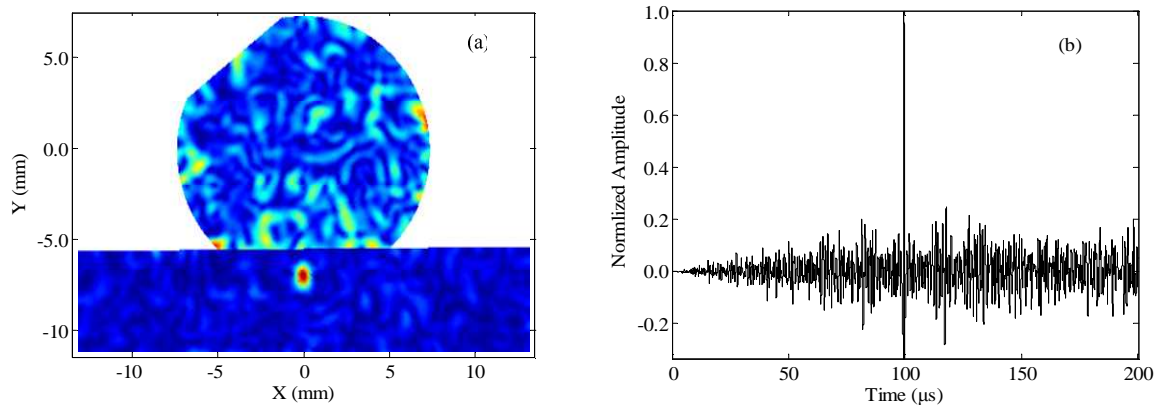


**Fig. 4.19** (a) Snapshot of the particle velocity at the instant of time recompression, and (b) retro-focalized signal calculated, for a copper chaotic cavity glued on a composite plate of finite size, with a RK-DG-FEM O4 scheme.

Finally, the use of the “chaotic cavity transducer” on non-reverberating sample is studied. To simulate the non-reverberating sample a NPML absorbing layer is placed on three of its boundaries. The remaining boundary is left free where it is not in contact with the cavity. So, the sample can be considered as a semi infinite medium. The snapshot of the particle velocity at the instant of time recompression and the retro-focalized signal calculated with a fourth order RK-DG-FEM scheme are shown on Fig. 4.20. These results demonstrate the ability of the “chaotic cavity transducer” to focus energy even in non-reverberating samples.

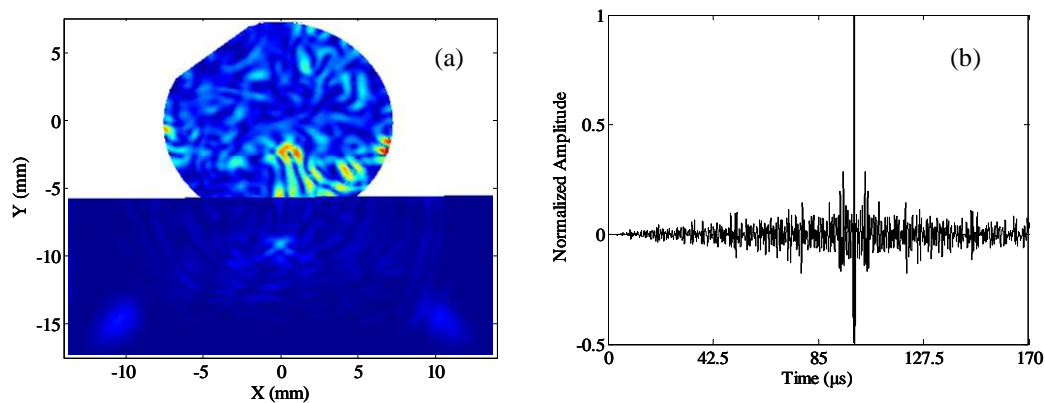


**Fig. 4.20** (a) Snapshot of the particle velocity at the instant of time recompression, and (b) retro-focalized signal calculated, for a copper chaotic cavity glued on a non reverberating composite plate, with a RK-DG-FEM O4 scheme.

Snapshots of the particle velocity at five instants around the time recompression are displayed on Fig. 4.21. On these snapshots one can clearly see that the wave does not come from all around the focal point as in the case where the “chaotic cavity transducer” is glued on a reverberant sample, but seems to propagate from the cavity. A point, which can not be measured experimentally, is the fact that in the considered case, where the sample presents a high impedance mismatch with the cavity, the focusing properties is mainly linked to surface

waves propagating at the interface between the cavity and the sample. Moreover, a careful look at the snapshots brings to light a “phantom” focal point, inside the cavity. Even if less visible than in the first considered case, within the chaotic cavity alone, the waves seem to come from every direction around this “phantom” focal spot.

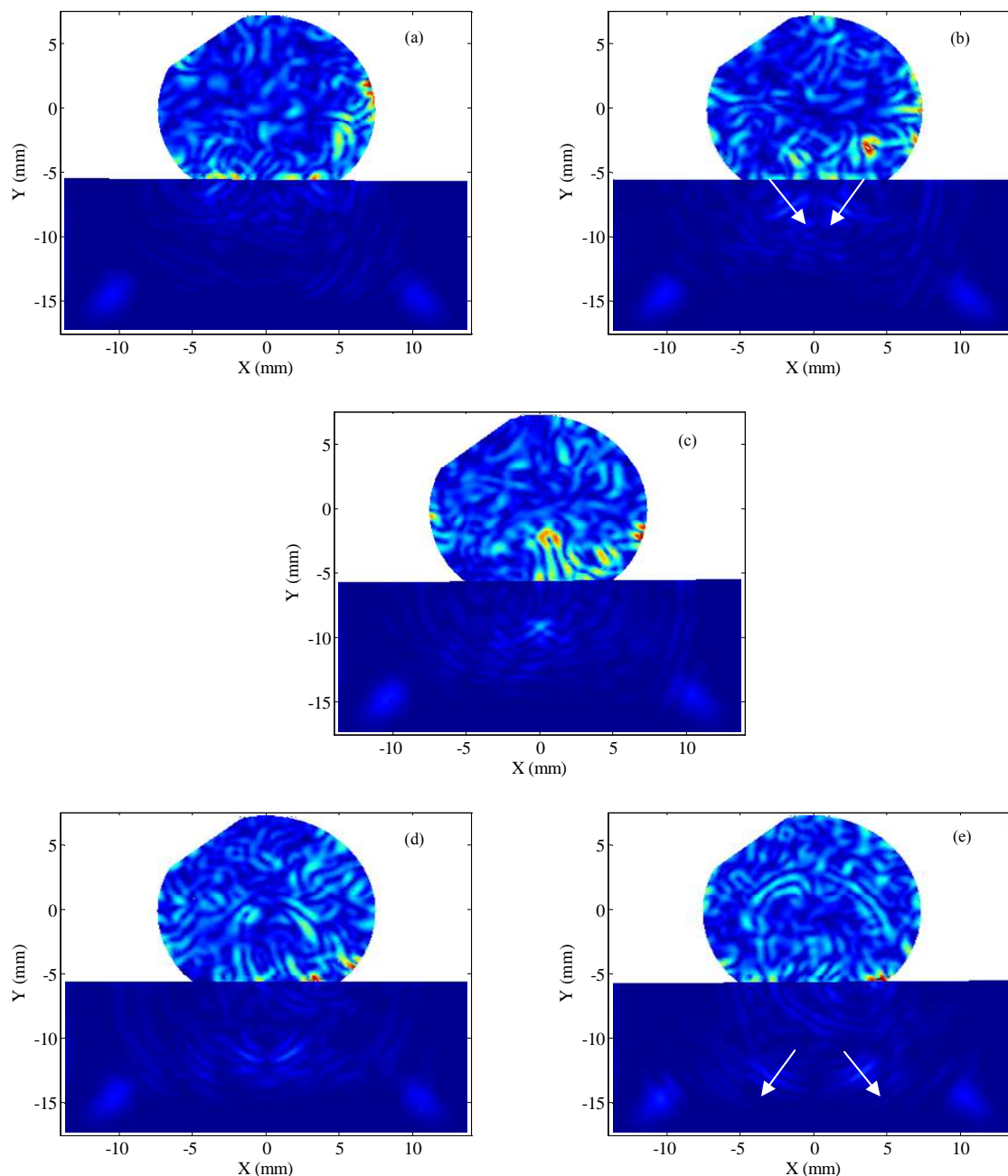


**Fig. 4.21** Snapshots of the particle velocity at five instants around the time recompression for a copper chaotic cavity glued on a non reverberating composite sample, calculated with a RK-DG-FEM O4 scheme. (a)  $t = 97.3 \mu\text{s}$ , (b)  $t = 98.3 \mu\text{s}$ , (c)  $t = 99.2 \mu\text{s}$ , (d)  $t = 100.4 \mu\text{s}$ , and (e)  $t = 101.4 \mu\text{s}$ .

These first numerical results give some insight into the behavior of a “chaotic cavity transducer” when used for imaging application in solids.

## 4.3 Experiments in a Reverberant Medium

### 4.3.1 Set-up of the Experiment

In the experiment discussed here a  $12 \times 2.5 \times 1.0$  cm steel sample has been used. With such boundary conditions, no information can escape from the system and a reverberant acoustic field is created. The experiment is setup as shown on Fig. 4.22. A single PZT ceramic disk is glued to a chaotic cavity and, similarly, the cavity is glued onto the sample. The cavity made in copper has been designed in order to have the ergodic and mixing properties. A source signal, generated by an arbitrary wave generator coupled to a power amplifier, is applied to the PZT and generates travelling waves propagating in the cavity and radiating in the sample medium. In order to guarantee the synchronization of time reversal waves, the arbitrary wave generator AWG2021 is triggered by an external trigger generator. The surface velocity of sample medium has been measured by a laser vibrometer. The signal is acquired through an oscilloscope LeCroy 9361. The reciprocal time reversal process and the scanning of the laser are computer controlled by Labview.

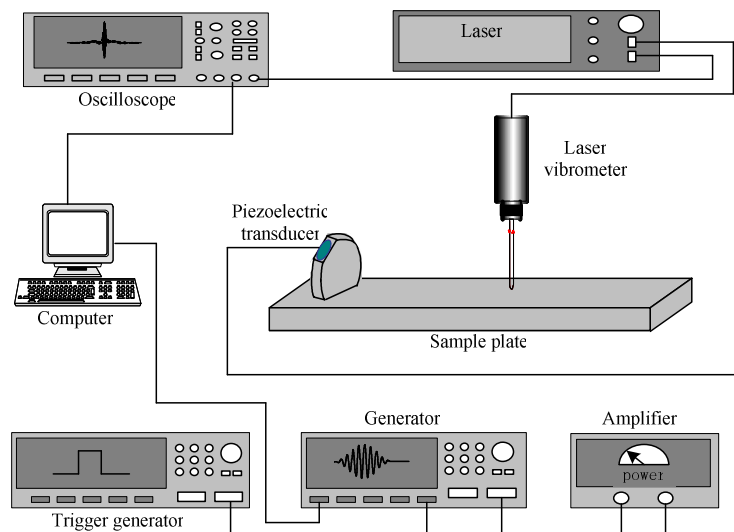
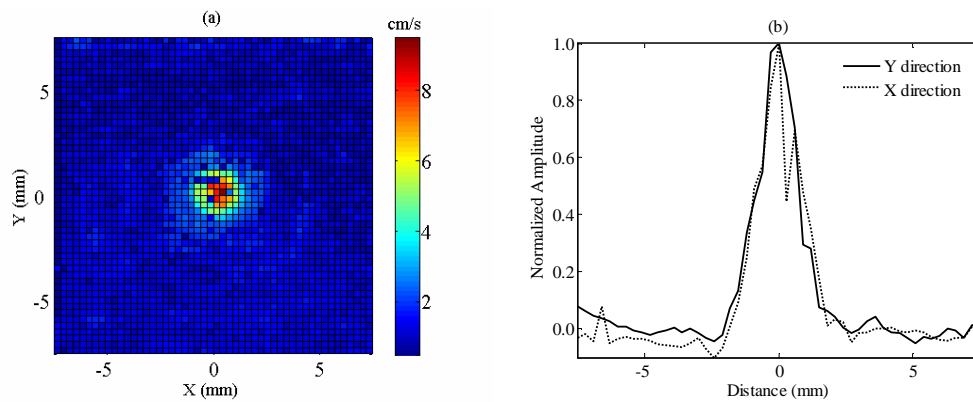


**Fig. 4.22** Experimental set-up used for the demonstration of the focusing properties of a “chaotic cavity transducer” in a reverberant sample.

### 4.3.2 Experimental Results

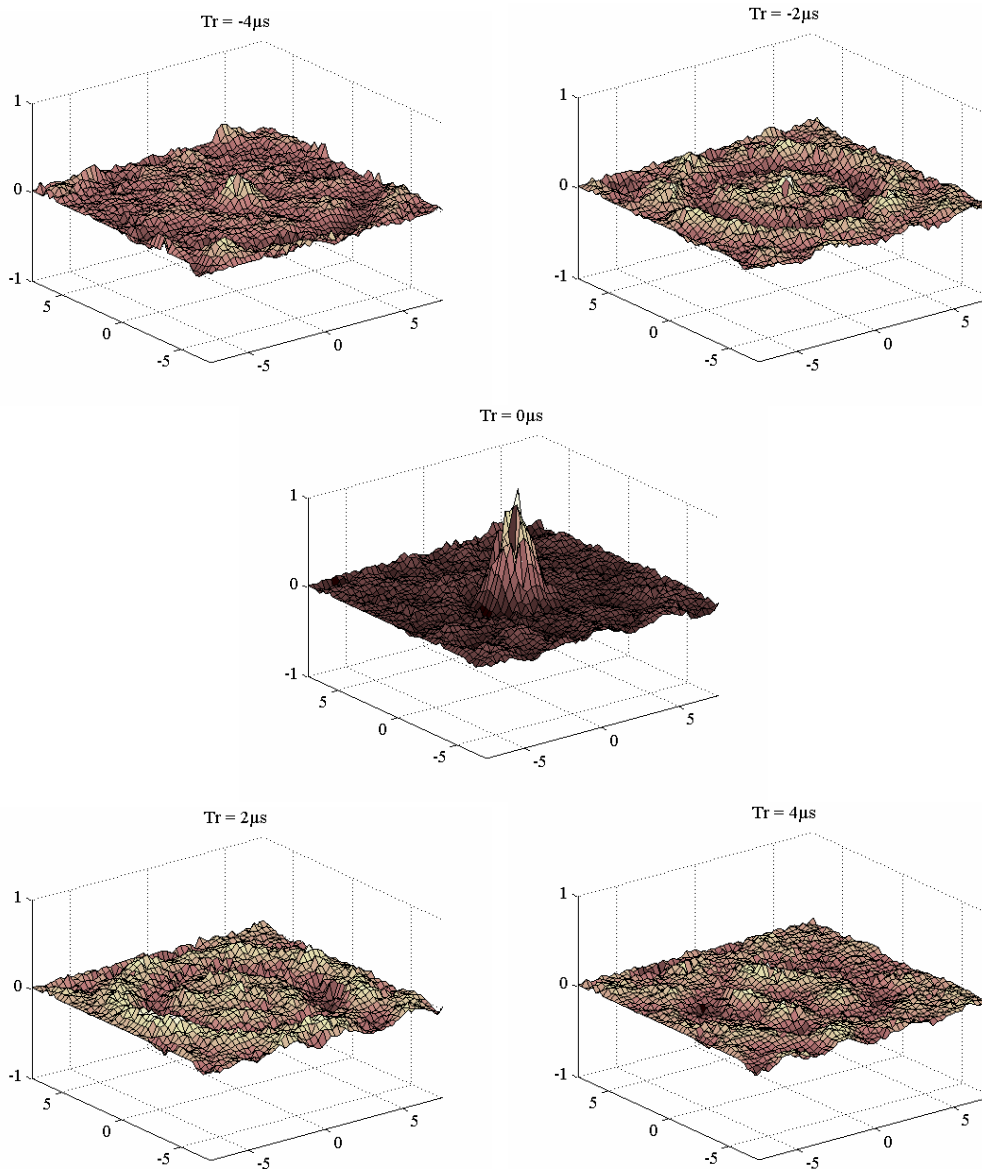
In this part, experimental results obtained with Time Reversal (TR) or Inverse Filter (IF) methods will be presented. In all the experiments, a linear sweep source signal has been used with the following parameters:  $T = 100 \mu\text{s}$ ,  $f_1 = 200 \text{ kHz}$ , and  $f_2 = 1200 \text{ kHz}$ . In the whole process of each experiments, for the linear sweep source signal, the convolution operation can not only be done before the TR or IF process, but also at the end of the whole process.

First, the spatial recompression experiment for the steel sample, obtained with the Time Reversal (TR) method, will be presented. In the first step, the focalization procedure presented in the previous paragraph is used to retro-focus on the chosen position on the surface of the sample. Here, the convolution operation has been made before the TR process. Then a 2D scan of  $15 \times 15 \text{ mm}^2$ , with a spatial step of 0.30 mm, of the wave field around the focal spot is made. The obtained 2D map shown on Fig. 4.23(a) demonstrates the high quality of the retro-focalization, with a spot size of 2 mm radius. Moreover, the spatial distributions of focalized signal in the two axis directions (Fig. 4.23(b)) show no increase of the strain at the stress free boundary (upper boundary on Fig. 4.23(a)). These results confirm that a single PZT ceramic with a chaotic cavity can be used as a time reversal mirror (TRM) when the sample is multi-reverberant.



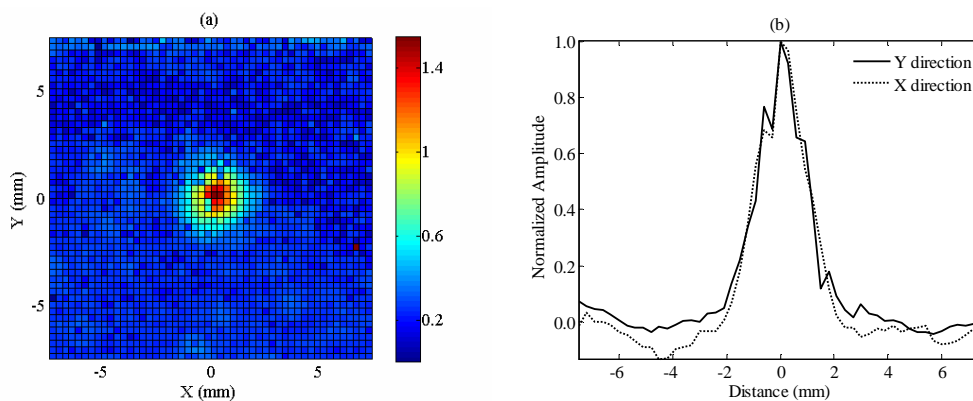
**Fig. 4.23** Time Reversal (TR) recompression experiment. (a) 2D scan of the focalization points. (b) Spatial distributions of focalized signal in  $x$  and  $y$  axis directions at the time  $T_r = 0 \mu\text{s}$ .

Fig. 4.24 displays snapshots of the wave field at the surface of the sample around the focus point. Here  $T_r = 0 \mu\text{s}$  corresponds to the instant of time recompression. In the first and second figures at  $T_r = -4 \mu\text{s}$  and  $T_r = -2 \mu\text{s}$ , respectively, we can see the wave propagating in the centerward direction, as if there are many transducers surrounding the focalization point in all the directions. The third figure shows that the energy has focalized at  $T_r = 0 \mu\text{s}$  in the reference focal point. Then, the waves propagate away from the center as shown on the fourth and fifth figures at  $T_r = 2 \mu\text{s}$  and  $T_r = 4 \mu\text{s}$ , respectively. These snapshots clearly show that the focusing wave come from all around the focus point. This is due to the fact that, here, as the sample is multi-reverberant, it contributes to the retro-focusing process as previously demonstrated numerically.



**Fig. 4.24** Snapshots of the surface particle velocity around the focal point at different time showing the TR focalization process obtained with a “chaotic cavity transducer”.

Secondly, the same experiment obtained now with the Inverse Filter (IF) method in place of the TR, will be presented. The 2D scan ( $15 \times 15 \text{ mm}^2$  with a spatial step of  $0.30 \text{ mm}$ ) of the wave field around the focal spot is shown on Fig. 4.25. The obtained 2D map demonstrates the high quality of the retro-focalization with the IF method, and the spatial distribution of focalized signal in the two axis directions shows no increase of the strain at the stress free boundary as for the TR method. Fig. 4.26 shows the process of the focalization at five different time  $T_r = -4 \mu\text{s}$ ,  $-2 \mu\text{s}$ ,  $0 \mu\text{s}$ ,  $2 \mu\text{s}$  and  $4 \mu\text{s}$ . Here, contrary to what Quieffin *et al.* [150] have obtained in water with a chaotic cavity, the focal spot size is not decreased by the use of IF technique. Indeed, in both experiments with TR and IF the same  $2 \text{ mm}$  focal spot radius has been obtained, and is an estimate of the correlation length of the scattered wave field as demonstrated by de Rosny *et al.* [72].



**Fig. 4.25** Inverse Filter (IF) recompression experiment. (a) 2D scan of the focalization points. (b) Spatial distributions of focalized signal in  $x$  and  $y$  axis directions at the time  $T_r = 0 \mu\text{s}$ .

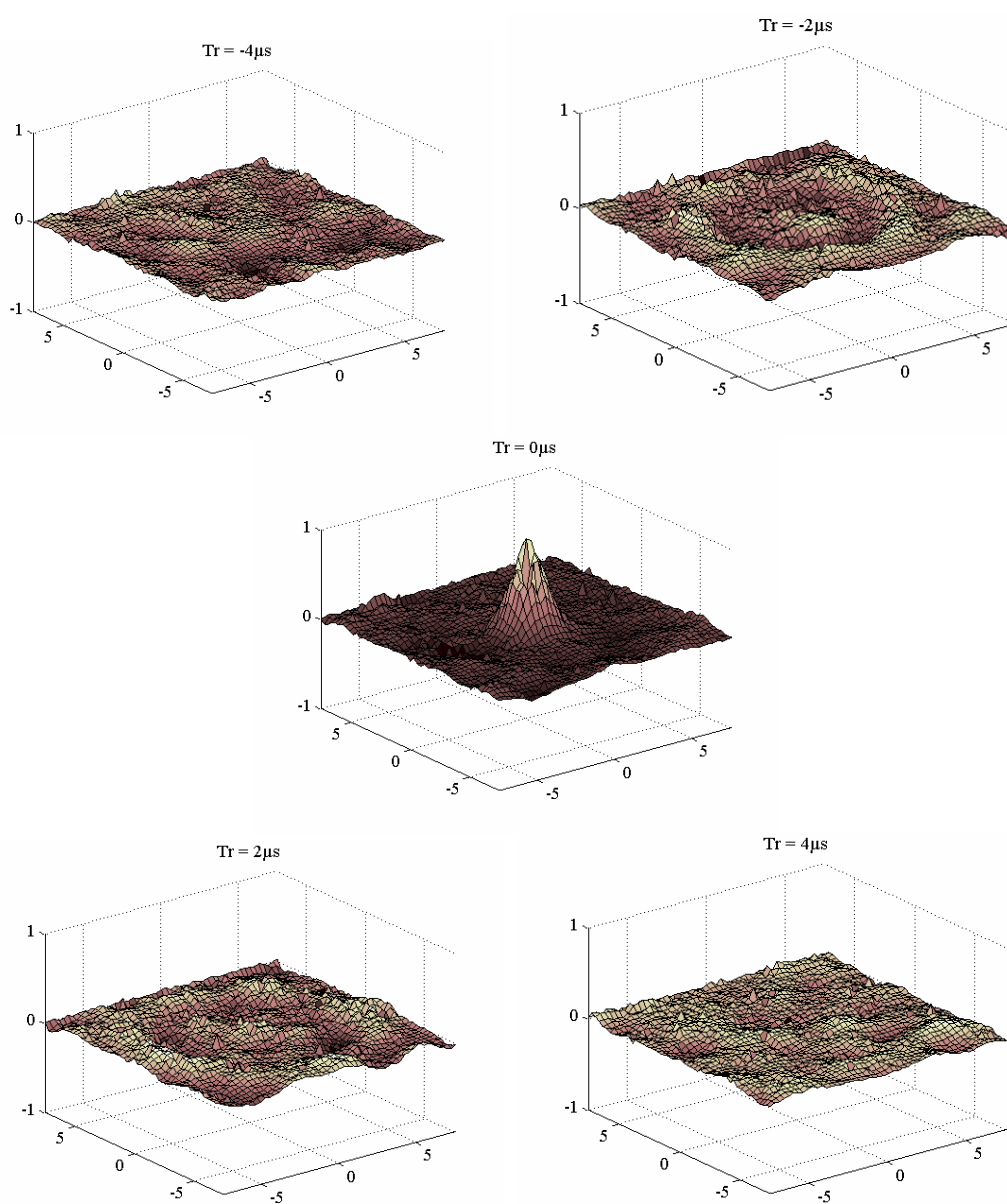


**Fig. 4.26** Snapshots of the surface particle velocity around the focal point at different time showing the IF focalization process obtained with a “chaotic cavity transducer”.

Now, to demonstrate the ability of the “chaotic cavity transducer” to focus even on the border of the material sample, the TR focalization experiment has been performed once again with the steel sample, but this time, the retro-focusing point has been chosen directly on the border of the sample. A 2D map of the maximum amplitude measured on a surface of  $15 \times 15$  mm<sup>2</sup> around the selected focal point (Fig. 4.27(a)) and the spatial distribution of focalized signal in two perpendicular directions (Fig. 4.27(b)) demonstrates the high quality of the retro-focusing, with a spot size of 2 mm radius. Remark that, also in this case, there is no increase of the strain at the stress free boundary (upper boundary on Fig. 4.27(a)) contrary to the case when a PZT ceramic is directly glued on the reverberating sample. The focalization process is displayed on Fig. 4.28 at the same five times as in the preceding experiments. As before, the wave comes from all around the focus point. All these results demonstrate that it is possible to get a high quality focalization also on stress free boundaries of multi-reverberant samples with a “chaotic cavity transducer”.

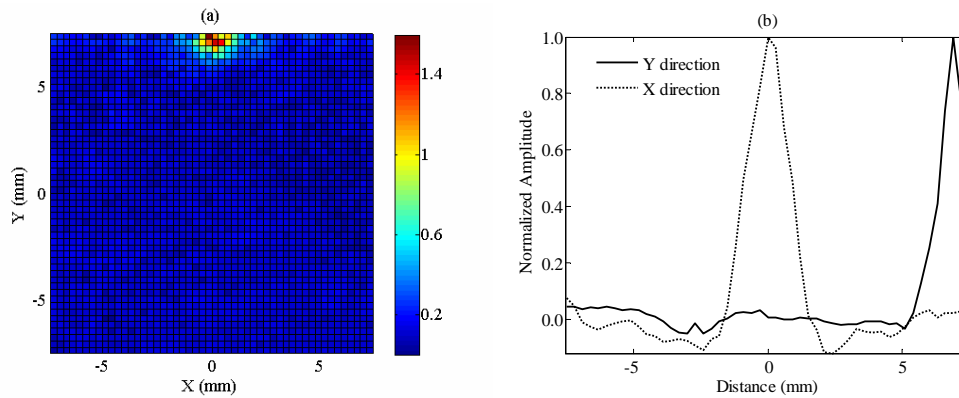


**Fig. 4.27** Time Reversal (TR) recompression experiment with a focus point on the border of the sample. (a) 2D scan of the focalization on the border, (b) spatial distributions of focalized signal in  $x$  and  $y$  axis directions at the time  $T_r = 0 \mu\text{s}$ .

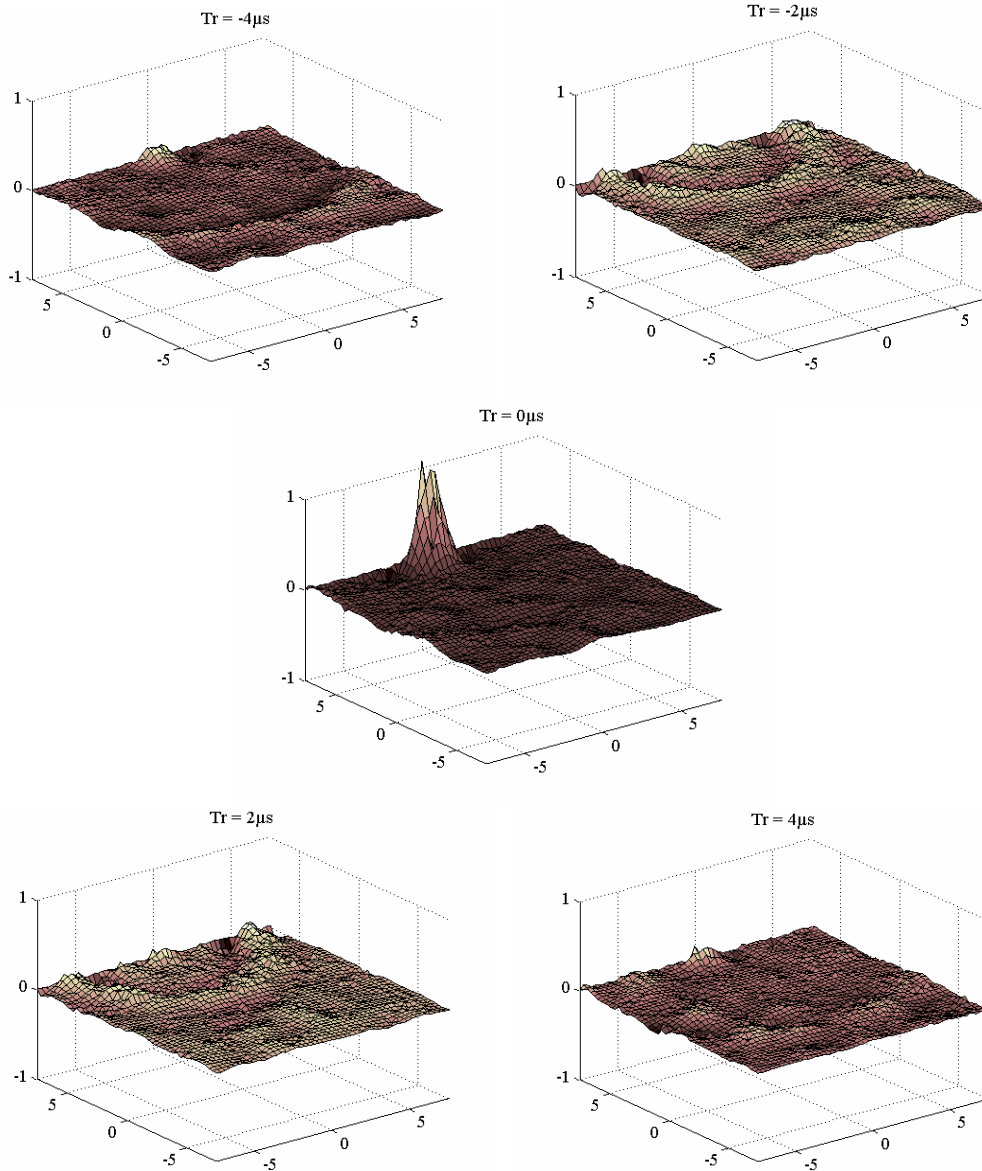


**Fig. 4.28** Snapshots of the surface particle velocity around the focal point at different time showing the TR focalization process obtained with a “chaotic cavity transducer” on the border of the steel sample.

### 4.3.3 Contrast of the Retro-Focalized Signal

One of the more important parameters of the “chaotic cavity transducers” is the “signal-to-noise” contrast. As proposed by Quieffin *et al.* [150], this contrast is the ratio between the energy of the signal at the recompression time  $T_r = 0$  and the energy of the signal at all the others times. The equation of the contrast can be expressed as follows

$$C = \frac{(s(t=0))^2}{(s(t \neq 0))^2} = \frac{I_{peak}}{I_{corr. noise}}. \quad (4.14)$$

A physical interpretation of the contrast in terms of information grains has been given by Derode *et al.* [56]. An impulse response can be viewed as a recurrence of decorrelated

information grains of duration equal to the initial pulse one. The peak of recompression results in the coherent sum of the information grains and the surrounding noise on their incoherent sum. In the case of reverberating cavity, the information grains can be identified with the vibration eigenmodes of the cavity. Thus a contrast theory, for time reversal focusing in a cavity, can be developed using these vibration eigenmode formalism. Several physical parameters should be taken into account in this formalism:

- The absorption time  $\tau_a$  of the material describing the damping of the impulse response;
- The Heisenberg time  $T_H$  of the cavity which could be viewed as the modal density of the cavity, that is to say the number of eigenmodes per frequency unit, and which depends on the volume of the cavity;
- The emission signal duration of the time reversed window  $\Delta T$  ;
- The statistic of the distribution of the eigenmode amplitudes  $\alpha$  and the frequency bandwidth  $\Delta\Omega$  .

The result, obtained by Quieffin [151] in his PhD dissertation, can be written as:

$$C = \frac{4\sqrt{\pi}.T_H.\Delta\Omega.shc^2\left(\frac{\Delta T}{\tau_a}\right)}{\frac{\langle\alpha^4\rangle}{\langle\alpha^2\rangle^2}shc^2\left(\frac{\Delta T}{\tau_a}\right) + \frac{T_H}{\Delta T}shc\left(\frac{2\Delta T}{\tau_a}\right) - \frac{1}{\Delta T^2}\int_{-\infty}^{+\infty}z(t)\otimes_t z(-t).b\left(\frac{t}{T_H}\right)dt}. \quad (4.15)$$

From this expression three asymptotic behaviors can be considered. First, when the duration of the time reversed window  $\Delta T$  is less than the Heisenberg time  $T_H$  and the attenuation time  $\tau_a$ , the contrast becomes proportional to the duration time and to the frequency bandwidth  $\Delta\Omega$ :

$$C = 4\sqrt{\pi}.\Delta\Omega.\Delta T, \quad (\text{when } \Delta T \ll T_H, \tau_a) \quad (4.16)$$

In this case, the contrast linearly increases with the duration  $\Delta T$  .

In the second situation, the Heisenberg time is less than the duration  $\Delta T$  and the attenuation time. In this case, the contrast becomes proportional to the Heisenberg time  $T_H$  :

$$C = 4\sqrt{\pi}.\Delta\Omega.T_H \frac{\langle\alpha^2\rangle^2}{\langle\alpha^4\rangle}. \quad (\text{when } T_H \ll \tau_a, \Delta T) \quad (4.17)$$

The third situation corresponds to the case where the attenuation time is shorter than both the Heisenberg time and the duration  $\Delta T$  . The contrast becomes then proportional to the attenuation time:

$$C = 4\sqrt{\pi}.\Delta\Omega.\tau_a. \quad (\text{when } \tau_a \ll T_H, \Delta T) \quad (4.18)$$

Fig. 4.29 shows an example of the “signal-to-noise” contrast, measured in the case of the copper chaotic cavity glued on a  $12 \times 2.5 \times 1.0$  cm rectangular steel sample, as a function of the duration  $\Delta T$  of the time reversed or inverse filtered signal. An improvement by a factor of three can be observed using the IF technique. The overall evolution of the contrast as a function of the duration of the time reversed window  $\Delta T$  is in accordance with the theoretical description. When  $\Delta T$  is less than the Heisenberg time  $T_H$  of the cavity (which is related to the modal density of the cavity) and less than the characteristic attenuation time  $\tau_a$ , the contrast linearly increases with  $\Delta T$ . When  $\Delta T$  is increased and becomes larger than  $T_H$  or  $\tau_a$ , a saturation of the contrast appears. As a matter of fact, as the vibration eigenmodes represent the only frequencies present in the cavity, and as the frequency bandwidth is limited by the transducer that is used, the number of vibration eigenmodes of the cavity is limited as well, and consequently the contrast saturates.

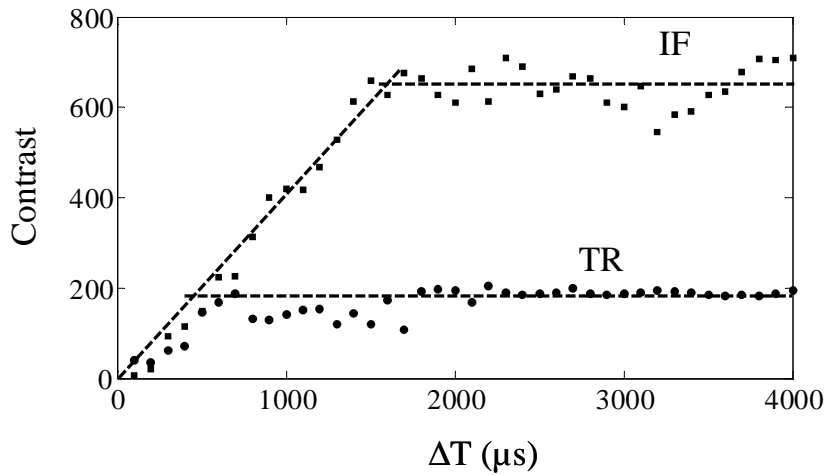


**Fig. 4.29** Contrast of the retro-focalised signal for Time Reversal (TR) and Inverse Filter (IF) processes, showing the improvement by a factor of three for the inverse filter technique.

To understand which is the limiting factor between  $T_H$  and  $\tau_a$ , an estimate of both of these time needs to be calculated. Unfortunately, as the chaotic cavity is glued on the sample, the absorption is not the main cause of decrease of the energy inside the cavity. Indeed, we want that a non negligible part of the energy propagates in the sample. In this case, the attenuation time  $\tau_a$  of the cavity depends on the sample material. So, only an estimate of the Heisenberg time is accessible. The “breaking time” or Heisenberg time, which corresponds to the time needed in order to resolve neighbouring modes, is given by:

$$T_H = \frac{\partial N}{\partial f}, \quad (4.19)$$

where  $N$ , the cumulative eigenfrequency density in a chaotic cavity, is well represented by a Weyl type formula [65], [125], [202]:

$$\begin{aligned}
 N(f) &= \frac{4\pi V}{3} \left( \frac{2}{c_s^3} + \frac{1}{c_l^3} \right) f^3 + \frac{\pi S}{4} \frac{2 - 3(c_l/c_t)^2 + 3(c_l/c_t)^4}{c_l^2((c_l/c_t)^2 - 1)} f^2 \\
 &\approx \frac{4\pi V}{3} \left( \frac{2}{c_s^3} + \frac{1}{c_l^3} \right) f^3 + \frac{\pi S}{c_s^2} f^2,
 \end{aligned} \tag{4.20}$$

where  $V$  and  $S$  are the volume and surface of the cavity, and  $c_l$ ,  $c_t$  are velocities of longitudinal wave and transverse wave, respectively. This amount of time  $T_H$  is required to allow two modes separated by an average level spacing to achieve  $360^\circ$  phase difference. Moreover, it has also been argued [125] that this time  $T_H$  is the time at which a ray description must fail. Eq. (4.20) can be written as a function of the wavelengths:

$$N(f) = \frac{4\pi V}{3} \left( \frac{1}{\lambda_s^3} + \frac{1}{\lambda_l^3} \right) + \frac{\pi S}{\lambda_s^2}. \tag{4.21}$$

The number of modes increases, for a given frequency, if we increase the volume and the surface of the cavity, and if we decrease the wavelengths.

So, in obtaining the results of Fig. 4.29, the attenuation, mainly due to the radiation losses of the sample, appears to be the limiting factor. Indeed, for the considered copper cavity, with a volume of  $2.8 \text{ cm}^3$  and a surface of  $6.22 \text{ cm}^2$ , the estimated Heisenberg time  $T_H$  is 10 ms, which is 10 times larger than the duration of the measured reverberating signal. As a result, for large values of  $\Delta T$  the contrast simply becomes proportional to  $\tau_a$ .

## 4.4 Experiments on a Non-Reverberant Medium

The combination of traditional single channel TRA with non-reverberant samples poses serious problems for the technique as the sample cannot be used as a chaotic cavity. In this case, the use of the ‘‘chaotic cavity transducer’’ can be a good solution to extend the possibility to focus in such sample with a one channel TRA system.

Here, the same experiments as the one done in the preceding subsection for multi-reverberating steel sample will be repeated for a 2 mm thick non-reverberant composite plate of large dimension ( $30 \times 20 \times 0.2 \text{ cm}$ ), as shown on Fig. 4.30.

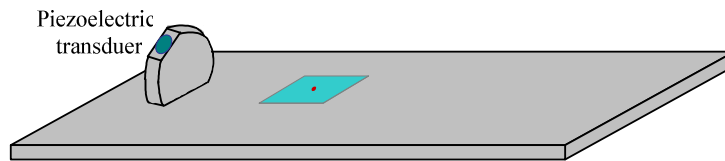


**Fig. 4.30** ‘‘Chaotic cavity transducer’’ used with a 2 mm thick non-reverberant composite plate.

We have used a  $1 \times 2 \times 12$  cm chaotic cavity glued on the composite plate. The chaotic behavior of the rectangular cavity used is induced by holes sparsely made in it. The 2 cm width edge is the emitting edge of the “chaotic cavity transducer”. As in the preceding reverberant sample experiments, a sweep of  $100 \mu\text{s}$  duration and  $f_{\min} = 200 \text{ kHz}$  and  $f_{\max} = 1.2 \text{ MHz}$  combined with an inverse filter technique enable the focalization of elastic wave everywhere in the sample. The 2D scan of the amplitude of wave field around the chosen focal spot, on a square of  $15 \times 15 \text{ mm}^2$  with a spatial step of  $0.30 \text{ mm}$ , is plotted in Fig.4.31. This figure demonstrates that the “chaotic cavity transducer” works also on non-reverberating samples, even if the focalization quality is not as good as in the case of reverberating sample. Here, as the sample is highly attenuating in the frequency range used,  $200 \text{ kHz}$  to  $1.2 \text{ MHz}$ , the surface particle velocity is quite small and difficult to measure with the laser vibrometer.

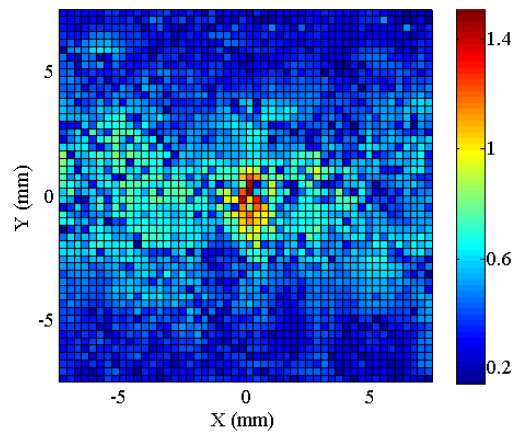


**Fig. 4.31** 2D scan of maximum amplitude measured during the retro-focalization process with the cavity  $1 \times 2 \times 12$  cm on the non-reverberant composite plate.

As displayed on Fig. 4.32 the process of retro-focalization in this case of non-reverberating sample is different from the one obtained previously with the reverberant sample. Indeed, here, as already seen in the numerical simulations the wave does not come from all around the focal point, but seems to propagate from the cavity.

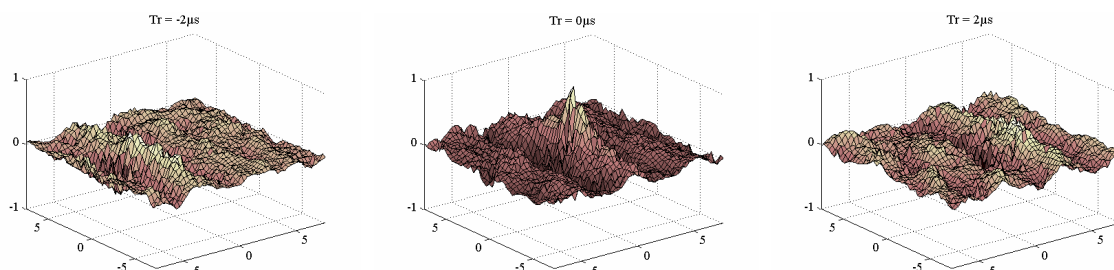


**Fig. 4.32** Snapshots of the surface particle velocity at different time showing the process of the retro-focalization in the non-reverberant composite plate with a  $1 \times 2 \times 12$  cm cavity.

In fact, the behavior of the “chaotic cavity transducer” is now similar to the one we would obtain with a multi-elements transducer as shown on Fig. 4.33. The width of the focalization area depends on three parameters: the width of the chaotic cavity  $D$  in the direction of focalization, the distance between the cavity and the chosen point or focal distance  $F$ , and the wavelength  $\lambda$  of the dominant transmitted mode. The resolution should be expressed by the following equation:

$$\Delta R = \lambda \frac{F}{D}. \quad (4.22)$$

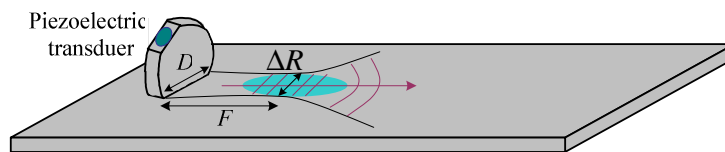


**Fig. 4.33** Schematic explanation of the behavior of the “chaotic cavity transducer” in a non-reverberating sample.

This behavior of the “chaotic cavity transducer” is similar to the one obtained at the Laboratoire Ondes et Acoustique (LOA) in Paris when used for 3D imaging in water [149], [129]. So, their idea of “synthetic time-reversal” technique [149], [150], [151] can be developed for non-reverberating solid samples, and specially plates, even if this will be more difficult due to anisotropic and dispersive effects in such media. This, will suppress the need to measure, with a laser vibrometer, the particle velocity at all the imaged points, which is one of the main limitations for the development of NDT applications of “chaotic cavity transducer”. This method consists in the creation of a large aperture virtual Phased Array using a “Chaotic Cavity Transducer” to focus at any point in the sample as shown on Fig. 4.34. The multiple-scattered field is measured at several points in front of the solid cavity. These signals are then time reversed or inverse filtered and added with delays calculated in order to generate a plane (Fig. 4.34(a)) or focused (Fig. 4.34(b)) wave. Finally the obtained signal is remitted by the transducer. Up to now, promising preliminary results have been obtained in Kortrijk in collaboration with Koen Van Den Abeele on the same composite plate, showing the validity of the “synthetic time-reversal” technique for focusing in plate.

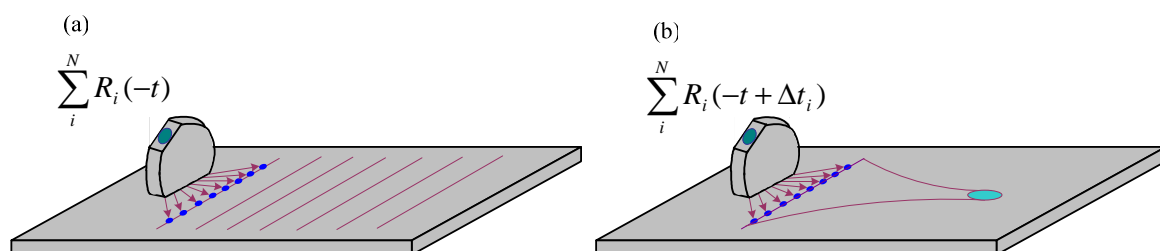


**Fig. 4.34** Principle of multi-elements imaging with a “chaotic cavity transducer” in a non-reverberating sample: All the virtual point sources are excited (a) in phase and a plane wave is emitted, and (b) with phase delays calculated to focus the wave on a chosen position.

To develop a complete imaging system, subsequent imaging can be done using a similar “Chaotic Cavity Transducer” as a receiver.

## 4.5 Nonlinear Acoustic Imaging with Chaotic Cavity Transducer

The chaotic cavity transducer focusing process can be used, in combination with NEWS techniques such as the pulse inversion method [195], to obtain an image of localized nonlinearity. Indeed, as shown on Fig. 4.35, by successively focusing a pulse (in black) and its inverse (in blue), and subsequently summing the two results, we can extract the nonlinear response of the sample at the focal position. Repeating the same process for a 2D array of points at the surface of a sample, an image based on nonlinear information can be obtained. Similarly, a scale subtraction or harmonic filtering method to reveal the nonlinearity [164], and a 1-Bit process to increase the amplitude of the retro-focused signal even further, could be used.

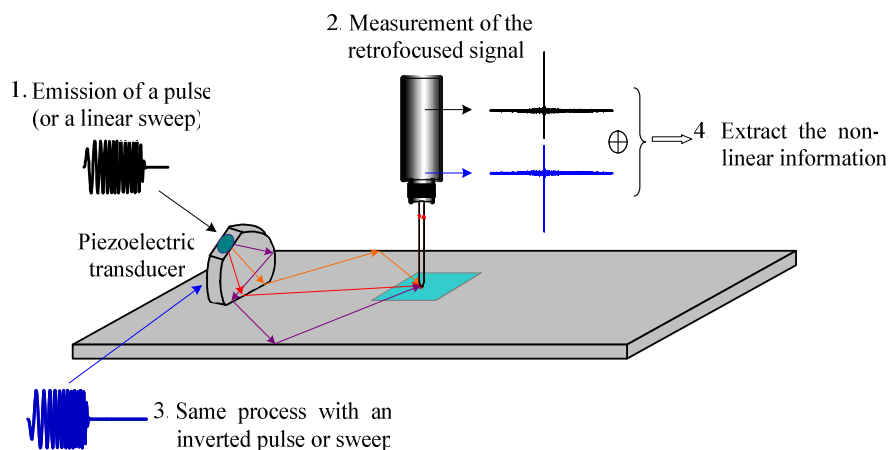


**Fig. 4.35** Principle of TR-NEWS with a chaotic cavity transducer.

### 4.5.1 TR-NEWS Experiment with Chaotic Cavity Transducer

The NEWS based TRA technique was applied to a fatigue cracked steel sample ( $12 \times 2.5 \times 1.0$  cm) as shown on Fig 4.36. The same “chaotic cavity transducer” as the one already used in the reverberant sample experiment has been used here. Two sweeps, of  $100 \mu\text{s}$  duration and  $f_{\min} = 200$  kHz and  $f_{\max} = 1.2$  MHz, with inverted signs and an inverse filter 1-bit reversal have been used to focus at the same position a pulse and its inverse. Nonlinear response of the sample at this position is then extracted with a pulse inversion analysis. This process has been repeated on a surface of  $20 \times 6$  mm<sup>2</sup> around the crack position with a step, in both dimensions, of 1 mm.

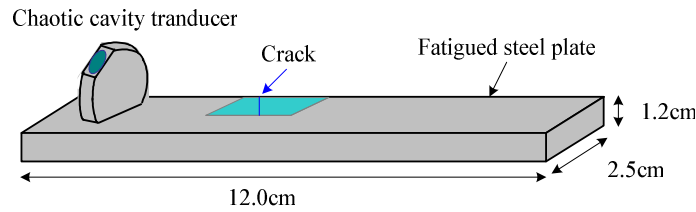


**Fig. 4.36** Schematic of the fatigue steel sample and the “chaotic cavity transducer” used for the TR-NEWS imaging of a crack.

The resulting distribution of the analyzed nonlinearity, corresponding to the sum of the normal particle velocity induced by the two focused inverted pulses, is shown in Fig. 4.37. On the displayed image, the crack clearly appears. The main nonlinear contribution of the crack seems to come from its tip, thereby confirming the results of Ulrich *et al.* [185]. Moreover, as in the linear cases of the previous sections, no increase of the induced vibrations can be noticed on a boundary of the sample, here on the upper side of the 2D scan displayed on Fig. 4.37.

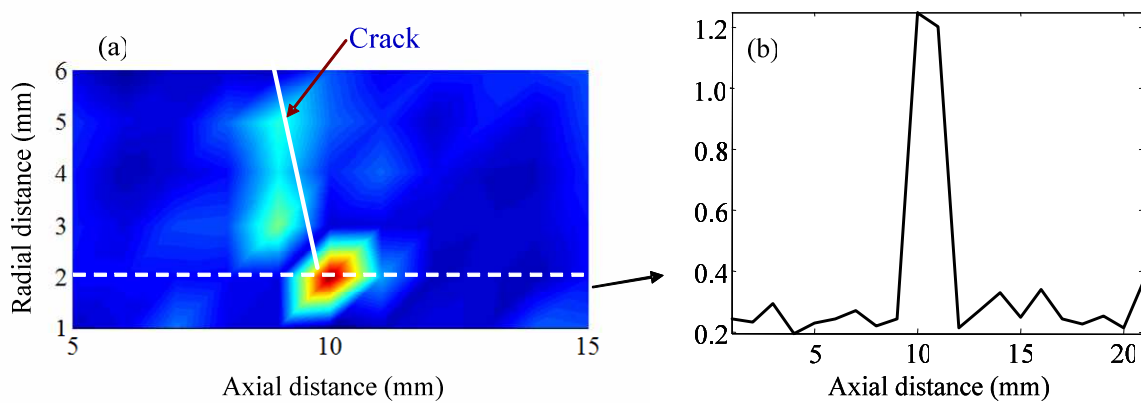


**Fig. 4.37** Image of a crack at the surface of a steel sample obtained with a combination of TR-NEWS method and “chaotic cavity transducer”.

In order to improve our understanding of the interaction between an elastic wave and a crack, a prototype sample made by nanotechnology techniques has been realized. The sample is a silicon wafer on which four 100  $\mu\text{m}$  grooves has been cut by a Focused Ion Beam (FIB), as shown on Fig. 4.38. The widths of the four notches,  $f_1$  to  $f_4$ , are 50, 100, 200 and 300 nm, respectively. Here, 50 nm is the smallest width we were able to obtain by FIB.

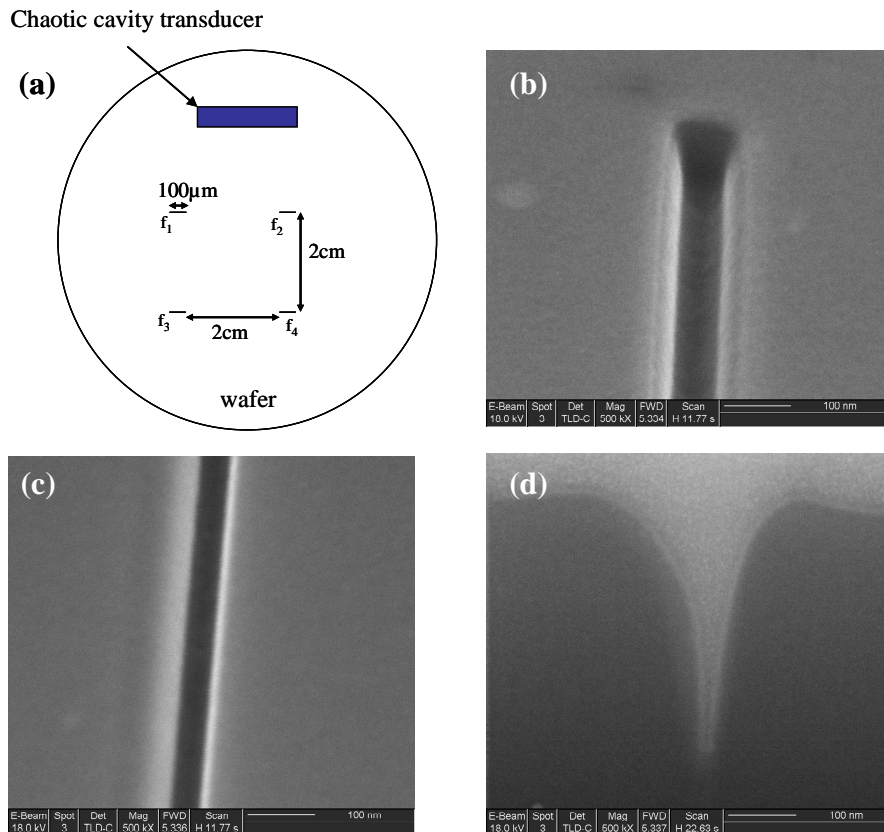


**Fig. 4.38** (a) Schematic of the wafer sample with four 100  $\mu\text{m}$  long grooves made by FIB. (b)-(d) FIB Images showing (b) the tip, (c) the width (50 nm) and (d) the depth (200 nm) of the groove with the smallest width ( $f_1$ ).

The same NEWS based TRA technique has been used, with the same “chaotic cavity transducer” and sweep parameters, to image these “fabricated cracks”. Unfortunately, on all the attempts realized, the grooves made by FIB, even the one with the smallest width (50 nm), have never been detected by TR-NEWS method. This result tend to demonstrate that a real crack, at least for the used frequency range, 200 kHz to 1.2 MHz, can not be simply represented as clapping interfaces. Indeed, the amplitudes of the displacement induced in the wafer, and measured by the laser interferometer, were always less than 50 nm, the minimum distance between the two borders of the notches. One envisaged improvement in the realization of a prototype sample is to use the FIB not to make the “crack”, but to initiate it [121]. In this case, a notch is made by FIB and, afterwards, a crack, with a perfectly controlled position, is initiated at this notch by oscillatory loading.

#### 4.5.2 NEWS-TR Experiment with Chaotic Cavity Transducer

The NEWS-TR application is based on signal retro-focusing on the defect position when only the nonlinear components of the received signal are time reversed [77], [79], [185], as shown on Fig. 4.39. This method, described for the first time by Bou Matar *et al.* [23] in 2005, has only been validated experimentally recently [185]. In this experimental validation,

the obtained results display ‘phantom’ images and some points of particle displacement increase on the stress free boundary close to the crack position.

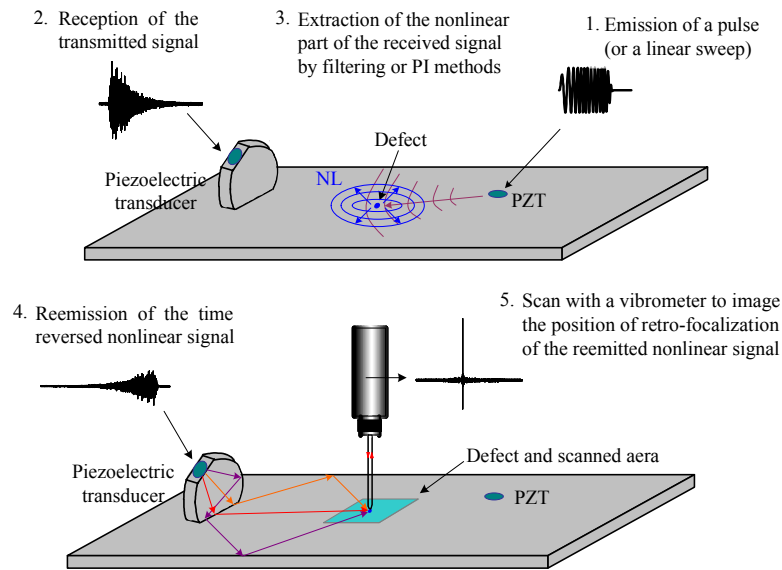


**Fig. 4.39** Principle of NEWS-TR for defect imaging in a non-reverberant sample.

A preliminary experiment on the possibility of using a “chaotic cavity transducer” for NEWS-TR method in a non-reverberant sample has been conducted. The experiment has been made on the  $30 \times 30$  cm<sup>2</sup> composite plate with a  $1 \times 5 \times 6$  cm cavity. Here, no nonlinear treatment, as pulse inversion for example, has been used. The experiment has only been designed in order to validate the use of a “chaotic cavity transducer” as a receiver as explained on Fig. 4.40. A  $5 \times 5$  mm<sup>2</sup> PZT ceramic, used as a source of small size, is excited by a sweep ( $T = 100$   $\mu$ s,  $f_{\min} = 200$  kHz,  $f_{\max} = 600$  kHz). The signal measured by the PZT of the “chaotic cavity transducer” is then numerically processed (an inverse filter is applied), and re-emitted by the same “chaotic cavity transducer”. Finally, a 2D scan of the out of plane particle velocity around the position of the initial source is made with the laser interferometer. This last step is realized after removing the  $5 \times 5$  mm<sup>2</sup> PZT ceramic to enable a correct vibrometric measurement.

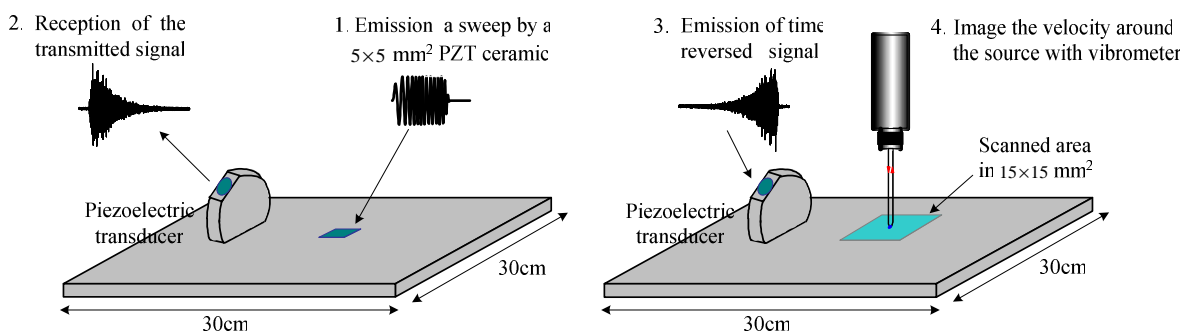


**Fig. 4.40** Principle of the preliminary experiment on the possibility of using a “chaotic cavity transducer” for NEWS-TR method in a non-reverberant sample. The experiment has been made on the composite plate with a  $1 \times 5 \times 6$  cm cavity.

Snapshots of the particle velocity on a surface of  $15 \times 15 \text{ mm}^2$  around the source position showing the process of retro-focalization on the source position are displayed on Fig. 4.41. The snapshot at time  $T_r = 0 \text{ }\mu\text{s}$  shown that the wave emitted by the “chaotic cavity transducer” focused simultaneously on the two borders of the PZT source. This demonstrates that the main contribution of the  $5 \times 5 \text{ mm}^2$  PZT source corresponds to plate modes excited by its border.

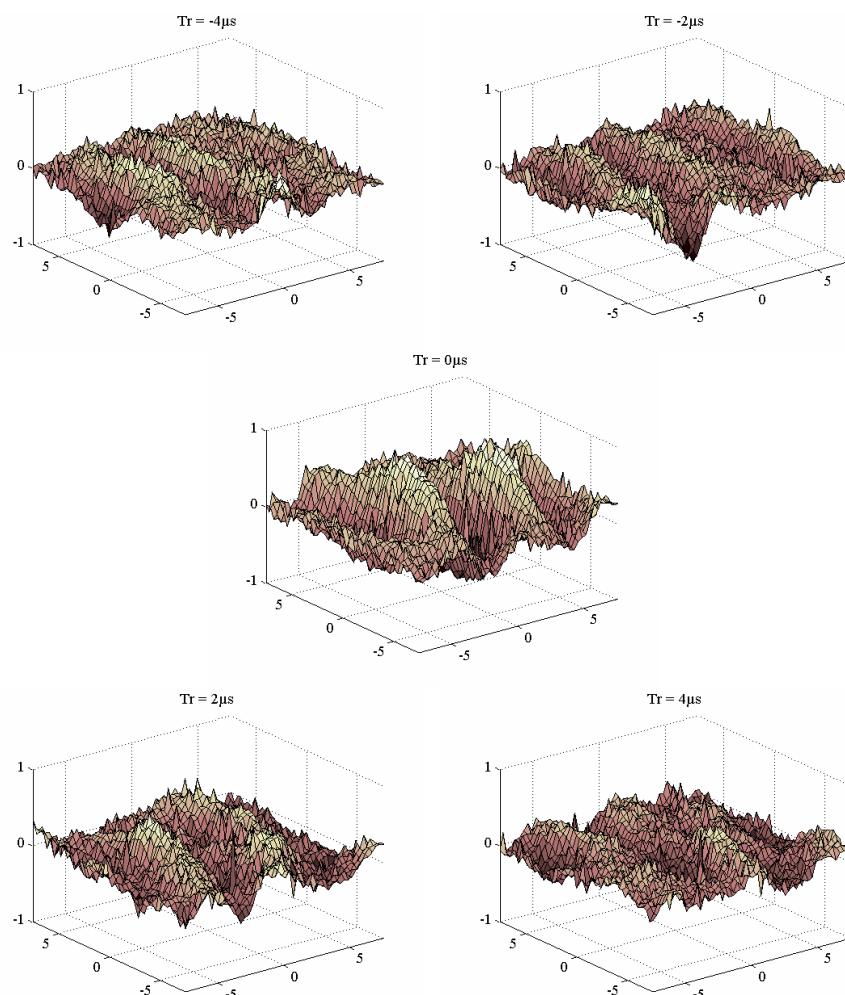


**Fig. 4.41** Snapshots of the surface particle velocity at different time showing the process of the retro-focalization on the position where the small  $5 \times 5 \text{ mm}^2$  PZT ceramic source was glued.

## 4.6 Conclusion

In this chapter, a numerical and experimental study has been performed in order to demonstrate the possibility of linear and nonlinear ultrasonic imaging of defects in solids offered by the “chaotic cavity transducer” concept. As an extension of the classical time reversal process, three signal processing techniques have been studied in order to improve both the signal to noise ratio (contrast) and the quality of the focalization: Chirped excitation, Inverse Filter and 1 bit processing. Chirp-coded excitation instead of single-carrier short

pulses is studied in order to transmit more energy per time on the defect without increasing the peak intensity of the excitation. Moreover, the experimental results show that the used bandwidth and so the signal to noise contrast is increased with this sweep excitation. Using inverse filter method in stead of time reversal, the focusing process takes advantage of all the eigenmodes of the cavity including those with the weakest energy which are poorly exploited in the time reversal focusing process. This greatly improves the time recompression and the signal to noise contrast.

One of the major advantages of using chaotic cavities that has been demonstrated both numerically and experimentally is the elimination of phantom images and boundary effects in the retro-focalization process. Experimental results obtained in a small reverberating steel sample have demonstrated without doubt the ability of the “chaotic cavity transducers” to focus even on the border of the material sample.

Experiments performed on a 2 mm thick non-reverberant composite plate with relatively large dimensions ( $30 \times 20 \times 0.2$  cm) have demonstrated a second advantage of chaotic cavities: their potential to focus energy in non-reverberating samples. In this case, the sample does not contribute to the focusing process and the focusing is achieved by propagating wave that solely come from the direction of the transducer and not from every direction around the focal spot, contrary to what is obtained in a reverberant sample.

We have also demonstrated that the “chaotic cavity transducer” can be used, in combination with the pulse inversion and 1-bit methods, to obtain an image of localized nonlinearity. The preliminary image of a crack at the surface of a steel sample shows that the benefit of using a chaotic cavity transducer, in combination of TR and NEWS techniques, is clearly found in breaking any obvious or hidden symmetry of the problem, leading to an unambiguous retro-focusing. Moreover, the main nonlinear contribution of the crack appears to come from its tip, thereby confirming previously published results. This opens the possibility for high resolution imaging of nonlinear defects.

A last opportunity offered by the “chaotic cavity transducer” which needs to be explored is the use of embedded transducers with chaotic emission characteristics in order to perform Structural Health Monitoring (SHM). Obviously, the first step will be to find the minimum impedance mismatch needed in order that an embedded transducer has a sufficient reverberant behaviour to conserve its chaotic properties.

## CONCLUSION

In this thesis, a new NDT imaging method using a combination of NEWS and “chaotic cavity transducer” techniques has been developed and experimentally validated on a fatigued steel plate. In order to support the development of this damage localization method, it has been vital to develop a reliable, efficient, and fast numerical DG-FEM scheme with validated material constitutive models able to capture and reproduce the propagation of nonlinear waves in objects of finite geometry and in the presence of micro-damage.

In order to profoundly understand the nonlinear elastic properties of fatigued solids, 1D simulations of nonlinear propagation of elastic wave in heterogeneous media with different kinds of nonlinearity have been numerically studied. This study can help in the determination of the predominant nonlinear mechanism in specific experiment. This was a first step in the development of the proposed numerical tools and “chaotic cavity transducer” imaging system.

A nodal Discontinuous Galerkin Finite Element Method (DG-FEM) scheme, which is an intelligent combination of the FEM and FVM methods, has been presented. Different numerical fluxes, as the central and Lax-Freidrich flux, have been used. Open boundary, surface-free boundary and fixed boundary conditions have also been discussed. The main contributions of the present thesis to this numerical scheme was to extend it to nonlinear elasto-dynamic including source terms, and to introduce the possibility to use quadrilateral elements. Moreover a Perfectly Matched Layer (PML) type of absorbing boundary condition well adapted to the DG-FEM scheme, called Nearly Perfectly Matched Layer (NPML), was also developed. Finally, a sub-domain implementation was developed to increase the efficiency of the scheme when PML are used. It will also enable to easily implement, in the future, multiphysics problems. The results of simulations for isotropic Lamb’s problem and elastic wave propagation in apatite, an anisotropic medium, have authorized a validation of the DG-FEM scheme, by comparison to known analytical solutions. In the nonlinear case, as only a few analytical results are available, a plane wave propagation has been considered. The obtained results compare perfectly to previously published numerical calculations and approximate analytical solutions.

A new C-PML formulation based on the second-order systems describing wave propagation in displacement and stress formulation for anisotropic elastic and piezoelectric solids has been introduced. This formulation has been implemented in the commercial software COMSOL Multiphysics and in a home made PS code. The results of simulation, in anisotropic and piezoelectric solids, have confirmed the C-PML excellent absorbing efficiency for long time simulation, surface waves and elongated domain of calculation. Although not directly linked to the main objectives of the Thesis, the second-order equation

C-PML implementation has opened the opportunity to begin fruitful collaborations both in our laboratory and outside. For example, the good agreement between simulations and experimental results for the integrated Surface Acoustic Wave (SAW) streaming system, opened to us the opportunity to optimize this system developed by the Microfluidic group. A numerical study of an integrated high frequency (around 1 GHz) ultrasonic system for a unique cell characterization has begun in collaboration with the Ultrasons group. Finally, the optimization for linear imaging application of a “chaotic cavity transducer”, a concept we will describe in the last chapter, is undertaken with the Koen Van Den Abeele group.

In all presented implementations of C-PML supplementary PDE are introduced to actualize the C-PML variables. These PDE, as they contain spatial derivative terms, are cumbersome and difficult to introduce in the developed DG-FEM scheme, and especially when a Godunov type flux is used. To overcome this difficulty, Nearly Perfectly Matched Layer (NPML) has been applied to the elastic wave propagating in an anisotropic medium. The main advantages of this formulation are linked to the fact that the obtained system of equations is in exactly the same form as the original system, and so strongly hyperbolic, and the introduced stretched fluxes are linked by ODEs to the physical fluxes. This last point reduces the burden and time of calculation. Moreover, comparison of energy decay shows that the NPML has the same absorbing ability of C-PML.

In the case of orthotropic material stability problems have appeared, as in the first-order velocity-stress implementation. Following the “MPML” implementation, we have introduced a mixture of C-PML and of sponge layer, with a controllable ratio of these two kinds of absorbing layers, in order to stabilize the C-PML or NPML, and shown that this stabilized C-PML is in fact not perfectly matched to the physical domain. A stability analysis has been made. It gives a physical interpretation of the stability criteria previously obtained in the literature by Meza-Fajardo and Papageorgiou [126]: the slowness (or phase velocity) and the group velocity of the wave incoming in the PML need to be of the same sign. For Lamb waves simulations, this absorbing layer has been shown to absorb “inverse modes” both in non-piezoelectric and piezoelectric plates at the expense to have, at least, a length of two times the maximum wavelength of the waves existing in the plate in the frequency range investigated. In this case the reflection induced by the C-PML was -80 dB smaller than the incident energy.

Finally, an experimental and numerical study of the use of the concept of “chaotic cavity transducer” to focalize in reverberant and non-reverberant solid media with only one source has been made. Classical time reversal, inverse filter and 1 Bit time reversal process have been discussed and compared. In order to send more energy into the detect media and improve the contrast of signal to noise ratio, a linear sweep source signal has been used. Using inverse filter method in place of time reversal, it was shown that the focusing process

takes advantage of all the eigenmodes of the cavity including those with the weakest energy which are poorly exploited in the time reversal focusing process. This has greatly improved the time recompression and the signal to noise contrast. One of the main advantages of using chaotic cavities that has been demonstrated both numerically and experimentally is the elimination of phantom images and boundary effects in the retro-focalization process. Experimental results obtained in a small reverberating steel sample have demonstrated without doubt the ability of the “chaotic cavity transducers” to focus even on the border of the material sample. Experiments performed on a 2 mm thick non-reverberant composite plate with relatively large dimensions (30×20×0.2 cm) have demonstrated a second advantage of chaotic cavities: their potential to focus energy in non-reverberating samples. In this case, the sample does not contribute to the focusing process and the focusing is achieved by propagating wave that solely come from the direction of the transducer and not from every direction around the focal spot, contrary to what is obtained in a reverberant sample.

We have also demonstrated that the “chaotic cavity transducer” can be used, in combination with the pulse inversion and 1-bit methods, to obtain an image of localized nonlinearity. The preliminary image of a crack at the surface of a steel sample shows that the benefit of using a chaotic cavity transducer, in combination of TR and NEWS techniques, is clearly found in breaking any obvious or hidden symmetry of the problem, leading to an unambiguous retro-focusing. Moreover, the main nonlinear contribution of the crack appears to come from its tip, thereby confirming previously published results. This opens the possibility for high resolution imaging of nonlinear defects. A last opportunity offered by the “chaotic cavity transducer” which needs to be explored is the use of embedded transducers with chaotic emission characteristics in order to perform Structural Health Monitoring (SHM). Obviously, the first step will be to find the minimum impedance mismatch needed in order that an embedded transducer has a sufficient reverberant behaviour to conserve its chaotic properties. Numerical simulations should be performed to support and optimise further the development of the proposed nonlinear acoustic technique.

So, in conclusion, we can expect that this thesis is a first step to the advanced concept for smart maintenance by employing existing NEWS technology in the development of ultrasonic nonlinear imaging systems using “chaotic cavity transducer” for early stage damage detection.



## APPENDIX A: ANALYTICAL SOLUTION FOR THE PROPAGATION OF ELASTIC WAVES IN UNBOUNDED ANISOTROPIC SOLID

In this appendix the analytical solution for the propagation of an elastic wave in unbounded anisotropic solid derived by Carcione *et al.* [34] is presented.

Defining the dimensionless variable

$$\bar{y} = y/\tau,$$

with

$$\tau = V_s t \text{ and } V_s = \sqrt{C_{66}/\rho_0}.$$

The solution for class IV transversely isotropic material along the symmetry axis  $y$  is

$$u_{xy}(y,t) = u_{yx}(y,t) = 0, \quad (\text{A1})$$

$$u_{xx}(y,t) = \begin{cases} 0 & 0 \leq t \leq t_p \\ F_1(\bar{y}) & t_p < t < t_s \\ 0 & t_s \leq t \leq t_1 \\ F_2(\bar{y}) & t > t_1 \end{cases}, \quad (\text{A2})$$

with

$$F_1(\bar{y}) = \frac{1}{\pi\tau} \left[ \frac{1}{4\beta} - \frac{2\beta(\alpha - \bar{y}^2) - (\gamma - (\beta+1)\bar{y}^2)}{4\beta\sqrt{D}} \right] \left[ \frac{-(\gamma - (\beta+1)\bar{y}^2) + \sqrt{D}}{-2(\alpha - \bar{y}^2)(1 - \bar{y}^2)} \right]^{\frac{1}{2}}, \quad (\text{A3})$$

$$F_2(\bar{y}) = \frac{1}{2\pi\tau} \left[ \frac{1}{\sqrt{\beta}} + \sqrt{\frac{\alpha - \bar{y}^2}{1 - \bar{y}^2}} \right] \left[ (\gamma - (\beta+1)\bar{y}^2) + 2\sqrt{\beta(\alpha - \bar{y}^2)(1 - \bar{y}^2)} \right]^{\frac{1}{2}}, \quad (\text{A4})$$

and

$$u_{yy}(y,t) = \begin{cases} 0 & 0 \leq t \leq t_p \\ G_1(\bar{y}) & t_p < t < t_s \\ 0 & t_s \leq t \leq t_1 \\ G_2(\bar{y}) & t > t_1 \end{cases}, \quad (\text{A5})$$

with

$$G_1(\bar{y}) = \frac{1}{\pi\tau} \left[ \frac{1}{4} - \frac{2(1 - \bar{y}^2) - (\gamma - (\beta+1)\bar{y}^2)}{4\sqrt{D}} \right] \left[ \frac{-(\gamma - (\beta+1)\bar{y}^2) + \sqrt{D}}{-2(\alpha - \bar{y}^2)(1 - \bar{y}^2)} \right]^{\frac{1}{2}}, \quad (\text{A6})$$

$$G_2(\bar{y}) = \frac{1}{2\pi\tau} \left[ \frac{1}{\sqrt{\beta}} + \sqrt{\frac{1-\bar{y}^2}{\alpha-\bar{y}^2}} \right] \left[ (\gamma - (\beta+1)\bar{y}^2) + 2\sqrt{\beta(\alpha-\bar{y}^2)(1-\bar{y}^2)} \right]^{\frac{1}{2}}, \quad (\text{A7})$$

where

$$t_s = y/\sqrt{C_{66}/\rho_0}, \quad t_p = y/\sqrt{C_{22}/\rho_0}, \quad t_1 = t_s/\bar{y}_1, \quad (\text{A8})$$

with

$$\bar{y}_1 = \left[ \gamma(\beta+1) - 2\beta(\alpha+1) + 2\sqrt{(\beta(1+\alpha\beta-\gamma)(\alpha+\beta-\gamma))} \right]^{\frac{1}{2}} / (\beta-1). \quad (\text{A9})$$

The quantity  $D(\bar{y})$  is given by

$$D(\bar{y}) = (\gamma - (\beta+1)\bar{y}^2)^2 - 4\beta(\alpha - \bar{y}^2)(1 - \bar{y}^2). \quad (\text{A10})$$

The definition of  $\alpha$ ,  $\beta$  and  $\gamma$  are given by

$$\alpha = C_{22}/C_{66}, \quad \beta = C_{11}/C_{66}, \quad \gamma = 1 + \alpha\beta - (C_{12}/C_{44} + 1)^2. \quad (\text{A11})$$

## APPENDIX B: C-PML MEMORY VARIABLES EVOLUTION EQUATIONS

For completeness all the evolution equations of the introduced memory variables of C-PML in anisotropic and piezoelectric solids are reproduced here.

### C-PML for elastic waves in anisotropic solids:

$$\frac{\partial A_x}{\partial t} = -\delta_x \frac{\partial \tau_{11}}{\partial x} - \beta_x A_x, \quad (\text{B.1})$$

$$\frac{\partial B_y}{\partial t} = -\delta_y \frac{\partial \tau_{12}}{\partial y} - \beta_y B_y, \quad (\text{B.2})$$

$$\frac{\partial C_x}{\partial t} = -\delta_x \frac{\partial \tau_{12}}{\partial x} - \beta_x C_x, \quad (\text{B.3})$$

$$\frac{\partial D_y}{\partial t} = -\delta_y \frac{\partial \tau_{22}}{\partial y} - \beta_y D_y, \quad (\text{B.4})$$

$$\frac{\partial E_x}{\partial t} = -\delta_x \frac{\partial u_1}{\partial x} - \beta_x E_x, \quad (\text{B.5})$$

$$\frac{\partial F_y}{\partial t} = -\delta_y \frac{\partial u_2}{\partial y} - \beta_y F_y, \quad (\text{B.6})$$

$$\frac{\partial G_x}{\partial t} = -\delta_x \frac{\partial u_2}{\partial x} - \beta_x G_x, \quad (\text{B.7})$$

$$\frac{\partial H_y}{\partial t} = -\delta_y \frac{\partial u_1}{\partial y} - \beta_y H_y. \quad (\text{B.8})$$

### C-PML for piezoelectric solids:

$$\frac{\partial A_x}{\partial t} = -\delta_x \frac{\partial \tau_{11}}{\partial x} - \beta_x A_x, \quad (\text{B.9})$$

$$\frac{\partial B_z}{\partial t} = -\delta_z \frac{\partial \tau_{13}}{\partial z} - \beta_z B_z, \quad (\text{B.10})$$

$$\frac{\partial C_x}{\partial t} = -\delta_x \frac{\partial \tau_{13}}{\partial x} - \beta_x C_x, \quad (\text{B.11})$$

$$\frac{\partial D_z}{\partial t} = -\delta_z \frac{\partial \tau_{33}}{\partial z} - \beta_z D_z, \quad (\text{B.12})$$

$$\frac{\partial E_x}{\partial t} = -\delta_x \frac{\partial u_1}{\partial x} - \beta_x E_x, \quad (\text{B.13})$$

$$\frac{\partial F_z}{\partial t} = -\delta_z \frac{\partial u_3}{\partial z} - \beta_z F_z, \quad (\text{B.14})$$

$$\frac{\partial G_x}{\partial t} = -\delta_x \frac{\partial u_3}{\partial x} - \beta_x G_x, \quad (\text{B.15})$$

$$\frac{\partial H_z}{\partial t} = -\delta_z \frac{\partial u_1}{\partial z} - \beta_z H_z, \quad (\text{B.16})$$

$$\frac{\partial I_x}{\partial t} = -\delta_x \frac{\partial \phi}{\partial x} - \beta_x I_x, \quad (\text{B.17})$$

$$\frac{\partial J_z}{\partial t} = -\delta_z \frac{\partial \phi}{\partial z} - \beta_z J_z, \quad (\text{B.18})$$

$$\frac{\partial K_x}{\partial t} = -\delta_x \frac{\partial D_1}{\partial x} - \beta_x K_x, \quad (\text{B.19})$$

$$\frac{\partial L_z}{\partial t} = -\delta_z \frac{\partial D_3}{\partial z} - \beta_z L_z. \quad (\text{B.20})$$

# BIBLIOGRAPHY

- [1] V. Aleshin, V. Gusev, and V. Zaitsev, “*Propagation of initially bi-harmonic sound waves in a 1D semi-infinite medium with hysteretic non-linearity*,” *Ultrasonics* **1-9**, 1053-1059 (2004).
- [2] D. Appelö and G. Kreiss, “*A new absorbing layer for elastic waves*,” *J. Comp. Phys.* **215**, pp. 642-660 (2006).
- [3] D. Appelö and G. Kreiss, “*Application of the perfectly matched layer to the nonlinear wave equation*,” *Wave Motion* **44**, pp. 531-548 (2007).
- [4] H. Atkins and C.W. Shu, “*Quadrature-free implementation of the Discontinuous Galerkin method for hyperbolic equations*,” *AIAA Journal* **36**(5), pp. 775-782 (1998).
- [5] J.-F. Aubry, M. Tanter, J. Gerber, J.-L. Thomas and M. Fink, “*Optimal focusing by spatio-temporal inverse filter. II. Experiments. Application to focusing through absorbing and reverberating media*,” *J. Acoust. Soc. Am.* **110**(1), pp. 48-58 (2001).
- [6] B.A. Auld. *Acoustic Fields and Waves in Solids*, Vol. 1. Krieger Publishing Company, Malabar, Florida (1990).
- [7] S. Ballandras, D. Gachon, J. Masson and W. Daniau, “*Development of absorbing conditions for the analysis of finite dimension elastic wave-guides*,” *Proc. Of the 2007 IEEE Int. Freq. Contr. Symp.*, pp. 729-732, May 2007.
- [8] E. Barbieri, M. Meo, and U. Polimeno, “*Nonlinear wave propagation in damaged hysteretic materials using a frequency domain-based PM space formulation*,” *Int. J. Solids & Struct.* **46**, pp. 165-180 (2009).
- [9] F. Bassi and S. Rebay, “*A high-order accurate discontinuous Galerkin finite element method for numerical solution of the compressible Navier-Stokes equations*,” *J.Comp. Phys.* **131**, pp. 267-279 (1997).
- [10] E. Bécache, S. Fauqueux, and P. Joly, “*Stability of perfectly matched layers, group velocities and anisotropic waves*,” *J. Comput. Phys.* **188**, pp. 399-433 (2003).
- [11] E. Bécache, and A.S. Bonnet-Ben Dhia, “*PMLs for the numerical simulation of harmonic diffracted waves in an elastic plate*,” *Proceedings of the WCU 2003*, pp. 1019-1022, Paris, September 7-10 2003.
- [12] E. Bécache, P.G. Petropoulos and S.D. Gedney, “*On the long-time behavior of unsplit perfectly matched layers*,” *IEEE Trans. Antennas Propagat.* **52** (5), pp. 1335-1342 (2004).
- [13] F. Benmeddour, “*Etude expérimentale et numérique de l’interaction des ondes de Lamb en présence d’endommagements présents dans des structures d’aluminium*,” Ph’D thesis of the Valenciennes University (2006) [in French]
- [14] F. Benmeddour, S. Grondel, J. Assaad, and E. Moulin, “*Study of the fundamental Lamb modes interaction with symmetrical notches*,” *NDT&E International* **41**, pp. 1–9 (2008).
- [15] A. Ben-Menahem, “*Effect of a non-linear boundary layer on the radiation from earthquakes and underground nuclear explosions*,” *Geophys. J. Int.* **132**, pp. 549-576 (1998).
- [16] J.P. Berenger, “*A perfectly matched layer for the absorption of electromagnetic waves*,” *J. Comput. Phys.* **114**, pp. 195-200 (1994).
- [17] J.P. Berenger, “*On the reflection from Cummert’s Nearly Perfectly Matched Layer*,” *IEEE Microwave Wireless Comp. Lett.* **14**(7), pp. 334-336 (2004).

## BIBLIOGRAPHY

- [18] P. Berg, F. If, P. Nielsen, and O. Skovgaard, "Analytical reference solutions," in *Modeling the earth for oil exploration*, edited by K. Helbig, (Pergamon Press, Brussels), pp. 421–427 (1994).
- [19] M.V. Berry, "Regular and irregular semiclassical wavefunctions," *J. Phys. A: Math. Gen.* **10**, pp. 2083-2090 (1977).
- [20] J.O. Blanch, J.O.A. Robertsson, and W.W. Symes, "Modeling of a constant Q: Methodology and algorithm for an efficient and optimally inexpensive viscoelastic technique," *Geophysics* **60**(1), pp. 176-184 (1995).
- [21] L. Borcea, G. Papanicolaou, and C. Tsogka, "Theory and applications of time reversal and interferometric imaging," *Inverse Problems* **19**, pp. S139-S164 (2003).
- [22] O. Bou Matar, V. Preobrazhensky, and P. Pernod, "Two-dimensional axisymmetric numerical simulation of supercritical phase conjugation of ultrasound in active solid media," *J. Acoust. Soc. Am.* **118**(5), pp. 2880-2890 (2005).
- [23] O. Bou Matar, S. Dos Santos, J. Fortineau, T. Goursolle, L. Haumesser, and F. Vander Meulen, "Pseudo spectral simulations of elastic waves propagation in heterogeneous nonlinear hysteretic medium," *Proceedings of the 17th International Symposium of Nonlinear Acoustics*, pp. 95–98 (2005).
- [24] O. Bou Matar, S. Dos Santos, S. Calle, T. Goursolle, S. Vanaverbeke, K. Van Den Abeele, "Simulations of Nonlinear Time Reversal Imaging of Damaged Materials," *Proceedings of the Ninth European Conference on Non-Destructive Testing*, Berlin Sept. 2006.
- [25] O. Bou Matar, E. Galopin, Y.F. Li and O. Ducloux, "An optimized Convolution-Perfectly Matched Layer (C-PML) Absorbing Boundary Condition for the Second-Order Elastic Wave Equation-Application to Surface and Lamb Waves Propagation," *Proceeding of the 1<sup>st</sup> European COMSOL conference*, Grenoble, Oct. 2007.
- [26] O. Bou Matar, Y.F. Li, and K. Van Den Abeele, "On the use of a chaotic cavity transducer in nonlinear elastic imaging," submitted to *Appl. Phys. Lett.*
- [27] E. Brodal, J.S. Hesthaven and F. Melandso, "Numerical modeling of double-layered piezoelectric transducer systems using a high-order discontinuous Galerkin method," *Comput Struct.* **86**, pp. 1747-1756 (2008).
- [28] C.L.E. Bruno, A.S. Gliozzi, M. Scalerandi, and P. Antonaci, "Analysis of elastic nonlinearity using the scaling subtraction method," *Phys. Rev. B* **79**, 064108 (2009).
- [29] A.P. Brysev, F.V. Bunkin, D.V. Vlasov, L.M. Krutyanskii, V.L. Preobrazhenskii, and A.D. Stakhovskii, "Regenerative amplification of acoustic waves with phase conjugation in a ferrite," *Sov. Phys. Acoust.* **34**(6), pp. 567-569 (1988).
- [30] A.P. Brysev, L.M. Krutyansky, and V.L. Preobrazhensky, "Wave phase conjugation of ultrasonic beams," *Phys. Usp.* **41**(8), pp. 793-805 (1998).
- [31] A. Brysev, L. Krutyansky, V. Preobrazhensky, and P. Pernod, "Nonlinear ultrasonic phase conjugate beams and their application in ultrasonic imaging," *Acoust. Phys.* **50**, pp. 623–640 (2004).
- [32] O. Buck, W.L. Morris, and J.M. Richardson, "Acoustic harmonic generation at unbounded interfaces and fatigue cracks," *Appl. Phys. Lett.* **33**(5), pp. 371-373 (1978).
- [33] F.V. Bunkin, D.V. Vlasov, and Yu.A. Kravtsov, "Problem of reversal of an acoustic wavefront and amplification of the reversed wave," *Sov. J. Quantum Electron.* **11**(5), pp. 687-688 (1981).

BIBLIOGRAPHY

- [34] J.M. Carcione, D. Kosloff, and R. Kosloff, “Wave-propagation simulation in an elastic anisotropic (transversely isotropic) solid,” *Mech. Appl. Math.* **41**(3), pp. 319-345 (1988).
- [35] M.H. Carpenter and C.A. Kennedy, “Fourth-Order 2N-Storage Runge-Kutta Schemes,” NASA Technical Memorandum (1994).
- [36] A. Cassereau and M.Fink, “Time-Reversal of Ultrasonic Fields. III: Theory of the Closed Time-Reversal Cavity,” *IEEE Trans. Ultrason. Ferroelectr. Freq. Contr.* **39**, pp. 579-592 (1992).
- [37] M. Castaings, C. Bacon, B. Hosten, and M.V. Predoi, “Finite element predictions for the dynamic response of thermo-viscoelastic material structures,” *J. Acoust. Soc. Am.* **115**, pp. 1125–1133 (2004).
- [38] F. Chagla and P.M. Smith, “Finite difference time domain methods for piezoelectric crystals,” *IEEE Ultrason., Ferroelectr., Freq. Contr.* **53**(10), pp. 1895-1901 (2006).
- [39] C. Cerjan, D. Kosloff, R. Kosloff, and M. Reshef, “A nonreflecting boundary condition for discrete acoustic and elastic wave equations,” *Geophysics* **50**(4), pp. 705–708 (1985).
- [40] N. Chakroun, M. Fink, and F. Wu, “Time reversal processing in non destructive testing,” *IEEE Trans. Ultrason. Ferroelectr. Freq. Control* **42**, pp. 1087-1098 (1995).
- [41] Q. Chen and I. Babuska, “Approximate optimal points for polynomial interpolation of real functions in an interval and in a triangle,” *Comput. Meth. In App. Mech. And Eng.* **128**, pp. 405-417 (1995).
- [42] H.Chen, X. Wang, and W. Lin, “Parallel numerical simulation of the ultrasonic waves in a prestressed formation,” *Ultrasonics* **44**, pp. 1013-1017 (2006).
- [43] W.C. Chew and Q.H. Liu, “Perfectly matched layers for elastodynamics: a new absorbing boundary condition,” *J. Comput. Acoust.* **4**, pp. 341-359 (1996).
- [44] W.C. Chew, J.M. Jin, and E. Michelssen, “Complex coordinate system as a generalized absorbing boundary condition,” *Microwave Opt. Technol. Lett.* **15**, pp. 363-369 (1997).
- [45] R. Clayton and B. Engquist, “Absorbing boundary conditions for acoustic and elastic wave equations,” *Bull. Seismol. Soc. Am.* **67**, pp. 1529-1540 (1977).
- [46] G. Cohen, X. Ferrieres and S. Pernet, “Discontinuous Galerkin method for Maxwell’s equations in time domain,” *Comp. Rend. Phys* **7**, pp. 494-500 (2006).
- [47] F. Collino, P.B. Monk, “Optimizing the perfectly matched layer,” *Comput. Meth. Appl. Mech. & Engin.* **164** (1-2), pp. 157-171 (1998).
- [48] F. Collino and C. Tsogka, “Application of the Perfectly Matched Absorbing Layer Model to the Linear Elastodynamic Problem in Anisotropic Heterogeneous Media,” *Geophysics* **66**(1), pp. 294-307 (2001).
- [49] S.A. Cummer, “A simple, Nearly Perfectly Matched Layer for General Electromagnetic Media,” *IEEE Microwave and Wireless Components Lett.* **13**(2), pp. 128-130 (2003).
- [50] G. Dace, R. Thompson, and O. Buck, “Measurement of the acoustic harmonic generation for materials characterization using contact transducers,” *Rev. Prog. Quant. Nondestr. Eval.* **11**, pp. 2069–2076 (1992).
- [51] A.T. De Hoop, “A modification of Cagniard’s method for solving seismic pulse problems,” *Appl. Sci. Res. B* **8**(1), pp. 349-356 (1960).
- [52] J. Dellinger, D. Vasicek, and C. Sondergeld, “Kelvin notation for stabilizing elastic-constant inversion,” *Revue de l’Institut Français du Pétrole* **53**(5), pp. 709-719 (1998).
- [53] P.P. Delsanto, A.S. Gliozzi, M. Hirsekorn, and M. Nobili, “A 2D spring model for the simulation of ultrasonic wave propagation in nonlinear hysteretic media,” *Ultrasonics* **44**, pp. 279-286 (2006).

BIBLIOGRAPHY

- [54] L. Demkowicz, "Computing with hp-Adaptive Finite Elements: Volume 1, One and Two Dimensional Elliptic and Maxwell Problems," *In Applied Mathematics & Nonlinear Science 7*, Chapman & Hall/CRC, London (2006).
- [55] A. Derode, P. Roux, and M. Fink, "Robust Acoustic Time Reversal with High-Order Multiple Scattering," *Phys. Rev. Lett.* **75**(23), pp. 4206-4209 (1995).
- [56] A. Derode, A. Tourin and M. Fink, "Ultrasonic pulse compression with one bit time reversal through multiple scattering," *J. App. Phys.* **85**(9), pp.6343-6352 (1999).
- [57] C. Draeger and M. Fink, "One-Channel Time Reversal of Elastic Waves in a Chaotic 2D-Silicon Cavity," *Phys. Rev. Lett.* **79**(3), pp. 407-410 (1997).
- [58] C. Draeger, J.C. Aime and M. Fink, "One-channel time-reversal in chaotic cavities: Experimental results," *J. Acoust. Soc. Am.* **105**(2), pp. 618-625 (1999).
- [59] C. Draeger and M. Fink, "One-channel time-reversal in chaotic cavities: Theoretical limits," *J. Acoust. Soc. Am.* **105**(2), pp. 611-617 (1999).
- [60] F.H. Drossaert and A. Giannopoulos, "Complex frequency shifted convolution PML for FDTD modeling of elastic waves," *Wave motion*, **44**(7-8), pp. 593-604 (2007).
- [61] F.H. Drossaert and A. Giannopoulos, "A nonsplit complex frequency-shifted PML based on recursive integration for FDTD modeling of elastic waves," *Geophysics* **72**(2), T9-T17 (2007).
- [62] O. Ducloux *et al.*, "Surface acoustic wave  $\mu$ streaming to enhance biosensing in a droplet-based  $\mu$ TAS platform," *Proceed. of the International Conference on Miniaturized Systems for Chemistry and Life Sciences (MicroTAS)*, Paris (2007).
- [63] M. Dumbser and M. Käser, "An arbitrary high-order discontinuous Galerkin method for elastic waves on unstructured meshes – II. The Three-Dimensional Isotropic Case," *Geophys. J. Int.* **167**, pp. 319-336 (2006).
- [64] M. Dumbser, M. Käser, and E.F. Toro, "An arbitrary high-order discontinuous Galerkin method for elastic waves on unstructured meshes – V. Local Time Stepping and p-Adaptivity," *Geophys. J. Int.* **171**, pp. 695-717 (2007).
- [65] C. Ellegaard, T. Guhr, K. Lindemann, H. Q. Lorensen, J. Nygard, and M. Oxborrow, "Spectral statistics of acoustic resonances in aluminum blocks," *Phys. Rev. Lett.* **75**(8), pp. 1546-1549 (1995).
- [66] A.P. Engsig-Karup, J.S. Hesthaven, H.B. Bingham, and P.A. Madsen, "Nodal DG-FEM solution of high-order Boussinesq-type equations," *J Eng Math* **56**, pp. 351–370 (2006).
- [67] L. Fillinger, A. Sutin, and A. Sarvazyan, "Time Reversal Focusing of the Short Pulses," *Proc. of the 2007 IEEE Ultrason. Symp.*, pp. 220-223 (2007).
- [68] M. Fink, C. Prada, F. Wu, and D. Cassereau, "Self-focusing in inhomogeneous media with time-reversal acoustic mirrors," *Proc. IEEE Ultrason. Symp.*, (2), pp. 681–686 (1989).
- [69] M. Fink, "Time-reversal of ultrasonics fields. I. Basic principles," *IEEE Trans. Ultrason. Ferroelectr. Freq. Contr.* **39**, pp. 555–566 (1992).
- [70] M. Fink, "Time-reversal in acoustics," *Contemp. Phys.* **37**(2), pp. 95–109 (1996).
- [71] M. Fink, D. Cassereau, A. Derode, C. Prada, P. Roux, M. Tanter, J.-L. Thomas and F. Wu, "Time-reversal acoustics," *Rep. Prog. Phys.* **63**, pp. 1933-1995 (2000).

## BIBLIOGRAPHY

- [72] M. Fink and J. Rosny, “*Time-reversed acoustics in random media and in chaotic cavities*,” *Nonlinearity* **15**, R1-R18 (2002).
- [73] S.D. Gedney, “*An anisotropic perfectly matched layer-absorbing medium for the truncation of FDTD lattices*,” *IEEE Transactions on Antennas and Propagation*. **44**, pp. 1630-1639 (1996).
- [74] S.D. Gedney, “*Perfectly matched layer absorbing boundary conditions*,” in *Computational Electrodynamics: The Finite-Difference Time-Domain Method*, edited by A. Taflove and S.C. Hagness (Artech House, Norwood, (2005), Chap. 7, pp. 273-328.
- [75] A.A. Gedroits and V.A. Krasil’nikov, “*Finite-amplitude elastic waves amplitude in solids and deviations from the Hook’s law*,” *Sov. Phys. JETP*. **16**, pp. 1122-1126 (1963).
- [76] M. Ghrist, B. Fornberg and T.A. Driscoll, “*Staggered time integrators for wave equations*,” *SIAM J. Numer. Anal.* **38**(3), pp. 718-741 (2000).
- [77] A. Gliozzi, M. Griffa, and M. Scalerandi, “*Efficiency of time-reversed acoustics for nonlinear damage detection in solids*,” *J. Acoust. Soc. Am.* **120**, pp. 2506–2517 (2006).
- [78] A.S. Gliozzi, M. Nobili, and M. Scalerandi, “*A LISA model of the nonlinear and hysteretic response of interstitial regions to applied stresses*,” in *Universality of non classical nonlinearity*, Ed. P.P. Delsanto, Springer, New York, pp. 251-267 (2007).
- [79] T. Goursolle, S. Calle, S. Dos Santos, and O. Bou Matar, “*A two-dimensional pseudospectral model for time reversal and nonlinear elastic wave spectroscopy*,” *J. Acoust. Soc. Am.* **122**(6), pp.3220–3229 (2007).
- [80] T. Goursolle, S. Dos Santos, S. Calle, and O. Bou Matar “*3D PSTD Simulations of NEWS-TR and TR-NEWS Methods: Application to Nonclassical Nonlinearity Ultrasonic Imaging*,” *Proceeding of 2007 IEEE Ultrasonic Symp.* pp. 585-588 (2007).
- [81] T. Goursolle, S. Dos Santos, O. Bou Matar and S. Calle, “*Non-linear based time reversal acoustic applied to crack detection: Simulation and experiments*,” *Int. J. NonLin. Mech.* **43**, pp. 170-177 (2008).
- [82] G. Grégoire, V. Tournat, D. Mounier, V. Gusev, “*Nonlinear photothermal and photoacoustic processes for crack detection*,” *Eur. Phys. J. Special Topics* **153**, pp. 313–315 (2008).
- [83] J. Grooss and J.S. Hesthaven, “*A level set discontinuous Galerkin method for free surface flows*,” *Comput. Methods Appl. Mech. Engrg.* **195**, pp. 3406–3429 (2006).
- [84] B. Gustafsson, H. O. Kreiss and J. Olinger. *Partial Differential Equations and Difference Approximations*. John Wiley & Sons, New York (2001).
- [85] R.A. Guyer, K.R. McCall and G.N. Boitnott, “*Hysteresis, discrete memory and nonlinear wave propagation in rock: a new paradigm*,” *Phys. Rev. Lett.* **74**(17), pp. 3491–3494 (1995).
- [86] R.A. Guyer and P.A. Johnson, “*Nonlinear mesoscopic elasticity: Evidence for a new class of material*,” *Phys. Today* **52**, pp. 30-36 (1999).
- [87] M. F. Hamilton and D. T. Blackstock, “*Nonlinear Acoustics*,” Academic Press, Austin Texas (1997).
- [88] F.D. Hasting, J.B. Schneider, and S.L. Broschat, “*Application of the perfectly matched layer (pml) absorbing boundary condition to elastic wave propagation*,” *J. Acoust. Soc. Am.* **100**(5), pp. 3061-3069 (1996).

## BIBLIOGRAPHY

- [89] K. Helbig and P.N.J. Rasolofosaon, "A theoretical paradigm for describing hysteresis and nonlinear elasticity in arbitrary anisotropic rocks," Proceedings of the 9th Int. Workshop on Seismic Anisotropy, Society of Exploration Geophysicists, Tulsa (2000).
- [90] J.S. Hesthaven, "From electrostatics to almost optimal nodal sets for polynomial interpolation in a simplex," SIAM J. Num. Anal. **35**, pp. 655-676 (1998).
- [91] J.S. Hesthaven and T. Warburton, "High-order nodal methods on unstructured grids. I. Time-domain solution of Maxwell's Equations," J. Comput. Phys. **181**, pp. 186-221 (2002).
- [92] J.S. Hesthaven and T. Warburton, "High-order nodal discontinuous Galerkin methods for the Maxwell eigenvalue problem," Phil. Trans. R. Soc. Lond. A **362**, 493-524 (2004).
- [93] J.S. Hesthaven, S. Gottlieb, and D. Gottlieb. Spectral methods for time-dependent problems. Providence: Cambridge University Press (2006).
- [94] J.S. Hesthaven and T. Warburton. *Nodal Discontinuous Galerkin Methods, Algorithms, Analysis, and Applications*. Springer. New York (2007).
- [95] W.Y. Hu and S.A. Cummer, "The Nearly Perfectly Matched Layer is a Perfectly Matched Layer," IEEE Trans. Antennas Propagat Lett. **13**, pp. 137-140 (2004).
- [96] W. Hu, A. Abubakar, and T.M. Habashy, "Application of the nearly perfectly matched layer in acoustic wave modelling," Geophysics **72**, SM169 (2007).
- [97] T. Hughes. The Finite Element Method: Linear static and Dynamic Finite Element Analysis. Dover Publications, New York (2000).
- [98] R.K. Ing, M. Fink, and O. Casula, "Self-focusing Rayleigh wave using a time reversal mirror," Appl. Phys. Lett. **68**(2), pp. 161-163 (1996).
- [99] R.K. Ing and M. Fink, "Time-reversed Lamb waves," IEEE Trans. Ultrason. Ferroelectr. Freq. Control **45**(4), pp. 1032-1043 (1998).
- [100] M. Israeli and S.A. Orzag, "Approximation of radiation boundary conditions," J. Comput. Phys. **41**, pp. 115-135 (1981).
- [101] P.A. Johnson, B. Zinszner, P.N.J Rasolofosaon , "Resonance and elastic nonlinear phenomena in rock," J Geophys Res. **101**, pp. 11553-11564 (1996).
- [102] G.E. Karniadakis and S.J. Sherwin. Spectral/hp Element Methods for CFD, Numerical Mathematics and Scientific Computation. Clarendon Press, Oxford (1999).
- [103] M. Käser and M. Dumbser, "An arbitrary high-order discontinuous Galerkin method for elastic waves on unstructured meshes – I. The two-dimensional isotropic case with external source term," Geophys. J. Int. **166**, pp. 855-877 (2006).
- [104] M. Käser, M. Dumbser, J. de la Puente, and H. Igel, "An arbitrary high-order discontinuous Galerkin method for elastic waves on unstructured meshes – III. Viscoelastic Attenuation," Geophys. J. Int. **168**, pp. 224-242 (2007).
- [105] D. Komatitsch, C. Barnes, and J. Tromp, "Simulation of anisotropic wave propagation based upon a spectral element method," Geophysics **65**(4), pp. 1251-1260 (2000).
- [106] D. Komatitsch and J. Tromp, "A perfectly matched layer absorbing boundary condition for the second-order seismic wave equation," Geophys. J. Int. **154**, 146-153 (2003).

BIBLIOGRAPHY

- [107] D. Komatitsch and R. Martin, “*An unsplit convolutional Perfectly Matched Layer improved at grazing incidence for the seismic wave equation,*” *Geophysics* **72**(5), SM155-SM167 (2007).
- [108] U. Kuhl, H.J. Stöckmann, and R. Weaver, “*Classical wave experiments on chaotic scattering,*” *J. Phys. A: Math. Gen.* **38**, 10433-10463 (2005).
- [109] M. Kuzuoglu and R. Mittra, “*Frequency dependence of the constitutive parameters of causal perfectly matched anisotropic absorbers,*” *IEEE Microwave Guided Wave Lett.* **6**, pp. 447-449 (1996).
- [110] L.D. Landau and E.M. Lifshitz. *Theory of elasticity.* Pergamon, New York (1986).
- [111] G. Lazzi and O.P. Gandhi, “*On the optimal design of the PML absorbing boundary condition for the FDTD code,*” *IEEE Trans. Antennas Propagat.* **45**(5), pp. 914-916 (1997).
- [112] P.-Y. Le Bas, K. Van Den Abeele, S. Dos Santos, T. Goursolle, and O. Bou Matar, “*Experimental Analysis for Nonlinear Time Reversal Imaging of Damaged Materials,*” *Proceedings of the Ninth European Conference on Non-Destructive Testing,* (2006).
- [113] P. Lesaint and P. A. Raviart, “*On a Finite Element Method for solving the Neutron Transport Equation,*” *In Mathematical Aspects of Finite Elements in Partial Differential Equations,* Academic Press, New York, pp. 89-145 (1974).
- [114] A.R. Levander, “*Fourth-order finite-difference P-SV seismograms,*” *Geophysics* **53**, pp.1425-1436 (1988).
- [115] R.J. Leveque. *Finite Volume Methods for Hyperbolic Problems.* Cambridge University Press, Cambridge (2002).
- [116] Y.F. Li, O. Bou Matar, V. Preobrazhensky and P. Pernod, “*Convolution-Perfectly Matched Layer (C-PML) absorbing boundary condition for wave propagation in piezoelectric solid,*” *Proceeding of 2008 IEEE Ultrasonic Symp.,* pp. 1568-1571 (2008).
- [117] Y.F. Li and O. Bou Matar, “*Convolution-Perfectly Matched Layer for elastic second-order wave equation,*” submitted to *J. Acoust. Soc. Am.*
- [118] Q.H. Liu and J. Tao, “*The perfectly matched layer for acoustic waves in absorptive media,*” *J. Acoust. Soc. Am.* **102**(4), pp. 2072-2082 (1997).
- [119] Q.H. Liu, “*PML and PSTD algorithm for arbitrary lossy anisotropic media,*” *IEEE Microwave Guided Wave Lett.* **9**, pp. 48-50 (1999).
- [120] R. Martin, D. Komatitsch, and S.D. Gedney, “*A variational formulation of a stabilized unsplit Convolutional Perfectly Matched Layer for the isotropic or anisotropic wave equation,*” *CMES* **37**(3), pp. 274-304 (2008).
- [121] M. Marx, W. Schäf, H. Vehoff, and C. Holzapfel, “*Interaction of microcracks with selected interfaces: Focused ion beam for a systematic crack initiation,*” *Mat. Sci. Eng. A* **435-436**, pp. 595-601 (2006).
- [122] M. Mayer, S. Zaglmayr, K. Wagner and J. Schöberl, “*Perfectly matched layer finite element simulation of parasitic acoustic wave radiation in microacoustic devices,*” *Proc. Of the 2007 IEEE Ultrason. Symp.,* pp. 702-706, Oct. 2007.
- [123] K.R. McCall, “*Theoretical study of nonlinear elastic wave propagation,*” *J. Geophys. Res.* **99**(B2), pp. 2591–2600 (1994).
- [124] K.R. McCall and R.A. Guyer, “*Hysteresis, discrete memory and nonlinear elastic wave propagation in rock: a new theoretical paradigm,*” *Nonlinear Proc. Geophys.* **3**, pp. 89–101 (1996).

BIBLIOGRAPHY

- [125] S. McDonald and A.N. Kaufman, “*Wave chaos in the stadium: Statistical properties of short-wave solutions of the Helmholtz equation,*” *Phys. Rev. A* **37**(8), pp. 3067-3086 (1988).
- [126] K.C. Meza-Fajardo and A.S. Papageorgiou, “*A Nonconvolutional, Split-Filed, Perfectly Matched Layer for Wave Propagation in Isotropic and Anisotropic Elastic Media: Stability Analysis,*” *Bull. Seismol. Soc. Am.* **98**(4), pp. 1811-1836 (2008).
- [127] T. Misaridis and J.A. Jensen, “*Use of modulated excitation signals in medical ultrasound. Part I. Basic concepts and expected benefits,*” *IEEE Trans. Ultrason, Ferroelect, Freq. Contr.* **52**(2), pp. 177-191 (2005).
- [128] G. Montaldo, P. Roux, C. Negreira and M. Fink, “*Generation of very high pressure pulses with 1-bit time reversal in a solid waveguide,*” *J. Acoust. Soc. Am.* **110**(6), pp. 2849-2857 (2001).
- [129] G. Montaldo, D. Palacio, M. Tanter and M. Fink, “*Time reversal kaleidoscope: A smart transducer for three-dimensional ultrasonic imaging,*” *Appl. Phys. Lett.* **84**(19), 3879-3881 (2004).
- [130] G. Montaldo, M. Tanter and M. Fink, “*Revisiting iterative time reversal processing: Application to detection of multiple targets,*” *J. Acoust. Soc. Am.* **115**(2), pp. 776-784 (2004).
- [131] A. Moussatov, B. Castagnède, and V. Gusev, “*Frequency up-conversion and frequency down-conversion of acoustic waves in damaged materials,*” *Phys. Lett. A* **301**, pp. 281–290 (2002).
- [132] D.S. Mountain and J.M.B. Webber “*Stress pattern analysis by thermal emission /SPATE/*”, In: *European Electro-Optics Conference Proceedings*. Bellingham, Wash., Society of Photo-Optical Instrumentation Engineers, pp. 189-196, Oct. (1979).
- [133] G. Mur, “*Absorbing boundary conditions for the finite-difference approximation of time-domain electromagnetic-field equations,*” *IEEE Tran. Electromag. Compat.* **23**, pp. 377- 382 (1981).
- [134] V.E. Nazarov, L.A. Ostrovsky, I .Soustova, A.M. Sutin, “*Nonlinear acoustics of micro-inhomogeneous media,*” *Phys Earth and Planet Interiors* **50**(1) pp.65-73 (1988).
- [135] V. Nazarov and A. Sutin, “*Harmonic generation in the propagation of elastic waves in nonlinear solid media,*” *Sov. Phys. Acoust.* **35**, pp. 410–413 (1989).
- [136] V.E. Nazarov and A.B. Kolpakov, “*Experimental investigations of nonlinear acoustic phenomena in polycrystalline zinc,*” *J. Acoust. Soc. Am.* **107**(4), pp.1915–1921 (2000).
- [137] V.E. Nazarov, A.V. Radostin, L.A. Ostrovsky and I.A. Soustova, “*Wave Processes in Media with Hysteretic Nonlinearity, Part I,*” *Acoust Phys.* **49**(3), pp. 405-415 (2003).
- [138] V.E. Nazarov, A.V. Radostin, L.A. Ostrovsky and I.A. Soustova, “*Wave Processes in Media with Hysteretic Nonlinearity, Part II,*” *Acoust Phys.* **49**(4), pp. 529-534. (2003).
- [139] D.A. Okaya and T.V. McEvelly, “*Elastic wave propagation in anisotropic crustal material possessing arbitrary internal tilt,*” *Geophys. J. Int.* **153**, pp. 344-358 (2003).
- [140] J. Ortin, “*Preisach modeling of hysteresis for a pseudoelastic Cu-Zn-Al single crystal,*” *J. Appl. Phys.* **71**, pp. 1454-1461 (1992).
- [141] L.A. Ostrovsky, “*Nonlinear properties of an elastic medium with cylindrical pores,*” *Sov. Phys. Acoust.* **35**(3), pp. 286-289 (1986).
- [142] L.A. Ostrovsky, “*Wave processes in media with strong acoustic nonlinearity,*” *J. Acoust. Soc. Am.* **90**(6), pp. 3332-3337 (1991).
- [143] T. Özdenvar and G.A. McMechan, “*Causes and reduction of numerical artifacts in pseudo-spectral wavefield extrapolation,*” *Geophys. J. Int.* **126**, pp. 819-828 (1996).

## BIBLIOGRAPHY

- [144] C.B. Peng and M.N. Toksoz, “*An optimal absorbing boundary condition for elastic wave modeling,*” *Geophysics* **60**, pp. 296-301 (1995).
- [145] C. Prada and M. Fink, “*Separation of interfering acoustic scattered signals using the invariants of the time-reversal operator. Application to Lamb wave characterization,*” *J. Acoust. Soc. Am.* **104**(2), pp. 801-807 (1998).
- [146] C. Prada, E. Kerbrat, D. Cassereau, M. and Fink, “*Time reversal techniques in ultrasonic nondestructive testing of scattering media,*” *Inverse Problems* **18**, pp. 1761-1773 (2002).
- [147] C. Prada and J.L. Thomas, “*Experimental subwavelength localization of scatterers by decomposition of the time reversal operator interpreted as a covariance matrix,*” *J. Acoust. Soc. Am.* **114**(1), pp. 235-243 (2003).
- [148] J. Puente, M. Käser, M. Dumbser and H. Igel, “*An Arbitrary High-Order Discontinuous Galerkin method for Elastic Waves on Unstructured Meshes – IV. Anisotropy,*” *Geophys. J. Int.* **169**, pp.1210-1228 (2007).
- [149] N. Quieffin, S. Catheline, R.K Ing and M. Fink, “*Real-time focusing using an ultrasonic one channel time-reversal mirror coupled to a solid cavity,*” *J. Acoust. Soc. Am.* **115**(5), pp. 1955-1960 (2004).
- [150] N. Quieffin, S. Catheline, R.K. Ing and M. Fink, “*2D pseudo-array using an ultrasonic one channel time-reversal mirror,*” *Proc. Of the 2004 IEEE Ultrason. Symp.*, pp. 801-804 (2004).
- [151] N. Quieffin, “*Etude du rayonnement acoustique de structures solides : vers un système d’imagerie haute resolution,*” Thèse de Doctorat de l’Université Paris VI (2004).
- [152] W.H. Reed and T.R. Hill, “*Triangular mesh method for the neutron transport equation,*” Los Alamos Scientific Laboratory Report, LA-UR-73-479 (1973).
- [153] J.M. Richardson, “*Harmonic generation at an unbounded interface – I. Planar interface between semi-infinite elastic media,*” *Int. J. Engng.* **17**, pp. 73-85 (1979).
- [154] J.O.A. Robertsson, J.O. Blanch, and W.W. Symes, “*Viscoelastic finite-difference modeling,*” *Geophysics* **59**(9), pp. 1444-1456 (1994).
- [155] J.O.A. Robertsson, “*A numerical free-surface condition for elastic/viscoelastic finite-difference modeling in the presence of topography,*” *Geophysics* **61** (6). pp.1921-1934 (1996).
- [156] J.A. Roden and S.D.Gedney, “*Convolution PML(CPML): An efficient FDTD implementation of the CFS-PML for arbitrary media,*” *Microwave Opt. Technol. Lett.* **27**, pp. 334-339 (2000).
- [157] A.J. Rogovsky, “*Development and application of ultrasonic dry-contact and air-contact C-scan systems for non-destructive evaluation of aerospace components,*” *Material Evaluation* **50**, pp. 1491-1497 (1991).
- [158] P. Roux, B. Roman, and M. Fink, “*Time-reversal in an ultrasonic waveguide,*” *Appl. Phys. Lett.* **70**(14), pp. 1811-1813 (1997).
- [159] P. Roux and M. Fink, “*Time-reversal in a waveguide: Study of the temporal and spatial focusing,*” *J. Acoust. Soc. Am.* **107**, pp. 2418-2429 (2000).
- [160] H. Salman, J.S. Hesthaven, T. Warburton, G. Haller, “*Predicting transport by Lagrangian coherent structures with a high-order method,*” *Theor. Comput. Fluid Dyn.* **21**, pp. 39–58 (2007).
- [161] B. Sarens, G. Kalogiannakis, C. Glorieux, D. Van Henelrijck, “*Full-field imaging of nonclassical acoustic nonlinearity,*” *Appl. Phys. Lett.* **91**, 264102 (2007).

## BIBLIOGRAPHY

- [162] M. Scalerandi, V. Agostini, P.P. Delsanto, K. Van Den Abeele and P.A. Johnson, “*Local interaction simulations approach to modeling nonclassical, nonlinear elastic behavior in solids,*” J. Acoust. Soc. Am. **113**(6), pp.3049–3059 (2003).
- [163] M. Scalerandi, M. Nobili, M. Griffa, A.S. Gliozzi, and F. Bosia, “*Numerical analysis of the anomalous elastic behaviour of hysteretic media: Quasistatic, dynamic and relaxation experiments,*” in *Universality of non classical nonlinearity*, Ed. P.P. Delsanto, Springer, New York, pp. 269-285 (2007).
- [164] M. Scalerandi, A.S. Gliozzi, C.L.E. Bruno, D. Masera, and P. Bocca, “*A scaling method to enhance detection of a nonlinear elastic response,*” Appl. Phys. Lett. **92**, 101912 (2008).
- [165] M. Scalerandi, A.S. Gliozzi, C.L.E. Bruno, and K. Van Den Abeele, “*Nonlinear acoustic time reversal imaging using the scaling subtraction method,*” J. Phys. D: Appl. Phys. **41**, 215404 (2008).
- [166] J.B. Schneider, C.L. Wagner and S.L. Broschat, “*Implementation of transparent sources embedded in acoustic finite-difference time-domain grids,*” J. Acoust. Soc. Am. **103**(1), pp. 136-142 (1998).
- [167] Y. Shi and C.H. Liang, “*Simulations of The Left-handed Medium Using Discontinuous Galerkin Method Based on The Hybrid Domains,*” Progress In Electromagnetics Research, PIER **63**, pp. 171-191 (2006).
- [168] C.W. Shu and S. Osher, “*Efficient Implementation of Essentially Non-Oscillatory Shock-Capturing schemes,*” J. Comput. Phys. **77**(77), pp. 439-471 (1988).
- [169] D.H. Simpson, C.T. Chin, and P.N. Burns, “*Pulse inversion Doppler: A new method for detecting nonlinear echoes from microbubble contrast agents,*” IEEE Tans. Ultrason. Ferroelectr. Freq. Control. **46**, pp. 372-382 (1999).
- [170] E.A. Skelton, S.D.M. Adams and R.V. Craster, “*Guided elastic waves and perfectly matched layers,*” Wave Motion **44**, pp. 573-592 (2007).
- [171] J. Sochacki, R. Kubichek, J. George, W.R. Fletcher, and S. Smithson, “*Absorbing boundary conditions and surface waves,*” Geophysics **52**, pp. 60-71 (1987).
- [172] H. Sohn, H.W. Park, K.H. Law, and C.H. Farrar, “*Damage detection in composite plates by using an enhanced time reversal method,*” J. Aerospace Eng., ASCE **20**(3), pp. 141-151 (2007).
- [173] I.Yu. Solodov, A.F. Asainov, and K. Sel Len, “*Non-linear SAW reflection: experimental evidence and NDE applications,*” Ultrasonics **31**(2), pp. 91-96 (1993).
- [174] I. Solodov, J. Wackerl, K. Pfeleiderer, and G. Busse, “*Nonlinear self-modulation and subharmonic acoustic spectroscopy for damage detection and location,*” Appl. Phys. Lett. **84**, 5386-5388 (2004).
- [175] I. Solodov and G. Busse, “*Nonlinear air-coupled emission: The signature to reveal and image microdamage in solid materials,*” Appl. Phys. Lett. **91**, 251910 (2007).
- [176] A. Sutin, J.A. TenCate, and P.A. Johnson, “*Development of nonlinear time reversed acoustics (NLTRA) for applications to crack detection in solids,*” Proceedings of the Fifth World Congress on Ultrasonics, pp. 121–124. (2003).
- [177] A. Sutin, J.A. TenCate and P.A. Johnson, “*Single-channel time reversal in elastic solids,*” J. Acoust. Soc. Am. **116**, 2779-2784 (2004).
- [178] A. Taflove and S.C. Hagness. *Computational Electrodynamics: The Finite-Difference Time-Domain Method*. Arthch House, Boston, Third Edition (2005).
- [179] M. Tanter, J.L. Thomas, and M. Fink, “*Time reversal and the inverse filter,*” J. Acoust. Soc. Am. **108**, pp. 223-234 (2000).

BIBLIOGRAPHY

- [180] M. Tanter, J.-F. Aubry, J. Gerber, J.-L. Thomas and M. Fink, "Optimal focusing by spatio-temporal inverse filter. I. Basic principles," J. Acoust. Soc. Am. **110**(1), pp.37-47 (2001).
- [181] M. Taylor, B. Wingate, and R.E. Vincent, "An algorithm for computing Fekete points in the triangle," SIAM J.Num. Anal. **38**, pp. 1707-1720 (2000).
- [182] F.L. Teixeira and W.C. Chew, "A general approach to extend Berenger's absorbing boundary condition to anisotropic and dispersive media," IEEE Transactions on Antennas and Propagation. **46**, pp. 1386-1387 (1998).
- [183] F.L. Teixeira and W.C. Chew, "General closed-form PML constitutive tensors to match arbitrary bianisotropic and dispersive linear media," IEEE Microwave and Guided Wave Lett. **8**, pp. 223-225 (1998).
- [184] T.J. Ulrich, P.A. Johnson and A. Sutin, "Imaging nonlinear scatters applying the time reversal mirror," J. Acoust. Soc. Am. **119**, pp. 1514-518 (2006).
- [185] T.J. Ulrich, P.A. Johnson, and R. Guyer, "Interaction Dynamics of Elastic Waves with a Complex Nonlinear Scatterer through the Use of a Time Reversal Mirror," Phys. Rev. Lett. **98**, 104301 (2007).
- [186] S. Vanaverbeke and K. Van Den Abeele, "Two-dimensional modeling of wave propagation in materials with hysteretic nonlinearity," J. Acoust. Soc. Am. **122**(1), pp. 58-72 (2007).
- [187] K. Van den Abeele, "Elastic pulsed wave propagation in media with second or higher order nonlinearity. Part I. Theoretical Framework," J. Acoust. Soc. Am. **99**(6), pp. 3334–3345 (1996).
- [188] K. Van den Abeele, "Elastic pulsed wave propagation in media with second or higher order nonlinearity. Part II. Simulation of experimental measurements on Berea sandstone," J. Acoust. Soc. Am. **99**(6), pp. 3346–3352 (1996).
- [189] K. Van Den Abeele, P.A. Johnson and A.M. Sutin, "Nonlinear elastic wave spectroscopy (NEWS) techniques to discern material damage, part I: Nonlinear wave modulation spectroscopy (NWMS)," Res Nondest Eval. **12**/1, pp. 17-30 (2000).
- [190] K. Van Den Abeele, J. Carmeliet, J.A. TenCate, P.A. Johnson, "Nonlinear Elastic Wave Spectroscopy (NEWS) techniques to discern material damage. Part II: Single Mode Nonlinear Resonant Acoustic Spectroscopy (SIMONRAS)," Res Nondestr Eval. **12**/1, pp. 31-42 (2000).
- [191] K. Van Den Abeele, K. Van De Velde, J. Carmeliet, "Inferring the degradation of pultruded composites form dynamic nonlinear resonance measurements," Polymer Composites **22**(4), pp. 555-567 (2001).
- [192] K. Van Den Abeele, A. Sutin, J. Carmeliet, and P.A. Johnson, "Microdamage diagnostics using nonlinear elastic wave spectroscopy (NEWS)," NDT & E Int. **34**, pp. 239–248 (2001).
- [193] K. Van Den Abeele, F. Schubert, V. Aleshin, F. Windels and J. Carmeliet, "Resonant bar simulations in media with localized damage," Ultrasonics **42**, pp.1017-1024 (2004).
- [194] K. Van Den Abeele, S. Vanaverbeke, "Multiscale approach and simulations of wave propagation and resonance in media with localized microdamage: 1-D and 2-D cases," in Universality of non classical nonlinearity, Ed. P.P. Delsanto, Springer, New York, pp. 177- 201 (2007).
- [195] X. Verbeek, L. Ledoux, J. Willigers, P. Brandsi and A. Hoeks, "Experimental investigation of the pulse inversion technique for imaging ultrasound contrast agents," J. Acoust. Soc. Am. **107**, pp. 2281-2290 (2000).

## BIBLIOGRAPHY

- [196] H.K. Versteeg and W. Malalasekera. An introduction to computational fluid dynamics: the finite volume method. Pearson Education, Second Edition. (2007).
- [197] M. Vila, F. Vander Meulen, S. Dos Santos, L. Haumesser, O. Bou Matar, “*Contact phase modulation method for acoustic nonlinear parameter measurement in solid,*” *Ultrasonics* **42**, pp. 1061-1065 (2004).
- [198] P. Voinovich, A. Merlen, E. Timofeev, and K. Takayama, “*A Godunov-type finite-volume scheme for unified solid-liquid elastodynamics on arbitrary two-dimensional grids,*” *Shock wave*. **13**(3), pp. 221-230 (2003).
- [199] C.H. Wang, J.T. Rose, and F.K. Chang, “A computerized time-reversal method for structural health monitoring,” Proc. of SPIE Conference on Smart Structures and NDE, San Diego, CA, USA (2003).
- [200] L. Wang and S.I. Rhokhlin, “*Modeling of Wave Propagation in Layered Piezoelectric Media by a Recursive Asymptotic Method,*” *IEEE Trans. Ultrason., Ferroelectr., Freq. Contr.* **51**(9), pp.1060-1071 (2004).
- [201] W. Wang, X. Li, and C.W. Shu, “*The discontinuous Galerkin method for the multiscale modeling of dynamics of crystalline solids,*” *Multiscale Model. Simul.* **7**(1), pp. 294-320 (2008).
- [202] R. L. Weaver, “*On diffuse waves in solid media,*” *J. Acoust. Soc. Am.* **71**(6), pp. 1608-1609 (1982).
- [203] R. Weaver and J. Burkhardt, “*Weak Anderson localization and enhanced backscatter in reverberation rooms and quantum dots,*” *J. Acoust. Soc. Am.* **96**, pp. 3186-3190 (1994).
- [204] P. Wilcox, “*Omni-directional guided wave transducer arrays for the rapid inspection of large areas of plate structures,*” *IEEE Trans. Ultrason. Ferroelectr. & Freq. Contr.* **50**(6), pp. 699-709 (2003).
- [205] F. Wu, J.L. Thomas, and M. Fink, “*Time-reversal of ultrasonic fields. II. Experimental results,*” *IEEE Trans. Ultrason. Ferroelectr. Freq. Control* **39**, pp. 567-578 (1992).
- [206] T. Xiao and Q.H. Liu, “*Three-Dimensional unstructured-grid Discontinuous Galerkin method for Maxwell’s equation with well-posed perfectly matched layer,*” *Microwave & Opt. Technol. Lett.* **46**(5), pp. 459-463 (2005).
- [207] H. Xu, S.M. Day, and J.B.H. Minster, “*Model for nonlinear wave propagation derived from rock hysteresis measurements,*” *J. Geophys. Res.* **103**, pp. 29915-29929 (1998).
- [208] H. Xu, S.M. Day, and J.B.H. Minster, “*Two-dimensional linear and nonlinear wave propagation in a half-space,*” *Bull. Seism. Soc. Am.* **89**(4), pp. 903-917 (1999).
- [209] H. Xu, S.M. Day, and J.B.H. Minster, “*Hysteresis and two-dimensional nonlinear wave propagation in Berea Sandstone,*” *J. Geophys. Res.* **105**, pp. 6163-6175 (2000).
- [210] K.S. Yee, “*Numerical solution of initial boundary value problems involving Maxwell’s equations in isotropic media,*” *IEEE Trans. Antennas Propag.* **AP-14**, pp. 302-307 (1966).
- [211] X.J. Yuan, D. Borup, J.W. Wiskin, M. Berggren, R. Eidens and S.A. Johnson, “*Formulation and Validation of Bergenger’s PML Absorbing Boundary for the FDTD Simulation of Acoustic Scattering,*” *IEEE Trans. Ultrason. Ferroelectr. Freq.* **44**(4), pp. 816-822 (1997).
- [212] V.Yu. Zaitsev, V. Gusev, and B. Castagnede, “*Observation of the “Luxemburg-Gorky” effect for elastic waves,*” *Ultrasonics* **40**, pp. 627-631 (2002).
- [213] V.Yu. Zaitsev, V. Gusev, and B. Castagnede, “*Luxemburg-Gorky effect retooled for elastic waves: A mechanism and experimental evidence,*” *Phys. Rev. Lett.* **89**(10), 105502 (2002).

## BIBLIOGRAPHY

- [214] L.K. Zarembo and V.A. Krasil'nikov, "*Some problems in the propagation of ultrasonic waves of finite amplitude in liquids,*" *Sov. Phys. Usp.* **2**(68), pp. 580-599 (1959).
- [215] L.K. Zarembo and V.A. Krasil'nikov. *Introduction to Nonlinear Acoustic.* Nauka, Moscow (1966).
- [216] Y. Zeng, Q.H. Liu and G. Zhao, "*Multidomain pseudospectral time-domain method for acoustic waves in lossy media,*" *J. Comp. Acoustic* **12**, pp. 277-299 (2004).
- [217] Y. Zheng and X. Huang, "*Anisotropic Perfectly Matched Layers for elastic waves in cartesian and curvilinear coordinates,*" in: *Earth Resources Laboratory 2002 Industry Consortium Meeting.*, Dept. Earth, Atmospheric, and Planetary sciences, Massachusetts Institute of Technology, Cambridge, MA USA (2002).
- [218] H.S. Zheng, Zh.J. Zhang and E. Liu, "*Non-linear seismic wave propagation in anisotropic media using the flux-corrected transport technique,*" *Geophys. J. Int.* **165**, pp.943-956 (2006).
- [219] G. Zumpano and M. Meo, "*A new nonlinear elastic time reversal acoustic method for the identification and localisation of stress corrosion cracking in welded plate-like structures – A simulation study,*" *Int. J. Solids & Struct.* **44**, pp. 3666-3684 (2007).
- [220] G. Zumpano and M. Meo, "*Damage localization using transient non-linear elastic wave spectroscopy on composite structures,*" *Int. J. Non-Lin. Mech.* **43**, pp. 217-230 (2008).
- [221] Th. Zweschper, A. Dillenz, G. Riegert, D. Scherling, and G. Busse, "*Ultrasound excited thermography using frequency modulated elastic waves,*" *Insight*, **45**(3), pp. 178-182 (2003).



## PUBLICATION LIST

### International Conference with proceedings

O. Bou Matar, E. Galopin, **Y.F. Li** and O. Ducloux, “*An optimized Convolution-Perfectly Matched Layer (C-PML) Absorbing Boundary Condition for the Second-Order Elastic Wave Equation-Application to Surface and Lamb Waves Propagation,*” Proceeding of the 1<sup>st</sup> European COMSOL conference, Grenoble, Oct. 2007. (CD-ROM)

**Y.F. Li**, O. Bou Matar, V. Preobrazhensky and P. Pernod, “*Convolution-Perfectly Matched Layer (C-PML) absorbing boundary condition for wave propagation in piezoelectric solid,*” Proceeding of 2008 IEEE Ultrasonic Symp., pp. 1568-1571 (2008).

### International Conference without proceedings

O. Bou Matar, **Y.F. Li**, V. Preobrazhensky, and P. Pernod, “*An optimized Convolution-Perfectly Matched Layer (C-PML) absorbing boundary condition for the second-order elastic wave equation,*” International Congress on Ultrasonics – World Congress on Ultrasonics, Vienne, Avril 2007.

O. Bou Matar, **Y.F. Li**, V. Preobrazhensky, and P. Pernod, “*Pseudo-spectral simulation of 1D nonlinear propagation in heterogeneous elastic media,*” International Congress on Ultrasonics – World Congress on Ultrasonics, Vienne, Avril 2007.

O. Bou Matar, **Y.F. Li**, V. Preobrazhensky and P. Pernod, “*Localized nonlinearity time reversal imaging with chaotic cavities,*” Acoustic’s08, Paris, 29 Juin - 4 Juill. 2008. (**invité**)

O. Bou Matar, **Y.F. Li**, V. Preobrazhensky, and P. Pernod, “*Application of chaotic cavities to localized nonlinearity imaging with time reversal: A numerical and experimental study,*” 18<sup>th</sup> ISNA, Stockholm, 7-10 Juillet 2008.

O. Bou Matar, **Y.F. Li**, V. Preobrazhensky, and P. Pernod, “*Application of chaotic cavities to localized nonlinearity imaging with time reversal,*” IEEE UFFC Symp., Pékin, 2-5 Novembre 2008.

**Y.F. Li**, O. Bou Matar, S. Delrue, and K. Van Den Abeele, “*Optimization of chaotic cavities transducers to time reversal nonlinear elastic wave spectroscopy,*” International Congress on Ultrasonics, Santiago, Chile, 11-17 Janvier 2009.

### Submitted to international journal

**Y.F. Li** and O. Bou Matar, “*Convolution-Perfectly Matched Layer for elastic second-order wave equation,*” submitted to J. Acoust. Soc. Am.

O. Bou Matar, **Y.F. Li**, and K. Van Den Abeele, “*On the use of a chaotic cavity transducer in nonlinear elastic imaging,*” submitted to Appl. Phys. Lett.



## RESUME

Dans cette thèse nous proposons de développer un système d'imagerie ultrasonore innovante de micro- défauts basé sur l'utilisation conjointe de techniques d'acoustique non linéaire et du concept de "transducteur à cavité chaotique". Ce transducteur correspond à la combinaison d'une céramique piézoélectrique collée sur une cavité de forme chaotique et du principe de retournement temporel. La faisabilité et les performances de ce nouveau système sont explorées par des simulations numériques. Des paramètres optimaux d'utilisation pour une implémentation expérimentale sont proposés.

Une grande partie des travaux menés dans le cadre de cette thèse se concentre sur le développement d'outils numériques permettant l'amélioration de telles techniques d'imagerie. Un schéma d'éléments finis de type Galerkin Discontinu (GD) est étendu à l'elastodynamique non linéaire. Un type de zone absorbante parfaitement adaptée, appelée "Nearly Perfectly Matched Layer" (NPML) a aussi été développé. Dans le cas de matériaux orthotropes comme des problèmes de stabilité apparaissent, un mélange de NPML et de zone atténuante, dont on contrôle la proportion respective, est introduit afin de stabiliser les NPML.

Une validation expérimentale du concept de "transducteur à cavité chaotique" pour la focalisation dans un milieu solide, réverbérant ou non, en utilisant une seule source est réalisée. Les méthodes de retournement temporel et de filtre inverse sont présentées et comparées. La démonstration expérimentale qu'un "transducteur à cavité chaotique" peut être utilisé conjointement avec les méthodes d'inversion d'impulsion afin de réaliser une image de non linéarités localisées est présentée.

## SUMMARY

In this thesis we propose the development of an innovative micro-damage imaging system based on a combination of Nonlinear Elastic Wave Spectroscopy techniques and "chaotic cavity transducer" concept. It consists of a combination of a PZT ceramic glued to a cavity of chaotic shape with the time reversal principle. The feasibility and capabilities of these new ideas is explored by numerical simulations, and optimal operational parameters for experimental implementation are suggested based on the modelling support.

A large part of the research work conducted in this thesis is concentrated on the development of numerical simulation tools to help the improvement of such nonlinear imaging methods. A nodal Discontinuous Galerkin Finite Element Method (DG-FEM) scheme is extended to nonlinear elastodynamic including source terms. A Perfectly Matched Layer absorbing boundary condition well adapted to the DG-FEM scheme, called Nearly Perfectly Matched Layer (NPML), is also developed. In the case of orthotropic material as stability problems appear, a mixture of NPML and sponge layer, with a controllable ratio of these two kinds of absorbing layers, is introduced.

The experimental validation of "chaotic cavity transducer" to focalize in reverberant and non-reverberant solid media with only one source is made. Classical time reversal, inverse filter and 1 Bit time reversal process are discussed and compared. The experimental demonstration of the use of a "chaotic cavity transducer", in combination with the pulse inversion and 1-bit methods, to obtain an image of localized nonlinearity is made. This opens the possibility for high resolution imaging of nonlinear defects.